MAGNETIC FLUX ROPES: FROM THE SUN TO THE EARTH AND BEYOND

EDITED BY: Rui Liu, Jie Zhang, Yuming Wang and Hongqiang Song
PUBLISHED IN: Frontiers in Astronomy and Space Sciences and Frontiers in Physics

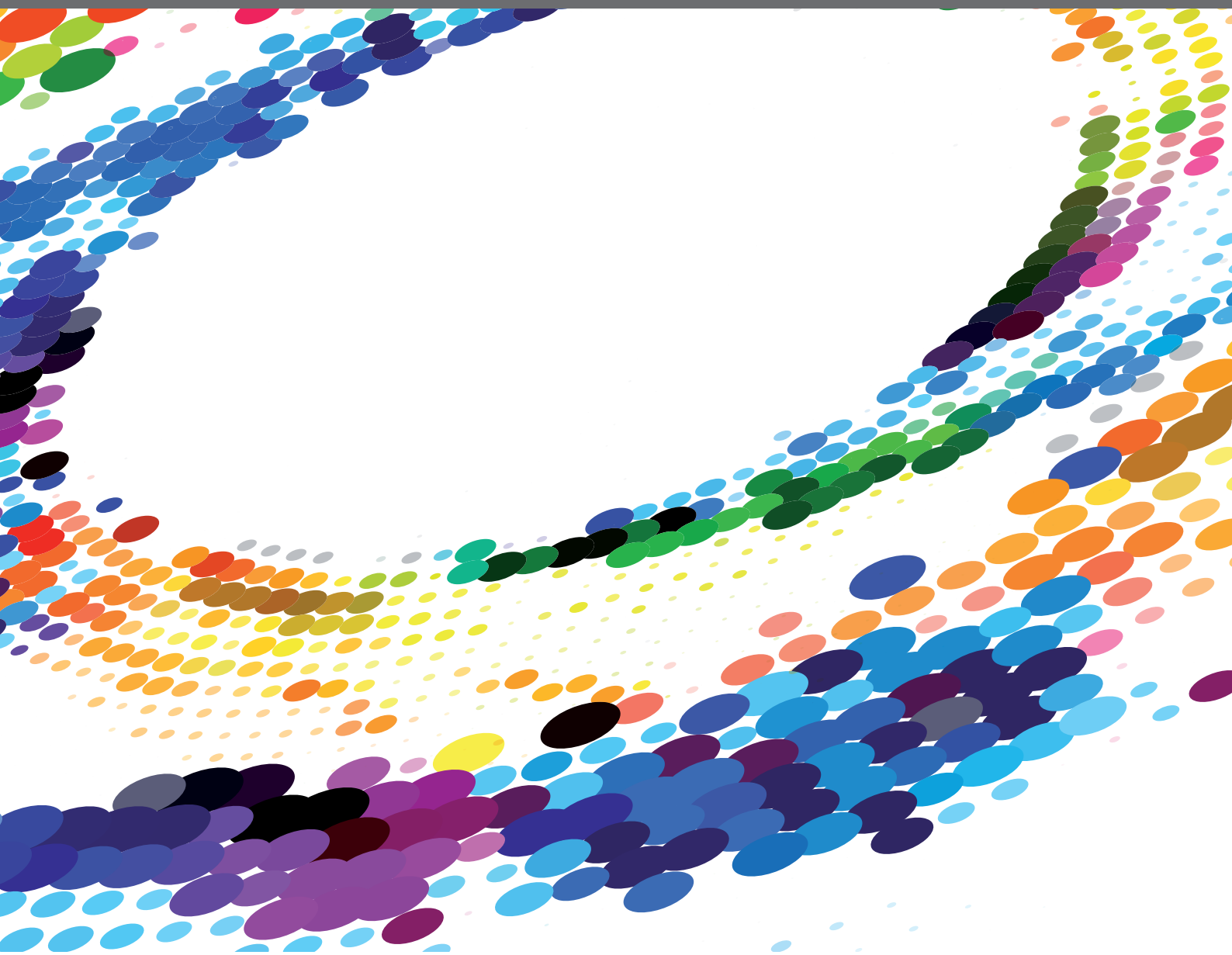

frontiers Research Topics

frontiers

ISSN 1664-8714
ISBN 978-2-88966-336-1
DOI 10.3389/978-2-88966-336-1

About Frontiers

Frontiers is more than just an open-access publisher of scholarly articles: it is a pioneering approach to the world of academia, radically improving the way scholarly research is managed. The grand vision of Frontiers is a world where all people have an equal opportunity to seek, share and generate knowledge. Frontiers provides immediate and permanent online open access to all its publications, but this alone is not enough to realize our grand goals.

Frontiers Journal Series

The Frontiers Journal Series is a multi-tier and interdisciplinary set of open-access, online journals, promising a paradigm shift from the current review, selection and dissemination processes in academic publishing. All Frontiers journals are driven by researchers for researchers; therefore, they constitute a service to the scholarly community. At the same time, the Frontiers Journal Series operates on a revolutionary invention, the tiered publishing system, initially addressing specific communities of scholars, and gradually climbing up to broader public understanding, thus serving the interests of the lay society, too.

Dedication to Quality

Each Frontiers article is a landmark of the highest quality, thanks to genuinely collaborative interactions between authors and review editors, who include some of the world's best academicians. Research must be certified by peers before entering a stream of knowledge that may eventually reach the public - and shape society; therefore, Frontiers only applies the most rigorous and unbiased reviews.
Frontiers revolutionizes research publishing by freely delivering the most outstanding research, evaluated with no bias from both the academic and social point of view. By applying the most advanced information technologies, Frontiers is catapulting scholarly publishing into a new generation.

What are Frontiers Research Topics?

Frontiers Research Topics are very popular trademarks of the Frontiers Journals Series: they are collections of at least ten articles, all centered on a particular subject. With their unique mix of varied contributions from Original Research to Review Articles, Frontiers Research Topics unify the most influential researchers, the latest key findings and historical advances in a hot research area! Find out more on how to host your own Frontiers Research Topic or contribute to one as an author by contacting the Frontiers Editorial Office: researchtopics@frontiersin.org

MAGNETIC FLUX ROPES: FROM THE SUN TO THE EARTH AND BEYOND

Topic Editors:
Rui Liu, University of Science and Technology of China, China
Jie Zhang, George Mason University, United States
Yuming Wang, University of Science and Technology of China, China
Hongqiang Song, Shandong University, China

Citation: Liu, R., Zhang, J., Wang, Y., Song, H., eds. (2021). Magnetic Flux Ropes: From the Sun to the Earth and Beyond. Lausanne: Frontiers Media SA. doi: 10.3389/978-2-88966-336-1

Table of Contents

frontiers in Astronomy and Space Sciences

EDITORIAL
published: 16 November 2020
doi: 10.3389/fspas.2020.605957

Editorial: Magnetic Flux Ropes: From the Sun to the Earth and Beyond

Rui Liu[1,2,3]*, *Jie Zhang*[4], *Yuming Wang*[1,2] *and Hongqiang Song*[5]

[1] CAS Key Laboratory of Geospace Environment, Department of Geophysics and Planetary Sciences, University of Science and Technology of China, Hefei, China, [2] CAS Center for Excellence in Comparative Planetology, Hefei, China, [3] Mengcheng National Geophysical Observatory, School of Earth and Space Sciences, University of Science and Technology of China, Hefei, China, [4] Department of Physics and Astronomy, George Mason University, Fairfax, VA, United States, [5] School of Space Science and Physics, Shandong University, Weihai, China

Keywords: solar physics, interplanetary physics, space physics, solar magnetism, coronal mass ejection, interplanetary coronal mass ejection

Editorial on the Research Topic:

Magnetic Flux Ropes: From the Sun to the Earth and Beyond

The eruptions in the solar atmosphere exhibit distinctly diverse patterns across a vast range of spatio-temporal scales, from ever-expanding large-scale coronal mass ejections (CMEs), to localized flares within active regions harboring sunspots, to collimated jets down to the resolution limit of modern telescopes. As the core structure of various eruptive phenomena in the solar atmosphere, magnetic flux ropes, which are characterized by coherently twisted magnetic field lines, hold the key to understanding the physical mechanisms of solar eruptions and to our predictive capability of space weather. The purpose of this Frontiers Research Topic on magnetic flux ropes is to provide a forum to bring together multi-wavelength remote sensing and in-situ diagnostics, to integrate observation and numerical modeling, and to confront established models with new observations. The articles published in this Topic represent the most active fronts of research on a few important questions, namely, how flux ropes originate and evolve toward destabilization and beyond, how they are structured, and how they interact with each other and with surrounding magnetic fields and plasma. Below we briefly summarize the major results achieved by these articles.

Solar filaments (or prominences if appearing above the solar limb) are an important indicator of magnetic flux ropes on the Sun, although it has been controversially debated how a filament is magnetically structured, more specifically, whether the dense filament mass is supported against gravity by magnetic dips in a flux rope or a sheared arcade. Since the coronal magnetic field is extremely difficult to measure, filament mass serves as a valuable field tracer, especially when the individual threads are resolved and their dynamic motions are monitored. In equilibrium, dense filament plasmas may only trace a portion of magnetic field lines, but when disturbed, they must flow dominantly along field lines in a low-β plasma environment. Mainly in chromospheric Hα filtergrams, signatures of flux ropes in the lower atmosphere have been detected by meter-class ground-based telescopes with a spatial resolution as high as 0.1 to 0.2 arcsec [see the review article by Wang and Liu, 2019]. Combining Doppler maps with flow maps in the plane of sky, [Awasthi and Liu, 2019] revealed a complex yet organized flow pattern inside a bubble underneath a prominence, which could be envisaged as counter-streaming mass motions in a helically distorted field resulting from the internal kink mode $m = 2$.

Magnetic twist is an inherent property of flux ropes. A CME flux rope is often envisaged to build up like an onion with nested layers of magnetic flux added sequentially as the eruption progresses, which

OPEN ACCESS

Edited by:
Scott William McIntosh, National Center for Atmospheric Research (UCAR), United States

Reviewed by:
Abhishek Kumar Srivastava, Indian Institute of Technology (BHU), India

***Correspondence:**
Rui Liu
rliu@ustc.edu.cn

Specialty section:
This article was submitted to Frontiers in Astronomy and Space Sciences, a section of the journal Frontiers in Stellar and Solar Physics

Received: *14 September 2020*
Accepted: *09 October 2020*
Published: *16 November 2020*

Citation:
Liu R, Zhang J, Wang Y and Song H (2020) Editorial: Magnetic Flux Ropes: From the Sun to the Earth and Beyond. Front. Astron. Space Sci. 7:605957. doi: 10.3389/fspas.2020.605957

leads naturally to a non-uniform twist profile. Heating and dynamic motions as well as substructures are expected inside non-uniformly twisted flux ropes. MHD simulations of the prominence-cavity system [Fan and Liu, 2019] corroborated that there exist different types of twisted field lines threading the cavity. These field lines also possess different thermodynamic properties, therefore giving rise to the substructures of different appearances in EUV. In contrast to moderately twisted flux ropes (less than 2 turns) that are normally reconstructed within active regions by non-linear force-free field (NLFFF) extrapolations, [Jiang et al., 2019] found a highly twisted magnetic flux rope (over 6 turns) that connects two active regions, but a different NLFFF extrapolation fails to yield a flux rope in the same region, which poses again two controversial questions: 1) how the different NLFFF results can be reconciled? 2) what is the role of the kink instability in solar eruptions? To bear on the question as to how much twist a kink-stable flux rope could contain, [Liu et al., 2019] studied magnetic twist in rotational solar coronal jets and found a lower limit of 1.3 turns of twist as released by the rotation.

The evolution of magnetic flux ropes near the Sun and in interplanetary space has significant space-weather implications. [Vršnak, 2019] studied the pre-eruptive gradual rise of flux ropes with an analytical model, considering three different driving processes. [Ma and Chen, 2020] investigated two Type II radio bursts associated with three slow CMEs. [Mishra et al, 2020] made an effort to extrapolate the internal thermodynamic properties of a CME flux rope near the Sun to 1 AU by using a model constrained by the CME kinematics. They concluded that the CME of interest releases heat throughout its journey from the Sun to Earth. Employing spacecrafts orbiting Venus and at the L1 point close to Earth, [Kilpua et al., 2019] found two CMEs coalesce into one coherent flux rope. [Zhao et al., 2019] concluded that the coalescence process between interplanetary CME flux ropes can operate in scales of hundreds of Earth radii and persist for hundreds of minutes.

In this Research Topic, we also identify two important trends: 1) utilizing high-resolution observations [e.g., Awasthi and Liu, 2019; Wang and Liu, 2019], and 2) integrating observations with models [e.g., Fan and Liu, 2019; Jiang et al., 2019; Kilpua et al., 2019; Mishra et al., 2020]. To further advance our understanding of the origin, structure, and evolution of magnetic flux ropes in the heliosphere, we look forward to observations obtained by next-generation instruments such as the 4-m Daniel K. Inouye Solar Telescope, Parker Solar Probe (PSP), Solar Orbiter, as well as the Advanced Space-based Solar Observatory (ASO-S) that is scheduled to launch in 2022 by China.

AUTHOR CONTRIBUTIONS

RL drafted the editorial. All authors contributed to its finalization.

FUNDING

RL acknowledge support by the National Natural Science Foundation of China (NSFC; Grant Nos. 41761134088, 41774150, and 11925302).

ACKNOWLEDGMENTS

We acknowledge all the authors, reviewers, editors, and publishers who have supported this Research Topic.

REFERENCES

Awasthi, A. K., and Liu, R. (2019). Mass motion in a prominence bubble revealing a kinked flux rope configuration. *Front. Phys.* 7, 218. doi:10.3389/fphy.2019.00218.

Fan, Y., and Liu, T. (2019). Mhd simulation of prominence-cavity system. *Front. Astron. Space Sci.* 6, 27. doi:10.3389/fspas.2019.00027.

Jiang, C., Duan, A., Feng, X., Zou, P., and Wang, Y. (2019). Reconstruction of a highly twisted magnetic flux rope for an inter-active-region X-class solar flare. *Front. Astron. Space Sci.* 6, 63. doi:10.3389/fspas.2019.00063.

Kilpua, E. K. J., Good, S. W., Palmerio, E., Asvestari, E., Lumme, E., Ala-Lahti, M., et al. (2019). Multipoint observations of the june 2012 interacting interplanetary flux ropes. *Front. Astron. Space Sci.* 6, 50. doi:10.3389/fspas.2019.00050.

Liu, J., Wang, Y., and Erdélyi, R. (2019). How many twists do solar coronal jets release? *Front. Astron. Space Sci.* 6, 44. doi:10.3389/fspas.2019.00044.

Ma, S., and Chen, H. (2020). Two successive type ii radio bursts associated with b-class flares and slow cmes. *Front. Astron. Space Sci.* 7, 17. doi:10.3389/fspas.2020.00017.

Mishra, W., Wang, Y., Teriaca, L., Zhang, J., and Chi, Y. (2020). Probing the thermodynamic state of a coronal mass ejection (cme) up to 1 au. *Front. Astron. Space Sci.* 7, 1. doi:10.3389/fspas.2020.00001.

Vršnak, B. (2019). Gradual pre-eruptive phase of solar coronal eruptions. *Front. Astron. Space Sci.* 6, 28. doi:10.3389/fspas.2019.00028.

Wang, H., and Liu, C. (2019). Signatures of magnetic fFront. Astron. Space Sci.lux ropes in the low solar atmosphere observed in high resolution. *Front. Astron. Space Sci.* 6, 18. doi:10.3389/fspas.2019.00018.

Zhao, Y., Feng, H., Liu, Q., and Zhao, G. (2019). Coalescence of magnetic flux ropes within interplanetary coronal mass ejections: multi-cases studies. *Front. Phys.* 7, 151. doi:10.3389/fphy.2019.00151.

Conflict of Interest: The authors declare that the research was conducted in the absence of any commercial or financial relationships that could be construed as a potential conflict of interest.

frontiers in Astronomy and Space Sciences

REVIEW
published: 04 April 2019
doi: 10.3389/fspas.2019.00018

Signatures of Magnetic Flux Ropes in the Low Solar Atmosphere Observed in High Resolution

Haimin Wang[1,2]* *and Chang Liu*[1,2]

[1] Big Bear Solar Observatory, New Jersey Institute of Technology, Big Bear City, CA, United States, [2] Institute of Space Weather Sciences, New Jersey Institute of Technology, Newark, NJ, United States

Magnetic flux ropes (MFRs) are important physical features closely related to solar eruptive activities with potential space weather consequences. Studying MFRs in the low solar atmosphere can shed light on their origin and subsequent magnetic structural evolution. In recent years, observations of solar photosphere and chromosphere reached a spatial resolution of 0.1 to 0.2 arcsec with the operation of meter class ground-based telescopes, such as the 1.6 m Goode Solar Telescope at Big Bear Solar Observatory and the 1 m New Vacuum Solar Telescope at Yunnan Observatory. The obtained chromospheric Hα filtergrams with the highest resolution thus far have revealed detailed properties of MFRs before and during eruptions, and the observed pre-eruption structures of MFRs are well consistent with those demonstrated by non-linear force-free field extrapolations. There is also evidence that MFRs may exist in the photosphere. The magnetic channel structure, with multiple polarity inversions and only discernible in high-resolution magnetograph observations, may be a signature of photospheric MFRs. These MFRs are likely formed below the surface due to motions in the convection zone and appear in the photosphere through flux emergence. Triggering of some solar eruptions is associated with an enhancing twist in the low-atmospheric MFRs.

Keywords: sun, flux rope, eruption, chromosphere, photosphere

OPEN ACCESS

Edited by:
Hongqiang Song,
Shandong University, China

Reviewed by:
Mingde Ding,
Nanjing University, China
Xiaoli Yan,
National Astronomical Observatories (CAS), China

***Correspondence:**
Haimin Wang
haimin.wang@njit.edu

Specialty section:
This article was submitted to Stellar and Solar Physics, a section of the journal Frontiers in Astronomy and Space Sciences

Received: *28 January 2019*
Accepted: *11 March 2019*
Published: *04 April 2019*

Citation:
Wang H and Liu C (2019) Signatures of Magnetic Flux Ropes in the Low Solar Atmosphere Observed in High Resolution. Front. Astron. Space Sci. 6:18. doi: 10.3389/fspas.2019.00018

1. INTRODUCTION

Magnetic flux ropes are generally defined as a bundle of magnetic fields that are twisted about each other and wrap around a common axis. These current-carrying magnetic field systems are crucially important as they may exhibit eruptive activities while being subject to different modes of instabilities and forces (Myers et al., 2017). Significant attention has been drawn to the structure and evolution of solar magnetic flux ropes, as they are believed to constitute the key component of coronal mass ejections (CMEs), a major form of solar eruptions that can have a direct impact on space weather (Filippov et al., 2015; Chen, 2017; Cheng et al., 2017). On the large scale, magnetic flux ropes are detected in the interplanetary magnetic clouds formed by CMEs (Burlaga et al., 1982), which may cause geomagnetic disturbances when interacting with Earth's magnetic field. In the solar corona, some studies suggest that flux ropes are produced via a magnetic reconnection between different branches of loops during the process of eruptions (e.g., Liu et al., 2010; Cheng et al., 2011; Green et al., 2011); however, there is also evidence that flux ropes pre-exist before eruptions as they may be built up gradually (e.g., Zhang et al., 2012; Cheng et al., 2014). Many models have also been developed to address the formation of magnetic

flux ropes, such as via magnetic reconnection (e.g., van Ballegooijen and Martens, 1989; Amari et al., 2000; Priest and Longcope, 2017) and sunspot rotation (e.g., Yan et al., 2015). The genesis and evolution of solar magnetic flux ropes is therefore an intriguing and challenging question, the answer of which can benefit from a quantitative characterization of solar magnetic fields in terms of physical parameters (e.g., magnetic twist, electric current). This can now be routinely obtained by magnetic field modeling methods, such as the non-linear force-free field (NLFFF) extrapolations, based on the advanced vector magnetograph observations such as from *Hinode* and the Helioseismic and Magnetic Imager (HMI) on board the *Solar Dynamics Observatory* (*SDO*). Reconstructing coronal magnetic field enables not only the identification of magnetic flux ropes through computing magnetic twist of individual field lines and mapping magnetic connectivities, but also the scrutinization of flux rope evolution by monitoring their physical properties (Liu et al., 2016). A wealth of studies have since then explored the magnetic environment of flux ropes (e.g., Guo et al., 2010; Jiang et al., 2014) and attempted to understand successful vs. failed eruptions under the context of kink and torus instabilities (e.g., Liu et al., 2015, 2016; Amari et al., 2018; Jing et al., 2018).

Obviously, high-resolution observations can be invaluable in shedding light on the central question above, by visualizing flux rope structures and helping disentangle their relation to eruptions. However, previous research has primarily relied on spaceborne coronal observations with moderate resolution. It is notable that enormous advances in revealing and studying the fine-scale structures and dynamics of the low solar atmosphere has been achieved thanks to the recent development of large ground-based solar telescopes that produce observations with highest spatiotemporal resolution available thus far. These

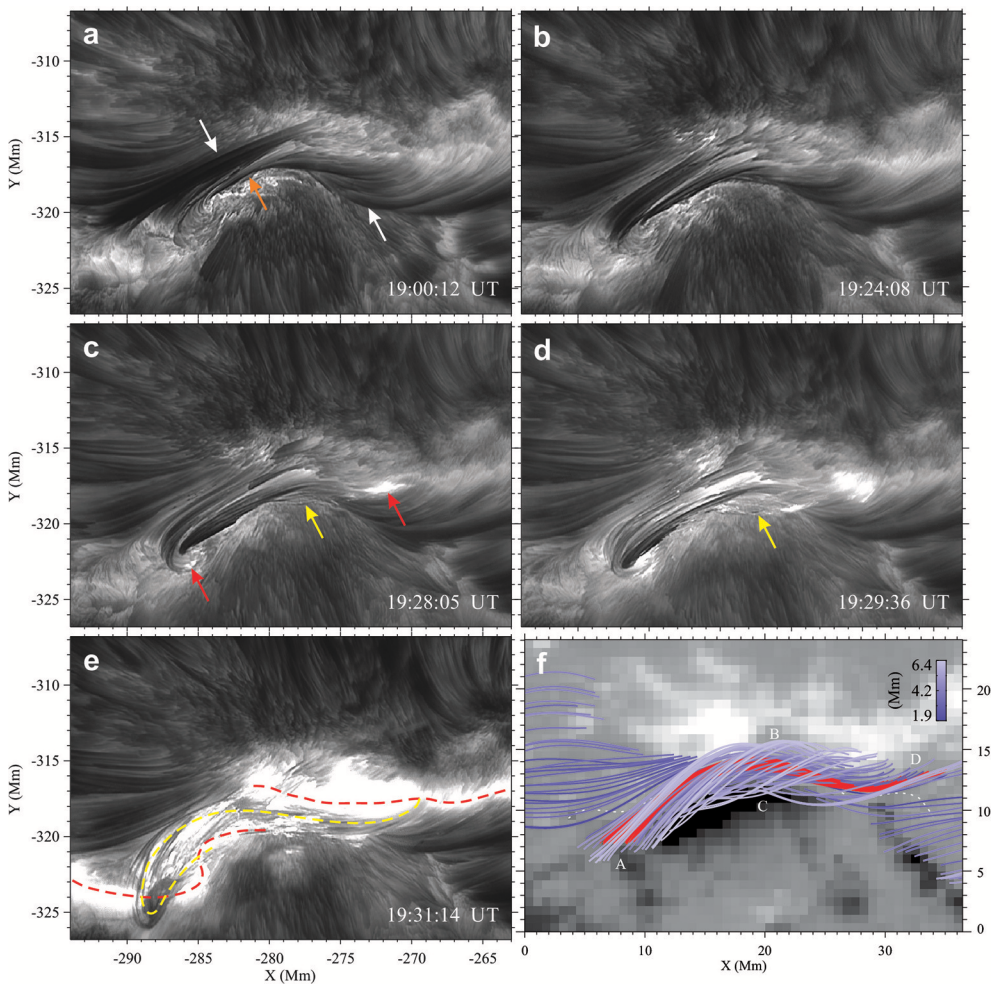

FIGURE 1 | BBSO/GST Hα time-sequence observations **(a–e)** and NLFFF modeling **(f)** of a magnetic flux rope in NOAA active region 11817 on 2013 August 11. The white (orange) arrows point to the weakened (enhanced) loops at the event onset, and the red arrows indicate the initial footpoint brightening. The yellow arrows and dashed line delineate the active flux rope in motion, and the red dashed line mark the induced double ribbons of a C2.1 flare. The plotted representative field lines are from a preflare optimization NLFFF extrapolation model, which is based on the *SDO*/HMI vector magnetic field data remapped with a Lambert cylindrical equal area projection. The twisted flux rope in red (with a maximum height $\lesssim$4.0 Mm) is embedded in sheared arcade fields (largely AB and CD) in blue (with a maximum height $\lesssim$6.4 Mm) (Wang et al., 2015). Credit: Nature Communications.

include the Swedish 1 m Solar Telescope on La Palma, 1.6 m Goode Solar Telescope (GST; Goode et al., 2010) at Big Bear Solar Observatory (BBSO), 1.5 m solar telescope GREGOR on Tenerife, and 1 m New Vacuum Solar Telescope (NVST; Liu et al., 2014) at Yunnan Observatory. In this review, we highlight the most important observational signatures of magnetic flux ropes in the chromosphere as seen by BBSO/GST and NVST, and, remarkably, even in the photosphere as seen by BBSO/GST. We also discuss the future prospects and challenges in this important research field.

2. CHROMOSPHERIC SIGNATURES OF FLUX ROPES

The key advancement in the observation of magnetic flux ropes has been made using Hα filtergrams with a spatial resolution in the order of 0.1″ and a temporal cadence of 10–20 s. The twisted magnetic structure of flux ropes in Hα is discernible before eruptive activities and becomes much more obvious during the process of their activation or eruption. Using BBSO/GST Hα observations, Wang et al. (2015) clearly demonstrated that a bunch of flux loops seemingly peeled off from an inverse S-shaped flux system to unveil itself as a twisted flux rope and meanwhile induced a two-ribbon C2.1 flare (**Figures 1a–e**). This marks the first witness of the structural evolution of a flux rope in the chromosphere. NLFFF extrapolation models (constructed with the optimization method) suggest that sheared arcades embed this twisted flux rope (**Figure 1f**), which evolves to an unstable state as its twist enhances (and thus subjects to the helical kink instability) but ultimately fails to erupt due to the strong confinement of the ambient strapping field. Liu et al. (2016) further showed that such a pre-eruption enhancement of a magnetic twist also occurred for other homologous events, either confined or eruptive, in this active region.

It is generally considered that filaments are a reliable proxy of flux ropes. Since its operation, NVST has produced excellent observations of filament activities. As a good example, Li et al. (2017) studied sympathetic, failed eruptions of two filaments near the east limb with NVST Hα observations (**Figures 2a,b**) and NLFFF extrapolations (constructed with the flux rope insertion method; **Figure 2c**). The authors attributed the activation of the left filament to kink instability, and that of the right filament to the weakening of overlying fields following an induced X-point reconnection between the filaments. Notably, they found a clear rotational motion of the southern portion of both filaments, which is likely to indicate an untwisting of the erupting filaments. In another study, Yang et al. (2014) observed that a filament is activated by magnetic field cancellation and undergoes a failed eruption, during the process of which it clearly tracks a twisted flux rope structure.

The above studies mainly deal with the evolution of flux ropes that already exist. Importantly, high-resolution observations are powerful in disclosing the complete dynamic evolution of magnetic flux ropes related to the initiation of flares/CMEs. Using BBSO/GST Hα data, Yan et al. (2017) presented that a small-scale flux rope (**Figures 2d–h**), with its footpoints showing a rotational motion, emerges near a large sunspot and subsequently erupts, driving an M1.0 flare and a CME. The presence of the flux rope was evidenced by both optimization NLFFF (**Figure 2i**) and data-driven magnetohydrodynamic modeling. Kumar et al. (2015) reported that a small, twisted chromospheric flux rope is formed between two sheared J-shaped Hα loops by magnetic reconnection, which is associated with flux cancellation and shear flows and causes an M1.0 flare (**Figure 3**, upper six panels). Jet activities and cool plasma inflow are also observed at the reconnection site. Kumar et al. (2017) further showed another clear example of the formation of a small unstable, rotating flux rope from a series of magnetic reconnection between chromospheric Hα loops together with very rapid flux cancellation. Such a formation process of flux ropes via the tether-cutting-like reconnection accompanied by magnetic cancellations was also observed by Xue et al. (2017) using NVST Hα data. The authors detailed various signatures of the reconnection between two branches of highly sheared arcades, and found that the central part of the newly formed long flux rope connecting two far footpoints bears a concave-up-shape structure with many fine threads; the expected another sets of shorter loops are also seen (**Figure 3**, lower six panels). For the sake of completeness, we note that NVST Hα images display twisted structures of two active-region eruptive filaments in Yan et al. (2015), where the authors identified the filaments as magnetic flux ropes with NLFFF modeling and suggested that they are formed after horizontal magnetic fields are twisted as a result of sunspot rotation.

3. PHOTOSPHERIC SIGNATURES OF FLUX ROPES

The above chromospheric observations evince that flux ropes can be formed due to magnetic reconnection above the surface, and also that they might emerge from below the surface, in which case flux ropes must be formed in the solar convection zone. In retrospect, one of the pioneering studies of the intrinsic relationship between occurrence of flares and evolution of photospheric magnetic configuration was conducted by Tanaka (1991) to infer the subsurface magnetic field structure of a flare-productive δ-spot group. The characteristic pattern of the unusually fast evolution of this sunspot group consists of a shearing phase when spots grow and a shear reduction phase when spots decay. This observation led the author to construct a cartoon model of a complex magnetic system comprising twisted magnetic knots and a long-winding flux rope, the consecutive emergence of which was shown to be consistent with the abnormal evolution of the flaring active region of interest. This approach was adopted and further explored by studies such as Ishii et al. (1998) and Kurokawa et al. (2002), in which the authors schematically illustrated that the emergence of twisted magnetic flux ropes may explain the observed proper motions of sunspots and other drastic evolution of magnetic structures, and may be the source of strong flaring activities.

Along the same line, Zirin and Wang (1993) made the discovery that channel-like magnetic structures were formed

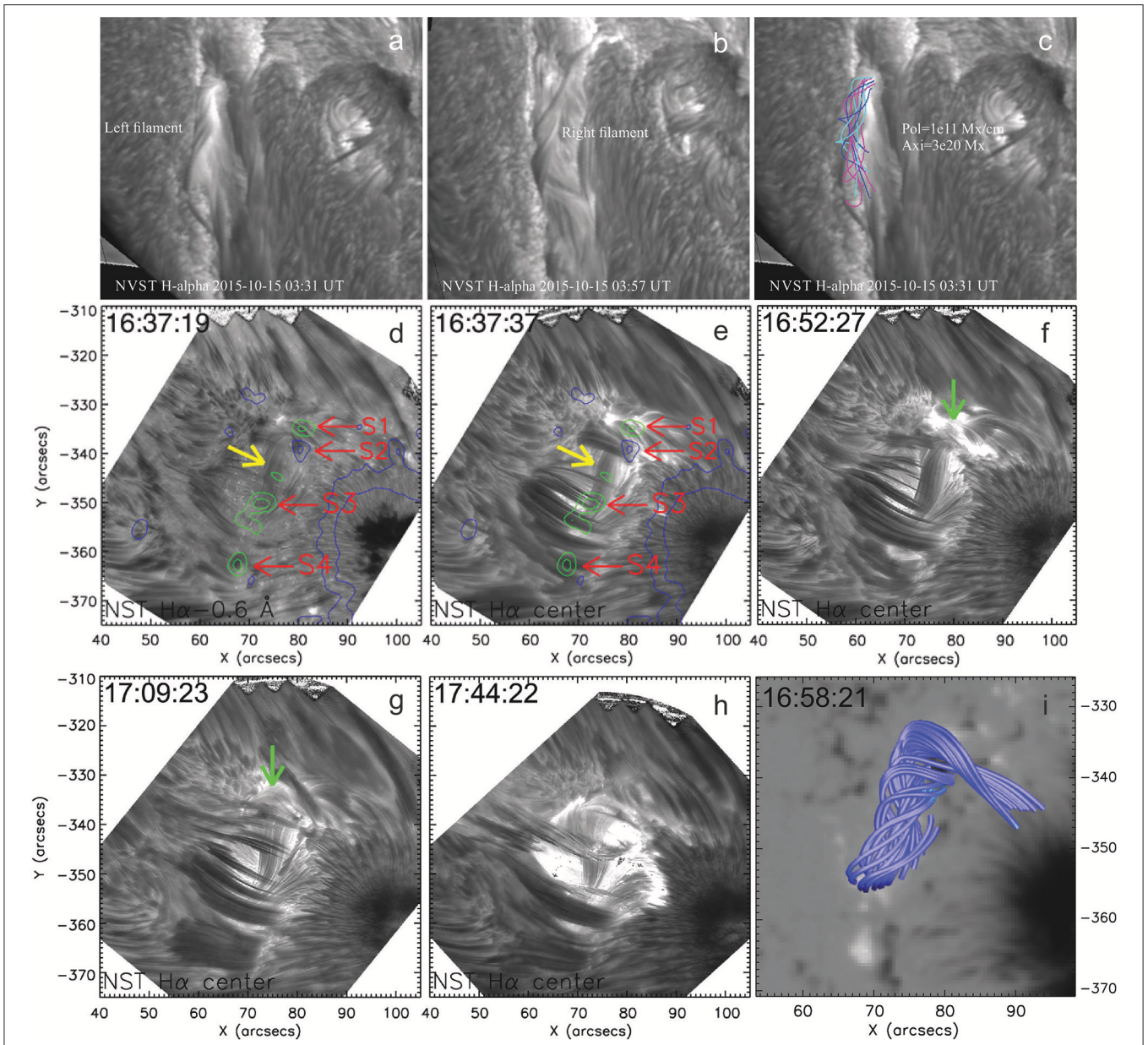

FIGURE 2 | (a–c) NVST observations of two near-limb active filaments with clear twist structure in NOAA active region 12434 on 2015 October 15 and the NLFFF extrapolation model of the left filament. The poloidal and axial fluxes used by the flux-rope-insertion method are indicated. The model of the right filament is similar (Li et al., 2017). **(d–i)** BBSO/GST Hα − 0.6 Å and Hα center observations and optimization NLFFF model of a small-scale emerging flux rope in NOAA active region 12403 on 2015 August 24 that drives an M1.0 flare and a CME. The green (blue) contours represent small satellite sunspots (pointed to by the red arrows) in positive (negative) polarity field. The yellow and green arrows point to the flux rope and its upper portion, respectively (Yan et al., 2017). Reproduced by permission of AAS.

when magnetic fluxes emerged inside the common penumbra of a δ-spot group. These magnetic channels on the surface take the form of elongated, opposite-polarity flux system with multiple polarity inversions, along which there are strong transverse magnetic field and surface flows. Using observations from *Hinode* (which provides magnetic field measurement with the highest resolution before the BBSO/GST era) and with the aid of NLFFF extrapolation, several studies analyzed magnetic channels in detail and suggested that they may originate from the emergence of twisted flux tubes from below the surface (e.g., Kubo et al., 2007; Wang et al., 2008; Lim et al., 2010). This view is supported by recent theoretical modeling, which has been able to reveal detailed flux emergence process in relation to the generation of magnetic channels. Toriumi and Takasao (2017) carried out a series of flux emergence modeling, among which an emerging highly twisted, kink-unstable flux tube from the convection zone to the corona is employed to simulate the formation of a compact δ-spot group. It was shown

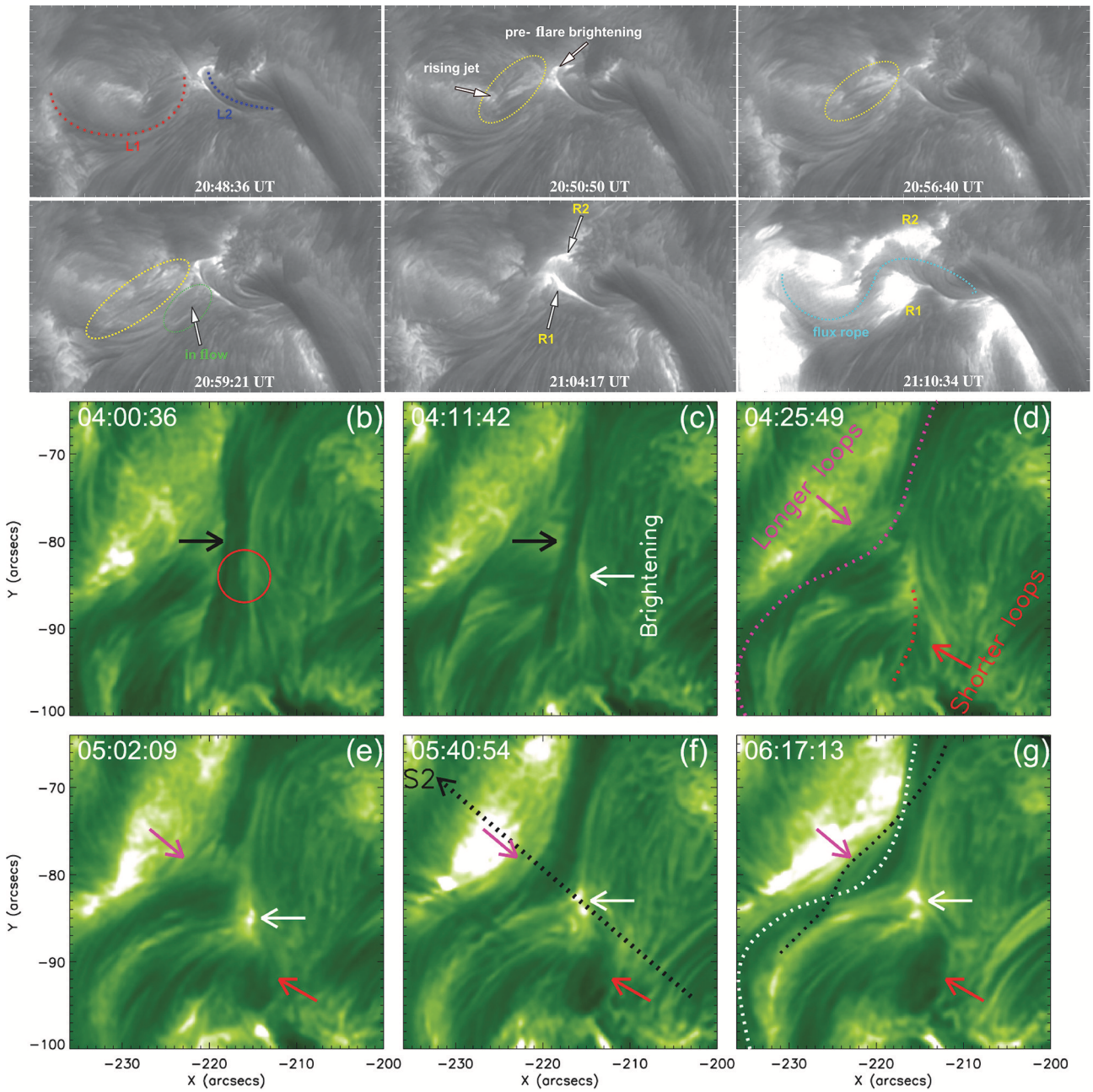

FIGURE 3 | Upper BBSO/GST Hα line center images of NOAA active region 12087 on 2014 June 12, showing the formation of a S-shaped twisted flux rope between two pre-existing Hα loops L1 and L2 by magnetic reconnection. The reconnection is associated with rising untwisting jets (yellow ellipse) and cool plasma inflow (green ellipse) and produces a two-ribbon (R1 and R2) M1.0 flare. The field of view is 32″ × 17″ (Kumar et al., 2015). **Lower** NVST Hα images of NOAA active region 11967 on 2014 February 2, showing that the reconnection between two sheared arcades produces a long flux rope (pink dotted line and arrow) with fine threads (e.g., those delineated by the black and white dotted lines) and shorter loops (red dotted line and arrow). The black and white arrows mark the quick disappearing part of one arcade and brightening region, respectively (Xue et al., 2017). Reproduced by permission of AAS.

that as magnetic fields are advected, stretched, and compressed during their emergence, a highly sheared magnetic polarity inversion line (PIL) of the δ spot is formed with an elongated, alternating pattern of both polarities, which is greatly reminiscent of magnetic channels. The simulation results of Knizhnik et al. (2018) corroborate the kink-unstable emerging flux ropes as a promising mechanism of δ spot formation, and their results also showed the development of elongated, secondary opposite-polarity regions between primary polarities, which are similar to the observed magnetic channels. Therefore, it is appealing to

suggest that magnetic channels are a photospheric signature of emerging flux ropes.

Previous studies have shown that high spatial resolution and high polarimetry accuracy are required to observe the magnetic channel structure in detail. Meeting these properties, BBSO/GST can provide vector magnetograms at 0.24″ resolution and up to about 30 s cadence through the spectropolarimetric observations of the Fe I 1564.8 nm line with the Near InfraRed Imaging Spectropolarimeter (NIRIS). The unprecedented high spatiotemporal resolution NIRIS vector field data allowed Wang et al. (2017) to not only detect a magnetic channel not discernible with *SDO*/HMI but also study its temporal evolution with related to the flare occurrence in an extended active region with the δ configuration (**Figures 4a,b**). The authors found that the channel structure at the PIL is located near the footpoints of sheared arcades, and its strengthening in terms of enhancement of magnetic fluxes and currents is cotemporal with episodes of flare precursor brightening observed close by (**Figure 4c**).

As emerging magnetic fluxes on the surface carry signatures of the pre-existing flux ropes, some photospheric appearance of flux ropes may also be reflected in white light observations, especially at high resolution. BBSO/GST's Broad-Band Filter Imager provides direct imaging in the broadband TiO (a proxy for continuum in photosphere at 705.7 nm) at 0.1″ resolution and 15 s cadence, which has been shown to be another effective diagnosis of photospheric flux ropes. Sharykin et al. (2017) reported TiO flux rope structures observed along

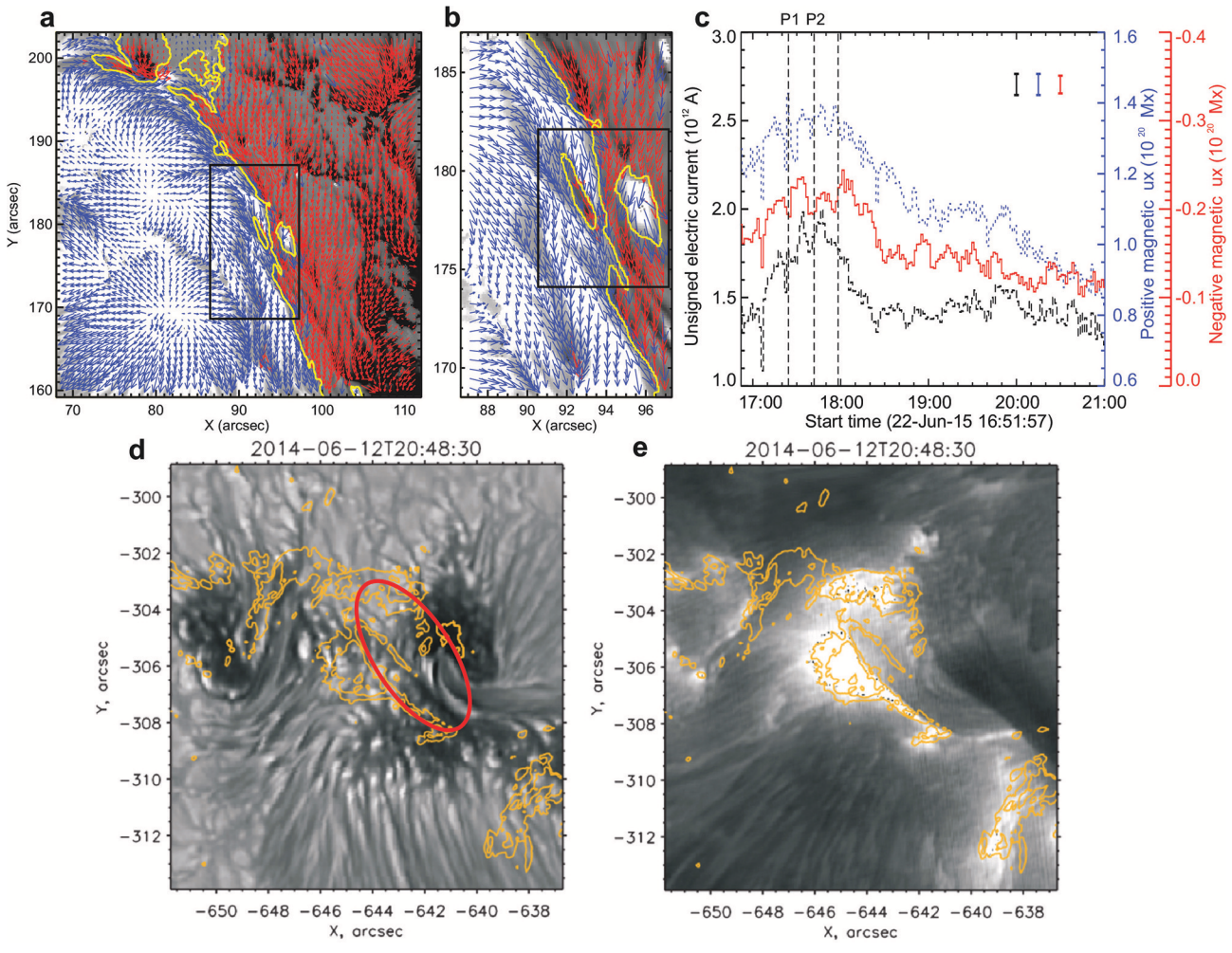

FIGURE 4 | Upper three panels: BBSO/GST near-infrared vector magnetic field map of NOAA AR 12371 on 2015 June 22 **(a)**, the identified magnetic channel structure at the PIL [**b**; a subregion denoted by the box in **(a)**], and time profiles of total positive (blue) and negative (red) magnetic fluxes and the unsigned electric current (black), calculated over the boxed region in **(b)**. The three vertical dashed lines in **(c)** mark the times of precursor episodes P1 and P2 and the peak time of the flare nonthermal emission, respectively (Wang et al., 2017). Credits: Nature Astronomy. Lower two panels: Photospheric manifestations of flux ropes seen as a sheared arcade along the PIL (marked by the red ellipse in **d**), as observed in broadband TiO with BBSO/GST in NOAA active region 12087 on 2014 June 12. Besides the double ribbons of the confined M1.0 flare in Hα line core **(e)**, a third thread-like ribbon in Hα red wing (yellow contours) is cospatial with the flux rope structure (Sharykin et al., 2017). Reproduced by permission of AAS.

the PIL as a compact sheared arcade, which corresponds to twisted structures in Hα line core and a third tiny thread-like ribbon in Hα red wing besides the double ribbons of a confined M1.0 flare (**Figures 4d,e**). After combining analyses of photospheric flows and magnetic field topology, the authors suggested that interacting flux ropes form an elongated current sheet along the PIL to trigger the flare. Thus far, the most prominent signatures of possible flux ropes observed at the photospheric level was described by Wang et al. (2018b) for the famous NOAA active region 12673 in September 2017. Within the light bridge sections of the δ-spot groups, the authors observed alternating bright-dark spiral structures in TiO and showed evidence that these structures possess strong magnetic fields with a surprising magnitude above ∼5,500 G (**Figure 5**). The unusual magnetic property of this possibly twisted flux rope structure right at the photosphere may be responsible for the strong activities in this region including the X9.3 flare on 2017 September 6 and the X8.2 limb flare on September 10. For future investigations, we caution that photospheric images should be combined with other diagnoses to give a definite identification of photospheric flux rope structures. Magnetic field extrapolations certainly can be helpful, while the height of extrapolated fields need to be considered.

4. DISCUSSION AND FUTURE PROSPECTIVE

Flux ropes are one of the most important targets in solar physics research due to their potential space weather effects caused by their eruptions. With the operation of meter class ground-based telescopes, significant advancements have been recently made in detecting signatures of flux ropes in the chromosphere and photosphere and studying their structures during eruptive activities. It is anticipated that more detailed and clearer dynamic structures of flux ropes will be revealed when the 4 m Daniel K. Inouye Solar Telescope (DKIST) is online (Tritschler et al., 2016). Additional spectroscopy tools will also provide accurate measurement of magnetic and velocity fields, which are critical in quantitatively understanding the physical mechanism that drives the flux rope evolution.

As demonstrated in previous studies, the topological structure observed in Hα may provide hints on the magnetic twist of flux ropes. With higher resolution observations and advanced machine learning techniques, it is expected that such a twist can be quantitatively examined by tracing Hα features (Aschwanden et al., 2016). The obtained results can also be compared with those deduced from magnetic field extrapolation models. Characterizing magnetic twist within and properties of strapping

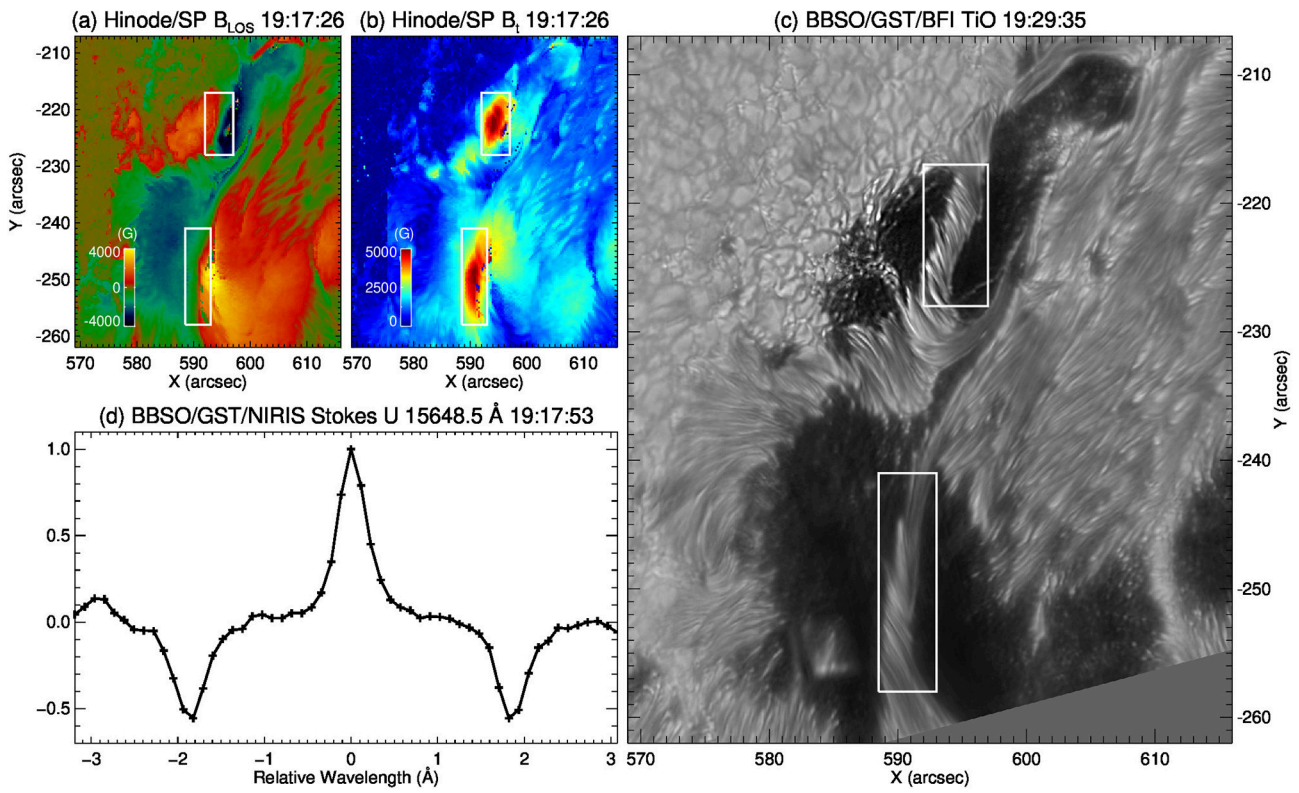

FIGURE 5 | Unusual structures of NOAA AR 12673 on 2017 September 6 as revealed in *Hinode* line of sight **(a)** and transverse **(b)** magnetic field maps and BBSO/GST TiO image **(c)**. The white boxes mark the two strong transverse field regions along the PIL, where photospheric signatures of twisted flux ropes are present. Panel **(d)** shows the Stokes U profile of a selected pixel with strong transverse field in the upper box measured by BBSO/GST's NIRIS. A field strength of 5570 G is obtained by the direct measurement of Zeeman splitting (Wang et al., 2018b). Reproduced by permission of AAS.

field above flux ropes will be important for understanding the kink and torus instabilities related to the onset of flux rope eruptions (Jing et al., 2018).

Beyond flux rope tracing, a direct measurement of vector magnetic field in flux ropes and filaments is highly desired. Spectropolarimetric observations using the He I 1083.0 nm line can provide a very useful diagnosis of magnetic field and flows in filaments and prominences. Hanaoka and Sakurai (2017) used data from full-disk 1083.0 spectropolarimetry to obtain a statistic evaluation of magnetic field orientation in filaments. Sasso et al. (2014) analyzed the 1083.0 spectropolarimetric observation of an active region filament activated by a flare and found evidence of a coronal flux rope. High-resolution observations in 1083.0 nm and corresponding advanced data analysis tools are being developed for DKIST. In addition to the He I 1083.0 nm line, spectral diagnostics using the chromospheric lines (e.g., the Ca II line at 854 nm and Hα line from BBSO/GST's Fast-Imaging Solar Spectrograph) in combination with other lines formed from the chromosphere to corona (observed with the *Interface Region Imaging Spectrograph*) can provide valuable information about flux rope formation especially the reconnection process (e.g., Cheng et al., 2015). Furthermore, studying the linkage of filaments to the photosphere by investigating their barb structure and anchoring footpoints observed in high resolution is also important for understanding the filament stability and related dynamics (e.g., Kuckein et al., 2016; Wang et al., 2018a).

Finally, the data-based magnetohydrodynamic modeling in high resolution will certainly advance our knowledge of flux ropes and their evolution from the lower to the upper solar atmosphere (Chen, 2017). For example, it may help eventually elucidate different scenarios, whether a flux rope is formed below the surface and brought up during flux emergence or is formed above the photosphere via such as magnetic reconnection. Recent high-resolution modeling has begun to make significant progress toward a more realistic framework for simulating the formation of complex active regions including their many fine-scale structures (e.g., light bridges, magnetic channels) during the emerging process of twisted magnetic field (e.g., Cheung et al., 2010; Toriumi and Takasao, 2017). We believe that joint efforts of high-resolution modeling and observations will yield breakthroughs in understanding the structure, evolution, and eruption of magnetic flux ropes.

AUTHOR CONTRIBUTIONS

HW initiated the writing of the paper. CL revised the paper. Both studied related literatures.

FUNDING

We acknowledge the funding support by NASA grants NNX16AF72G, 80NSSC17K0016, 80NSSC18K0673, and 80NSSC18K1705, and by NSF grants AGS 1408703 and 1821294.

REFERENCES

Amari, T., Canou, A., Aly, J.-J., Delyon, F., and Alauzet, F. (2018). Magnetic cage and rope as the key for solar eruptions. *Nature* 554, 211–215. doi: 10.1038/nature24671

Amari, T., Luciani, J. F., Mikic, Z., and Linker, J. (2000). A twisted flux rope model for coronal mass ejections and two-ribbon flares. *Astrophys. J. Lett.* 529, L49–52. doi: 10.1086/312444

Aschwanden, M. J., Reardon, K., and Jess, D. B. (2016). Tracing the chromospheric and coronal magnetic field with AIA, IRIS, IBIS, and ROSA data. *Astrophys. J.* 826:61. doi: 10.3847/0004-637X/826/1/61

Burlaga, L. F., Klein, L., Sheeley N. R. Jr., Michels, D. J., Howard, R. A., Koomen, M. J., et al. (1982). A magnetic cloud and a coronal mass ejection. *Geophys. Res. Lett.* 9, 1317–1320. doi: 10.1029/GL009i012p01317

Chen, J. (2017). Physics of erupting solar flux ropes: coronal mass ejections (CMEs)-Recent advances in theory and observation. *Phys. Plasmas* 24:090501. doi: 10.1063/1.4993929

Cheng, X., Ding, M. D., and Fang, C. (2015). Imaging and spectroscopic diagnostics on the formation of two magnetic flux ropes revealed by SDO/AIA and IRIS. *Astrophy. J.* 804:82. doi: 10.1088/0004-637X/804/2/82

Cheng, X., Ding, M. D., Guo, Y., Zhang, J., Vourlidas, A., Liu, Y. D., et al. (2014). Tracking the evolution of a coherent magnetic flux rope continuously from the inner to the outer corona. *Astrophy. J.* 780:28. doi: 10.1088/0004-637X/780/1/28

Cheng, X., Guo, Y., and Ding, M. (2017). Origin and structures of solar eruptions I: magnetic flux rope. *Sci. China Earth Sci.* 60, 1383–1407. doi: 10.1007/s11430-017-9074-6

Cheng, X., Zhang, J., Liu, Y., and Ding, M. D. (2011). Observing flux rope formation during the impulsive phase of a solar eruption. *Astrophys. J. Lett.* 732:L25. doi: 10.1088/2041-8205/732/2/L25

Cheung, M. C. M., Rempel, M., Title, A. M., and Schüssler, M. (2010). Simulation of the formation of a solar active region. *Astrophys. J.* 720, 233–244. doi: 10.1088/0004-637X/720/1/233

Filippov, B., Martsenyuk, O., Srivastava, A. K., and Uddin, W. (2015). Solar magnetic flux ropes. *J. Astrophys. Astron.* 36, 157–184. doi: 10.1007/s12036-015-9321-5

Goode, P. R., Yurchyshyn, V., Cao, W., Abramenko, V., Andic, A., Ahn, K., and Chae, J. (2010). Highest resolution observations of the quietest sun. *Astrophys. J. Lett.* 714, L31–L35. doi: 10.1088/2041-8205/714/1/L31

Green, L. M., Kliem, B., and Wallace, A. J. (2011). Photospheric flux cancellation and associated flux rope formation and eruption. *Astron. Astrophys.* 526:A2. doi: 10.1051/0004-6361/201015146

Guo, Y., Schmieder, B., Démoulin, P., Wiegelmann, T., Aulanier, G., Török, T., et al. (2010). Coexisting flux rope and dipped arcade sections along one solar filament. *Astrophys. J.* 714, 343–354. doi: 10.1088/0004-637X/714/1/343

Hanaoka, Y., and Sakurai, T. (2017). Statistical study of the magnetic field orientation in solar filaments. *Astrophys. J.* 851:130. doi: 10.3847/1538-4357/aa9cf1

Ishii, T. T., Kurokawa, H., and Takeuchi, T. T. (1998). Emergence of a twisted magnetic flux bundle as a source of strong flare activity. *Astrophys. J.* 499, 898–904.

Jiang, C., Wu, S. T., Feng, X., and Hu, Q. (2014). Nonlinear force-free field extrapolation of a coronal magnetic flux rope supporting a large-scale solar filament from a photospheric vector magnetogram. *Astrophys. J. Lett.* 786:L16. doi: 10.1088/2041-8205/786/2/L16

Jing, J., Liu, C., Lee, J., Ji, H., Liu, N., Xu, Y., et al. (2018). Statistical analysis of torus and kink instabilities in solar eruptions. *Astrophys. J.* 864:138. doi: 10.3847/1538-4357/aad6e4

Knizhnik, K. J., Linton, M. G., and DeVore, C. R. (2018). The role of twist in kinked flux rope emergence and delta-spot formation. *Astrophys. J.* 864:89. doi: 10.3847/1538-4357/aad68c

Kubo, M., Yokoyama, T., Katsukawa, Y., Lites, B., Tsuneta, S., Suematsu, Y., et al. (2007). Hinode observations of a vector magnetic field change associated with a flare on 2006 December 13. *Public. Astron. Soc. Jpn.* 59, S779–S784. doi: 10.1093/pasj/59.sp3.S779

Kuckein, C., Verma, M., and Denker, C. (2016). Giant quiescent solar filament observed with high-resolution spectroscopy. *Astron. Astrophys.* 589:A84. doi: 10.1051/0004-6361/201526636

Kumar, P., Yurchyshyn, V., Cho, K.-S., and Wang, H. (2017). Multiwavelength observations of a flux rope formation by series of magnetic reconnection in the chromosphere. *Astron. Astrophys.* 603:A36. doi: 10.1051/0004-6361/201629295

Kumar, P., Yurchyshyn, V., Wang, H., and Cho, K.-S. (2015). Formation and eruption of a small flux rope in the chromosphere observed by NST, IRIS, and SDO. *Astrophys. J.* 809:83. doi: 10.1088/0004-637X/809/1/83

Kurokawa, H., Wang, T., and Ishii, T. T. (2002). Emergence and drastic breakdown of a twisted flux rope to trigger strong solar flares in NOAA active region 9026. *Astrophys. J.* 572, 598–608. doi: 10.1086/340305

Li, S., Su, Y., Zhou, T., van Ballegooijen, A., Sun, X., and Ji, H. (2017). High-resolution observations of sympathetic filament eruptions by NVST. *Astrophys. J.* 844:70. doi: 10.3847/1538-4357/aa78f5

Lim, E.-K., Chae, J., Jing, J., Wang, H., and Wiegelmann, T. (2010). The formation of a magnetic channel by the emergence of current-carrying magnetic fields. *Astrophys. J.* 719, 403–414. doi: 10.1088/0004-637X/719/1/403

Liu, C., Deng, N., Liu, R., Lee, J., Pariat, É., Wiegelmann, T., et al. (2015). A circular-ribbon solar flare following an asymmetric filament eruption. *Astrophys. J. Lett.* 812:L19. doi: 10.1088/2041-8205/812/2/L19

Liu, R., Kliem, B., Titov, V. S., Chen, J., Wang, Y., Wang, H., et al. (2016). Structure, stability, and evolution of magnetic flux ropes from the perspective of magnetic twist. *Astrophys. J.* 818:148. doi: 10.3847/0004-637X/818/2/148

Liu, R., Liu, C., Wang, S., Deng, N., and Wang, H. (2010). Sigmoid-to-flux-rope transition leading to a loop-like coronal mass ejection. *Astrophys. J. Lett.* 725, L84–L90. doi: 10.1088/2041-8205/725/1/L84

Liu, Z., Xu, J., Gu, B.-Z., Wang, S., You, J.-Q., Shen, L.-X., et al. (2014). New vacuum solar telescope and observations with high resolution. *Res. Astron. Astrophys.* 14, 705–718. doi: 10.1088/1674-4527/14/6/009

Myers, C. E., Yamada, M., Ji, H., Yoo, J., Jara-Almonte, J., and Fox, W. (2017). Quasi-static and dynamic magnetic tension forces in arched, line-tied magnetic flux ropes. *Plasma Phys. Control. Fusion* 59:014048. doi: 10.1088/0741-3335/59/1/014048

Priest, E. R. and Longcope, D. W. (2017). Flux-rope twist in eruptive flares and CMEs: due to zipper and main-phase reconnection. *Sol. Phys.* 292:25. doi: 10.1007/s11207-016-1049-0

Sasso, C., Lagg, A., and Solanki, S. K. (2014). Magnetic structure of an activated filament in a flaring active region. *Astron. Astrophys.* 561:A98. doi: 10.1051/0004-6361/201322481

Sharykin, I. N., Sadykov, V. M., Kosovichev, A. G., Vargas-Dominguez, S., and Zimovets, I. V. (2017). Flare energy release in the lower solar atmosphere near the magnetic field polarity inversion line. *Astrophys. J.* 840:84. doi: 10.3847/1538-4357/aa6dfd

Tanaka, K. (1991). Studies on a very flare-active delta group - Peculiar delta SPOT evolution and inferred subsurface magnetic rope structure. *Sol. Phys.* 136, 133–149. doi: 10.1007/BF00151700

Toriumi, S. and Takasao, S. (2017). Numerical simulations of flare-productive active regions: δ-sunspots, sheared polarity inversion lines, energy storage, and predictions. *Astrophys. J.* 850:39. doi: 10.3847/1538-4357/aa95c2

Tritschler, A., Rimmele, T. R., Berukoff, S., Casini, R., Kuhn, J. R., Lin, H., et al. (2016). Daniel K. inouye solar telescope: high-resolution observing of the dynamic Sun. *Astron. Nachrich.* 337:1064. doi: 10.1002/asna.201612434

van Ballegooijen, A. A. and Martens, P. C. H. (1989). Formation and eruption of solar prominences. *Astrophys. J.* 343, 971–984.

Wang, H., Cao, W., Liu, C., Xu, Y., Liu, R., Zeng, Z., et al. (2015). Witnessing magnetic twist with high-resolution observation from the 1.6-m New Solar Telescope. *Nat. Commun.* 6:7008. doi: 10.1038/ncomms8008

Wang, H., Jing, J., Tan, C., Wiegelmann, T., and Kubo, M. (2008). Study of magnetic channel structure in active region 10930. *Astrophys. J.* 687, 658–667. doi: 10.1086/592082

Wang, H., Liu, C., Ahn, K., Xu, Y., Jing, J., Deng, N., et al. (2017). High-resolution observations of flare precursors in the low solar atmosphere. *Nat. Astron.* 1:0085. doi: 10.1038/s41550-017-0085

Wang, H., Liu, R., Li, Q., Liu, C., Deng, N., Xu, Y., et al. (2018a). Extending counter-streaming motion from an active region filament to a sunspot light bridge. *Astrophys. J. Lett.* 852:L18. doi: 10.3847/2041-8213/aaa2f4

Wang, H., Yurchyshyn, V., Liu, C., Ahn, K., Toriumi, S., and Cao, W. (2018b). Strong transverse photosphere magnetic fields and twist in light bridge dividing delta sunspot of active region 12673. *Res. Notes Am. Astron. Soc.* 2:8. doi: 10.3847/2515-5172/aaa670

Xue, Z., Yan, X., Yang, L., Wang, J., and Zhao, L. (2017). Observing formation of flux rope by tether-cutting reconnection in the sun. *Astrophys. J. Lett.* 840:L23. doi: 10.3847/2041-8213/aa7066

Yan, X. L., Jiang, C. W., Xue, Z. K., Wang, J. C., Priest, E. R., Yang, L. H., et al. (2017). The eruption of a small-scale emerging flux rope as the driver of an M-class flare and of a coronal mass ejection. *Astrophys. J.* 845:18. doi: 10.3847/1538-4357/aa7e29

Yan, X. L., Xue, Z. K., Pan, G. M., Wang, J. C., Xiang, Y. Y., Kong, D. F., et al. (2015). The formation and magnetic structures of active-region filaments observed by NVST, SDO, and hinode. *Astrophys. J. Suppl. Ser.* 219:17. doi: 10.1088/0067-0049/219/2/17

Yang, S., Zhang, J., Liu, Z., and Xiang, Y. (2014). New vacuum solar telescope observations of a flux rope tracked by a filament activation. *Astrophys. J. Lett.* 784:L36. doi: 10.1088/2041-8205/784/2/L36

Zhang, J., Cheng, X., and Ding, M.-D. (2012). Observation of an evolving magnetic flux rope before and during a solar eruption. *Nat. Commun.* 3:747. doi: 10.1038/ncomms1753

Zirin, H., and Wang, H. (1993). Narrow lanes of transverse magnetic field in sunspots. *Nature* 363, 426–428. doi: 10.1038/363426a0

Conflict of Interest Statement: The authors declare that the research was conducted in the absence of any commercial or financial relationships that could be construed as a potential conflict of interest.

frontiers in Astronomy and Space Sciences

ORIGINAL RESEARCH
published: 17 April 2019
doi: 10.3389/fspas.2019.00027

MHD Simulation of Prominence-Cavity System

Yuhong Fan[1]* *and Tie Liu*[2,3]

[1] High Altitude Observatory, National Center for Atmospheric Research, Boulder, CO, United States, [2] Key Laboratory for Dark Matter and Space Science, Purple Mountain Observatory, CAS, Nanjing, China, [3] School of Astronomy and Space Science, University of Science and Technology of China, Hefei, China

We present magnetohydrodynamic simulation of the evolution from quasi-equilibrium to onset of eruption of a twisted, prominence-forming coronal magnetic flux rope underlying a corona streamer. The flux rope is built up by an imposed flux emergence at the lower boundary. During the quasi-static phase of the evolution, we find the formation of a prominence-cavity system with qualitative features resembling observations, as shown by the synthetic SDO/AIA EUV images with the flux rope observed above the limb viewed nearly along its axis. The cavity contains substructures including "U"-shaped or horn-like features extending from the prominence enclosing a central "cavity" on top of the prominence. The prominence condensations form in the dips of the highly twisted field lines due to runaway radiative cooling and the cavity is formed by the density depleted portions of the prominence-carrying field lines extending up from the dips. The prominence "horns" are threaded by twisted field lines containing shallow dips, where the prominence condensations have evaporated to coronal temperatures. The central "cavity" enclosed by the horns is found to correspond to a central hot and dense core containing twisted field lines that do not have dips. The flux rope eventually erupts as its central part rises quasi-statically to a critical height consistent with the onset of the torus instability. The erupting flux rope accelerates to a fast speed of nearly 900 km/s and the associated prominence eruption shows significant rotational motion and a kinked morphology.

Keywords: magnetohydrodynamics (MHD), methods: numerical simulation, sun: corona, sun: coronal mass ejection, sun: magnetic fields, sun: prominences

OPEN ACCESS

Edited by:
Hongqiang Song,
Shandong University, China

Reviewed by:
Chun Xia,
Yunnan University, China
Bernhard Kliem,
Institute of Physics and Astronomy, Faculty of Mathematics and Natural Sciences, University of Potsdam, Germany

***Correspondence:**
Yuhong Fan
yfan@ucar.edu

Specialty section:
This article was submitted to Stellar and Solar Physics, a section of the journal Frontiers in Astronomy and Space Sciences

Received: *28 January 2019*
Accepted: *01 April 2019*
Published: *17 April 2019*

Citation:
Fan Y and Liu T (2019) MHD Simulation of Prominence-Cavity System. Front. Astron. Space Sci. 6:27. doi: 10.3389/fspas.2019.00027

1. INTRODUCTION

Solar filaments and prominences are observed to be a major precursor of coronal mass ejections (CMEs) (e.g., Webb and Hundhausen, 1987). When observed in white light or EUV above the limb viewed nearly along their lengths, they often display a prominence-cavity system with a relatively dark cavity surrounding the lower central prominence (see review by Gibson, 2015). EUV observations of prominence-cavity systems have also shown substructures within the cavities with "U"-shaped prominence "horns" extending from the prominence, enclosing a central "cavity" or "void" on top of the prominence, see e.g., Figures 8, 12 in Gibson (2015) and Figure 2c in Su et al. (2015). The first 3D MHD simulations of prominence formation in a stable equilibrium coronal magnetic flux rope were carried out by Xia et al. (2014); Xia and Keppens (2016). With the use of adaptive grid refinement and including the chromosphere as the lower boundary, their 3D simulations obtained a prominence-cavity system with the prominence showing fine-scale, highly dynamic fragments, reproducing many observed features seen in SDO/AIA observations.

Recently, Fan (2017) (hereafter F17) and Fan (2018) (hereafter F18) have carried out 3D MHD simulations of prominence forming coronal flux ropes under coronal streamers, with the flux rope evolving from quasi-equilibrium to onset of eruption, leading to a CME with associated prominence eruption. In those simulations, a significantly twisted, longitudinally extended flux rope is built up in the corona under a pre-existing coronal streamer solution by an imposed flux emergence at the lower boundary. During the quasi-static evolution of the emerged flux rope, cool prominence condensations are found to form in the dips of the significantly twisted field lines due to the radiative instability driven by the optically thin radiative cooling of the relatively dense plasma in the emerged dips. In the prominence-forming flux rope simulation in F18 (labeled as the "PROM" simulation in that paper), we find that the prominence weight is dynamically important and can suppress the onset of the kink instability and hold the flux rope in quasi-equilibrium for a significantly longer period of time, compared to a case without prominence formation. We also find the formation of a cavity surrounding the prominence, and substructures inside the cavity such as prominence "horns" and a central "cavity" on top of the prominence. However in the simulations in F18, a pre-existing streamer solution (the "WS" solution in F17) with a wide mean foot-point separation of the arcade field lines are used and the corresponding potential field has a slow decline with height. As a result, we obtained a prominence and cavity that extend to rather large heights that are larger than typically observed before the onset of eruption. Here we extend the work of F17 and F18 by modeling the prominence-forming flux rope under a pre-existing coronal streamer with a significantly narrower mean foot-point separation for its closed arcade field lines. We find the formation of a prominence-cavity system with the heights for the prominence and the cavity that are more in accordance with those of the typically observed quiescent prominence-cavity systems. We carry out a more detailed analysis of the characteristics of the 3D magnetic fields comprising the different features of the prominence-cavity system. We also find that the flux rope begins to erupt at a significantly lower height, consistent with the onset of the torus instability, and results in a fast CME with an associated prominence eruption that shows a kinked morphology.

2. MODEL DESCRIPTION

For the MHD simulation presented in this paper, we use the same numerical MHD model described in detail in F17. The readers are referred to that paper's sections 2 and 3.1 for the description of the equations solved, the numerical code, and the initial and boundary conditions for the simulation set-up. As a brief overview, we use the "Magnetic Flux Eruption" (MFE) code to solve the set of semi-relativistic MHD equations [Equations (1–6) in F17] in spherical geometry, with the energy equation explicitly taking into account the non-adiabatic effects of an empirical coronal heating (which depends on height only), optically thin radiative cooling, and the field-aligned electron heat conduction. The inclusion of these non-adiabatic affects allow for the development of the radiative instability that leads to the formation of prominence condensations in the coronal flux rope as shown in the simulations of F17 and F18. The simulation domain is in the corona, ignoring the photosphere and chromosphere layers, with the lower boundary temperature ($T = 5 \times 10^5$ K) set at the base of the corona, but with an adjustable base density (and hence base pressure) that depends upon the downward heat conduction flux to crudely represent the effect of chromospheric evaporation (Equations (17, 18) and the associated descriptions in F17). The radiative loss function $\Lambda(T)$ used for the radiative cooling in Equation (13) in F17 is the "actual" curve shown in **Figure 1** of F17 (also the same as the "PROM" case in F18). As described in F17, the radiative loss function used is modified to suppress cooling for $T \leq 7 \times 10^4$ K, so that the smallest pressure scale height of the coolest plasma that can form does not go below two grid points given our simulation resolution. In the following we describe the specific changes that have been made in the set-up of the current simulation.

The empirical coronal heating used in this simulation is modified to use two exponentially decaying (with height) components instead of just one used in F17, i.e., we change Equation (14) in F17 to the following:

$$H = \frac{F_1}{L_1}\frac{R_s^2}{r^2}\exp\left[-(r-R_s)/L_1\right] + \frac{F_2}{L_2}\frac{R_s^2}{r^2}\exp\left[-(r-R_s)/L_2\right] \quad (1)$$

where the input energy flux densities for the two components are $F_1 = F_2 = 5 \times 10^5\,\mathrm{ergs\,cm^{-2}s^{-1}}$, and the decay lengths are $L_1 = 5 \times 10^{10}$ cm and $L_2 = 2.5 \times 10^9$ cm, r is the radial distance to the center of the sun and R_s denotes the solar radius. The first much more extended component is aimed to heat and accelerate the background solar wind and open up the ambient coronal magnetic field. The second more spatially confined heating is aimed to enhance the heating near the base to enhance the base pressure and plasma inflow into the corona, which promotes the formation of prominence condensations in the emerged flux rope.

As described in section 3.1 of F17, we first initialize a 2D quasi-steady solution of a coronal steamer with an ambient solar wind in a longitudinally extended (in ϕ) spherical wedge domain. We use the same simulation domain (with $r \in [R_s, 11.47R_s]$, $\theta \in [75^\circ, 105^\circ]$, and $\phi \in [-75^\circ, 75^\circ]$, where R_s is the solar radius) and the grid as those for the "WS-L" (wide-streamer/long flux-rope) simulation in F17 (also the "PROM" simulation in F18). However, we use the initial normal flux distribution of a narrow bipolar pair of bands on the lower boundary as that for the NS (narrow-streamer) solution in F17 (see Figure 2b in F17), and increase the field strength by a factor of two. We obtain the relaxed 2D quasi-steady streamer solution for the initial state as shown in **Figure 1**. The cross-sections (panels a,b) of the initial state show a dense helmet dome of closed magnetic field approximately in static equilibrium, surrounded by an ambient open field region with a solar wind outflow with flow speed that accelerates to supersonic and super Alfvénic speed (see panel c).

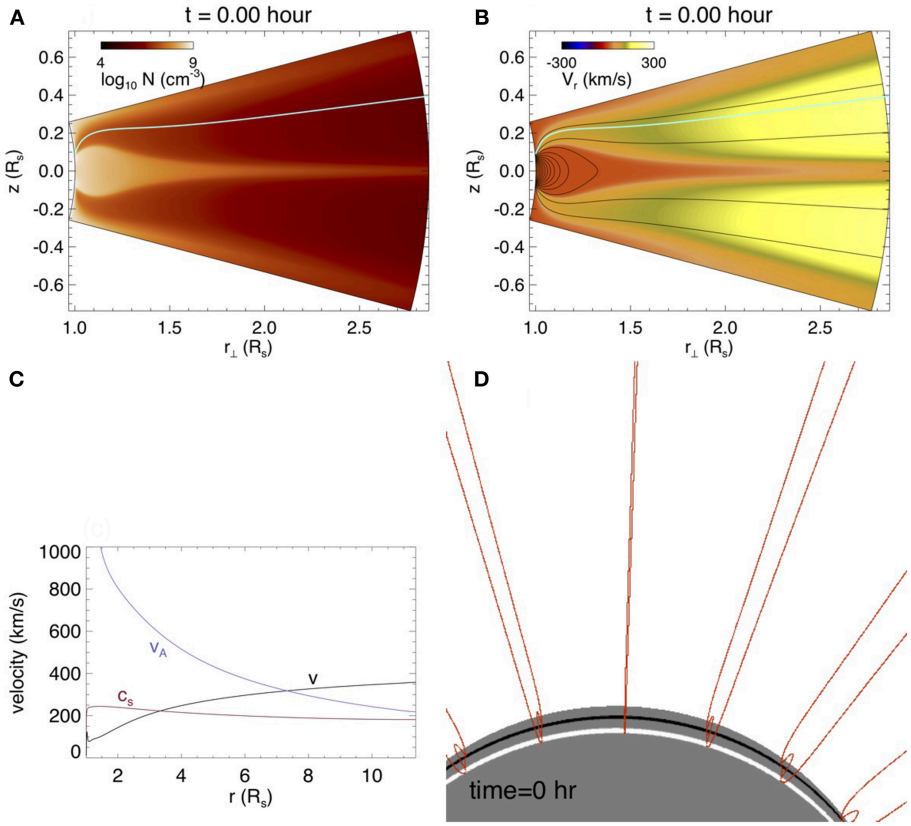

FIGURE 1 | The relaxed 2D quasi-steady streamer solution for the initial state. **(A)** shows the cross-section density, **(B)** shows the cross-section radial velocity over-plotted with magnetic field lines, **(C)** shows the parallel velocity V, the Alfvén speed V_A, and sound speed C_S along an open field line [marked as the green line in **(A,B)**] in the ambient solar wind. **(D)** shows a 3D view of the initial streamer field lines in the simulation domain with the lower boundary color showing the normal flux distribution of the initial bipolar bands.

A 3D view of the initial streamer field lines in the simulation domain is shown in **Figure 1D**.

Into this initial streamer field, we then impose at the lower boundary the emergence of a twisted magnetic torus by specifying an electric field as described in F17 (see Equations (19–22) and the associate description in F17). The specific parameters for the driving emerging torus (see the definitions of the parameters in F17) used for the present simulation are: the minor radius $a = 0.04314R_s$, twist rate per unit length $q/a = -0.0166$ rad Mm^{-1}, major radius $R' = 0.75R_s$, axial field strength $B_t a/R' = 106$ G, and the driving emergence speed $v_0 = 1.95$ km/s. The driving flux emergence at the lower boundary is stopped when the total twist in the emerged flux rope reaches about 1.76 winds of field-line twist between the two anchored ends.

We note that the present simulation and the PROM simulation in F18 are similar in the driving flux emergence, where a long flux rope of similar total twist is driven into the corona. The essential difference is that the pre-existing arcade field in the streamer of the present simulation has a significantly narrower foot-point separation and a stronger foot-point field strength (compare **Figure 1B** in this paper and Figure 2b in F18). The mean foot-point separation in the present case is $0.13R_s$ compared to $0.24R_s$ for that in the PROM simulation in F18. The narrower foot-point separation results in a faster decline of field strength with height for the corresponding potential field in the present case. With a stronger arcade foot-point field strength, we expect a stronger confinement of the emerging flux rope to a lower height, and hence smaller cavity and prominence heights, improving upon the PROM case in F18, in which the cavity and prominence heights obtained are too high compared to the typical observed values. Furthermore, the stronger field strength lower down and the faster decline with height of the corresponding potential field are expected to have significant effects on the height for the onset of the torus instability and the acceleration of the erupting flux rope as shown in previous simulations by Török and Kliem (2007).

3. SIMULATION RESULTS

3.1. Overview of Evolution

Figures 2a–f show snapshots of the 3D coronal magnetic field lines during the course of the evolution of the emerged coronal flux rope, from the quasi-static phase to the onset of eruption. The field lines shown in the snapshots are selected as follows.

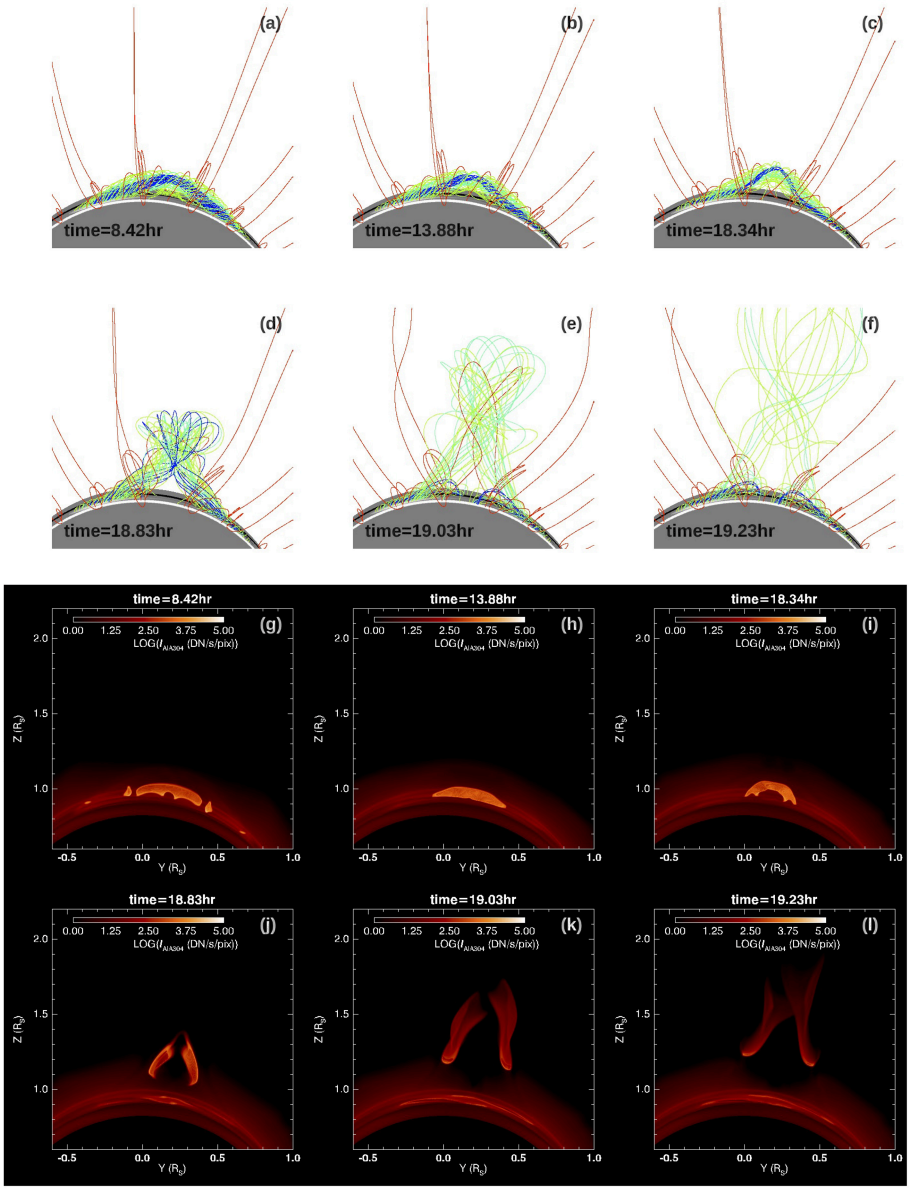

FIGURE 2 | (a–f) show a sequence of snapshots of the 3D magnetic field lines through the course of the evolution of the emerged coronal flux rope, and **(g–l)** show the corresponding synthetic SDO/AIA EUV images in 304 Å channel from the same perspective view.

A set of field lines from a set of fixed foot points in the pre-existing bipolar bands are traced as the red field lines (same field lines as those traced in **Figure 1D** for the initial state). For the representative field lines in the emerged flux rope, we trace field lines from a set of tracked foot points at the lower boundary that connect to a set of selected field lines of the subsurface emerging torus and color the field lines (green, cyan, and blue) based on the flux surfaces of the subsurface torus. **Figures 2g–l** show the synthetic SDO/AIA EUV images in 304 Å channel as viewed from the same line of sight (LOS) corresponding to the snapshots shown in **Figures 2a–f**. The synthetic AIA images are computed by integrating along individual line-of-sight (LOS) through the simulation domain:

$$I_{\text{channel}} = \int n_e^2(l)\, f_{\text{channel}}(T(l))\, dl, \tag{2}$$

where l denotes the length along the LOS through the simulation domain, I_{channel} denotes the integrated emission intensity at each pixel of the image in units of DN/s/pixel (shown in LOG scale in the images), "channel" denotes the AIA wavelength channel (which is 304 Å in the case for **Figures 2g–l**), n_e is the electron number density, and $f_{\text{channel}}(T)$ is the temperature response function that takes into account the atomic physics and the properties of the AIA channel filter. We obtain the temperature

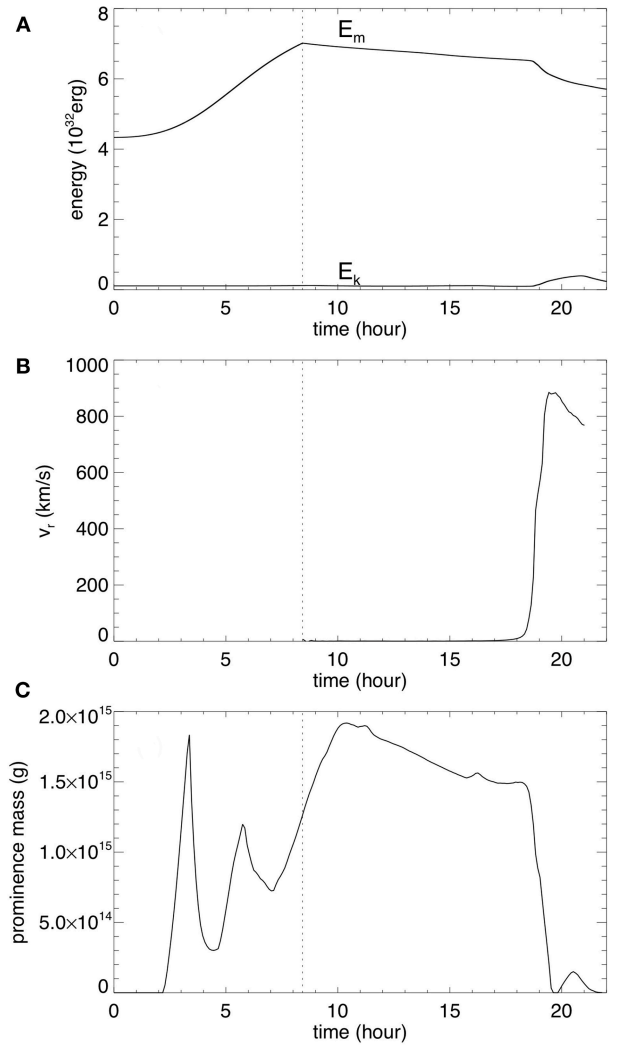

FIGURE 3 | (A) The evolution of the total magnetic energy E_m and total kinetic energy E_k, **(B)** the evolution of the rise velocity at the apex of the axial field line of the emerged flux rope, and **(C)** the evolution of the cool prominence mass in the corona evaluated as the total mass with temperature below 10^5 K.

dependent function $f_{\text{channel}}(T)$ for the individual filters using the SolarSoft routine `get_aia_response.pro`. The response function for the AIA 304 Å channel peaks at the temperature of about 8×10^4K, thus the synthetic emission images show where the cool prominence plasma condensations form in the flux rope. For the LOS integration, we also have assumed that the prominence condensations are "optically thick" such that when the LOS reaches a plasma where both the temperature goes below 7.5×10^4 K and the number density is above 10^9cm^3, we stop the integration for that LOS assuming the emission from behind the plasma is blocked and does not contribute to the integrated emission for the LOS. **Figure 3** shows the evolution of the total magnetic energy E_m, the total kinetic energy E_k, the rise velocity at the apex of the axial field line of the emerged flux rope, and the temporal evolution of the cool prominence mass in the corona evaluated as the total mass with temperature below 10^5 K. From $t = 0$ to 8.42 h, E_m increases as the emergence of a twisted magnetic torus is imposed at the lower boundary, and a long coronal flux rope is built up quasi-statically, confined by the coronal streamer as can be seen in the snapshot in **Figure 2a** at $t = 8.42$ h . The emergence is stopped at $t = 8.42$ h at which time the total field line twist about the axial field line of the emerged flux rope reaches about 1.76 winds between the anchored ends. This twist is above the critical value (about 1.25 winds) for the onset of the kink instability for a simple 1-dimensional cylindrical line-tied force-free flux rope (Hood and Priest, 1981). However subsequently, the flux rope is found to settle into a quasi-static rise phase over a long period of time (corresponding to about 131 Alfvén crossing times along the axis), from $t = 8.42$ h to about $t = 17$ h, with nearly zero acceleration (**Figure 3B**). We find that a long extended prominence has formed in the emerged flux rope (see **Figures 2g,h**), with the prominence condensations in the dips of the twisted field lines. In the PROM simulation in F18, it is shown that the cool prominence condensations form due to the development of the radiative instability of the dense plasma in the dips after their emergence. Here in the present case we find that cool prominence condensations begin to form even earlier in the flux emergence, soon after the apex of the flux rope emerges, as dense plasma is pushed into the corona with the stronger flux rope field. However these earlier forming condensations are unsteady and drain down as the flux rope emergence continues, and later more stable condensations form in the dips of the emerged field lines as in the PROM case. In **Figure 3C** we see large temporal fluctuations of the cool prominence mass during the early phase of the flux emergence. After the emergence is stopped (marked by the vertical dotted line in **Figure 3**), the prominence mass shows both a phase of continued increase and then a gradual decrease during the quasi-static phase (from $t = 8.42$ h to about $t = 17$ h). However this change from an increase of prominence mass to a decline does not seem to be associated with any significant change in the rise velocity in the quasi-static phase. During this quasi-static rise period the magnetic energy decreases slowly (see **Figure 3**) due to the continued magnetic reconnections, until about $t = 17$ h when it reaches a height of about $r = 1.17R_s$, where the flux rope begins a monotonic acceleration (see **Figure 4A**) and erupts subsequently with a sharp decrease of the magnetic energy and a significant increase of the kinetic energy (see **Figure 3A**). **Figure 4** shows that the height (marked by the vertical dotted line) at which the flux rope begins to accelerate monotonically (see panel a) corresponds to the height at which the decay rate of the corresponding potential field reaches a magnitude of about 1.6 (see panel b), which exceeds the critical decline rate of about 1.5 for the onset of the torus instability for a toroidal flux rope (e.g., Kliem and Török, 2006). Thus in the present case, the onset of eruption is compatible with the onset of the torus instability. We find that in the present simulation, the flux rope begins to erupt at a significantly lower height (at about $r = 1.17R_s$) compared to that (at about $r = 1.6R_s$) in the PROM simulation in F18. This is because the arcade field lines in the pre-existing streamer of the PROM simulation have a significantly wider mean foot-point separation and hence the corresponding

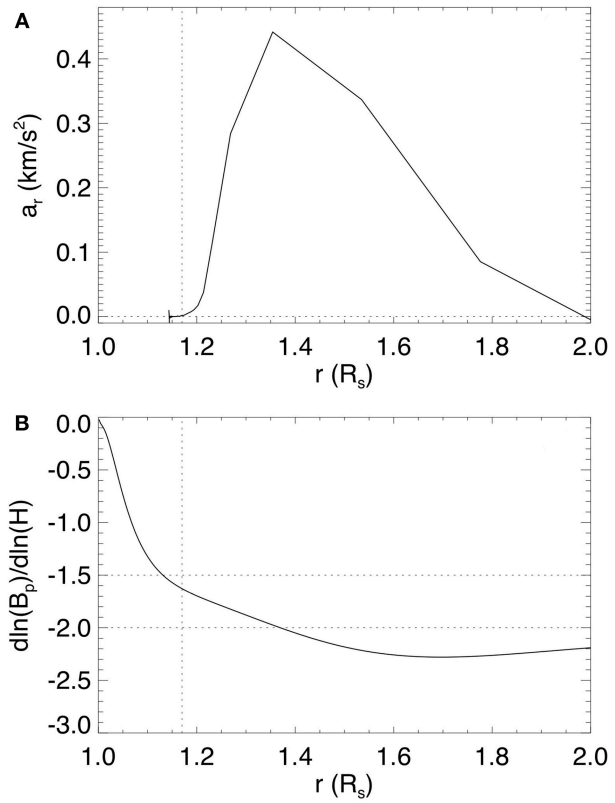

FIGURE 4 | (A) Acceleration at the apex of the flux rope's axial field line as a function of its height position, and **(B)** the decay rate of the corresponding potential magnetic field strength B_p with height H (above the surface) when the emergence is stopped (after which the lower boundary normal magnetic flux distribution and the corresponding potential field remain fixed).

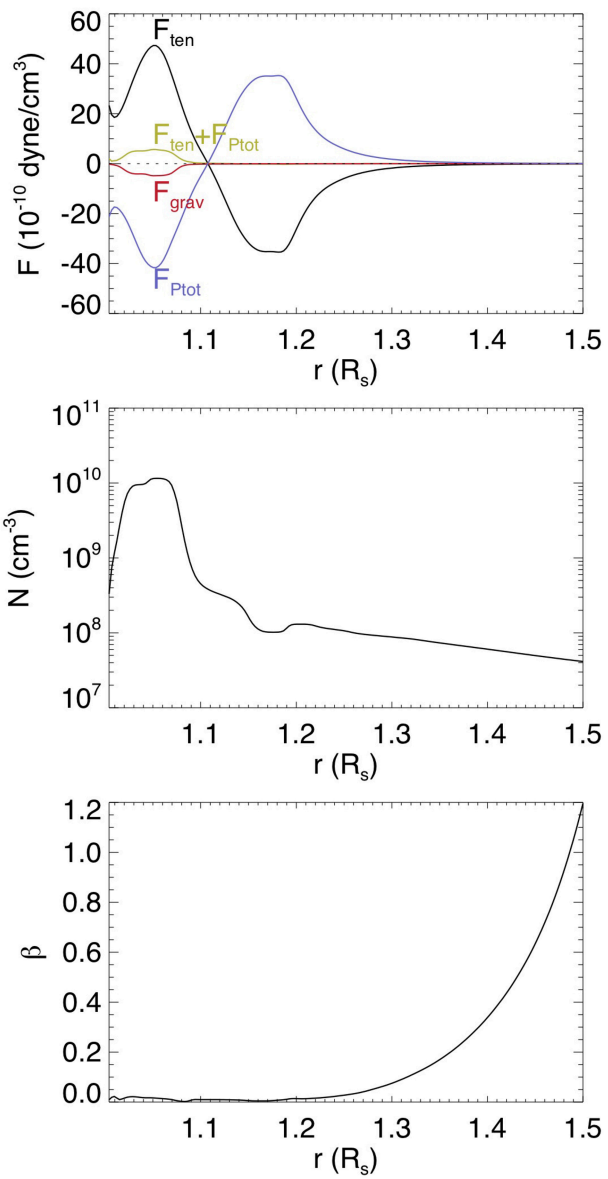

FIGURE 5 | Several radial forces **(Top)**, density **(Middle)**, and plasma-β (the ratio of gas pressure to magnetic pressure) **(Bottom)** along the central vertical line through the middle of the flux rope in **Figure 2b**. The radial forces shown in the top panel are the magnetic tension force F_{ten} (black curve), the total pressure gradient force F_{Ptot} (blue curve), which is predominantly the magnetic pressure gradient (because of the low plasma-β) as shown in the bottom panel), the sum $F_{ten} + F_{Ptot}$ (green curve), which is approximately the net Lorentz force, and the gravity force of the plasma F_{grav} (red curve). as a function of height.

potential field declines with height significantly more slowly, where the magnitude of the decay rate remains below 1.5 until about $r = 1.3R_s$ in that case.

Although the confining potential field in the present case declines with height more steeply, it is stronger lower down and hence the flux rope and the prominence during the quasi-static phase reach significantly lower heights compared to the PROM case, and the flux rope field strength is also significantly stronger. The peak Alfvén speed in the central flux rope cross-section in the present case reaches about 4,100 km/s with a peak field strength of about 24G, compared to the peak Alfvén speed of about 1,500 km/s and peak field strength of about 9G in the PROM case during the quasi-static stage. The stronger flux rope field strength causes the prominence-carrying field to be much closer to force-free compared to the PROM case, as shown in **Figure 5** compared to Figure 6 in F18. **Figure 5** shows that the net Lorentz force (the green curve in the top panel) that balances the gravity force (the red curve) of the prominence is at most about 0.1 of either the magnetic tension or magnetic pressure gradient. In contrast in the PROM case in F18, there is a significant net Lorentz force to balance the prominence gravity that is comparable to the magnetic tension, i.e., the prominence carrying fields in the flux rope is significantly non-force-free. In the present case however, the magnetic field is close to force-free throughout the flux rope, even for the prominence-carrying field. Thus we do not see a significant variation of the rise velocity during the quasi-static phase in response to the growth or decline of prominence condensation mass as found above, and the onset of eruption is consistent with the onset of the torus instability. The stronger flux rope field strength in the present case also

produces a stronger acceleration and a higher peak velocity of the erupting flux rope. In the present case the flux rope is found to accelerate to a peak velocity of nearly 900 km/s (see **Figure 3B**), compared to the peak velocity of about 600 km/s reached in the PROM simulation (see **Figure 4B** in F18). However, the ratio of the peak velocity over the peak Alfvén speed of the flux rope is found to be lower (0.22) in the present case compared to the PROM case (0.4).

Although the onset of eruption in the present simulation is consistent with the onset of the torus instability, because of the significant total twist in the emerged flux rope, the erupting flux rope shows significant rotational motion and a kinked morphology as can be seen in **Figures 2d–f**. The associated erupting prominence also shows a kinked morphology (see **Figures 2j–l**). The rotation of the erupting prominence is more clearly seen from the view shown in **Figure 6**, where the flux rope is viewed nearly along its length. We can clearly see the writhing motion of the erupting prominence due to the writhing motion of the hosting flux rope.

We also note that two brightening ribbons are visible in the AIA 304 Å images (**Figures 6e,f**) on the lower boundary under the erupting prominence. The brightening ribbons correspond to the foot points of the highly heated, post-reconnection loops just reconnected in the flare current sheet behind the erupting flux rope. The strong heat conduction flux coming down along the heated post-reconnection loops causes an increase of the pressure and density at the foot points at the lower boundary (based on the variable pressure lower boundary condition used here as described in F17). This enhanced density at the foot points leads to the brightening of the ribbons in 304 channel emission. They qualitatively represent the flare ribbons regularly seen in eruptive flares.

3.2. The Formation of Prominence-Cavity System

Figure 7 shows the limb view of the 3D magnetic field lines (panel a), and synthetic SDO/AIA EUV images in 304 Å (panel b), 171 Å (panel c), 193 Å (panel d), and 211 Å (panel e) channels, with the flux rope viewed along its axis at a time ($t = 13.88$hr) during the quasi-static phase. A similar limb view with the flux rope slightly tilted by 5° is shown in **Figure 8**. The AIA 171 Å, 193 Å, 211 Å channel images are computed in the same way as described in the previous section using Equation 2 with the temperature response function $f_{\rm channel}(T)$ replaced by that for the corresponding channel. The synthetic AIA images with the flux rope viewed nearly along its axis (as illustrated in **Figures 7**, **8**) show the formation of a prominence-cavity system with qualitative features similar to observations (e.g., Gibson, 2015). Inside the bright helmet dome, we see a dark cavity surrounding the lower central prominence (which appears dark in the 171 Å, 193 Å, or 211 Å images due to the optically thick assumption). In this simulation where we have used a pre-existing streamer solution with a narrower mean foot-point separation for the closed arcade field, we obtained

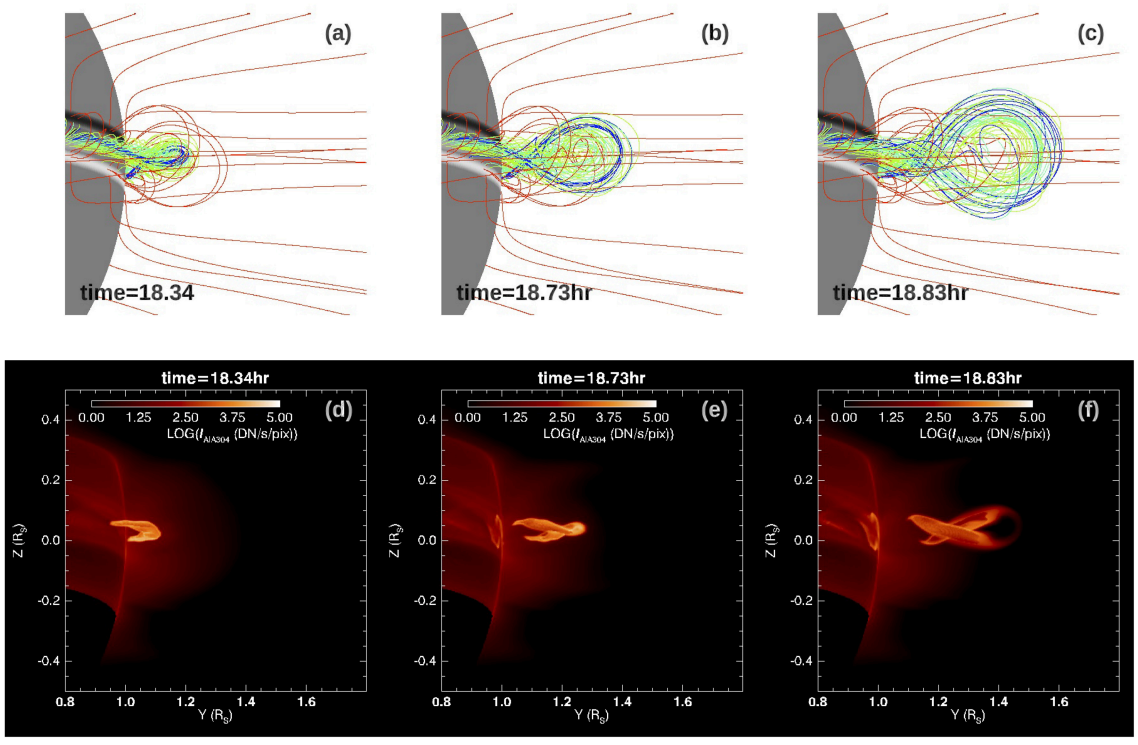

FIGURE 6 | Successive snapshots of the erupting flux rope field lines **(a–c)** and the corresponding synthetic AIA 304 Å images **(d–f)**, viewed with a LOS that is close to aligned with the length of the flux rope. They show the writhing motion of the flux rope and the associated erupting prominence.

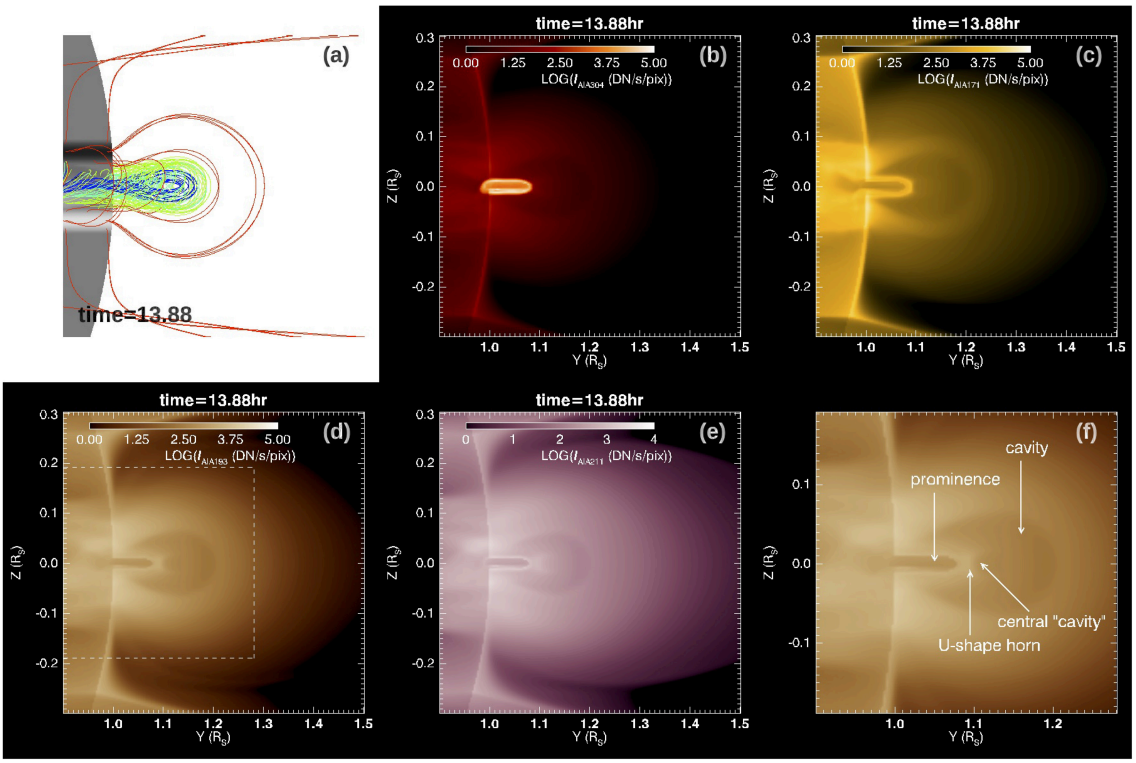

FIGURE 7 | 3D field lines **(a)**, and synthetic SDO/AIA EUV images in 304 Å **(b)**, 171 Å **(c)**, 193 Å **(d)**, and 211 Å **(e)** channels, with the flux rope viewed along its axis above the limb, at time $t = 13.88$hr during the quasi-static phase. **(f)** shows the zoomed in view of the boxed area of **(d)** with the cavity substructures labeled.

a significantly smaller cavity with lower heights for the cavity (about 0.2 R_s) and the prominence (about 0.1 R_s) compared to the previous PROM simulation in F18 (about 0.47 R_s for the cavity height and 0.17 R_s for the prominence height), in better agreement with observations (e.g., Gibson, 2015), which find a median height for EUV cavities of 0.2 R_s. In the synthetic 193 Å, or 211 Å images in **Figures 7d,e**, **8d,e**, we also find substructure inside the cavity, similar to some of the features described in (e.g., Gibson, 2015; Su et al., 2015). We find a central smaller cavity on top of the prominence enclosed by a"U"-shaped or horn-like bright structure extending above the prominence. Such substructure is similar to the features as shown in Figures 8, 12 in Gibson (2015) and Figure 2c in Su et al. (2015). Here we examine the characteristics of the 3D magnetic field comprising the different parts of the prominence-cavity system formed in our MHD model.

Figure 9 shows a set of selected prominence-carrying field lines that contain prominence dips and one representative arcade dome field line in the high density dome, together with a vertical cross-section of density placed at different locations (for the different panels a–e) along the flux rope. The prominence condensation is outlined by the pink temperature iso-surface with $T = 7.5 \times 10^4$K. It can be seen in **Figures 9a–e** that as the density cross-section slides along the flux rope, the prominence carrying field lines intersect the cross-section in the low density cavity region, except at the prominence dips. In other words, we find that the prominence and the surrounding cavity are threaded by the prominence-carrying field lines, with the cavity corresponding to the density-depleted portions of the prominence-carrying field lines extending up from the prominence dips. As was shown in F18, the runaway radiative cooling of the prominence condensations in the dips causes a lowered pressure and draining of plasma toward the dips, establishing a more rarefied atmosphere along the dip-to-apex portions of the prominence carrying field lines compared to the surrounding dome field lines without dips. We find that the cavity boundary corresponds to a sharp transition from the dipped prominence carrying field lines inside the cavity to the arcade-like field lines without dips outside in the higher density dome. This is illustrated in an example shown in **Figure 10**. Two field lines are traced from two adjacent points on the two sides of the cavity boundary, and they show very different connectivity to the lower boundary, with the one from inside the cavity being a long twisting field line carrying two prominence dips and the other from just outside the cavity being a significantly shorter arcade-like field line with no dips (see **Figure 10c**). Because of the drastic difference in the connectivity and whether there are prominence condensations, the two field lines show very different thermodynamic properties at their two adjacent points near the cavity boundary, giving rise to the sharp appearance of the EUV cavity boundary. Note that the arcade-like field line in the dome region shows mixed types of foot points, with one foot point

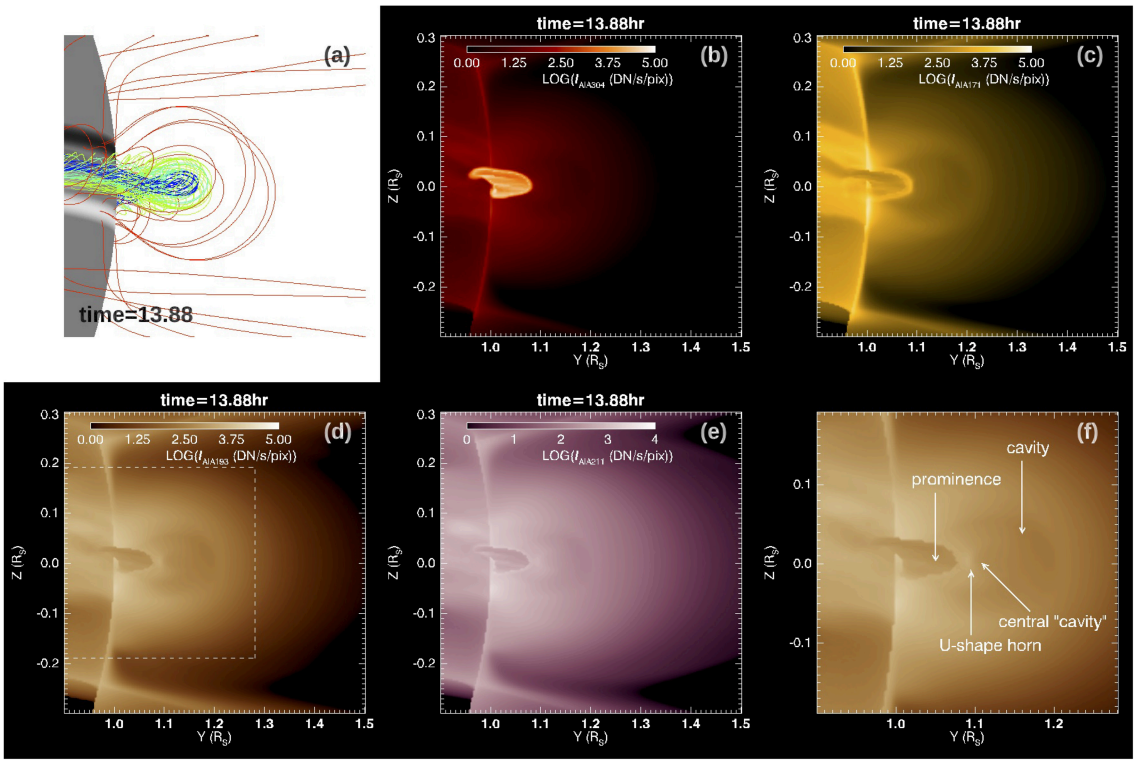

FIGURE 8 | Same as **Figure 7** but with the flux rope viewed slightly tilted by 5°.

connecting to the pre-existing bipolar bands and the other foot point in the emerging flux rope foot points, suggesting that there have been continued reconnections between the flux rope and the pre-existing arcade field.

To examine the magnetic field that produces the substructure inside the EUV cavity, we have also traced field lines that thread through the region that contributes to the EUV emission of the prominence "horns." **Figure 11** shows a set of such field lines, together with a cross section showing the local emission intensity in EUV 193 Å channel (the integrand $n_e^2 f_{193}(T)$ in Equation 2), with the cross-section placed at different locations along the flux rope for the different panels (a–e), and without showing the cross-section in panel (f). It can be seen that as the cross-section slides along the flux rope, the field lines intersect the central "U"-shaped region of enhanced EUV emission. As shown in **Figure 11f**, we find that these field lines that contribute to the prominence-horn emission are field lines containing relatively shallow dips, where the prominence condensations have evaporated to coronal temperatures (above 4×10^5 K and with most parts of the field lines ranging between 8×10^5 K and 2.2×10^6 K) while the density is still relatively high compared to the surrounding cavity, and hence producing a favorable conditions for the enhanced EUV 193 Å channel emission. The cross-sections showing the EUV 193 Å channel emission intensity in **Figures 11a–e** also illustrate that enclosed inside the bright "U"-shaped prominence "horns" is another central region of reduced emission, corresponding to the central "cavity" seen in the synthetic EUV images (**Figures 7d**, **8d**). Tracing field lines through this central "cavity" region, we find that it is threaded by long twisted field lines that contain no dips as shown in **Figure 12**. However as shown in the cross-sections in **Figures 12a–c**, this central "cavity" region is rather a relatively dense and hot central core. Its reduced EUV emission (compared to the horns and the outer dome region) is due to the high temperature (reaching about 2.5 MK) that is out of the peak of the EUV response function, instead of due to a low density as is the case for the outer cavity. We find that the outer boundary of the outer cavity has a hot rim of even higher temperature (see the cross section in **Figure 12c**) due to the heating resulting from continued reconnections between the dipped, twisted field lines that approach the cavity boundary and their neighboring arcade like field lines.

4. CONCLUSIONS

We have carried out MHD simulation of the quasi-static evolution and onset of eruption of a prominence-forming coronal flux rope under a coronal streamer, extending the previous work of F17 and F18. Previous simulations of the prominence-hosting coronal flux rope (the WS-L simulation in F17 and the PROM simulation in F18) have used the WS streamer solution in F17 for the pre-existing field, whose arcade field lines have a wide mean foot-point separation. This results in a corresponding potential field that declines slowly with height.

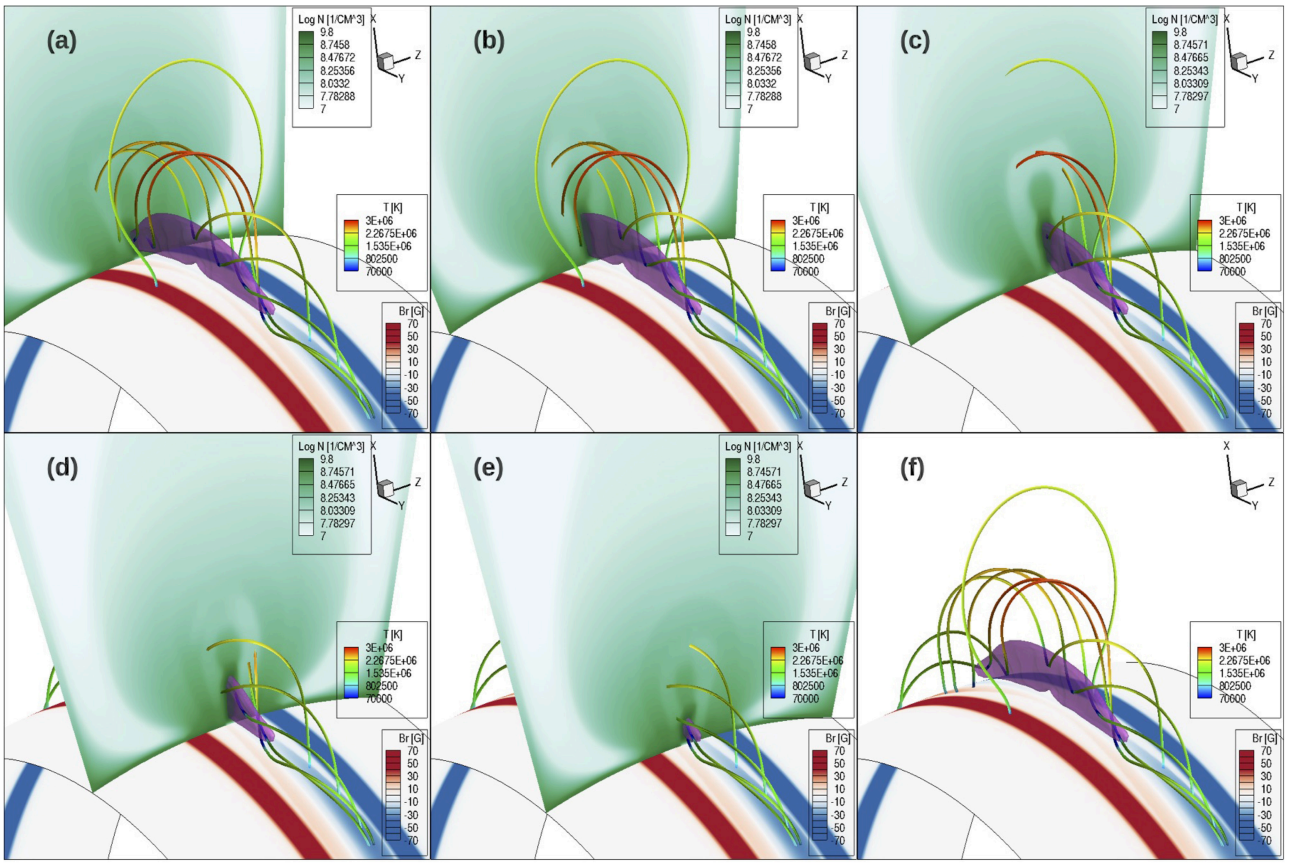

FIGURE 9 | A set of prominence-carrying field lines containing prominence dips and one representative arcade dome field line, all colored with temperature, plotted with a cross-section of density placed at different locations along the flux rope for the different panels **(a–e)**. **(f)** shows the same field lines without the density cross-section. A pink iso-surface of temperature at $T = 7.5 \times 10^4$K outlines the location of the prominence condensation. The lower boundary surface is colored with the normal magnetic field strength. All the images are at the time $t = 13.88$hr during the quasi-static stage.

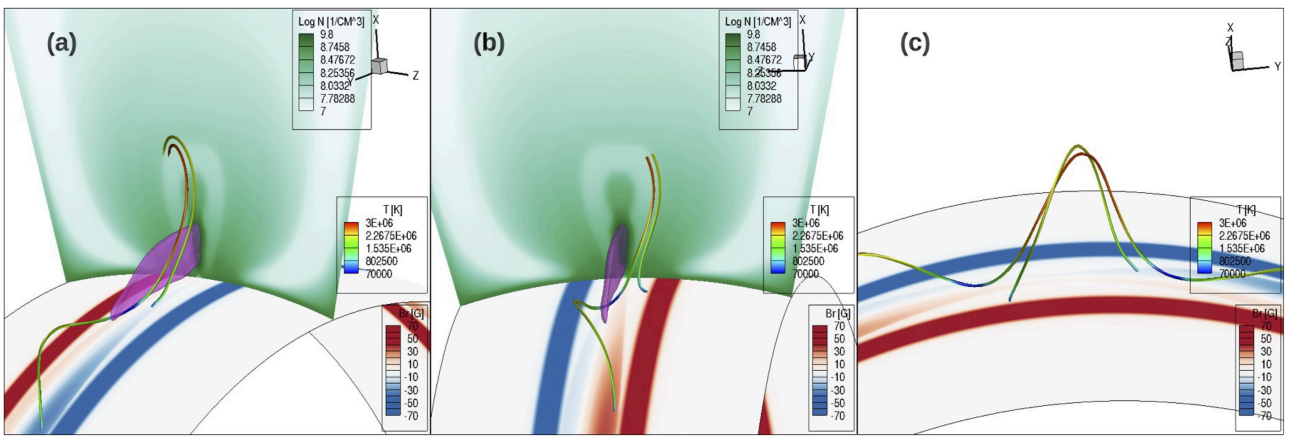

FIGURE 10 | Two field lines traced from two adjacent points on the two sides of the cavity boundary in the density cross-section shown in **(a,b)** viewed from two different perspectives from opposite sides of the cross-section. The pink iso-surface of temperature at $T = 7.5 \times 10^4$ K outlines the prominence condensations. **(c)** shows the same field lines from a different view without the density cross-section and the iso-surface for the prominence. The lower boundary shows the normal magnetic field distribution B_r.

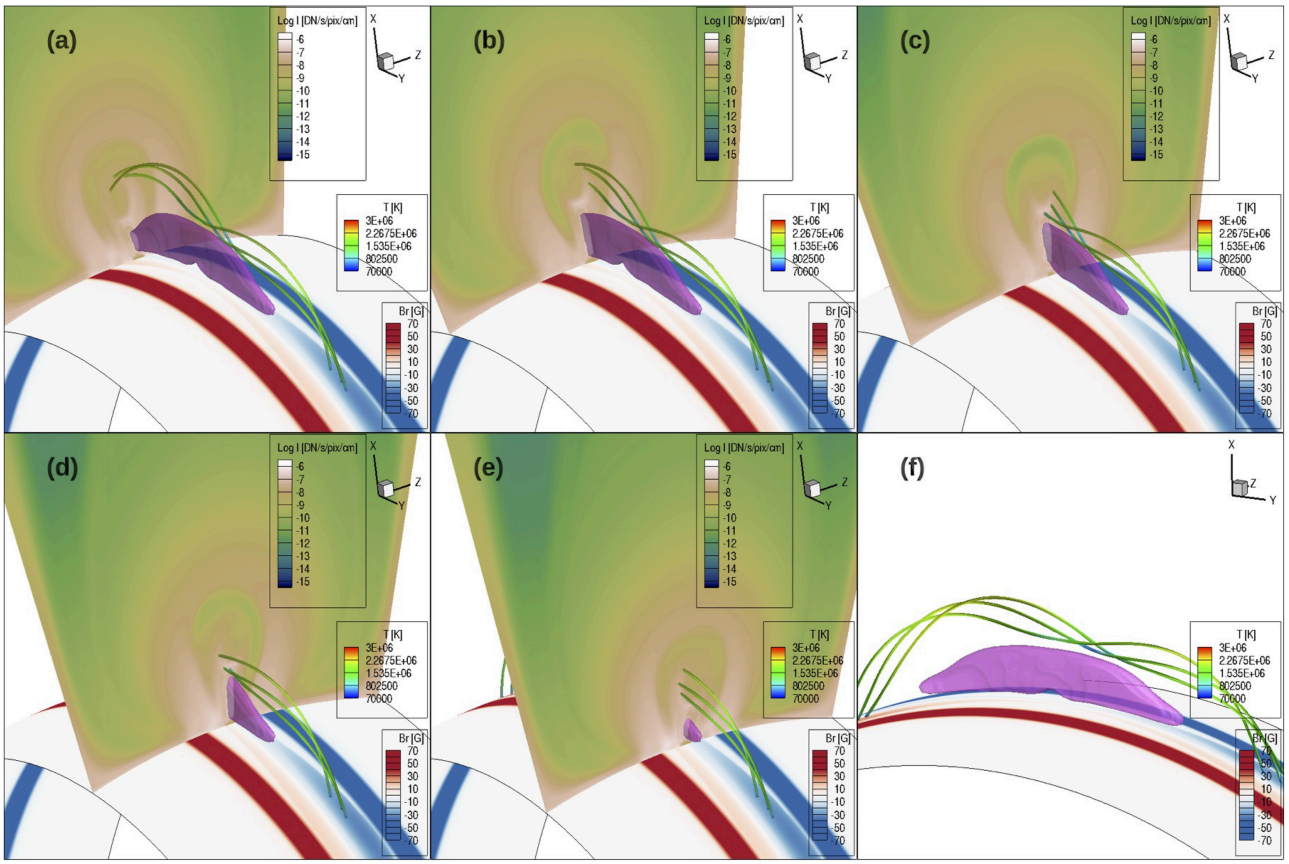

FIGURE 11 | A set of field lines threading through the region that contributes to the EUV 193 Å channel emission that produces the horn-like structure inside the cavity, together with a cross-section showing the local emission intensity in EUV 193 Å channel (the integrand $n_e{}^2 f_{193}(T)$ in Equation 2) placed at different locations along the flux rope for the different panels **(a–e)**. **(f)** shows the same field lines without the cross-section and viewed from a different perspective. The field lines are colored in temperature. A pink iso-surface of temperature at $T = 7.5 \times 10^4$K outlines the location of the prominence condensation. The lower boundary surface is colored with the normal magnetic field strength. All the images are at the same time ($t = 13.88$hr) as those in **Figure 9**.

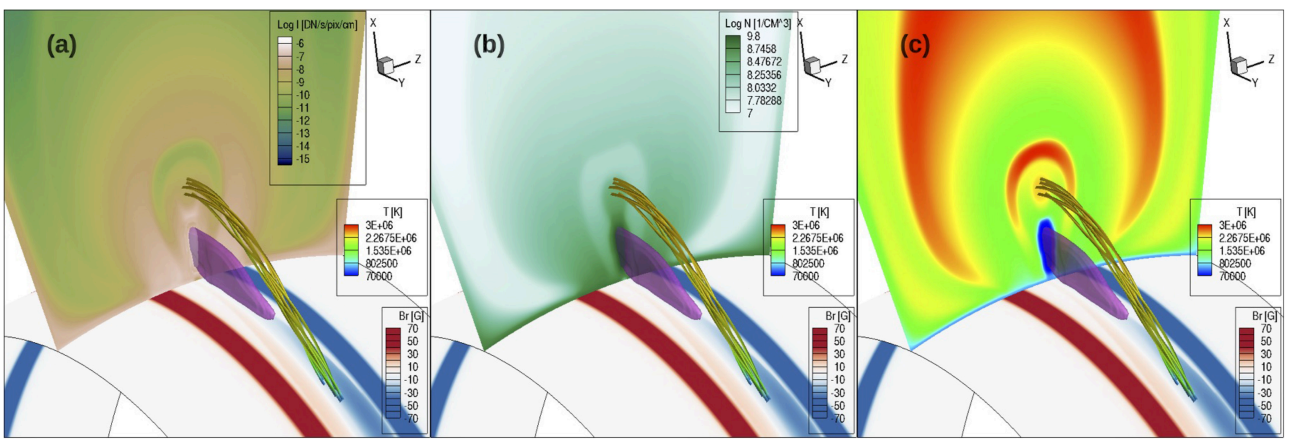

FIGURE 12 | A set of field lines threading through the central EUV cavity enclosed in the prominence horns, together with a middle cross-section showing the distribution of EUV 193 Å channel emission intensity **(a)**, density **(b)**, and temperature **(c)**. The field lines are colored in temperature and a pink iso-surface of temperature at $T = 7.5 \times 10^4$K outlining the location of the prominence condensation is also shown.

Consequently the emerged flux rope and the prominence and cavity that form during the quasi-static stage reach large heights (larger than typically observed) before the onset of eruption. For the present simulation we have used a pre-existing streamer solution with a significantly narrower mean foot-point separation and stronger foot-point field strength for the arcade field lines. This results in a stronger field strength lower down and steeper decline of field strength with height for the corresponding potential field at the end of the flux emergence. We still drive the emergence of a similar long twisted flux rope into the corona as in the PROM case in F18. Similar to the PROM case, we find the formation of a prominence-cavity system during the quasi-static evolution, but with significantly lower heights for the prominence (reaching about $0.1R_s$) and the cavity (extend to about $0.2R_s$), in better agreement with the properties of the typically observed quiescent prominence-cavity systems. We also find the formation of cavity substructures, such as the prominence "horns" and central "voids" or "cavities" on top of the prominences, in qualitative agreement with the observed features (e.g., Gibson, 2015; Su et al., 2015).

We have examined the properties of the magnetic fields that comprise the different parts of the prominence-cavity system seen in the synthetic EUV images from our MHD model to understand the nature of the corresponding observed features. We find that the prominence and the outer cavity is composed of the long twisted field lines with dips that contain prominence condensations (**Figure 9**), where the cavity is threaded by the density depleted portions of the field lines extending up from the prominence dips. As was shown in F18, the formation of the prominence condensations due to runaway radiative cooling causes an overall lowered pressure in the dips and plasma draining down toward the dips such that a more rarefied atmosphere is established for the dip-to-apex portions of the field lines, compared to the surrounding arcade field lines in the denser helmet dome. We find that the boundary of the outer cavity corresponds to a sharp transition of field line connectivity, where neighboring field lines connect very differently to the lower boundary, with long twisted dipped field lines just inside the boundary and simple arcade-like field lines with no dips just outside (**Figure 10**). The very different thermodynamic properties of the two types of neighboring field lines give rise to the sharp appearance of the EUV cavity boundary. There are also continued magnetic reconnections at the boundary, causing a high temperature rim at the outer cavity boundary (see the temperature cross-section shown in **Figure 12c**) In regard to the cavity substructures, we find that the region of the central "U"-shaped prominence "horns" with relatively enhanced EUV emission inside the cavity are threaded by twisted field lines with relatively shallow dips, where the prominence condensations have evaporated to coronal temperatures while the density is still relatively high compared to the surrounding cavity (**Figure 11**). For the central "void" or "cavity" enclosed in the prominence "horns" on top of the prominence, we find that it corresponds to a central high temperature and high density core threaded by long twisted field lines with no dips (**Figure 12**). It appears as a central "void" with weakened EUV emission not because of a lower density, but because it is heated to a high temperature reaching about 2.5 MK that is outside of the peak of the AIA 193 Å channel (and also the AIA 211 Å channel) temperature response function. We find that the central high temperature core is growing over the course of the quasi-static phase. The prominence "horns" and growth of the central hot core result from a gradual transition of dipped prominence carrying field lines to un-dipped but still twisted field lines as they rise quasi-statically with the dips becoming shallower and the prominence condensations evaporating. The continued magnetic reconnection at the cavity boundary between the dipped twisted field lines and their neighboring arcade like field lines may be contributing to the quasi-static rise by removing the confining field. We defer to a follow-up paper to conduct a quasi-separatrix layer analysis (e.g., Pariat and Démoulin, 2012) to study the evolution of magnetic reconnection and how it contributes to the removal of the prominence mass and the rise of the flux rope during the quasi-static phase.

As was noted in F18, previous 3D MHD simulation of prominence formation in a stable flux rope by Xia et al. (2014), which includes the chromosphere as the lower boundary, has also found the formation of a prominence-cavity system with similar internal structures in synthetic EUV images. Their explanation of the structures obtained in their simulation is different from that found in our simulation. They found that the central dark cavity enclosed by the horns is threaded by two types of field lines: both the dipped twisted field lines and the arched twisted field lines with no dips, while the outer cavity is formed by arched twisted field lines with no dips. The prominence horns are due to the LOS emission from the prominence-corona transition regions of the prominence loaded dipped field lines. They found that during prominence-cavity formation, density depletion occurs not only on prominence-loaded field lines threading the cavity and prominence where *in situ* condensation happens (as is the case in our simulation), but also on prominence-free field lines due to mass drainage into the chromosphere. We do not find the latter type of field lines forming the cavity. Our outer main cavity is threaded by the density depleted portions of the prominence carrying dipped field lines, and the inner cavity is threaded by arched twisted field lines with no dips, which are not density depleted but appear dark in the EUV emission because they are heated to a high temperature (about 2.5 MK). In our simulations, the exclusion of the chromosphere and fixing the lower boundary at the transition region temperature do not allow modeling the change of the transition region height and hence limit the ability to model the condensation/drainage of plasma to the chromosphere with the cool chromosphere temperature region extending upwards. Furthermore our 3D simulations that model both the quasi-static phase and the eruption of prominence-carrying coronal flux ropes have much lower numerical resolution (1.9 Mm), compared to that achieved in Xia et al. (2014); Xia and Keppens (2016), which use adaptive grid refinement. As described in F17 we have modified the radiative loss function to suppress cooling for $T \leq 7 \times 10^4$ K, so that the smallest pressure scale height (about 4.4 Mm) of the coolest plasma that forms does not go below two grid points given our simulation resolution. The low numerical resolution causes large numerical diffusion and viscosity that can impact

significantly the heating and hydrodynamic evolution of the plasma. Because of the above limitations of our 3D simulations, the results of the thermodynamic properties of the resulting prominence-cavity system have large uncertainties, and need to be confirmed or revised by future higher resolution simulations that include the chromosphere in the lower boundary, which are our future work. The current simulation qualitatively illustrates the effect of the runaway radiative cooling of the prominence condensations in the dips of the twisted field lines that causes drainage of plasma of the upper portions of these field lines and creates a cavity with a relatively sharp boundary that corresponds to the transition from the dipped prominence carrying field lines to neighboring arcade-like field lines. It does not explain the formation of filament channels or coronal cavities in the absence of filament or prominence condensations.

We find that in the current simulation with a significantly narrower mean foot-point separation for the arcade field of the pre-existing streamer, the emerged flux rope begins to erupt at a significantly lower height compared to the PROM case shown in F18. This is due to the steeper decline with height of the corresponding potential field which allows the onset of the torus instability lower down. The eruption also produces a significantly faster CME compared to the PROM case, mainly due to the stronger field strength of the pre-eruption flux rope confined lower down. Although we find that the onset of eruption in the present case is consistent with the onset of the torus instability, due to the large total twist (about 1.76 winds of field line twist) in the emerged flux rope, both the erupting flux rope and the associated erupting prominence show significant rotational motion and develop a kinked morphology (**Figures 2**, **6**).

AUTHOR CONTRIBUTIONS

YF is the primary author of the paper who carried out the simulation, computed the synthetic images and directed the data analysis. TL carried out the 3D analysis of the simulation data that lead to the major findings of the paper and contributed to the writing of the paper.

FUNDING

NCAR is sponsored by the National Science Foundation. YF is supported in part by the Air Force Office of Scientific Research grant FA9550-15-1-0030 to NCAR. Visiting graduate student TL is supported by the scholarship from the Chinese Scholarship Council of the Ministry of Education of China, the National Natural Science Foundation of China grant NOS. 11473071 and 11790302 (11790300) and the Natural Science Foundation of Jiangsu Province (China) grant No. BK20141043.

ACKNOWLEDGMENTS

We thank Dr. Jie Zhao for reading the paper and helpful comments on the paper.

REFERENCES

Fan, Y. (2017). MHD simulations of the eruption of coronal flux ropes under coronal streamers. *Astrophys. J.* 844:26. doi: 10.3847/1538-4357/aa7a56

Fan, Y. (2018). MHD simulation of prominence eruption. *Astrophys. J.* 862:54. doi: 10.3847/1538-4357/aaccee

Gibson, S. (2015). "Coronal cavities: Observations and implications for the magnetic environment of prominences," in *Solar Prominences*, eds. J. C. Vial and O. Engvold, Vol. 415, *Astrophysics and Space Science Library* (Cham: Springer), 323–353. doi: 10.1007/978-3-319-10416-4_13

Hood, A. W., and Priest, E. R. (1981). Critical conditions for magnetic instabilities in force-free coronal loops. *Geophys. Astrophys. Fluid Dynam.* 17, 297–318. doi: 10.1080/03091928108243687

Kliem, B., and Török, T. (2006). Torus Instability. *Phys. Rev. Lett.* 96:255002. doi: 10.1103/PhysRevLett.96.255002

Pariat, E., and Démoulin, P. (2012). Estimation of the squashing degree within a three-dimensional domain. *Astron. Astrophys.* 541: A78. doi: 10.1051/0004-6361/201118515

Su, Y., van Ballegooijen, A., McCauley, P., Ji, H., Reeves, K. K., and DeLuca, E. E. (2015). Magnetic structure and dynamics of the erupting solar polar crown prominence on 2012 March 12. *Astrophys. J.* 807: 144. doi: 10.1088/0004-637X/807/2/144

Török, T., and Kliem, B. (2007). Numerical simulations of fast and slow coronal mass ejections. *Astronom. Nachrich.* 328, 743–746. doi: 10.1002/asna.200710795

Webb, D. F., and Hundhausen, A. J. (1987). Activity associated with the solar origin of coronal mass ejections. *Solar Phys.* 108, 383–401. doi: 10.1007/BF00214170

Xia, C., and Keppens, R. (2016). Formation and plasma circulation of solar prominences. *Astrophys. J.* 823:22. doi: 10.3847/0004-637X/823/1/22

Xia, C., Keppens, R., Antolin, P., and Porth, O. (2014). Simulating the *in situ* condensation process of solar prominences. *Astrophys. J. Lett.* 792: L38. doi: 10.1088/2041-8205/792/2/L38

Conflict of Interest Statement: The authors declare that the research was conducted in the absence of any commercial or financial relationships that could be construed as a potential conflict of interest.

frontiers in Astronomy and Space Sciences

ORIGINAL RESEARCH
published: 18 April 2019
doi: 10.3389/fspas.2019.00028

Gradual Pre-eruptive Phase of Solar Coronal Eruptions

*Bojan Vršnak**

Hvar Observatory, Faculty of Geodesy, University of Zagreb, Zagreb, Croatia

Physical background of the evolution of a coronal magnetic flux rope embedded in the magnetic arcade during the gradual-rise pre-eruptive stage is studied. It is assumed that this stage represents an externally-driven evolution of the pre-eruptive structure through a series of quasi-equilibrium states, until a point when the system losses equilibrium and erupts due to unbalanced internal forces. In particular, three driving processes are considered: twisting motions of the flux-rope footpoints, emergence of new magnetic flux beneath the flux rope, and the mass leakage down the flux-rope legs. For that purpose, an analytical flux-rope model is employed, to inspect how fast the equilibrium height of the structure rises due to the increase of the poloidal-to-axial field ratio, the increase of axial electric current, and the decrease of mass. It is shown that the flux-rope twisting itself is not sufficient to reproduce the rising speeds observed during the pre-eruptive stage. Yet, it is essential for the loss-of-equilibrium process. On the other hand, the considered emerging flux and the mass loss processes reproduce well the rate at which the pre-eruptive structure rises before the main acceleration stage of the eruption sets in.

Keywords: sun, coronal mass ejections (CMEs), magnetohydrodynamics (MHD), MHD instabilities, twisted magnetic structures

OPEN ACCESS

Edited by:
Rui Liu,
University of Science and Technology of China, China

Reviewed by:
Yuhong Fan,
University Corporation for Atmospheric Research (UCAR), United States
Marilena Mierla,
Royal Observatory of Belgium, Belgium

***Correspondence:**
Bojan Vršnak
bvrsnak@geof.hr

Specialty section:
This article was submitted to Stellar and Solar Physics, a section of the journal Frontiers in Astronomy and Space Sciences

Received: *24 January 2019*
Accepted: *01 April 2019*
Published: *18 April 2019*

Citation:
Vršnak B (2019) Gradual Pre-eruptive Phase of Solar Coronal Eruptions. Front. Astron. Space Sci. 6:28. doi: 10.3389/fspas.2019.00028

1. INTRODUCTION

There is a general consensus that solar eruptions, which lead to coronal mass ejections (CMEs) and are frequently associated with solar flares, are a consequence of instability of coronal structures, most often considered to be coronal magnetic arcades embedding a helically twisted magnetic flux rope (for a review see, e.g., Schmieder et al., 2015; Green et al., 2018). Basically, there are three different scenarios that can explain the presence of the flux rope within the eruptive structure: (i) an already-formed flux rope emerged from the subphotospheric layers; (ii) rope is formed gradually by a series of reconnections within a sheared arcade; (iii) it forms during the eruption itself (e.g., Green et al., 2018, and references therein). In this paper a situation where the flux rope exists already prior to the eruption (i.e., the mentioned first two options) will be studied to get an insight into physical background of the evolution of the pre-eruptive arcade/flux-rope structure.

Most of eruptions show three basically different stages: a gradual pre-eruptive stage, main acceleration stage, and the propagation stage (e.g., Vršnak, 2001; Zhang et al., 2001, 2004; Chen, 2011; Mierla et al., 2013; D'Huys et al., 2017). The pre-eruptive stage, which is the main objective of this paper, most briefly can be described as externally-forced evolution of the pre-eruptive system through a series of equilibrium states until a stage when the system comes to the point when no equilibrium of forces is possible anymore (e.g., Priest, 1982; Vršnak, 1990; Green et al., 2018, and references therein). After that the system finds itself in an instability regime, dynamically erupting in trying to find a new equilibrium state. Such type of evolution is usually denoted as loss-of-equilibrium scenario. A critical height where the system losses equilibrium

and starts rapidly accelerating is usually comparable with the flux-rope footpoint half-separation(for the observatins see, e.g., Vršnak, 1990; Chen et al., 2006, for the theoretical aspect see, e.g., Vršnak 1990; Chen and Krall 2003; Chen et al. 2006).

From the observational point of view, the pre-eruptive stage, often called also a gradual-rise phase, is characterized by a number of different signatures. Frequently, the new magnetic flux emergence, shearing/twisting motions, and flux cancelation are observed (e.g., Schmieder et al., 2015; Green et al., 2018, and references therein). At the same time the pre-eruptive structure slowly rises at a low almost-constant velocity, and shows signatures of swelling (e.g., Tandberg-Hanssen, 1974; Vršnak et al., 1993; Maričić et al., 2004; Veronig et al., 2018), appearance of helical structures within the prominence (e.g., Tandberg-Hanssen, 1974; Sakurai, 1976; Vršnak et al., 1988, 1991, 1993; Rompolt, 1990; Romano et al., 2003; Ali et al., 2007), and mass-draining down the footpoints (e.g., Tandberg-Hanssen, 1974; Rust et al., 1975; Vršnak et al., 1987, 1993).

In this paper we analyze the influence of these processes on the evolution of the pre-eruptive system, focusing on the effects of the flux rope twisting, electric current increase, and the mass loss. The following analysis of these effects is based on the analytical semi-toroidal flux-rope model employed by Vršnak (2008), Vršnak (2016), and Green et al. (2018), where mainly a quantitative analysis of the acceleration stage of eruptions was considered. In contrast, this paper is focused on a quantitative study of characteristics of the pre-acceleration stage.

2. KINEMATICS OF THE GRADUAL-RISE PHASE

In **Figure 1** the kinematics of a limb CME that erupted on May 15, 2001 is presented (for details see, Maričić et al., 2004), to illustrate a typical example of the height–time evolution of the eruption (see, e.g., Tandberg-Hanssen, 1974, and references therein). The height–time measurements of the frontal rim, the top of the cavity, and the top of the embedded prominence are displayed in **Figure 1A**, whereas the corresponding velocity–time graph is shown in **Figure 1B**. In both graphs the gradual-rise phase and the impulsive acceleration stage are indicated.

In **Figure 2** the gradual-rise phase of the prominence is shown enlarged. The measured velocity slowly increases from 5 to 15 $\mathrm{km\,s^{-1}}$, within $\Delta t \sim 2\,\mathrm{h}$, which corresponds to a very weak acceleration on the order of $\sim 1\,\mathrm{m\,s^{-2}}$. In the following, effects of the flux-rope twisting, external flux emergence, and mass loss will be considered, to find out if these processes can explain the described flux-rope behavior.

3. FLUX-ROPE MODEL

For the previously mentioned purpose, let us apply the semi-toroidal flux-rope model **(Figure 3)** proposed by Vršnak (1990) and elaborated by Vršnak (2008), Vršnak (2016), and Green et al. (2018), to study the effects of the increase of the flux-rope twist, the increase of the flux-rope electric current, and the mass leakage through the flux-rope legs (the former two processes are illustrated schematically in **Figure 4**). A simplified equation of motion, relevant for the processes which are essential for comprehending processes that govern the gradual-rise phase, can be expressed in the form that defines the force per unit mass (i.e., acceleration):

$$a = \frac{C_\mathrm{L}}{\Lambda}\left[\frac{1}{2R_\mathrm{t}} - \frac{1}{R_\mathrm{t}X^2} + \frac{1}{Z}\right] - \frac{C_\mathrm{c}}{\Lambda^2 R_\mathrm{t}}\,. \tag{1}$$

where Λ, R_t, and Z are the length of the flux rope axis, major radius of the torus, and the height of its summit, all normalized with respect to the footpoint half-separation d [$\Lambda = \lambda/d$, $R_\mathrm{t} = \hat{R}_\mathrm{t}/d$, $Z = z/d$; for symbols see **Figure 3**; see also (Vršnak, 2008; Green et al., 2018)], whereas X represents the ratio of the poloidal and axial flux-rope field $X \equiv B_\varphi/B_\parallel$ at the flux-rope surface. The first two terms in brackets on the right-hand side of Equation (1) represent the so called "hoop force" (Chen, 1989), whereas the third term is due to the diamagnetic effect (Kuperus and Raadu, 1974). The last term represents the Lorentz force related to the background arcade magnetic field.

The expressions for the parameter C_L and C_c read:

$$C_\mathrm{L} = \frac{\mu_0\, I_\parallel^2\, \pi}{4M}\,, \tag{2}$$

$$C_\mathrm{c} = \frac{I_\parallel\, B_\mathrm{c}\, \pi^3\, d}{M}\,, \tag{3}$$

respectively. Here, $I_\parallel$ and M represent the axial electric current and total mass within the flux rope, respectively, B_c is the background arcade field and μ_0 stands for the permeability.

Note that a, C_L, and C_c are expressed in $\mathrm{m\,s^{-2}}$, and that in Equation (1) the drag force and gravity are neglected. Details of derivation of Equation (1) can be found in Vršnak (2008) and Green et al. (2018).

The geometrical quantities Λ, R_t, and Z are mutually related, i.e., $\Lambda \equiv \Lambda(Z)$ and $R_\mathrm{t} \equiv R_\mathrm{t}(Z)$. Taking approximately that the flux-rope axis remains a part of the circle with fixed footpoint separation $2d$, and inspecting **Figure 3**, where the angle ζ is introduced, one finds simple parametric relationships: $R_\mathrm{t} = 1/\cos\zeta$, $Z = (1+\sin\zeta)/\cos\zeta$, and $\Lambda = (\pi + 2\zeta)/\cos\zeta$. Thus, at given values of C_L and X, Equation (1) in fact defines a as a function of Z, $a \equiv a_{C_\mathrm{L},X}(Z)$. For low values of X and C_L, the structure is stable ($\mathrm{d}a/\mathrm{d}Z < 0$) and has only one equilibrium height Z_s, where $a_{C_\mathrm{L},X}(Z_s) = 0$ (e.g., black curve in **Figure 5A**). As X or C_L increase, the equilibrium height rises and the shape of $a(Z)$ transforms, which is illustrated in **Figure 5**. To distinguish what are the effects of increasing X and C_L, the graphs $a(Z)$ are shown separately for the case when the evolution of the system is driven by increasing X, and analogously, by increasing C_L. The former option is presented in **Figures 5A,B**, where the graph in **Figure 5B** shows an enlarged part of **Figure 5A** around the stable-equilibrium. Analogous graphs are displayed in **Figures 5C,D** for the effect of increasing C_L, where the increase of C_L can be either due to the increasing current $I_\parallel$ or decreasing mass M [see Equation (2)]. In **Figure 5D**, the stable-equilibrium heights are explicitly denoted as Z_1 – Z_4, and the height at which

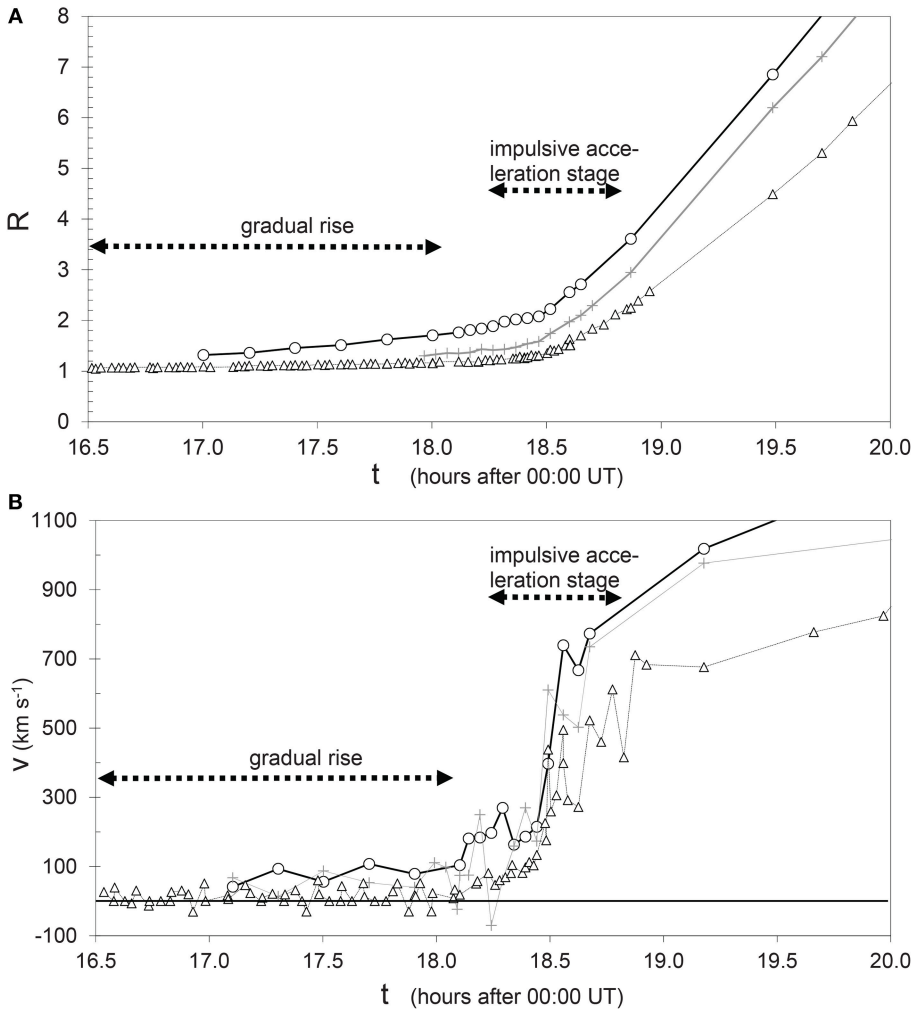

FIGURE 1 | Kinematics of the eruption of May 15, 2001: **(A)** height–time; **(B)** velocity–time. The heliocentric distance R is expressed in units of solar radius. Measurements of the frontal rim, top of the cavity, and top of the embedded prominence are shown by circles, crosses, and triangles, respectively. The gradual-rise phase and the impulsive acceleration stage are indicated by horizontal dashed arrows.

the system looses equilibrium as Z^* (red curve). In the insets of **Figures 5B,D** the change of the stable-equilibrium height $Z_s(X)$ and $Z_s(C_L)$ is presented, respectively, all the way to the state when the system looses equilibrium (marked by a square symbol).

Inspecting **Figure 5**, one finds that by increasing C_L and/or X, first the $a(Z)$ curve evolves into a shape where another equilibrium point occurs Z_u. However, this one is unstable (green, yellow, and blue curves in **Figures 5A,C**), since $da/dZ > 0$. Thus, in this stage the structure is metastable, since if pushed from a stable equilibrium height Z_s to a height above the unstable-equilibrium height Z_u, it will erupt, because beyond this height the acceleration becomes $a(Z) > 0$ for any $Z > Z_u$.

In other words, **Figure 5** shows that the increase of C_L or X implies rising of Z_s, and in the following this will be considered as a cause of the gradual rise of the pre-eruptive structure. Furthermore, one finds out that the unstable equilibrium height Z_u descends, so the distance between Z_s and Z_u decreases, implying that the structure becomes more and more unstable, since weaker and weaker push is required to move the structure from the stable to the unstable equilibrium point. Eventually, at a given critical combination of C_L and X, the stable and unstable heights merge, $Z_u = Z_s$, meaning that there is no equilibrium existing any more, i.e., equilibrium state is lost and the structure erupts ($a(Z) > 0$ for any Z; see red curve in **Figures 5A–D**).

In the following, Equation (1) will be employed to inspect the effects of the increasing C_L and X, as generally illustrated in **Figure 5**, by specifically considering the two processes depicted in **Figure 4**. These are twisting motions at the flux-rope footpoints (e.g., Török et al., 2013, and references therein) and emerging-flux process (e.g., Schmieder et al., 2015, and references therein). The former process leads to the increase of X, whereas the latter one directly induces an increase of the current $I_\parallel$, i.e., increases the value of the parameter C_L. It should be noted that the change of X causes also a change of $I_\parallel$, whereas the change of

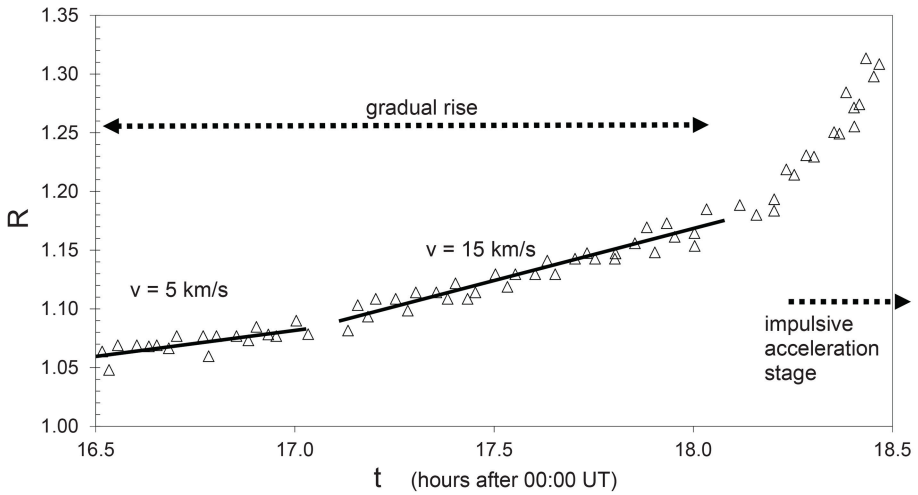

FIGURE 2 | Detailed kinematics of the gradual-rise phase of the eruptive prominence shown in **Figure 1A**.

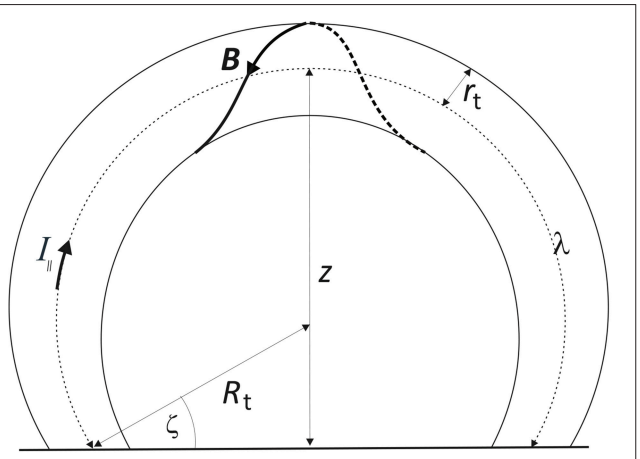

FIGURE 3 | Schematic presentation of a semi-toroidal flux-rope geometry. For details see the main text.

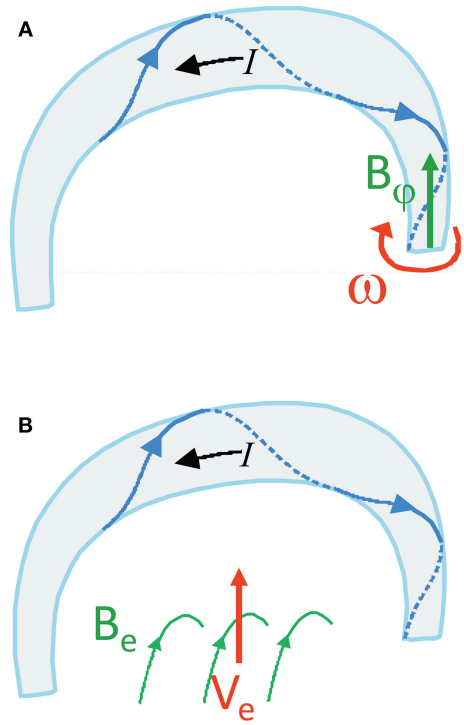

FIGURE 4 | Schematic presentation of: **(A)** poloidal flux injection (depicted by green arrow) into the rope, caused by twisting motion at the footpoint (red arrow); **(B)** emerging flux effect. For details see the main text.

$I_\parallel$ causes also the change of X, i.e., the behaviors of X and C_L are tightly physically related. Finally, note that from the point of view of Equation (1), the mass loss related to the material draining down the prominence legs is equivalent to the increase of axial electric current $I_\parallel$ related to emerging flux and/or twisting processes, since the mass loss also increases the value of C_L [see Equation (2)].

4. RESULTS

4.1. Poloidal Flux Injection

In **Figure 6** the effect of increasing poloidal flux caused by twisting motion at one of the flux-rope footpoints is illustrated for two initial C_L values, 145 and 150 $\mathrm{m\,s^{-2}}$, respectively, combined with two values of the normalized flux-rope initial minor radius, r/d = 0.1 and 0.2, where in all combinations the flux-rope footpoint half-separation is taken as d = 50 Mm and the axial field as $B_\parallel$ = 100 G. The presented cases correspond to the longitudinal magnetic flux of $\Psi_\parallel \approx 0.8 \times 10^{20}$ Mx (red curve) and $\Psi_\parallel \approx 3 \times 10^{20}$ Mx (gray and blue curve), as listed in 7th column of **Table 1**.

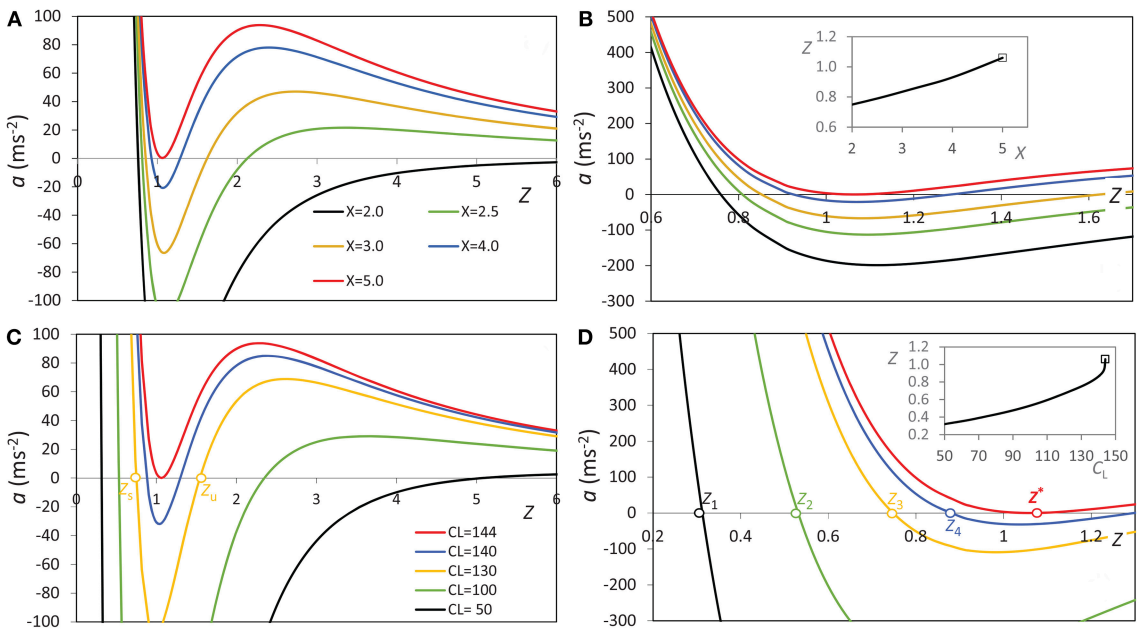

FIGURE 5 | Equation of motion results shown in the form $a(Z)$ dependencies: **(A)** $a(Z)$ curves for different values of X, combined with $C_L = 144\,\mathrm{m\,s^{-2}}$; **(B)** a part of **(A)** enlarged, focusing on the equilibrium heights; **(C)** $a(Z)$ curves for different values of C_L, combined with $X = 5$; **(D)** a part of **(C)** enlarged, focusing on the equilibrium heights. In **(C)** a pair of stable- and unstable-equilibrium heights on the yellow $a(Z)$ curve is denoted by Z_S and Z_U, respectively. In all graphs a fixed value $C_c = 1.3 \times 10^4\,\mathrm{m\,s^{-2}}$ is used [see Equation (3)]. In **(D)** the stable-equilibrium heights Z_S are marked as Z_1, Z_2, Z_3, and Z_4, whereas the height at which the flux rope losses equilibrium is denoted as Z^* (the red $a(Z)$ curve). Insets in **(B,D)** show the increase of stable-equilibrium height as a function of X and C_L, respectively.

Note that the values of the parameter C_L and r/d are not kept fixed, but they evolve due to change of the poloidal flux. The evolution of C_L is followed by taking into account that the poloidal flux and the axial current scale as $\Psi_\varphi \propto B_\varphi r\lambda$ and $I_\parallel \propto B_\varphi r$, respectively, where B_φ is the poloidal field at the flux-rope boundary. From this one finds $\Psi_\varphi \propto I_\parallel \lambda$, i.e., $I_\parallel \propto \Psi_\varphi/\lambda \propto \Psi_\varphi/\Lambda$. Substitution of this relation to Equations (2, 3) defines the evolution of C_L. Setting $a = 0$ in Equation (1) and taking into account the expressions for $C_L(\Psi_\varphi, \Lambda)$ and $C_L(\Psi_\varphi, \Lambda)$, Equation (1) becomes an implicit relation that defines the equilibrium value of the angle ζ as a function of prescribed values of X, i.e., Ψ_φ. The solution of this equation, giving the equilibrium ζ, then provides also the equilibrium values of R_t, z, and λ, as well as the equilibrium value of $I_\parallel$. In a similar manner, the evolution of the torus minor radius r can be traced. From the poloidal-to-axial flux ratio $\Psi_\varphi/\Psi_\parallel \propto (B_\varphi r\lambda)/(B_\parallel r^2)$ one finds $r \propto X\lambda\,\Psi_\parallel/\Psi_\varphi$. Since the rotational motions at the footpoints do not affect $\Psi_\parallel$ and thus it stays constant, the value of r scales as $r \propto X\lambda/\Psi_\varphi$, where the evolution of X and Ψ_φ is prescribed as the input.

For the twisting motion, i.e., rotational motion at one of footpoints (illustrated in **Figure 4A**), a typical value of ω = 100 deg/day (e.g., Török et al., 2013, and references therein) is applied to the flux rope characterized by the initial value X_1 = 3.5 (blue curve in **Figure 6**) and 4.5 (red and gray curves in **Figure 6**). The twisting motion increases the polidal flux, and consequently changes the value of X. The change of the parameter X can be expressed as $\mathrm{d}X/\mathrm{d}t = \omega r/\lambda$, where λ represents the length of the flux-rope axis. Since the poloidal and axial flux are related as $\Psi_\varphi = \Psi_\parallel \lambda X/2r\pi$, the rate at which the poloidal flux increases, $\mathrm{d}\Psi_\varphi/\mathrm{d}t$ can be calculated (the corresponding values are shown in Column 9 of **Table 1A**). Other relevant informations related to the graphs displayed in **Figure 6** are presented in the upper part of **Table 1**, where the first column identifies the curves in **Figure 6**. The duration of the pre-eruption interval, Δt over which the changes are followed is shown in Column 2. The height and speed of the flux-rope axis at the beginning of the interval (z_1 and v_1) are presented in Columns 3 an 5, respectively, whereas the height and speed at the onset of the eruption (z_2 and v_2) are given in Columns 4 and 6, respectively. The values of the axial and the initial poloidal flux are presented in the Columns 7 and 8. The rate by which the poloidal flux is changing due to the twisting motion at the flux-rope footpoint is displayed in Column 9, its total change over the interval Δt is presented in Column 10, and the relative change, expressed in percentages, is given in Column 11. The last two columns show the corresponding relative change of the parameter C_L and the flux-rope minor radius r, both presented in percentages.

The graph of the gradual-rise velocity presented in **Figure 6B** shows that the twisting motion itself cannot explain the characteristics of the gradual-rise pre-eruptive phase, since the obtained velocities are for at least an order of magnitude too low. Yet, note that the increase of X is important in reaching the critical loss-of-equilibrium state (see **Figures 5A,B**).

4.2. Increase of C_L (Emerging Flux Process or Mass Loss)

In **Figure 7** the evolution caused by increasing value of C_L, which can either be due to the increasing electric current in the flux rope, or the mass draining down the flux-rope legs, is illustrated. Particulary, in the following the increase of current is attributed to the emerging flux along the magnetic inversion line beneath the flux rope (**Figure 4B**). The change of the magnetic flux Ψ_e encircled by the flux-rope current channel causes the increase

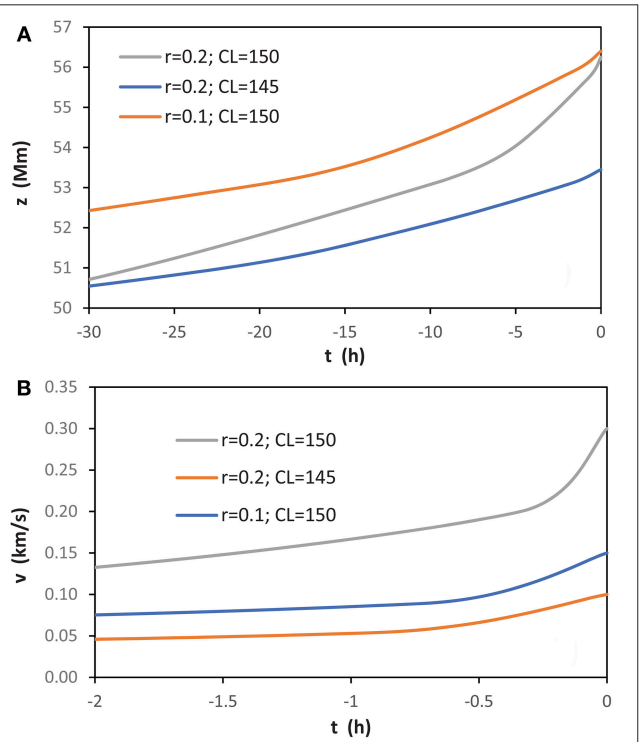

FIGURE 6 | Evolution of the flux rope caused by the poloidal flux injection, until the moment of the loss of equilibrium ($t = 0$): **(A)** height–time; **(B)** velocity–time. The blue curve represents the case where the initial value of X is 3.5, whereas red and gray curves represent the case when it is 4.5. To better resolve the evolution of the rising speed, in the lower panel only a segment of 2 h before the eruption is presented.

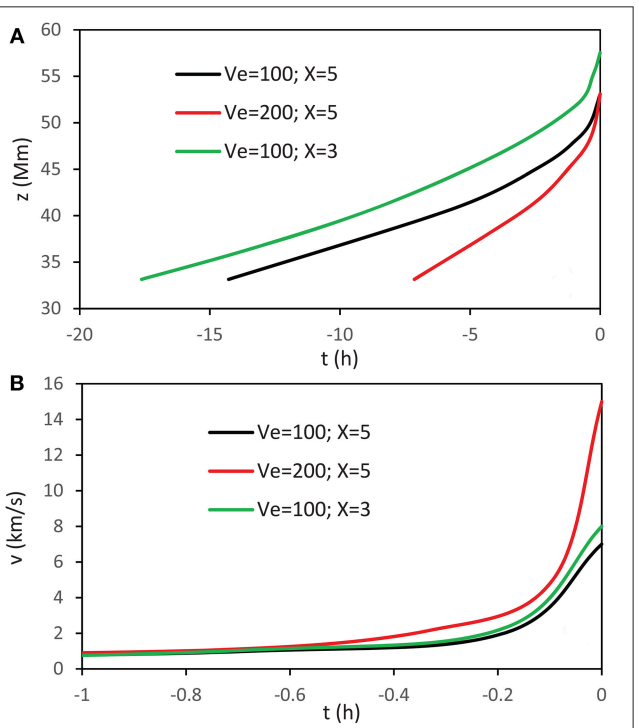

FIGURE 7 | Evolution of the flux rope caused by emerging flux, until the moment of the loss of equilibrium ($t = 0$): **(A)** height–time; **(B)** velocity–time. The black and red curves are calculated for the initial $C_{L1} = 11\,\mathrm{m\,s^{-2}}$, whereas green curve represents $C_{L1} = 12\,\mathrm{m\,s^{-2}}$. To better resolve the evolution of the rising speed, in the lower panel only the 1-h interval before the eruption is presented.

TABLE 1 | Comparison of the footpoint-twisting process and the emerging-flux process.

(A) POLOIDAL-FLUX INJECTION (FOOTPOINT TWISTING)												
Curve in **Figure 6**	Δt (h)	z1 (Mm)	z2 (Mm)	v1 (km/s)	v2 (km/s)	$\Psi_\parallel$ (Mx)	$\Psi_{\varphi 1}$ (Mx)	$d\Psi_\varphi/dt$ (Mx/s)	$\Delta\Psi_\varphi$ (Mx)	$\Delta\Psi_\varphi$ %	ΔC_L %	Δr %
Red	20	53.1	56.4	0.016	0.10	7.9×10^{19}	2.6×10^{21}	1.8×10^{15}	1.3×10^{20}	5.0	1.4	< 1
Gray	20	53.2	56.3	0.030	0.30	3.1×10^{20}	5.2×10^{21}	3.6×10^{15}	2.6×10^{20}	5.0	1.4	< 1
Blue	20	52.0	53.5	0.027	0.15	3.1×10^{20}	6.7×10^{21}	2.1×10^{15}	1.5×10^{20}	2.2	1.1	< 1
(B) EMERGING FLUX												
Curve in **Figure 7**	Δt (h)	z1 (Mm)	z2 (Mm)	v1 (km/s)	v2 (km/s)	$\Psi_\parallel$ (Mx)	Ψ_{e1} (Mx)	$d\Psi_e/dt$ (Mx/s)	$\Delta\Psi_e$ (Mx)	$\Delta\Psi_\varphi$ %	ΔC_L %	Δr %
Red	10	31.2	53.2	0.35	15.1	7.9×10^{19}	5.0×10^{21}	2.0×10^{16}	5.7×10^{21}	54.4	57.2	86.7
Black	10	37.1	53.1	0.27	7.1	7.9×10^{19}	5.0×10^{21}	1.0×10^{16}	5.4×10^{21}	26.4	53.6	92.4
Green	10	39.2	57.6	0.26	7.9	7.9×10^{19}	5.0×10^{21}	1.0×10^{16}	5.4×10^{21}	33.7	53.6	92.4

*In the first column the identification of the curves displayed in **Figures 6**, **7** is defined. Δt represents the time interval prior to the eruption over which the changes of the parameters presented in the rest of the table are followed. Subscript "1" denotes the values at the beginning of the interval, whereas the subscript "2" represents the values at the onset of the eruption. For details see the main text.*

of the flux-rope current, due to the relation $d\Psi_e/dt = \mu_0\, dI_\parallel/dt$ (see e.g., Batygin and Toptygin, 1962; Jackson, 1998), implying also the change of I, i.e., C_L. Note that the change of I leads also to change of Ψ_φ, X, and r, which can be followed employing a procedure analogous to that presented in section 4.1 for the evolution of I and r, where the change of Ψ_φ was used as the input.

Let us consider a situation where the magnetic field of B_e = 100 G emerges (see the sketch in **Figure 4B**) at the speed of V_e = 100 m s^{-1} (black and green curves in **Figure 7**) and V_e = 200 m s^{-1} (red curve in **Figure 7**), which implies that the external unit-length magnetic flux increases at the rate $d\Psi_e/dt = B_e V_e$ = 1 and 2 $\times 10^6$ Mx s^{-1} cm^{-1}, respectively. Assuming that the flux emerges over the distance of $2d$ = 100 Mm, one finds that the rate at which the magnetic flux encircled by the flux-rope, Ψ_e, increases as listed in Column 9 of **Table 1B** ($d\Psi_e/dt$). The total increase of Ψ_e over the time of Δt = 10 h is shown in Cloumn 10. Taking for the initial flux encircled by the flux rope the value of $\Psi_{e1} = 10^{12}$ Mx cm^{-1} (Column 8 in **Table 1B**), and the initial value C_{L1} = 11 m s^{-2} (black and red curves in **Figure 7**) and 12 m s^{-2} (green curve in **Figure 7**), one gets the relative change of Ψ_φ, C_L, and r , as displayed in the last three columns of **Table 1B** (all expressed in percentages).

Figure 7B shows that at the stage when the system approaches the loss-of-equilibrium point, the rise caused by increasing C_L results in rise-velocities on the order of 10 km s^{-1}, which is compatible with observations (**Figure 2**). Comparing **Figure 7B** with **Figure 6B** one finds that the rise related to the emerging flux process is more than an order of magnitude faster than that related to the poloidal flux injection.

5. DISCUSSION AND CONCLUSION

In the presented analysis three processes relevant for the evolution of the pre-eruptive structure during the gradual-rise phase are considered. In particular, we focused on the height–time and velocity–time evolution, to compare it with typical behavior usually observed during the gradual-rise stage.

The first process is twisting motion at the flux-rope footpoint, which leads to the increase of the flux-rope twist, indirectly enhancing also the axial electric current and minor radius of the flux rope at its summit, causing the rise of the pre-eruptive structure. All of these signatures drive the pre-eruptive system toward a point where the structure losses its equilibrium and erupts. However, the considered twisting process is not effective enough to cause a sufficiently fast rise of the pre-eruptive structure, i.e., its rise is for at least an order of magnitude slower than observed. Note that the three examples presented in **Figure 6** cover typical values coming from observations, and even increasing the parameter-values related the poloidal flux injection (including much too-high values) could not result in sufficiently high pre-eruptive rising speeds.

The second process is related to the emergence of a new magnetic flux beneath the flux rope. This causes an increase of the magnetic flux encircled by the flux rope, which induces an increase of the electric current flowing along the rope. The increase of the current causes also the increase of the flux-rope twist and its minor radius. The analysis has demonstrated that this process results in the rise of the pre-eruptive structure that is faster than in the case of twisting for almost two orders of magnitude, and is compatible with observations. This process is more effective than the footpoint twisting, since the emerging flux occurs on the spatial scale comparable with the flux-rope length, whereas the footpoint twisting is restricted to the footpoint radius, and that is generally an order of magnitude smaller than the flux-rope length. This results in an order of magnitude larger change of poloidal flux caused by the emerging flux (see **Table 1**). Note also that the processes like flux cancellation and other various forms of reconnection beneath the flux rope, as well as the converging motions of the arcade footpoints, can result in the same effects as described emerging flux process.

The third process, the mass leakage down the flux-rope legs, results in the pre-eruptive rise similar to that caused by the emerging flux process, except that the mass loss does not cause the increase of the flux-rope twist. Although the draining of the cold plasma from the embedded prominence is most prominent during the acceleration stage of the eruption, it is frequently observed already during the gradual-rise phase. This is caused by stretching of the flux rope as it rises, which makes the magnetic dips containing dense prominence plasma successively shallower, i.e., certain fraction of the prominence material is no longer supported against the gravity. Thus, the rise of the pre-eruptive structure caused by emerging flux is likely to be additionally enhanced by the mass-loss effect, making the pre-eruptive rise even faster than shown in **Figure 7**.

To conclude, the enhancement of the flux-rope electric current, the increase of the twist, and the mass loss, are tightly related phenomena, expected to occur during the gradual pre-eruptive phase of an eruption. Combination of these three processes is sufficiently effective to explain the nature of the gradual rise of the pre-eruptive structure and its evolution to the loss-of-equilibrium point.

AUTHOR CONTRIBUTIONS

The author confirms being the sole contributor of this work and has approved it for publication.

FUNDING

This work has been fully supported by Croatian Science Foundation under the project no. 7549 Millimeter and submillimeter observations of the solar chromosphere with ALMA (MSOC).

REFERENCES

Ali, S. S., Uddin, W., Chandra, R., Mary, D. L., and Vršnak, B. (2007). Helical eruptive prominence associated with a pair of overlapping CMEs on 21 April 2001. *Sol. Phys.* 240, 89–105. doi: 10.1007/s11207-006-0203-5

Batygin, V. V., and Toptygin, I. N. (1962). *Problems in Electrodynamics*. New York, NY: Academic Press.

Chen, J. (1989). Effects of toroidal forces in current loops embedded in a background plasma. *Astrophys. J.* 338, 453–470. doi: 10.1086/167211

Chen, J., and Krall, J. (2003). Acceleration of coronal mass ejections. *J. Geophys. Res.* 108:1410. doi: 10.1029/2003JA009849

Chen, J., Marqué, C., Vourlidas, A., Krall, J., and Schuck, P. W. (2006). The flux-rope scaling of the acceleration of coronal mass ejections and eruptive prominences. *Astrophys. J.* 649, 452–463. doi: 10.1086/506466

Chen, P. F. (2011). Coronal mass ejections: models and their observational basis. *Liv. Rev. Sol. Phys.* 8:1. doi: 10.12942/lrsp-2011-1

D'Huys, E., Seaton, D. B., De Groof, A., Berghmans, D., and Poedts, S. (2017). Solar signatures and eruption mechanism of the August 14, 2010 coronal mass ejection (CME). *J. Space Weather Space Clim.* 7:A7. doi: 10.1051/swsc/2017006

Green, L. M., Török, T., Vršnak, B., Manchester, W., and Veronig, A. (2018). The origin, early evolution and predictability of solar eruptions. *Space Sci. Rev.* 214:46. doi: 10.1007/s11214-017-0462-5

Jackson, J. D. (1998). *Classical Electrodynamics, 3rd Edn.* New Delhi: Wiley-VCH. 832 pp.

Kuperus, M., and Raadu, M. A. (1974). The support of prominences formed in neutral sheets. *Astron. Astrophys.* 31:189.

Maričić, D., Vršnak, B., Stanger, A. L., and Veronig, A. (2004). Coronal mass ejection of 15 May 2001: I. Evolution of morphological features of the eruption. *Sol. Phys.* 225, 337–353. doi: 10.1007/s11207-004-3748-1

Mierla, M., Seaton, D. B., Berghmans, D., Chifu, I., De Groof, A., Inhester, B., et al. (2013). Study of a prominence eruption using PROBA2/SWAP and STEREO/EUVI data. *Sol. Phys.* 286, 241–253. doi: 10.1007/s11207-012-9965-0

Priest, E. R. (1982). *Solar Magneto-Hydrodynamics*. Dordrecht; Boston, MA: D. Reidel Pub. Co. ; Hingham.

Romano, P., Contarino, L., and Zuccarello, F. (2003). Eruption of a helically twisted prominence. *Sol. Phys.* 214, 313–323. doi: 10.1023/A:1024257603143

Rompolt, B. (1990). Small scale structure and dynamics of prominences. *Hvar Observ. Bull.* 14:37.

Rust, D. M., Nakagawa, Y., and Neupert, W. M. (1975). EUV emission, filament activation and magnetic fields in a slow-rise flare. *Sol. Phys.* 41, 397–414.

Sakurai, T. (1976). Magnetohydrodynamic interpretation of the motion of prominences. *Publ. ASJ.* 28, 177–198.

Schmieder, B., Aulanier, G., and Vršnak, B. (2015). Flare-CME models: an observational perspective (invited review). *Sol. Phys.* 290, 3457–3486. doi: 10.1007/s11207-015-0712-1

Tandberg-Hanssen, E. (1974). Solar prominences. *Geophys. Astrophys. Monogr.* 12:169.

Török, T., Temmer, M., Valori, G., Veronig, A. M., van Driel-Gesztelyi, L., and Vršnak, B. (2013). Initiation of coronal mass ejections by sunspot rotation. *Sol. Phys.* 286, 453–477. doi: 10.1007/s11207-013-0269-9

Veronig, A. M., Podladchikova, T., Dissauer, K., Temmer, M., Seaton, D. B., Long, D., et al. (2018). Genesis and impulsive evolution of the 2017 September 10 coronal mass ejection. *Astrophys. J.* 868:107. doi: 10.3847/1538-4357/aaeac5

Vršnak, B. (1990). Eruptive instability of cylindrical prominences. *Sol. Phys.* 129, 295–312.

Vršnak, B. (2001). Dynamics of solar coronal eruptions. *J. Geophys. Res.* 106, 25249–25260. doi: 10.1029/2000JA004007

Vršnak, B. (2008). Processes and mechanisms governing the initiation and propagation of CMEs. *Ann. Geophys.* 26, 3089–3101. doi: 10.5194/angeo-26-3089-2008

Vršnak, B. (2016). Solar eruptions: the CME-flare relationship. *Astron. Nachr.* 337:1002. doi: 10.1002/asna.201612424

Vršnak, B., Ruzdjak, V., Brajsa, R., and Dzubur, A. (1988). Structure and stability of prominences with helical structure. *Sol. Phys.* 116, 45–60.

Vršnak, B., Ruždjak, V., Messerotti, M., Mouradian, Z., and Urbarz, H. (1987). Reconnection driven by an erupting filament in the May 14, 1981 flare. *Sol. Phys.* 114, 289–310.

Vršnak, B., Ruzdjak, V., and Rompolt, B. (1991). Stability of prominences exposing helical-like patterns. *Sol. Phys.* 136, 151–167.

Vršnak, B., Ruzdjak, V., Rompolt, B., Rosa, D., and Zlobec, P. (1993). Kinematics and evolution of twist in the eruptive prominence of August 18, 1980. *Sol. Phys.* 146, 147–162.

Zhang, J., Dere, K. P., Howard, R. A., Kundu, M. R., and White, S. M. (2001). On the temporal relationship between coronal mass ejections and flares. *Astrophys. J.* 559, 452–462. doi: 10.1086/322405

Zhang, J., Dere, K. P., Howard, R. A., and Vourlidas, A. (2004). A study of the kinematic evolution of coronal mass ejections. *Astrophys. J.* 604, 420–432. doi: 10.1086/381725

Conflict of Interest Statement: The author declares that the research was conducted in the absence of any commercial or financial relationships that could be construed as a potential conflict of interest.

frontiers in Astronomy and Space Sciences

ORIGINAL RESEARCH
published: 11 June 2019
doi: 10.3389/fspas.2019.00044

How Many Twists Do Solar Coronal Jets Release?

Jiajia Liu[1]*, *Yuming Wang*[2,3] *and Robert Erdélyi*[1,4]

[1] Solar Physics and Space Plasma Research Center, School of Mathematics and Statistics, The University of Sheffield, Sheffield, United Kingdom, [2] CAS Key Laboratory of Geospace Environment, Department of Geophysics and Planetary Sciences, University of Science and Technology of China, Hefei, China, [3] CAS Center for the Excellence in Comparative Planetology, Hefei, China, [4] Department of Astronomy, Eötvös Loránd University, Budapest, Hungary

Highly twisted magnetic flux ropes, with finite length, are subject to kink instabilities, and could lead to a number of eruptive phenomena in the solar atmosphere, including flares, coronal mass ejections (CMEs) and coronal jets. The kink instability threshold, which is the maximum twist a kink-stable magnetic flux rope could contain, has been widely studied in analytical models and numerical simulations, but still needs to be examined by observations. In this article, we will study twists released by 30 off-limb rotational solar coronal jets, and compare the observational findings with theoretical kink instability thresholds. We have found that: (1) the number of events with more twist release becomes less; (2) each of the studied jets has released a twist number of at least 1.3 turns (a twist angle of 2.6π); and (3) the size of a jet is highly related to its twist pitch instead of twist number. Our results suggest that the kink instability threshold in the solar atmosphere should not be a constant. The found lower limit of twist number of 1.3 turns should be merely a necessary but not a sufficient condition for a finite solar magnetic flux rope to become kink unstable.

Keywords: solar eruptions, solar coronal jets, MHD instabilities, magnetic flux ropes, magnetic twists

OPEN ACCESS

Edited by:
Dipankar Banerjee, Indian Institute of Astrophysics, India

Reviewed by:
P. Vemareddy, Indian Institute of Astrophysics, India
Abhishek Kumar Srivastava, Indian Institute of Technology (BHU), India

***Correspondence:**
Jiajia Liu
jj.liu@sheffield.ac.uk

Specialty section:
This article was submitted to Stellar and Solar Physics, a section of the journal Frontiers in Astronomy and Space Sciences

Received: *16 January 2019*
Accepted: *22 May 2019*
Published: *11 June 2019*

Citation:
Liu J, Wang Y and Erdélyi R (2019) How Many Twists Do Solar Coronal Jets Release? Front. Astron. Space Sci. 6:44. doi: 10.3389/fspas.2019.00044

1. INTRODUCTION

Eruption of solar magnetic flux ropes (see reviews in e.g., Raouafi, 2009; Schrijver, 2009; Chen, 2011; Filippov et al., 2015a; Karpen, 2015) has been considered as one of the main drivers of the so-called "space weather". According to magnetohydrodynamics (MHD) theories, highly twisted magnetic flux ropes, with finite length, are subject to the kink instability, which will develop and finally lead to a release of energy when the stored twist exceeds a certain threshold. Various theoretical studies have given similar but different estimations of the kink-unstable threshold. The Kruskal-Shafranov limit (Kruskal and Kulsrud, 1958; Shafranov, 1963) suggests a kink-unstable threshold 2π of the total twist angle in axisymmetric toroidal magnetized plasma columns. Further study on line-tying force-free coronal loops with uniform twist by Hood and Priest (1981) suggested a maximum twist angle of 2.5π a kink-stable, cylindrical flux tube might contain. 3D MHD numerical simulations (e.g., Pariat et al., 2009) gave a slightly higher limit of the twist angle, 2.6π, injected into the system for the onset of kink instability and the eruption of a solar coronal jet. Dungey and Loughhead (1954) suggested a kink-unstable threshold of $2l/R$, where l and R are the length and radius of the flux rope, respectively. All the above thresholds for kink instabilities are, however, theoretical and therefore somehow idealized. The realistic threshold(s) for flux ropes to become unstable in the solar atmosphere need to be further studied, and the theoretical thresholds to be confirmed or refuted observationally.

Kink-unstable magnetic flux ropes in the solar atmosphere could account for a wide range of observational phenomena. For instances, Hood and Priest (1979) suggested, using theoretical considerations, that the kink instability could be a main cause of solar flares. This hypothesis has then been supported by a number of observational studies (e.g., Pevtsov et al., 1996; Srivastava et al., 2010; Liu et al., 2016d). It has also been suggested that kink instability could be associated with small-scale (nano) flares (e.g., Browning et al., 2008). Meanwhile, plenty of literature is available to present abundant evidence in theories, numerical simulations and observations on how the eruptions of filaments and CMEs are related to kink-unstable magnetic flux ropes (e.g., Rust and Kumar, 1996; Kliem et al., 2004; Török and Kliem, 2005; Williams et al., 2005; Guo et al., 2010; Kumar et al., 2012; Liu et al., 2016c; Cheng et al., 2017; Vemareddy et al., 2017). Recently, Wang et al. (2016) has further identified the magnetic twist inside post-eruption flux ropes in the heliosphere from analyzing 115 magnetic clouds observed at 1 AU. They found the kink-unstable thresholds vary from case to case.

Besides flares and CMEs, rotational solar coronal jets (see reviews, e.g., Shibata et al., 1996; Raouafi et al., 2016) have also been suggested to be linked to kink instabilities. The relationship between rotational jets and kink instability has been further investigated in the context of magnetized astronomical jets, which are in scales of light years (e.g., Giannios and Spruit, 2006; Barniol Duran et al., 2017). Most theories and observations suggest that the rotational motion of solar coronal jets should be a process involving "untwisting" (e.g., Shibata and Uchida, 1986; Jibben and Canfield, 2004; Moreno-Insertis et al., 2008; Liu et al., 2009; Liu et al., 2016b; Pariat et al., 2009; Shen et al., 2012; Fang et al., 2014; Filippov et al., 2015b; Lee et al., 2015). The physical scenario of "untwisting" jets is usually described as follows: a newly emerging (e.g., observations in Liu et al., 2016b; Zheng et al., 2018) or a pre-existing closed flux system (disturbed by footpoint motions, e.g., observations in Chen et al., 2017) reconnects with the ambient open magnetic field, during which twists contained in the closed flux system could be passed into the open fields and are then released during the rotational motion of the associated jet. Following this idea, a natural question may be raised: will all the twists stored in the pre-reconnection flux rope be released during the coronal jet eruption? In other words, can we infer the twist stored in the pre-reconnection flux rope from the number of turns a jet rotates after it emerges from the magnetic reconnection?

We shall also note that, not all solar coronal jets show clear rotational motion during their lifetime. Different studies have slightly different (but similar in principle) explanations of why some solar coronal jets rotate and others do not (e.g., Shibata et al., 1996; Moore et al., 2010; Pariat et al., 2015). For examples, models (e.g., Shibata and Uchida, 1986; Canfield et al., 1996) summarized in Shibata et al. (1996) suggested that magnetic reconnection with a sheared/twisted flux system involved could result in a jet with obvious rotational motion. Such modeling approach was further confirmed by Moore et al. (2010) with observations of a number of X-ray jets with rotational motion (named as "blowout jets") and without rotational motion (named as "standard jets"). On the other hand, numerical simulations in e.g., Pariat et al. (2015) have shown that in certain circumstances, a non-rotational jet (names as "straight jet") may precede a rotational jet (named as "helical jet") and influences the behavior of the rotational jet. Most importantly, in the simulations, the pre-eruption twisted magnetic flux rope is not directly involved in the eruption of the non-rotational jet.

We have found it difficult to directly compare the twist released by a rotational jet and stored in its pre-reconnection flux rope from observations, because: (1) for an off-limb jet, we do not have accurate vector magnetic field observations to investigate the underlying magnetic flux rope; and (2) for an on-disk jet, even though we can study the twist stored in the underlying magnetic flux rope using magnetic field extrapolations (which are not always accurate), it is hard to investigate the rotational motion of the jet using imaging observations and spectral observations with sufficiently enough spectral resolution at the needed temperatures. Fortunately, we could find a way to go ahead for an answer from realistic numerical simulations. Pariat et al. (2016) performed a series of 3D MHD numerical simulations of solar jets in conditions with different plasma-β, where the plasma-β is the ratio of the plasma pressure to the magnetic pressure. It has been found that, under chromospheric and coronal conditions where plasma-β is less than unity, the number of turns a jet rotates is almost the same with the twist injected into the system before eruption. Though the possible scenario of partial eruption was not included in their simulations, we have found, through a detailed observational and numerical study of solar coronal twin jets (Liu et al., 2016a), that the residual twist remaining after the jet eruption is very small when compared to the total twist stored in the pre-eruption magnetic flux rope. Therefore, we may safely conclude that the twist released by a solar coronal jet should be the lower limit of, and most likely be similar to, the twist stored in the pre-reconnection flux rope.

In this article, we study twists released by 30 rotational solar coronal jets observed off-limb from 2010 to 2016, and compare them to kink instability thresholds proposed by theoreticians. The paper is organized as follows: data collection and event selection are presented in section 2; detailed examples of the analysis of two typical coronal jets are shown in sections 3, 4 is devoted to statistical results; conclusions and discussions are given in section 5.

2. DATA COLLECTION

The *Solar Dynamics Observatory* (SDO, Pesnell et al., 2012), lunched in 2010 to a geosynchronous orbit, carries three different scientific instruments, among which one is the *Atmospheric Imaging Assembly* (AIA, Lemen et al., 2012). Data used in this research was obtained from one of the AIA broadband images at He II 304 Å targeting at plasmas with a characteristic temperature of 0.05 MK. All the images were taken at a cadence of 12 seconds with a pixel size of 0.6″ (Lemen et al., 2012). To find usable coronal jet events for the purpose of this research, we performed the following steps to explore and collect data:

- First of all, we used the built-in Heliophysics Event Knowledgebase (HEK, Hurlburt et al., 2012, http://www.lmsal.

com/hek/index.html) module in *SunPy* (SunPy Community et al., 2015) to find all events labeled as "coronal jet" (with abbreviation of "CJ") from the year 2010 to 2017. These events were identified automatically or manually by various research groups from different institutes. To exclude all on-disk events, we then removed all entries with the central location of the event <1.02 solar radii from the disk center. 173 events have been found during this initial search.

- In the second step, we downloaded the movies associated with all the 173 events using links provided in the HEK searching results. Movies of events without given links in their HEK entries were then generated locally from automatically downloaded SDO/AIA 304 Å image sequences.
- Next, all movies were carefully examined one-by-one. On-disk events, which were not eliminated by the first step, were further removed. Limb events which were not clear in AIA 304 Å images were also abandoned. We have also discarded events, when it was not sure whether they were coronal jets or filament eruptions. After applying all the above selection procedures, only 44 events were kept.
- All SDO/AIA 304 Å data were then downloaded with their original cadence (12 s). All the events would be studied into details one-by-one, which will be demonstrated with examples in section 3. We note 14 events which were either too close to other bright structures (e.g., complex loop systems, prominences, etc.) or too faint to allow us to obtain firm parameters, will not be included in the final statistics (section 4). The first two columns in **Table 1** show the times and locations of all 30 coronal jet events studied in this research.

Figure 1 depicts the locations of the apparent source regions on the solar limb of all 30 coronal jets, with colors denoting dates of eruptions. Animations of the SDO/AIA 304 Å observations of all 30 events are available at https://github.com/PyDL/jet-stat-movie.

TABLE 1 | Parameters of 30 rotational solar coronal jets observed between 2010 and 2016.

Time (UT)	θ (°)	LT (min)	L_{max} (Mm)	$\overline{w}$ (Mm)	v_a (km s^{-1})	v_r (km s^{-1})	P_r (min)	D_r (min)	T_r
2010-06-23 16:46	67.2	71.6	107.2	26.4 ± 1.7	101.4 ± 6.7	87.1 ± 14.3	7.4 ± 1.4	27.8	3.8 ± 0.7
2010-06-27 02:15	30.8	41.4	133.7	16.1 ± 5.3	148.0 ± 20.6	176.7 ± 49.8	5.8 ± 2.3	13.6	2.3 ± 0.9
2010-06-27 05:50	19.3	65.4	321.2	23.9 ± 9.4	230.6 ± 29.2	108.1 ± 69.7	9.8 ± 5.7	14.4	1.5 ± 0.9
2010-07-02 14:02	72.9	43.6	108.8	25.3 ± 8.2	103.0 ± 13.2	87.2 ± 13.4	7.4 ± 2.0	13.5	1.8 ± 0.5
2010-07-26 14:37	74.7	39.6	112.1	16.0 ± 1.1	101.0 ± 3.0	41.3 ± 4.1	9.6 ± 1.7	18.5	1.9 ± 0.3
2010-07-27 01:07	13.2	65.8	271.3	16.7 ± 7.7	258.3 ± 54.7	95.3 ± 1.0	4.0 ± 0.4	9.2	2.3 ± 0.2
2010-08-19 20:45	76.1	42.8	188.9	24.8 ± 4.4	149.7 ± 2.9	73.3 ± 9.8	9.6 ± 1.5	24.4	2.6 ± 0.4
2010-08-20 17:53	77.5	-	127.9	21.4 ± 8.7	163.4 ± 9.9	96.9 ± 22.8	6.6 ± 2.8	9.8	1.5 ± 0.6
2010-08-21 06:19	76.1	54.4	119.2	36.7 ± 2.7	113.4 ± 7.2	73.6 ± 18.6	11.0 ± 3.0	26.0	2.4 ± 0.6
2010-12-29 14:09	-27.8	59.4	242.1	22.0 ± 4.4	211.3 ± 0.0	136.1 ± 25.9	9.0 ± 1.6	30.6	3.4 ± 0.6
2011-01-20 09:16	-72.6	51.2	116.1	28.2 ± 6.3	127.3 ± 20.4	79.5 ± 26.5	10.1 ± 3.2	21.4	2.1 ± 0.7
2011-01-26 02:01	50.7	71.6	148.7	45.1 ± 3.8	123.5 ± 18.3	34.7 ± 22.5	27.4 ± 8.1	59.9	2.2 ± 0.6
2011-02-13 05:14	29.3	41.0	206.7	16.2 ± 3.7	226.6 ± 9.8	154.6 ± 45.0	3.4 ± 1.2	10.4	3.0 ± 1.0
2012-12-29 09:55	59.5	34.6	133.0	20.0 ± 6.1	120.5 ± 5.3	54.7 ± 21.8	12.5 ± 7.4	16.4	1.3 ± 0.8
2013-01-29 02:14	-23.4	-	245.1	34.6 ± 6.6	226.2 ± 42.9	112.7 ± 21.2	10.6 ± 3.7	14.2	1.3 ± 0.5
2013-03-19 23:17	17.9	59.4	208.2	17.0 ± 2.5	216.6 ± 46.1	94.2 ± 23.8	5.6 ± 1.2	8.9	1.6 ± 0.3
2013-05-05 06:59	-18.7	39.2	104.5	21.7 ± 7.2	153.5 ± 11.7	81.1 ± 7.9	6.9 ± 1.3	32.6	4.7 ± 0.9
2013-08-12 09:00	-17.8	32.8	123.4	16.7 ± 6.8	212.5 ± 18.2	155.7 ± 14.1	3.8 ± 0.9	15.2	4.0 ± 1.0
2013-08-14 17:33	76.1	28.6	78.1	8.5 ± 1.5	221.4 ± 54.6	49.7 ± 17.6	9.0 ± 0.3	24.2	2.7 ± 0.1
2013-09-21 18:34	-0.1	49.8	140.2	18.4 ± 1.5	139.4 ± 11.3	120.9 ± 27.0	6.6 ± 2.5	10.4	1.6 ± 0.6
2013-09-22 14:41	20.3	38.2	128.6	17.8 ± 1.5	163.0 ± 22.5	82.0 ± 22.2	5.7 ± 0.8	10.1	1.8 ± 0.3
2014-01-05 16:18	-14.7	28.8	70.9	15.0 ± 5.8	79.4 ± 2.2	70.6 ± 32.2	6.9 ± 2.9	16.0	2.3 ± 1.0
2015-02-06 12:46	10.4	53.4	159.7	16.7 ± 2.4	201.3 ± 23.3	147.1 ± 19.7	3.7 ± 0.7	9.2	2.5 ± 0.5
2015-04-05 23:03	8.9	-	193.4	23.7 ± 6.4	150.3 ± 21.7	115.9 ± 23.4	7.6 ± 2.2	28.3	3.7 ± 1.1
2015-04-10 10:15	16.7	-	268.8	29.7 ± 5.4	333.9 ± 4.7	208.2 ± 95.8	4.6 ± 1.8	9.2	2.0 ± 0.8
2015-11-10 16:52	-14.9	57.4	266.1	17.2 ± 4.8	144.8 ± 52.2	100.3 ± 8.5	8.7 ± 3.0	15.2	1.8 ± 0.6
2016-02-11 18:55	-69.9	34.6	101.4	30.3 ± 1.2	138.9 ± 30.1	54.4 ± 19.8	4.6 ± 1.1	6.5	1.4 ± 0.3
2016-06-08 04:10	57.6	39.2	79.6	21.2 ± 4.1	95.2 ± 4.8	84.6 ± 9.7	7.0 ± 2.3	9.2	1.3 ± 0.4
2016-07-07 23:42	72.8	24.4	81.9	37.0 ± 2.4	169.1 ± 8.5	105.7 ± 27.7	7.7 ± 1.7	13.2	1.7 ± 0.4
2016-07-12 08:25	14.6	44.2	142.7	11.9 ± 0.7	129.6 ± 13.9	96.5 ± 42.4	4.0 ± 1.2	8.9	2.2 ± 0.6

θ is the latitude, LT the lifetime, L_{max} the maximum projected length, $\overline{w}$ the average width, v_a the average axial speed during the period of the rotational motion, v_r the average rotational speed, P_r the average rotational period, D_r the duration of the rotational motion, and T_r the total number of turns, respectively.

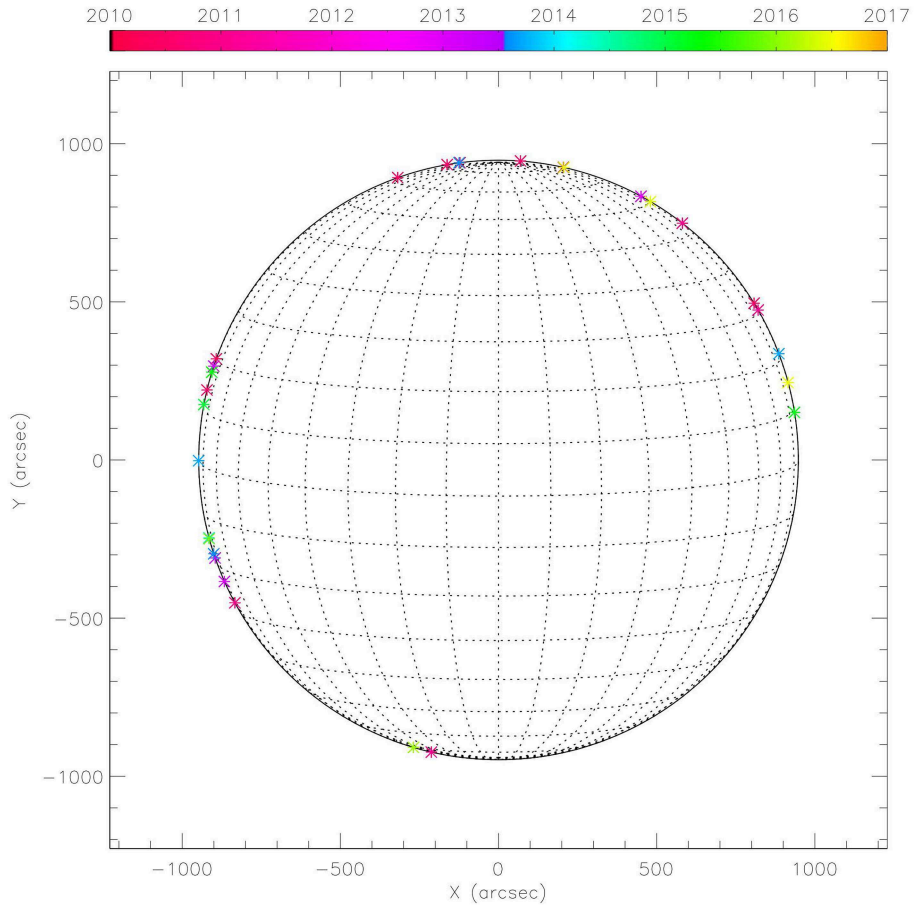

FIGURE 1 | Location of the apparent source regions on the solar limb of all the studied 30 rotational coronal jets from 2010 to 2017. Colors denote dates of eruptions.

3. EXAMPLES OF EVENTS

In this section, we will show, using two typical examples, our analysis of the temporal evolution, axial and rotational motion of all jets in details. The main difference between these two examples is the different behaviors in their rotational motions: the rotational motion of the first example jet manifests recurrent quasi-parallel stripes in the running-difference time-distance diagram of the slit perpendicular to its axis, while the second example jet shows sinusoidal-like features.

3.1. Coronal Jet on 27 June 2010

A coronal jet, together with a flaring event at its source region, started to erupt from the north-west limb with its root latitude of ∼31°, at around 02:16 UT on the 27*th* June 2010. After rising up to more than 100 Mm above the solar surface, the jet began to fall back from around 02:38 UT and finally arrived at the solar surface at around 02:57 UT. The visualization of whole evolution of this event is available as the online **Movie M1**, which, again, was generated from a sequence of base-difference AIA 304 Å images. Apparent "whip-like" motion, which has also been observed in many other jets (e.g., Shibata et al., 1996), could be observed during the very early stage of its eruption. After that, clear signatures of the rotational motion became visible during the ascending phase of this jet. Its rotational motion stopped before the jet reached its maximum projected length (the projection of its real length in the plane of the sky). **Figure 2A** depicts a snapshot of this jet at 02:38 UT observed by SDO/AIA 304 Å. The green dashed line is a 50-pixel (∼22 Mm) wide slit along the jet axis, and the blue dotted line is a 30-pixel (∼13 Mm) wide slit perpendicular to the jet axis.

Figure 2B shows the time-distance diagram of the green slit in panel (a) based on running-difference images of SDO/AIA 304 Å observations. We can identify a number of fine structures, as parts of the whole jet, appearing as alternating black and white curves in the time-distance diagram. These fine structures, known as "sub-jets", erupt successively and are common in many solar coronal jet events (e.g., Liu et al., 2014). Parabolic fittings to sample sub-jets (indicated by green dashed curves in **Figure 2B**) reveal an average axial speed of 148.0 ± 20.6 km s^{-1} of the jet during the period of its rotational motion (see next paragraph). The error of the average axial speed is the standard deviation of the linear speeds of the sample sub-jets (green dashed curves). The three vertical dashed lines (yellow) represent the starting, peak and ending time of the jet, respectively. Meanwhile, the horizontal dashed line (red) represents the maximum projected

length (∼133 Mm) of the jet, which was directly determined from the time-distance diagram.

It is worth noticing that, from **Figure 2B**, these successive sub-jets reached their maximum projected distances at different times. Via a careful examination on these sub-jets, we have found a trend that: (1) when the maximum projected distance is above about 100 Mm, a sub-jet with a larger maximum projected distance reached its maximum projected distance slightly earlier; and (2) when the maximum projected distance is below about 100 Mm, a sub-jet with a smaller maximum projected distance reached its maximum projected distance earlier. A similar behavior of sub-jets in a rotational coronal jet was also be found in our earlier study (Liu et al., 2014). We conjecture that the above behavior was caused by the following reason: (1) at the beginning of the eruption, a sub-jet erupted earlier only had a slightly higher initial speed than its successive sub-jet and thus reached its maximum projected distance somewhat earlier; and (2) toward the end of the magnetic reconnection, a sub-jet erupted later had a significantly lower initial speed than its previous sub-jet, and thus reached its maximum projected distance earlier. A similar relationship between the initial speeds of sub-jets can be found from column 1 of Table 1 in Liu et al. (2014).

Figure 2C shows the time-distance diagram of the blue slit in **Figure 2A**, again, based on running-difference images of SDO/AIA 304 Å observations. Lower values in distance correspond to lower latitudes in the blue slit. Several inclined quasi-parallel stripes could be identified, indicating plasma material moving toward higher latitudes. One might wonder whether these movements are the manifestation of either a "whip-like" motion or a rotational motion. We consider this as a representation of a rotational motion of the jet, mainly based on the following: (1) visual check on the temporal evolution of the jet in SDO/AIA 304 Å images suggests a significant rotational motion of the jet (online **Movie M1**); (2) a "whip-like" motion would lead to the jet moving as a whole. However, what we see here from **Figure 2C**, is that the location of the jet body stays almost unchanged, while plasma moves from one side to another across the width of the jet; and (3) there are signs of stripes "changing direction" in the time-distance diagram (indicated by the red arrow) showing plasmas travel from the front (back) to the back (front). Time-distance diagrams along slits perpendicular to most jets in this study reveal quasi-parallel trajectories as what we show here in **Figure 2C**. We suggest, this could have been caused by the combined effect of that: (1) most jets are intensive, and (2) the SDO/AIA 304 Å passband is optically thick, meaning that it would be hard to see movements of material behind the "back" of jets.

The purple solid lines in **Figure 2C** denote some typical inclined quasi-parallel stripes. The average rotational speed of the jet is then estimated as the average slope of linear fittings of these stripes. We note that, these example quasi-parallel stripes do not indicate the different rotating phases of the same material. In other words, stripes perpendicular to these marked example stripes, which mark the rotational motion of material behind the "back" of the jet, are not seen clearly between them.

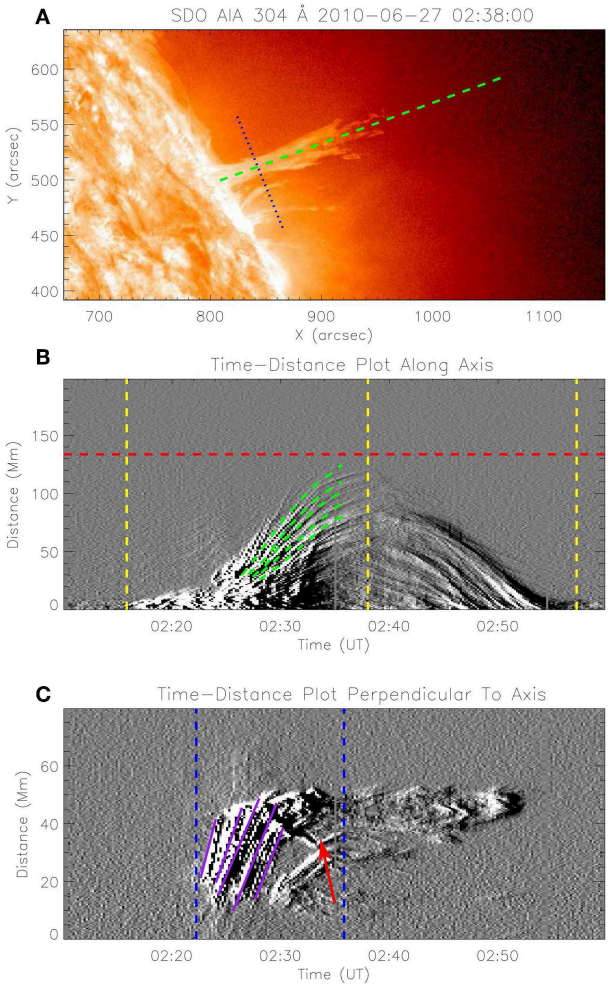

FIGURE 2 | (A) is an off-limb coronal jet observed by SDO/AIA 304 Å passband on 27*th* June 2010 at 02:38 UT. Green dashed and blue dotted lines are slits along and perpendicular to the jet axis, respectively. **(B)** is a running difference time-distance plot along the jet axis. Three yellow vertical dashed lines represent the starting, peak and ending time of the jet, respectively. The red horizontal dashed line denotes the maximum projected length of the jet. Green dashed curves indicate trajectories of sample sub-jets used to estimate the average projected axial speed of the jet during the period of its rotational motion. **(C)** is a running difference time-distance plot perpendicular to the jet axis. Two blue vertical dashed lines denote the estimated starting and ending time of the rotational motion, respectively. Purple solid lines are linear fittings of the inclined stripes. The red arrow marks a stripe as part of the evidence of the rotational motion. See the text for reasons why these stripes are manifestations of rotational motion, instead of "whip-like" motion.

Again, we suggest, this was caused by the combined effect of that: (1) most jets are intensive, and (2) the SDO/AIA 304 Å passband is optically thick. Further, the average rotational period of the jet is defined as twice of the average duration of these stripes. The average rotational speed and period of this jet are therefore estimated as 176.6 ± 49.8 km s^{-1} and 5.8 ± 2.3 min, respectively. Taking into account the starting time (02:22:14 UT, blue vertical dashed line on the left) and ending time (02:35:50 UT, blue vertical dashed line on the

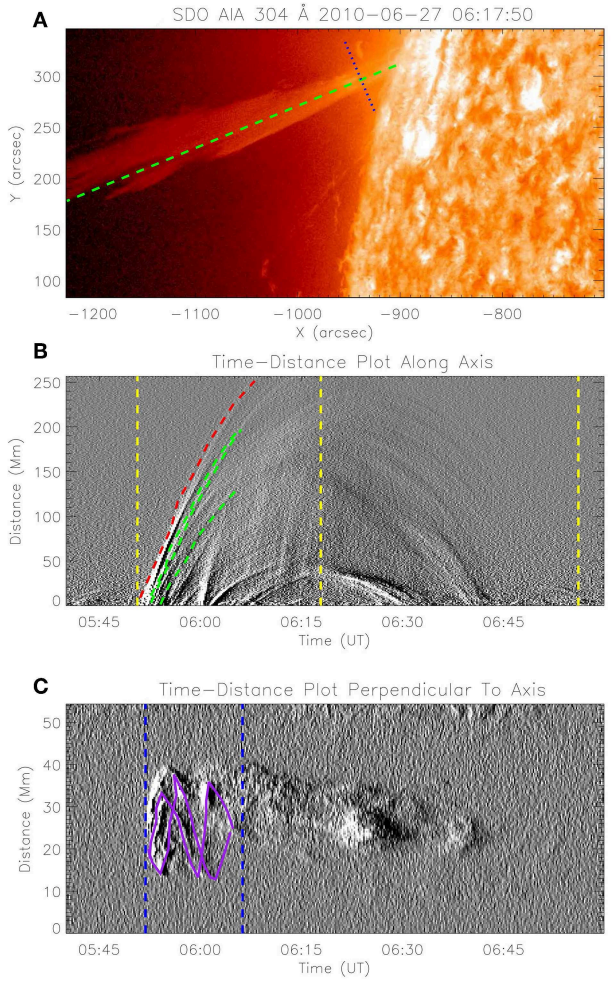

FIGURE 3 | (A) similar to **Figure 2A**, but for another off-limb coronal jet event on 27*th* June 2010 at 06:18 UT. **(B)** is a running difference time-distance plot along the jet axis. Again, three yellow vertical dashed lines represent the starting, peak and ending time of the jet, respectively. The red dashed curve denotes the parabolic fitting of the outermost sub-jet. Green dashed curves (together with the red dashed curve) indicate trajectories of sample sub-jets used to estimate the average projected axial speed of the jet during the period of its rotational motion. **(C)** is a running difference time-distance plot perpendicular to the jet axis. Two blue vertical dashed lines denote the estimated starting and ending time of the rotational motion, respectively. Purple solid curves are sinusoidal fittings of corresponding sinusoidal-like trajectories. These sinusoidal features are evidence of the rotational motion instead of the kink motion (see main text).

right), we can now estimate that the jet has rotated 2.3 ± 0.9 turns. We shall note, the ending time of the rotational motion was determined by investigating the time-distance plot (**Figure 2C**) and the original observations of the event (online movie M1). Clear evidence of rotational motion has vanished in both of the time-distance plot and original observations after the determined ending time. We demonstrate that the error of the determined ending time is <5 min, which introduces an uncertainty of <0.9 of the total number of turns the jet has rotated.

3.2. Another Coronal Jet on 27 June 2010

Unlike the previous example in section 3.1, this second jet erupted without strong flaring signatures at its source region. The jet began to erupt from the north-east limb of the Sun with a root latitude of ∼ 19° at around 05:50 UT on the same day as the first example. There are some other differences between this jet and the first example, namely, this jet: (1) did not show apparent "whip-like" motion during its early stage of eruption; and (2) reached a height which is beyond the FOV of SDO/AIA. However, this jet also showed some signatures of rotational motion during its ascending phase and stopped rotating before it reached its maximum projected length. The jet fell back to the solar surface at around 06:56 UT, having a lifetime of more than an hour. The visualization of whole evolution of this event is available as the online **Movie M2**, which was generated from a sequence of base-difference AIA 304 Å images. **Figure 3A** depicts a snapshot of this jet at 06:18 UT observed at the SDO/AIA 304 Å passband. Again, the green dashed line is a 50-pixel (∼22 Mm) wide slit along the jet axis, and the blue dotted line is a 30-pixel (∼13 Mm) wide slit perpendicular to the jet axis.

From the running-difference time-distance plot in **Figure 3B**, taken along the green dashed line in **Figure 3A** during the eruption, we can again find that, there are many "sub-jets," which could be evidence of successive magnetic reconnections (Liu et al., 2014). The relationship between the times when these sub-jets reached their maximum projected distances is similar to the previous jet. Parabolic fittings to sample sub-jets (indicated by red and green dashed curves in **Figure 3B**) reveal an average axial speed of 230.6± 29.2 km s^{-1} of the jet during the period of its rotational motion. Because the jet finally reached a height beyond the FOV of SDO/AIA, we used a parabolic fitting to the trajectory of the outermost sub-jet (red dashed curve), to estimate its maximum projected length. This jet has then been found to reach a maximum projected length of about 320 Mm at around 06:18 UT (middle yellow dashed line in **Figure 3B**).

Similar to **Figures 2C**, **3C** shows the time-distance diagram taken at the location of the blue slit in **Figure 3A**, based on the running-difference images of SDO/AIA 304 Å observations. Lower values in distance correspond to higher latitudes in this example. Instead of inclined quasi-parallel stripes, we can find several sinusoidal-like features (e.g., indicated by purple solid curves) in the time-distance diagram in **Figure 3C**. These sinusoidal-like features clearly manifest the rotational motion, instead of the kink motion, of the jet. In the case of the jet undergoing a kink motion, the whole jet body would move forwards and backwards periodically. This, however, is not found in **Figure 3C**. To evaluate the rotational period, we have performed sinusoidal fittings to these trajectories:

$$y = A \sin \omega(x - x_0) + y_0 \quad (1)$$

where, A, ω, x_0 and y_0 are the amplitude, frequency, phase shift and vertical shift, respectively. We shall note, due to the complexity of the sinusoidal fitting, one needs usually to make a good initial guess of the above parameters as inputs of the fitting, to avoid being trapped in a local minimum of the χ^2. For a given

trajectory, we have used its average y-value as the initial guess of the vertical shift y_0, and Fast Fourier Transform (FFT) on the series of the y-value of the trajectory to determine the initial guesses of the other three parameters. The average rotational period of this jet is 9.8 ± 5.7 min. Considering that the rotational motion started at around 05:51:50 UT (blue vertical dashed line on the left in **Figure 3C**) and ended at around 06:06:14 UT (blue vertical dashed line on the right in **Figure 3C**), the total number of turns the jet rotated is then estimated as 1.5 ± 0.8 turns. Similarly to the previous example, the ending time of the rotational motion was determined by investigating the time-distance plot (**Figure 3C**) and the original observations of the event (online **Movie M2**). The error of the determined ending time is, again, <5 min, resulting in <0.5 of the total number of turns the jet has rotated. The average rotational speed of this jet is estimated to be 108.1 ± 69.7 km s^{-1}.

4. STATISTICAL RESULTS

Table 1 lists parameters that we have obtained from all 30 rotational coronal jets studied. The first column represents the starting time of each jet, the second column (θ) is the latitude with positive (negative) values for the northern (southern) hemisphere, the third column (LT) is the lifetime and the forth column (L_{max}) is the maximum projected length obtained from time-distance plots along their axes similar to **Figures 2B**, **3B**. Jets of which we could not find clear evidence of when they fell back to the solar surface are denoted with "-" with their lifetimes. The fifth column is the average width ($\overline{w}$) of jet, obtained by averaging the distances between two edges of the jet when it reached its maximum projected length. The five remaining columns are the axial speed (v_a), rotational speed (v_r), rotational period (P_r), duration of the rotational motion (D_r), and total number of turns of the rotation (T_r), respectively.

Figure 4 depicts distributions of the lifetime, width, rotational speed and rotational period of the jets studied. Pink bars are the distributions of corresponding parameters, while blue dashed curves are the Gaussian fittings to these distributions. μ and σ are the arithmetic mean and standard deviations, respectively. The lifetime (**Figure 4A**) of all jets (excluding those that we are not sure when or whether they fell back to the solar surface) ranges from 20 to 80 min, with 73% being within the 1-σ range (25–58 min). The arithmetic mean of the lifetime is found to be about 42 min. Similarly, the average width (**Figure 4B**) of all jets ranges from 10 to 50 Mm, with an arithmetic mean of about 21 Mm. The distribution of the width matches well with a Gaussian distribution. The widths of about 67% jets lie within the 1-σ range (15–24 Mm). Note that for a perfect Gaussian distribution, the total probability within the 1-σ range is about 68%.

Figures 4C,D are the distributions of the rotational speed and rotational period, respectively. The rotational speed of jets ranges from 30 to 210 km s^{-1}, with an arithmetic mean of about 88 km s^{-1} and about 73% of them lying within the 1-σ range (49–127 km s^{-1}). Out of 30 jets, 29 have a rotational period ranging from 3 to 15 min. The arithmetic mean is about 7 min, with about 77% lying within the 1-σ range (4–10 min). All the studied jets have an axial speed ranging from 80 to 330 km s^{-1} (**Figure 5A**). The arithmetic mean is about 145 km s^{-1}, with about 67% of the jets lying within the 1-σ range (85–205 km s^{-1}).

Different from the distributions of lifetime, width, rotational speed and rotational period, the frequency of events decreases with increased projected length (**Figure 5B**). The distribution of the maximum projected length could be fitted with an exponential function $f \propto e^{\gamma h}$, where the index γ is found to be about -0.01. The projected length of jets ranges from 70 to 320 Mm, with 80% <220 Mm (black dashed line in **Figure 5B**). The frequency of events also decreases with increased duration of the rotational motion (**Figure 5C**). Eighty percent of the studied events rotated for <25 min.

Most importantly, the frequency of events also decreases with increased total number of turns of the rotational motion, and could be fitted well with an exponential function with an index γ of –0.85 (**Figure 5D**). This indicates that, the number of events with more twist release becomes less. All jets are associated with twist angles ($\Phi_j = 2\pi T_r$) between 2.6 and 9.4π. Among all the 30 studied events, there is not a single event revealing a rotational motion with <1.3 turns (twist angle of 2.6π). Moreover, 80% of the events released twist angles <5.6π (twist numbers <2.8 turns).

Figure 6 shows the dependencies of the total number of turns of the rotational motion on the lifetime (**Figure 6A**), the maximum projected length (**Figure 6B**), the average width (**Figure 6C**), the rotational speed (**Figure 6D**), the rotational period (**Figure 6E**), and the duration of the rotational motion (**Figure 6F**) of the jets investigated. From both the scatters and the correlation coefficients (CCs), we can find that there are neither positive nor negative correlations between the total number of turns of the rotational motion and the lifetime (the projected length, the average width or the rotational speed). Even though, the total number of turns was derived from the rotational period and duration of the rotational motion, the total number of turns has very low (moderate) correlation with the rotational period (duration of the rotational motion).

However, the product of the duration and the speed of the rotational motion has a strong positive correlation (with a CC of 0.72) with the total number of turns (**Figure 7A**). Considering that the twist a jet may release would be the lower limit of, and very likely similar to, the twist its pre-eruption flux rope contains, this strong correlation may indicate that a flux rope with a higher twist number would result in a jet with either a longer or a faster rotational motion. The linear fitting (blue dashed line in **Figure 6A**) using the "*fitxy.pro*" in the *SSW* package, which also accounts for the error bars, suggests that there might be a lower cut-off value around 1.0 of the total number of turns.

The twist angle and twist number of a magnetic flux rope are defined as:

$$\Phi = 2\pi T_w = \frac{lB_\phi}{rB_z}. \quad (2)$$

Here, l, r, B_ϕ, and B_z are the length, width, azimuthal and axial magnetic field strength of the pre-eruption magnetic flux rope, respectively. Then, the twist pitch $l_p = 2\pi l/\Phi$, represents the length traveled along the axis when the magnetic field rotates for

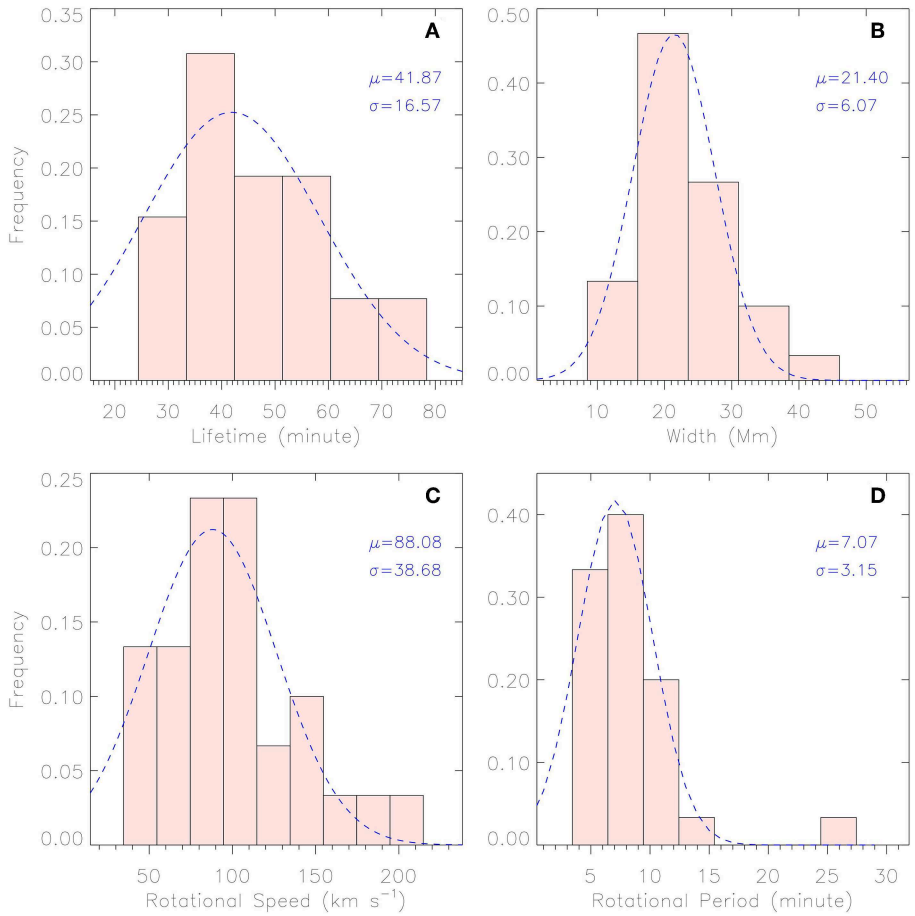

FIGURE 4 | Statistics of the lifetime **(A)**, average width **(B)**, rotational speed **(C)** and rotational period **(D)** of the studied rotational coronal jets. Blue dashed curves are Gaussian fitting results. μ and σ are the arithmetic mean and standard deviation, respectively.

a full turn. **Figure 7B** shows the relationship between the twist pitch of jets and the volume of jets. The twist pitch (l_{pj}) and volume (V) of a jet are defined as:

$$\begin{aligned} l_{pj} &= P_r \cdot v_a, \\ V &= \frac{\pi}{4} L_{max} \overline{w}^2, \end{aligned} \tag{3}$$

respectively. All variables in the above equation have the same meanings as defined in the caption of **Table 1**. It is shown in **Figure 7B**, that the volume of a jet is correlated positively very well to its twist pitch l_{pj}, with a CC of 0.77. Besides, the CCs between the twist pitch of jets and their length L_{max} and average width $\overline{w}$ are 0.39 and 0.52, respectively. If we consider that the twist pitch is conservative during magnetic reconnections (e.g., Birn and Priest, 2007), the above results may suggest that the size of a jet should not be determined by the total twist stored in its pre-reconnection magnetic flux rope, instead, by the twist pitch of its pre-reconnection magnetic flux rope.

5. CONCLUSIONS AND DISCUSSIONS

In this research, using high spatial- and temporal-resolution observations obtained at the SDO/AIA 304 Å passband, we have studied the detailed temporal and spatial evolution, especially the rotational motion, of 30 off-limb rotational solar coronal jets that had erupted between 2010 and 2017. These jets were obtained from the HEK database, and were identified either automatically or manually by different groups from different colleagues, to minimize any possible selection bias.

One of the major findings of this study is that all the rotating jets have rotated at least 1.3 turns during their lifetime. The number (occurrence/frequency) of jets decreases almost exponentially with increased total number of turns they have rotated. Most (80%) of them have rotated <2.8 turns. Note again that when plasma-β is <1 the twist released by a rotational jet is the lower limit of the twist stored in the pre-eruption magnetic flux rope (Pariat et al., 2016). From the above results, we conclude that flux ropes that finally erupted as coronal jet events contain twists of at least 1.3 turns ($\Phi = 2.6\pi$). This value is highly consistent with the suggested kink instability threshold given

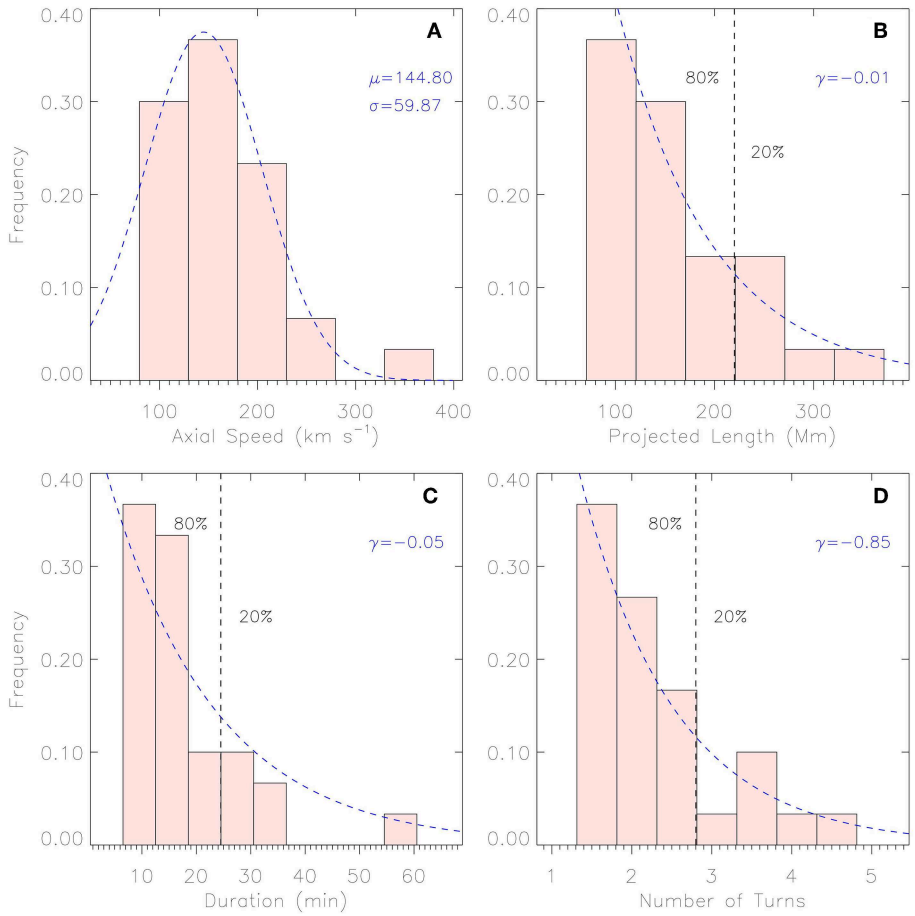

FIGURE 5 | Statistics of the average axial speed during the period of the rotational motion **(A)**, the projected length **(A)**, the duration of rotational motion **(B)** and the total number of turns **(C)** of all studied solar coronal jets. The blue dashed curve in **(A)** is the Gaussian fitting result. μ and σ are the arithmetic mean and standard deviation, respectively. Blue dashed curves in **(B–D)** are exponential fitting results. r is the exponential index. The integrated probabilities on the left of the black vertical dashed lines are 0.8.

by various theories and numerical simulations (e.g., Hood and Priest, 1981; Pariat et al., 2009). However, twists released by the studied jets are different from each other, indicating that the kink instability threshold in the solar atmosphere should not be seen as a constant. Further, the exponential decrease of the number of events with increased total number of turns these jets have rotated, suggests that, the more twist the pre-eruption magnetic flux rope contains, the rarer the event is. Most magnetic flux ropes associated with coronal jets would become unstable before their stored twist number (twist angle) is accumulated to 2.8 turns (5.6π). All the results we report here, suggest that containing a twist number of 1.3 turns should be a necessary but not a sufficient condition for a finite solar magnetic flux rope to become kink unstable.

We have found no clear correlation between the released twist by jets and their measured characteristic parameters including lifetime, maximum projected length, width, rotational speed and rotational period. However, there is a strong positive correlation (with a CC of 0.72) between the released twist and the product of the duration and the speed of the rotational motion, suggesting that pre-eruption magnetic flux ropes with higher twists tend to generate jets that rotate either for longer durations or with faster rotational speeds. On the other hand, we have found very strong positive correlation (with a CC of 0.77) between the jet twist pitch and volume of jets, indicating that a pre-eruption magnetic flux rope with a higher twist pitch would most likely result in a larger jet.

All the jets studied in this research have projected lengths of at least 70 Mm and lifetimes of at least 20 min. Therefore, one might wonder whether the lower limit of the twist (1.3 turns) released by rotating solar coronal jets would be different if we study more coronal jets with shorter length and lifetime? We shall note that: (1) Liu et al. (2018) analyzed four homologous recurrent jets, which had minimum length shorter than 20 Mm and lifetime <10 min. Detailed spectral analyses using high resolution IRIS data of one of these jets have suggested that, it released a twist of 1.3 turns (twist angle of 2.6π). (2) We have found no clear correlation between the twist released by

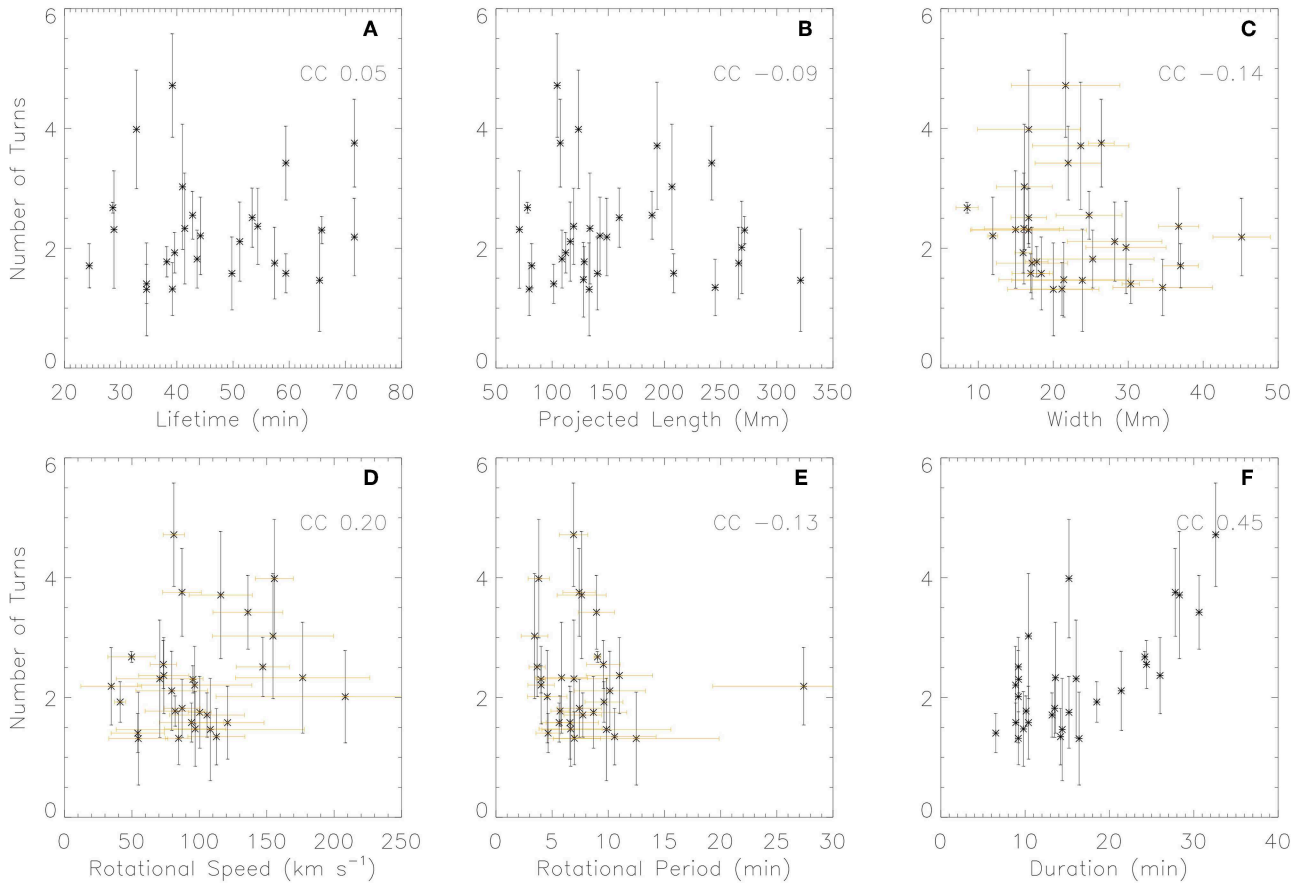

FIGURE 6 | Correlation between various jet parameters **(A)** lifetime, **(B)** maximum projected length, **(C)** width, **(D)** rotational speed, **(E)** rotational period, and **(F)** duration of the rotational motion and the total number of turns these jets rotate. The black vertical lines are indicating the associated errors of the total number of turns. The orange horizontal lines show the errors of the corresponding parameters.

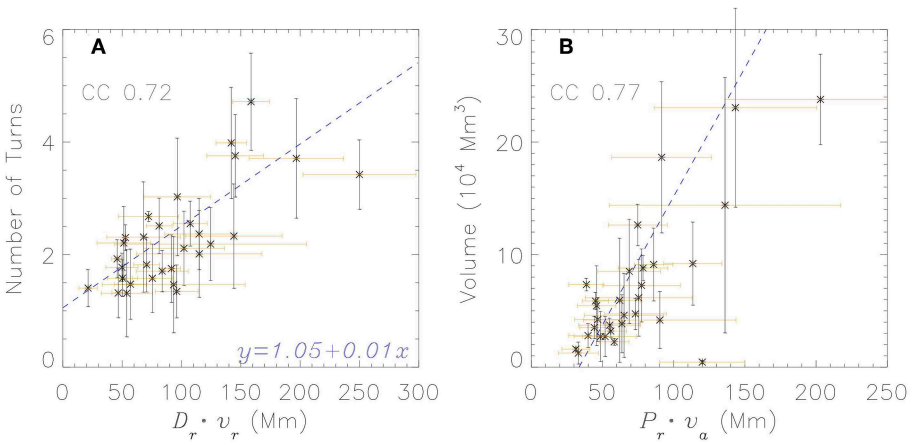

FIGURE 7 | (A) shows the correlation between the product of the duration and speed of the rotational motion and the total number of turns. **(B)** demonstrates correlation between the twist pitch and volume of jets (see Equation 3). Black vertical lines are errors of the total number of turns. Orange horizontal lines are propagated errors of corresponding parameters. Blue lines are the linear fitting results of the scattered points with error bars taken into account.

jets and their length or lifetime. And, (3) the linear fitting in **Figure 7** suggests a cut-off value of around 1.0 turns of the twist released by jets. Although more observations would be needed to confirm this conjecture, we suggest that the lower limit of the twist released by rotating solar coronal jets would not be significantly different.

The maximum twist of the jets analyzed here have released 4.7 turns (corresponding to a twist angle of 9.4π). The jet which triggered a coronal mass ejection event studied in Liu et al. (2015) was found to release a twist of at least 3.3 turns (twist angle of 6.6π). Liu et al. (2014) investigated in details the rotational motion and kinetic energy sources of a coronal jet erupted in July 2012. That jet studied in Liu et al. (2014) was still rotating even at the end of its descending phase and, finally, released a twist of at least 5.1 turns (corresponding to a twist angle of 10.2π). Throughout the study of a pair of solar coronal twin jets and their preceding jet, Liu et al. (2016a) found the preceding jet rotated for at least 8.9 turns (twist angle of 17.8π) during its lifetime. Considering all these previous studies and our findings in this research, we cannot conclude about an upper limit for the twist released by rotating solar coronal jets or stored by pre-eruption magnetic flux ropes. Instead, we have found that magnetic flux ropes with very high twist numbers ($>$ 2.8 turns or 5.6π), are much less in number.

Dungey and Loughhead (1954) suggested a kink-unstable threshold (in units of radians) of $\omega l/R$, where l and R are the length and radius of the flux rope, respectively. They found the constant ω as 2. If we assume that: (1) the magnetic twist pitch is conserved during the magnetic reconnections which triggered the observed jets (e.g., Birn and Priest, 2007); (2) the twists released by the observed coronal jets are similar to those stored in the pre-eruption magnetic flux ropes (e.g., Liu et al., 2016a; Pariat et al., 2016); and (3) the average width of each observed jet is similar to the diameter of its associated pre-eruption magnetic flux rope, we then have:

$$l/R \approx \frac{D_r \cdot v_a}{0.5\overline{w}}. \quad (4)$$

Here, all the variables have the same meaning as defined before. After removing a significant outlier (event 18), the correlation between Φ_j and l/R (defined in Equation 4) is found to be as high as 0.73. Linear fitting between Φ_j and l/R reveals an average value of about 0.6 of ω, with the maximum value of ω <2. Wang et al. (2016) studied the twist angle and other properties of 115 magnetic clouds observed at 1 AU. They also found an average ω value of 0.6 and a maximum ω value of <2. These highly consistent results between solar coronal jets and inter-planetary magnetic clouds, suggest the high possibility of a universal mechanism of different types of eruptions of magnetic flux ropes in the solar upper atmosphere. Nonetheless, we note that, we have made a number of assumptions to obtain the above results. Future work will be needed to focus on examining the above results without making such assumptions.

We would also stress that all the above findings are related to "large-scale" rotational solar coronal jets. Solar coronal jets with no rotational motion are also common, but are suggested to be resulted from different mechanisms and not directly being related to magnetic flux ropes (e.g., Moore et al., 2010; Pariat et al., 2015; Sterling et al., 2015). On the other hand, we would not extend our findings to the ubiquitous type-II spicules ("small-scale" jets with typical length $<$ 10 Mm and lifetime around 10 s, de Pontieu et al., 2007), which are believed to be resulted from magnetic reconnections in the upper photosphere or lower chromosphere, with the plasma-β being higher than unity (e.g., Shibata et al., 2007).

AUTHOR CONTRIBUTIONS

JL conducted the analysis of the data and drafted the manuscript. YW and RE led the interpretation of the result and commented on the manuscript. All authors reviewed the manuscript.

FUNDING

RE and JL are grateful to Science and Technology Facilities Council (STFC grant nr ST/M000826/1) UK and to The Royal Society for the support received. YW acknowledges the support received from the National Natural Science Foundation of China (NSFC grant no 41774178 and 41761134088).

ACKNOWLEDGMENTS

The Solar Dynamics Observatory is the first mission for NASA's Living With a Star (LWS) Program. Sunpy is an open-source and free community-developed solar data analysis package written in Python.

SUPPLEMENTARY MATERIAL

The Supplementary Material for this article can be found online at: https://www.frontiersin.org/articles/10.3389/fspas.2019.00044/full#supplementary-material

Video 1 | Online movie M1, generated from a sequence of base-difference AIA 304 A images for the example jet in Section 3.1.

Video 2 | Online movie M2, generated from a sequence of base-difference AIA 304 A images for the example jet in Section 3.2.

REFERENCES

Barniol Duran, R., Tchekhovskoy, A., and Giannios, D. (2017). Simulations of AGN jets: magnetic kink instability versus conical shocks. *Month. Notices R. Astron. Soc.* 469, 4957–4978. doi: 10.1093/mnras/stx1165

Birn, J., and Priest, E. R. (2007). *Reconnection of Magnetic Fields : Magnetohydrodynamics and Collisionless Theory and Observations*. New York, NY: Cambridge University Press. doi: 10.1017/CBO9780511536151

Browning, P. K., Gerrard, C., Hood, A. W., Kevis, R., and van der Linden, R. A. M. (2008). Heating the corona by nanoflares: simulations of energy

release triggered by a kink instability. *Astron. Astrophys.* 485, 837–848. doi: 10.1051/0004-6361:20079192

Canfield, R. C., Reardon, K. P., Leka, K. D., Shibata, K., Yokoyama, T., and Shimojo, M. (1996). H alpha Surges and X-Ray Jets in AR 7260. *Astrophys. J.* 464:1016. doi: 10.1086/177389

Chen, J., Su, J., Deng, Y., and Priest, E. R. (2017). A complex solar coronal jet with two phases. *Astrophys. J.* 840:54. doi: 10.3847/1538-4357/aa6c59

Chen, P. F. (2011). Coronal mass ejections: models and their observational basis. *Living Rev. Sol. Phys.* 8:1. doi: 10.12942/lrsp-2011-1

Cheng, X., Guo, Y., and Ding, M. (2017). Origin and structures of solar eruptions I: magnetic flux rope. *Sci. China Earth Sci.* 60, 1383–1407. doi: 10.1007/s11430-017-9074-6

de Pontieu, B., McIntosh, S., Hansteen, V. H., Carlsson, M., Schrijver, C. J., Tarbell, T. D., et al. (2007). A tale of two spicules: the impact of spicules on the magnetic chromosphere. *Publ. Astron. Soc. Jpn.* 59, S655–S662. doi: 10.1093/pasj/59.sp3.S655

Dungey, J. W., and Loughhead, R. E. (1954). Twisted magnetic fields in conducting fluids. *Aust. J. Phys.* 7:5. doi: 10.1071/PH540005

Fang, F., Fan, Y., and McIntosh, S. W. (2014). Rotating solar jets in simulations of flux emergence with thermal conduction. *Astrophys. J.* 789:L19. doi: 10.1088/2041-8205/789/1/L19

Filippov, B., Martsenyuk, O., Srivastava, A. K., and Uddin, W. (2015a). Solar magnetic flux ropes. *J. Astrophys. Astron.* 36, 157–184. doi: 10.1007/s12036-015-9321-5

Filippov, B., Srivastava, A. K., Dwivedi, B. N., Masson, S., Aulanier, G., Joshi, N. C., et al. (2015b). Formation of a rotating jet during the filament eruption on 2013 April 10-11. *Month. Notices R. Astron. Soc.* 451, 1117–1129. doi: 10.1093/mnras/stv1039

Giannios, D., and Spruit, H. C. (2006). The role of kink instability in Poynting-flux dominated jets. *Astron. Astrophys.* 450, 887–898. doi: 10.1051/0004-6361:20054107

Guo, Y., Ding, M. D., Schmieder, B., Li, H., Török, T., and Wiegelmann, T. (2010). Driving mechanism and onset condition of a confined eruption. *Astrophys. J. Lett.* 725, L38–L42. doi: 10.1088/2041-8205/725/1/L38

Hood, A. W., and Priest, E. R. (1979). Kink instability of solar coronal loops as the cause of solar flares. *Solar Phys.* 64, 303–321. doi: 10.1007/BF00151441

Hood, A. W., and Priest, E. R. (1981). Critical conditions for magnetic instabilities in force-free coronal loops. *Geophys. Astrophys. Fluid Dyn.* 17, 297–318. doi: 10.1080/03091928108243687

Hurlburt, N., Cheung, M., Schrijver, C., Chang, L., Freeland, S., Green, S., et al. (2012). Heliophysics event knowledgebase for the solar dynamics observatory (SDO) and beyond. *Solar Phys.* 275, 67–78. doi: 10.1007/s11207-010-9624-2

Jibben, P., and Canfield, R. C. (2004). Twist Propagation in Hα Surges. *Astrophys. J.* 610, 1129–1135. doi: 10.1086/421727

Karpen, J. T. (2015). *Solar Prominences*, Vol. 415. Cham: Springer International Publishing.

Kliem, B., Titov, V. S., and Török, T. (2004). Formation of current sheets and sigmoidal structure by the kink instability of a magnetic loop. *Astron. Astrophys.* 413, L23–L26. doi: 10.1051/0004-6361:20031690

Kruskal, M. D., and Kulsrud, R. M. (1958). Equilibrium of a magnetically confined plasma in a toroid. *Phys. Fluids* 1, 265–274. doi: 10.1063/1.1705884

Kumar, P., Cho, K.-S., Bong, S.-C., Park, S.-H., and Kim, Y. H. (2012). Initiation of coronal mass ejection and associated flare caused by helical kink instability observed by SDO/AIA. *Astrophys. J.* 746:67. doi: 10.1088/0004-637X/746/1/67

Lee, E. J., Archontis, V., and Hood, A. W. (2015). Helical blowout jets in the sun: untwisting and propagation of waves. *Astrophys. J.* 798:L10. doi: 10.1088/2041-8205/798/1/L10

Lemen, J. R., Title, A. M., Akin, D. J., Boerner, P. F., Chou, C., Drake, J. F., et al. (2012). The atmospheric imaging assembly (AIA) on the solar dynamics observatory (SDO). *Solar Phys.* 275, 17–40. doi: 10.1007/s11207-011-9776-8

Liu, J., Erdélyi, R., Wang, Y., and Liu, R. (2018). Untwisting jets related to magnetic flux cancellation. *Astrophys. J.* 852:10. doi: 10.3847/1538-4357/aa992d

Liu, J., Fang, F., Wang, Y., McIntosh, S. W., Fan, Y., and Zhang, Q. (2016a). On the observation and simulation of solar coronal twin jets. *Astrophys. J.* 817:126. doi: 10.3847/0004-637X/817/2/126

Liu, J., Wang, Y., Erdélyi, R., Liu, R., McIntosh, S. W., Gou, T., et al. (2016b). On the magnetic and energy characteristics of recurrent homologous jets from an emerging flux. *Astrophys. J.* 833:150. doi: 10.3847/1538-4357/833/2/150

Liu, J., Wang, Y., Liu, R., Zhang, Q., Liu, K., Shen, C., et al. (2014). When and how does a prominence-like jet gain kinetic energy? *Astrophys. J.* 782:94. doi: 10.1088/0004-637X/782/2/94

Liu, J., Wang, Y., Shen, C., Liu, K., Pan, Z., and Wang, S. (2015). A solar coronal jet event triggers a coronal mass ejection. *Astrophys. J.* 813:115. doi: 10.1088/0004-637X/813/2/115

Liu, L., Wang, Y., Wang, J., Shen, C., Ye, P., Liu, R., et al. (2016c). Why is a flare-rich active region CME-poor? *Astrophys. J.* 826:119. doi: 10.3847/0004-637X/826/2/119

Liu, R., Kliem, B., Titov, V. S., Chen, J., Wang, Y., Wang, H., et al. (2016d). Structure, stability, and evolution of magnetic flux ropes from the perspective of magnetic twist. *Astrophys. J.* 818:148. doi: 10.3847/0004-637X/818/2/148

Liu, W., Berger, T. E., Title, A. M., and Tarbell, T. D. (2009). AN INTRIGUING CHROMOSPHERIC JET OBSERVED BY HINODE : FINE STRUCTURE KINEMATICS AND EVIDENCE OF UNWINDING TWISTS. *Astrophys. J. Lett.* 707, 37–41. doi: 10.1088/0004-637X/707/1/L37

Moore, R. L., Cirtain, J. W., Sterling, A. C., and Falconer, D. A. (2010). Dichotomy of solar coronal jets: standard jets and blowout jets. *Astrophys. J.* 720, 757–770. doi: 10.1088/0004-637X/720/1/757

Moreno-Insertis, F., Galsgaard, K., and Ugarte-Urra, I. (2008). Jets in coronal holes: hinode observations and three-dimensional computer modeling. *Astrophys. J.* 673, L211–L214. doi: 10.1086/527560

Pariat, E., Antiochos, S. K., and DeVore, C. R. (2009). A MODEL FOR SOLAR POLAR JETS. *Astrophys. J.* 691, 61–74. doi: 10.1088/0004-637X/691/1/61

Pariat, E., Dalmasse, K., DeVore, C. R., Antiochos, S. K., and Karpen, J. T. (2015). Model for straight and helical solar jets. *Astron. Astrophys.* 573:A130. doi: 10.1051/0004-6361/201424209

Pariat, E., Dalmasse, K., DeVore, C. R., Antiochos, S. K., and Karpen, J. T. (2016). A model for straight and helical solar jets. II. Parametric study of the plasma beta. *Astron. Astrophys.* 596:A36. doi: 10.1051/0004-6361/201629109

Pesnell, W. D., Thompson, B. J., and Chamberlin, P. C. (2012). The solar dynamics observatory (SDO). *Solar Phys.* 275, 3–15. doi: 10.1007/s11207-011-9841-3

Pevtsov, A. A., Canfield, R. C., and Zirin, H. (1996). Reconnection and helicity in a solar flare. *Astrophys. J.* 473:533. doi: 10.1086/178164

Raouafi, N. E. (2009). Observational evidence for coronal twisted flux rope. *Astrophys. J.* 691, L128–L132. doi: 10.1088/0004-637X/691/2/L128

Raouafi, N. E., Patsourakos, S., Pariat, E., Young, P. R., Sterling, A. C., Savcheva, A., et al. (2016). Solar coronal jets: observations, theory, and modeling. *Space Sci. Rev.* 201, 1–53. doi: 10.1007/s11214-016-0260-5

Rust, D. M. and Kumar, A. (1996). Evidence for helically kinked magnetic flux ropes in solar eruptions. *Astrophys. J. Lett.* 464:L199. doi: 10.1086/310118

Schrijver, C. J. (2009). Driving major solar flares and eruptions : a review. *Adv. Sp. Res.* 43, 739–755. doi: 10.1016/j.asr.2008.11.004

Shafranov, V. D. (1963). Equilibrium of a toroidal plasma in a magnetic field. *J. Nuclear Energy* 5:251. doi: 10.1088/0368-3281/5/4/307

Shen, Y., Liu, Y., Su, J., and Deng, Y. (2012). ON A CORONAL BLOWOUT JET: THE FIRST OBSERVATION OF A SIMULTANEOUSLY PRODUCED BUBBLE-LIKE CME AND A JET-LIKE CME IN A SOLAR EVENT. *Astrophys. J.* 745:164. doi: 10.1088/0004-637X/745/2/164

Shibata, K., Nakamura, T., Matsumoto, T., Otsuji, K., Okamoto, T. J., Nishizuka, N., et al. (2007). Chromospheric anemone jets as evidence of ubiquitous reconnection. *Science* 318:1591. doi: 10.1126/science.1146708

Shibata, K., Shimojo, M., Yokoyama, T., and Ohyama, M. (1996). Theory and Observations of X-ray Jets. *ASP Conf. Ser.* 111:29.

Shibata, K., and Uchida, Y. (1986). Sweeping-magnetic-twist mechanism for the acceleration of jets in the solar atmosphere. *Solar Phys.* 103, 299–310. doi: 10.1007/BF00147831

Srivastava, A. K., Zaqarashvili, T. V., Kumar, P., and Khodachenko, M. L. (2010). Observation of kink instability during small B5.0 solar flare on 2007 June 4. *Astrophys. J.* 715, 292–299. doi: 10.1088/0004-637X/715/1/292

Sterling, A. C., Moore, R. L., Falconer, D. A., and Adams, M. (2015). Small-scale filament eruptions as the driver of X-ray jets in solar coronal holes. *Nature* 523:437. doi: 10.1038/nature14556

SunPy Community, Mumford, S. J., Christe, S., Pérez-Suárez, D., Ireland, J., Shih, A. Y., et al. (2015). SunPy-Python for solar physics. *Comput. Sci. Dis.* 8:014009. doi: 10.1088/1749-4699/8/1/014009

Török, T., and Kliem, B. (2005). Confined and Ejective Eruptions of Kink-unstable Flux Ropes. *Astrophys. J. Lett.* 630, L97–L100. doi: 10.1086/462412

Vemareddy, P., Gopalswamy, N., and Ravindra, B. (2017). Prominence eruption initiated by helical kink instability of an embedded flux rope. *Astrophys. J.* 850:38. doi: 10.3847/1538-4357/aa9020

Wang, Y., Zhuang, B., Hu, Q., Liu, R., Shen, C., and Chi, Y. (2016). On the twists of interplanetary magnetic flux ropes observed at 1 AU. *J. Geophys. Res. Sp. Phys.* 121, 9316–9339. doi: 10.1002/2016JA023075

Williams, D. R., Török, T., Démoulin, P., van Driel-Gesztelyi, L., and Kliem, B. (2005). Eruption of a kink-unstable filament in NOAA active region 10696. *Astrophys. J. Lett.* 628, L163–L166. doi: 10.1086/432910

Zheng, R., Chen, Y., Huang, Z., Wang, B., Song, H., and Ning, H. (2018). Two-sided-loop jets associated with magnetic reconnection between emerging loops and twisted filament threads. *Astrophys. J.* 861:108. doi: 10.3847/1538-4357/aac955

Conflict of Interest Statement: The authors declare that the research was conducted in the absence of any commercial or financial relationships that could be construed as a potential conflict of interest.

frontiers in Astronomy and Space Sciences

ORIGINAL RESEARCH
published: 18 July 2019
doi: 10.3389/fspas.2019.00050

Multipoint Observations of the June 2012 Interacting Interplanetary Flux Ropes

Emilia K. J. Kilpua[1], Simon W. Good[1], Erika Palmerio[1], Eleanna Asvestari[1,2], Erkka Lumme[1], Matti Ala-Lahti[1], Milla M. H. Kalliokoski[1], Diana E. Morosan[1], Jens Pomoell[1], Daniel J. Price[1], Jasmina Magdalenić[3], Stefaan Poedts[4] and Yoshifumi Futaana[5]*

[1] Department of Physics, University of Helsinki, Helsinki, Finland, [2] Institute of Physics, University of Graz, Graz, Austria, [3] Solar–Terrestrial Centre of Excellence—SIDC, Royal Observatory of Belgium, Brussels, Belgium, [4] Centre for Mathematical Plasma Astrophysics (CmPA), KU Leuven, Leuven, Belgium, [5] Swedish Institute of Space Physics, Kiruna, Sweden

We report a detailed analysis of interplanetary flux ropes observed at Venus and subsequently at Earth's Lagrange L1 point between June 15 and 17, 2012. The observation points were separated by about 0.28 AU in radial distance and 5° in heliographic longitude at this time. The flux ropes were associated with three coronal mass ejections (CMEs) that erupted from the Sun on June 12–14, 2012 (SOL2012-06-12, SOL2012-06-13, and SOL2012-06-14). We examine the CME–CME interactions using *in-situ* observations from the almost radially aligned spacecraft at Venus and Earth, as well as using heliospheric modeling and imagery. The June 14 CME reached the June 13 CME near the orbit of Venus and significant interaction occurred before they both reached Earth. The shock driven by the June 14 CME propagated through the June 13 CME and the two CMEs coalesced, creating the signatures of one large, coherent flux rope at L1. We discuss the origin of the strong interplanetary magnetic fields related to this sequence of events, the complexity of interpreting solar wind observations in the case of multiple interacting CMEs, and the coherence of the flux ropes at different observation points.

Keywords: sun, coronal mass ejection, heliosphere, flux rope, space weather

OPEN ACCESS

Edited by:
Yuming Wang, University of Science and Technology of China, China

Reviewed by:
Pascal Démoulin, Université de Sciences Lettres de Paris, France
Nandita Srivastava, Physical Research Laboratory, India

****Correspondence:***
Emilia K. J. Kilpua
emilia.kilpua@helsinki.fi

Specialty section:
This article was submitted to Stellar and Solar Physics, a section of the journal Frontiers in Astronomy and Space Sciences

Received: *01 February 2019*
Accepted: *01 July 2019*
Published: *18 July 2019*

Citation:
Kilpua EKJ, Good SW, Palmerio E, Asvestari E, Lumme E, Ala-Lahti M, Kalliokoski MMH, Morosan DE, Pomoell J, Price DJ, Magdalenić J, Poedts S and Futaana Y (2019) Multipoint Observations of the June 2012 Interacting Interplanetary Flux Ropes. Front. Astron. Space Sci. 6:50. doi: 10.3389/fspas.2019.00050

1. INTRODUCTION

Coronal mass ejections (CMEs; e.g., Webb and Howard, 2012) are the key drivers of space weather storms at Earth (e.g., Gosling et al., 1991; Webb et al., 2000; Huttunen et al., 2002; Richardson and Cane, 2012; Kilpua et al., 2017b) and related hazards for many modern technologies and infrastructures in orbit and on the ground (e.g., Schrijver et al., 2015; Eastwood et al., 2017). Particularly geoeffective are those interplanetary CMEs (ICMEs; e.g., Kilpua et al., 2017a) classified as magnetic clouds (e.g., Zhang et al., 2007; Kilpua et al., 2017b). Magnetic clouds are discrete large-scale structures in the solar wind that exhibit enhanced magnetic field magnitudes, coherent rotation of the magnetic field direction over a large angle, and depressed proton temperatures (e.g., Burlaga et al., 1981; Klein and Burlaga, 1982). Magnetic clouds can thus provide the sustained periods of strong and southward magnetic fields in the near-Earth solar wind that are a prerequisite for severe disturbances in the geomagnetic field (e.g., Pulkkinen, 2007). Soon after their discovery, it was suggested that magnetic clouds can be described in terms of cylindrically symmetric

force-free magnetic flux ropes (e.g., Goldstein, 1983; Burlaga, 1988). The current consensus holds that magnetic flux ropes are an integral part of all erupting CMEs (e.g., Vourlidas et al., 2013, 2017; Chen, 2017; Green et al., 2018), but are not always detected in interplanetary space due to significant deformations or due to probing of the flux rope far from its center (e.g., Gosling, 1990; Cane et al., 1997; Cane and Richardson, 2003; Huttunen et al., 2005; Jian et al., 2006; Kilpua et al., 2011, 2017a).

Magnetic clouds are often conceptualized as large, curved flux rope loops that extend back to the Sun at both ends, in which the field characteristics and flux rope orientation remain similar over large longitudinal distances (e.g., Burlaga et al., 1990; Crooker et al., 1998; Janvier et al., 2015). Such possible underlying longitudinal coherence is a highly important property both for understanding flux ropes as physical structures in the heliosphere and for forecasting their space weather effects. CME geoeffectiveness depends strongly on the magnetic field magnitude profile and on how the magnetic field vectors vary within the flux rope, i.e., on the "flux rope type" determined by the handedness (chirality) of the field, the axial field direction, and the orientation of the flux rope with respect to the ecliptic plane (e.g., Bothmer and Schwenn, 1998; Huttunen et al., 2005; Kilpua et al., 2017b; Palmerio et al., 2018).

Studies of the spatial and temporal variations of interplanetary flux ropes and their heliospheric interactions are complicated by the lack of suitable multipoint observations. Investigations have mostly taken the form of case studies combining observations from planetary missions (e.g., MESSENGER and Venus Express) and missions located near Earth's orbit (e.g., STEREO and the spacecraft located at L1). For instance, Farrugia et al. (2011), Möstl et al. (2012), and Ruffenach et al. (2012) have all reported significant differences in flux rope properties, in particular in the orientation of flux ropes when the observing spacecraft were separated by a few tens of degrees in heliographic longitude. For weak ICMEs at solar minimum, clear differences have also been reported over longitudinal separations of only a few degrees (e.g., Kilpua et al., 2011). In a recent study, Good et al. (2019) investigated 18 interplanetary flux ropes that were observed by pairs of radially aligned spacecraft in the inner heliosphere (with typical longitudinal separations of $\sim 5^{\circ}$) using a technique that maps the magnetic field profile from one spacecraft to the other. Observations matched well at two locations for most cases, but in two cases the tilt of the flux rope differed by more than 20°. In addition, Lugaz et al. (2018) have recently reported clear differences in the magnetic field components of ICME flux ropes at observation points only ~ 0.01 AU apart. These studies imply that flux ropes embedded in CMEs may not be coherent structures on a global-scale, or that significant temporal evolution can occur over relatively short radial distances in the heliosphere (see also discussion in Owens et al., 2017). It should be noted, however, that results derived from flux rope reconstructions may depend strongly on the model used and on boundary time identification, as shown, for example, by Al-Haddad et al. (2013). Multiple CMEs may also interact and merge in interplanetary space, leading to the observation of "complex ejecta" (Burlaga et al., 2002) in which individual characteristics of the flux ropes may no longer be discernible, the preceding flux rope may be compressed (e.g., Liu et al., 2014; Mishra and Srivastava, 2014), or the multiple flux ropes have coalesced into one large structure that resembles a single, coherent flux rope (e.g., Odstrcil et al., 2003; Lugaz et al., 2013, 2017; Chi et al., 2018; Feng et al., 2019).

In this paper, we investigate the interactions, magnetic field structure, and coherence of the interplanetary counterparts of a series of CMEs that erupted from the Sun between June 12 and 14, 2012. The last of these CMEs (June 14 CME) was considerably faster and brighter than the previous two and had a clear Earth-directed component. Observations at Earth's Lagrange L1 point (at 1 AU) show a weak ejecta (June 12 CME) followed by a coherent and strong flux rope structure. This flux rope had the highest magnetic field magnitudes (about 40 nT) measured in the near-Earth solar wind during Solar Cycle 24. Our close inspection of observations reveals that this flux rope was likely composed of the June 13 and June 14 CMEs, which coalesced on their way from Venus to Earth. The Venus Express spacecraft orbiting Venus (at a heliocentric distance of 0.72 AU) also observed the weak June 12 CME, but the June 13 and June 14 CMEs were still separate entities, just on the verge of interaction. As shown in **Figure 1**, Earth and Venus were almost radially aligned during the passage of the CMEs; their longitudinal separation was 5.4° and their latitudinal separation was 0.2°. The solar and heliospheric characteristics of these CMEs, as well as some of their *in-situ* signatures (particularly those at Earth), have been investigated in several previous studies (e.g., Kubicka et al., 2016; James et al., 2017, 2018; Palmerio et al., 2017; Srivastava et al., 2018; Pomoell et al., 2019; Scolini et al., 2019; Wang et al., 2019). Here, we focus on comparing interplanetary observations at Venus and Earth. We also discuss how the CMEs are connected with their *in-situ* counterparts by performing a heliospheric CME propagation simulation and examining heliospheric imagery.

The paper is organized as follows: in section 2 we describe the data sets used in this study; in section 3 we present remote-sensing observations of the Sun, the solar corona, and the inner heliosphere, together with *in-situ* observations at Venus and Earth; this section also includes results from a global heliospheric simulation of the CMEs' propagation; in section 4 we present *in-situ* flux rope reconstructions; and in section 5 we discuss and summarize our results.

2. SPACECRAFT DATA

Remote-sensing solar disc data used in this study come from the Atmospheric Imaging Assembly (AIA; Lemen et al., 2012) and the Helioseismic and Magnetic Imager (HMI; Schou et al., 2012) instruments onboard the Solar Dynamics Observatory (SDO; Pesnell et al., 2012). AIA provides Extreme Ultra-Violet (EUV) data and HMI provides photospheric vector magnetograms. White-light observations of the solar corona are provided by the COR1 and COR2 coronagraphs, which are part of the Sun Earth Connection Coronal and Heliospheric Investigation (SECCHI; Howard et al., 2008) package onboard the Solar Terrestrial Relations Observatory (STEREO; Kaiser et al., 2008), and by the C2 and C3 coronagraphs of the Large Angle

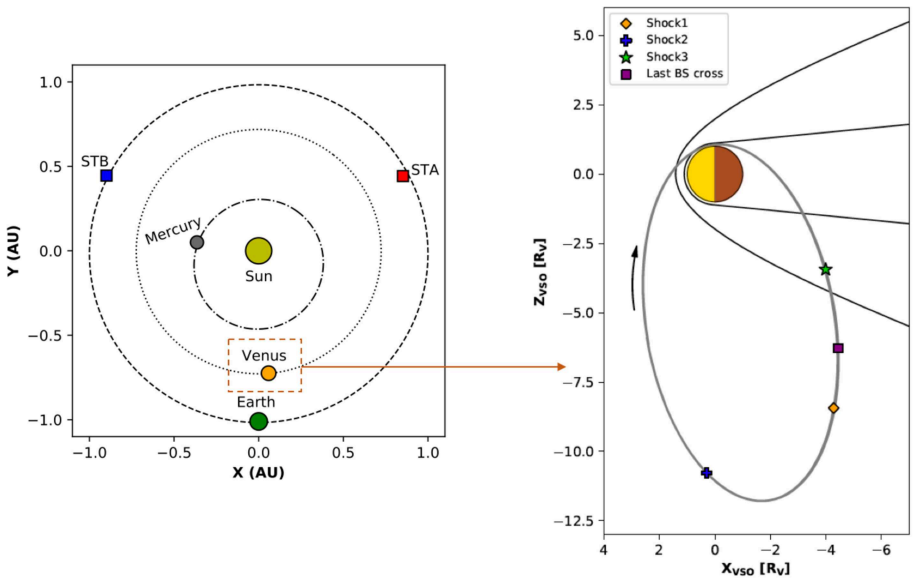

FIGURE 1 | Left: Position of the planets in the inner heliosphere in the ecliptic plane on June 14, 2012. The CME launched on June 14 subsequently arrived at Venus and Earth, which were almost radially aligned at this time. Venus Express (VEX) was orbiting Venus and the Wind and ACE spacecraft were located at the L1 point close to Earth. **Right**: The orbit of VEX (solid gray line, the orbital direction is indicated by the arrow) around Venus during the time when the June 14 CME reached Venus. The locations of the nominal bow shock (BS) and ion composition boundary (Martinecz et al., 2008) are indicated with black solid lines. Symbols along the orbit indicate the position of VEX during the passage of the interplanetary shocks and the last outbound BS crossing, when VEX entered from the magnetosheath into the solar wind.

Spectrometric Coronagraph (LASCO; Brueckner et al., 1995) instrument onboard the Solar and Heliospheric Observatory (SOHO; Domingo et al., 1995). The LASCO/C2 field of view extends from 1.5 to 6 solar radii (R_S) and the LASCO/C3 view from 3.7 to 30 R_S. Finally, observations of the inner heliosphere in white light were obtained from the Heliospheric Imager (HI; Eyles et al., 2009) cameras onboard STEREO.

The solar wind data around Venus were obtained from the Venus Express (VEX; Svedhem et al., 2007) spacecraft, which was orbiting Venus at the time of this study. We use magnetic field data from the Magnetometer (MAG; Zhang et al., 2006) instrument and plasma data from the Analyser of Space Plasmas and Energetic Atoms (ASPERA-4; Barabash et al., 2007) instrument. Data from ASPERA-4's Ion Mass Analyser (IMA) and Electron Spectrometer (ELS) sensors have been used. VEX had a 24 h orbit that was highly elliptical and quasi-polar (see **Figure 1**). It spent a few hours each day within the magnetosheath of Venus. ASPERA-4 was operational at periapsis and apoapsis only, while the magnetometer ran continuously.

Additional *in-situ* data were obtained from the Wind (Ogilvie and Desch, 1997) and Advanced Composition Explorer (ACE; Stone et al., 1998) spacecraft, which are continuously monitoring the solar wind ahead of Earth at L1. We use magnetic field data from the Magnetic Field Investigation (MFI; Lepping et al., 1995) instrument, plasma data from the Solar Wind Experiment (SWE; Ogilvie et al., 1995) instrument, ion moments, and electron pitch angle distributions from the Three-Dimensional Plasma and Energetic Particle Investigation (3DP; Lin et al., 1995) instrument, all onboard Wind, and ion charge state data from the Solar Wind Ion Composition Spectrometer (SWICS; Gloeckler et al., 1998) instrument onboard ACE.

3. SUN–TO–EARTH OBSERVATIONS AND CONNECTIONS

3.1. Solar Observations

A series of CMEs erupted from the Sun between June 12 and 14, 2012: (1) on June 12, 2012 at 17:24 UT (hereafter CME1), (2) on June 13, 2012 at 14:09 UT (hereafter CME2), and (3) on June 14, 2012 at 14:24 UT (hereafter CME3). These times correspond to their first appearance in the STEREO/SECCHI/COR2-A field of view. CME1 originated from two sympathetic eruptions (e.g., Török et al., 2011; Lynch and Edmondson, 2013) from an extended region of diffuse fields in the western hemisphere as seen from Earth. The two erupting structures can be clearly seen off-limb in STEREO/SECCHI/EUVI-A 195 Å data (not shown). CME2 and CME3 subsequently erupted from NOAA active region (AR) 11504 and were associated with solar flares M1.2, peaking on June 13 at 13:17 UT, and M1.9, peaking on June 14 at 14:35 UT, respectively. AR 11504 was located at S17E26 on June 12 and was at the central meridian of the Sun (S17W00) from Earth's viewpoint by June 14.

Given the complexity of CME1 at the Sun, the following analysis of the solar sources will concern CME2 and CME3 only. The remote-sensing analysis of the solar disc conducted by Palmerio et al. (2017) shows that the flux rope embedded in CME3 had a positive magnetic helicity (i.e., right-handed chirality) and a low inclination with respect to the ecliptic

plane. Its estimated flux rope type was North–East–South (NES), signifying that, at Earth, a flux rope would be observed where the field rotates from north at the leading edge to south at the trailing edge, while pointing eastwards at the center. **Figures 4**, **5** in Palmerio et al., 2017 present a complete analysis of the flux rope type of CME3 from solar observations. CME2, having erupted from the same source region as CME3, was expected to exhibit the same chirality and flux rope type as CME3. Indeed, the sheared coronal loops in AR 11504 before the eruption of CME2 display a clear forward-S shape, as was the case for CME3, and as expected for a right-handed source region (e.g., Green et al., 2007). Observations of the local polarity inversion line do not show significant changes in inclination between June 13 and June 14, indicating that the flux rope embedded in CME2 should also have had an NES type configuration upon eruption. **Figure 7** in Scolini et al., 2019 shows images of the pre- and post-eruptive configurations of AR 11504 for both CME2 and CME3.

Additionally, we estimate the poloidal magnetic flux gathered in the flux ropes during their eruption by analyzing the post-eruption arcades (PEAs; e.g., Tripathi et al., 2004), which are multi-loop structures visible in EUV. They are often used as indicators of the magnetic field that has been closed due to reconnection below the flux rope rising upwards in the corona. We apply the flux estimation technique developed by Gopalswamy et al. (2017), which is based on the derivation of the reconnected magnetic flux that lies under PEAs. For our analysis, we have used SDO/HMI vector magnetograms instead of the usual treatment based on line-of-sight (LOS) magnetograms. For each CME, we calculated the area of the PEAs in the SDO/AIA 131 Å and 193 Å channels and then considered their average for the total flux derivation, estimating the error bar to equal half of the range between the two values. The values that we obtain for the total unsigned flux are: $(4.60 \pm 0.54) \times 10^{21}$ Mx for CME2 (estimated on June 13, 14:30 UT) and $(6.04 \pm 0.56) \times 10^{21}$ Mx for CME3 (estimated on June 14, 17:00 UT). The estimate of the reconnected poloidal flux is equal to half these values. We compare the values to those derived by Kazachenko et al. (2017), who built a database of poloidal flux estimates using flare ribbons. Flare ribbons are structures also seen in EUV or X-rays that arise from flare-accelerated particles. The values based on flare ribbon analysis are: $(2.21 \pm 0.89) \times 10^{21}$ Mx for CME2 (derived from the related M1.2 flare on June 13, 11:29 UT) and $(3.88 \pm 1.2) \times 10^{21}$ Mx for CME3 (derived from the M1.9 flare on June 14, 12:52 UT). Our estimates based on PEAs are of the same order of magnitude, but about 1.6–2 times larger and not in agreement within the error bars. Such discrepancies between the flux values derived using the two methods for these same eruptions were also reported by Scolini et al. (2019), suggesting that they arise from the area under the PEAs being larger than the ribbon area by a factor of at least four. Indeed, differences between the two techniques are to be expected since PEAs span the local polarity inversion line (PIL) from both sides, whereas flare ribbons initially form at a certain distance from the PIL and then migrate further away. A more detailed comparison of the methods and their uncertainties is beyond the scope of this paper. We note that, when considering the order of magnitude comparison of (half of) the PEA and flare ribbon estimates to the poloidal fluxes F_ϕ from the *in-situ* analysis (see section 4.2), the PEA and flare ribbon flux estimates are broadly consistent. In fact, the results from both methods indicate that CME3 gathered more flux during its eruption than CME2, supporting the interpretation that CME3 was the most prominent of the CMEs investigated.

Next, we consider observations of the three CMEs in coronagraph imagery from three viewpoints (SOHO, STEREO-A, and STEREO-B). CME1 was clearly visible from the STEREO images as a structure propagating along the ecliptic, while in the LASCO field of view it appeared as a very faint halo that is only discernible in difference movies. The morphology of CME1 through the STEREO coronagraphs evolved from that of a double-fronted CME to that of a single, flattened CME, suggesting that the two sympathetic eruptions interacted at low altitudes. The resulting structure shall thus be considered as a single, merged CME in the rest of our analysis. CME2 appeared as a clear partial halo from all three viewpoints, although with its apex propagating around 30° south and only a small fraction of its body moving along the ecliptic. Finally, CME3 appeared as a full halo from all three viewpoints, and was significantly larger than the two preceding CMEs.

In order to quantify the geometrical and kinematic parameters of the CMEs under study in the outer corona (useful for the heliospheric simulation that will be presented in the following section), we have performed multi-spacecraft CME geometric reconstructions using the graduated cylindrical shell (GCS; Thernisien et al., 2006, 2009) model. An example of GCS reconstruction for CME3 using three viewpoints is shown in **Figure 2**. Since it is hard to identify CME1 from still images in the LASCO field of view, we have used the STEREO viewpoints only for its fitting. The Parameters needed to inject the three CMEs at the model's heliospheric inner boundary of 0.1 AU ($21.5\,R_\odot$) are injection time, latitude, longitude, half-angle, and speed. We obtain the geometric parameters for each CME from reconstructions performed at the last observation time available from the three viewpoints simultaneously, i.e., as close as possible to the simulation's inner boundary. Here, the CME half-angle is the face-on half-angular width, defined as $\omega/2 = \gamma + \psi$, where γ is the angle between the leg axis and the propagation axis and ψ is the edge-on half-angular width (Thernisien, 2011). The CME injection speeds are obtained from the difference in apex height between the latest observations and observations made 30 minutes earlier. Finally, the CME injection times are obtained by propagating the CME apexes from the last observations up to $21.5\,R_\odot$, assuming constant speeds. The resulting parameters are given in **Table 1** for the three CMEs.

3.2. Heliospheric Observations and Modeling

We now consider the arrival of the CMEs at Venus and Earth using 3D heliospheric modeling and heliospheric imaging. In order to estimate the global propagation of the three CMEs in the heliospheric context, we perform a 3D simulation using the EUropean Heliospheric FOrecasting Information Asset (EUHFORIA; Pomoell and Poedts, 2018) model. EUHFORIA

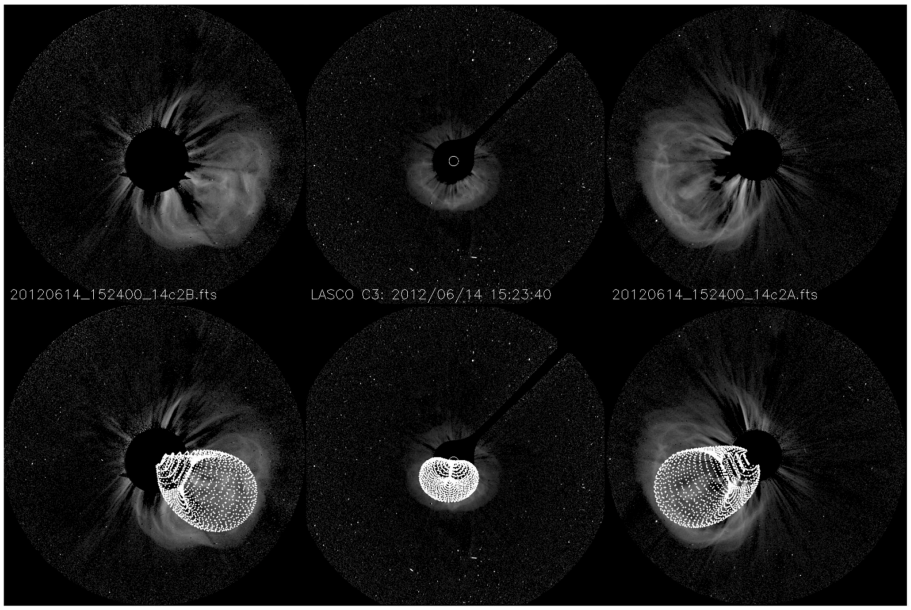

FIGURE 2 | Example of GCS fitting of CME3 using images at 15:24 UT from STEREO/SECCHI/COR2-B **(Left)**, SOHO/LASCO/C3 **(Middle)**, and STEREO/SECCHI/COR2-A **(Right)**.

TABLE 1 | Parameters obtained from GCS reconstructions of each CME in the outer corona and used as input to the EUHFORIA cone model described in section 3.2.

CME	Time at 0.1 AU [UT]	Θ [°]	Φ [°]	$\omega/2$ [°]	V [km/s]
CME1	6/13 00:35	0.0	–5.0	27.5	521.8
CME2	6/13 19:54	–35.0	–10.0	38.6	657.0
CME3	6/14 17:18	–28.0	–5.0	57.0	966.3

Columns show, from left to right: insertion time at the EUHFORIA inner boundary (at 0.1 AU or 21.5 $R_\odot$), latitude (Θ) and longitude (Φ) of the CME apex in Stonyhurst coordinates (Thompson, 2006), half-angle ($\omega/2$), and speed (V). The values used for mass density (ρ_m) and temperature (T) are $\rho_m = 10^{-18}$ kg/m^3 and $T = 8 \times 10^5$ K for all CMEs.

consists of a semi-empirical Wang–Sheeley–Arge (WSA; Arge et al., 2004) coronal model and a 3D time-dependent magnetohydrodynamic (MHD) heliospheric model. It allows propagation of CMEs through a steady background solar wind in the inner heliosphere from 0.1 AU onwards. We here use EUHFORIA with a cone CME model (e.g., Scolini et al., 2018) that treats CMEs as dense spheres with no internal magnetic field structure, using the input parameters presented in **Table 1**. The EUHFORIA simulation run for the three CMEs is shown in **Supplementary Video 1**. A snapshot from the simulation around the time of arrival at Earth of CME3 is shown in **Figure 3**. All three CMEs are seen to propagate close to the Sun–Earth line, with some differences in their latitudes. The apex of the relatively small CME1 propagates close to the ecliptic, while the propagation direction of CME2 is significantly toward the south (as expected from the latitude of −35.0° reported in **Table 1**). CME3 is clearly the widest and most prominent eruption in the simulation, with its apex propagating southward. However, this CME is wide enough to result in a significant component propagating along the ecliptic. The EUHFORIA simulation indicates that the three CMEs arrived at Venus in close proximity but still as mostly separated structures, while CME3 has reached the front of CME2 by the time the structures impact Earth. Finally, the merged CME2 and CME3 are seen to overtake CME1 after Earth's orbit. The arrival times of the three CMEs at Venus and Earth estimated by the EUHFORIA simulation are reported in **Table 2**.

We also follow the CMEs in heliospheric imagery. **Supplementary Video 2** includes a movie of HI1-A and -B data that shows the CMEs' propagation. The HI1 observations show, in agreement with coronagraph observations and heliospheric modeling results, that CME1 was fairly narrow and propagating along the ecliptic, that CME2 propagated mostly toward the south but with a non-zero component along the ecliptic, and that CME3 was the largest of the three, expanding in latitude well beyond the HI1 field of view. HI2 observations (not shown) suggest that CME3 subsumed CME2 between the orbits of Venus and Earth.

The HELCATS (http://www.helcats-fp7.eu) project has cataloged a number of CMEs from 2007 through 2015 using the wide-angle HIs onboard STEREO. The ARRCAT catalog (Möstl et al., 2017) produced by HELCATS gives arrival times of CMEs at various locations in the solar system that are estimated with a self-similar expansion fitting of HI data with a fixed 30° CME angular half-width (SSEF30; Davies et al., 2012). According to the ARRCAT catalog (see also the discussion in Kubicka et al., 2016), CME1 made a glancing encounter with Venus and Earth, CME2 did not encounter either of these locations, and CME3 impacted Earth almost centrally. The arrival times of

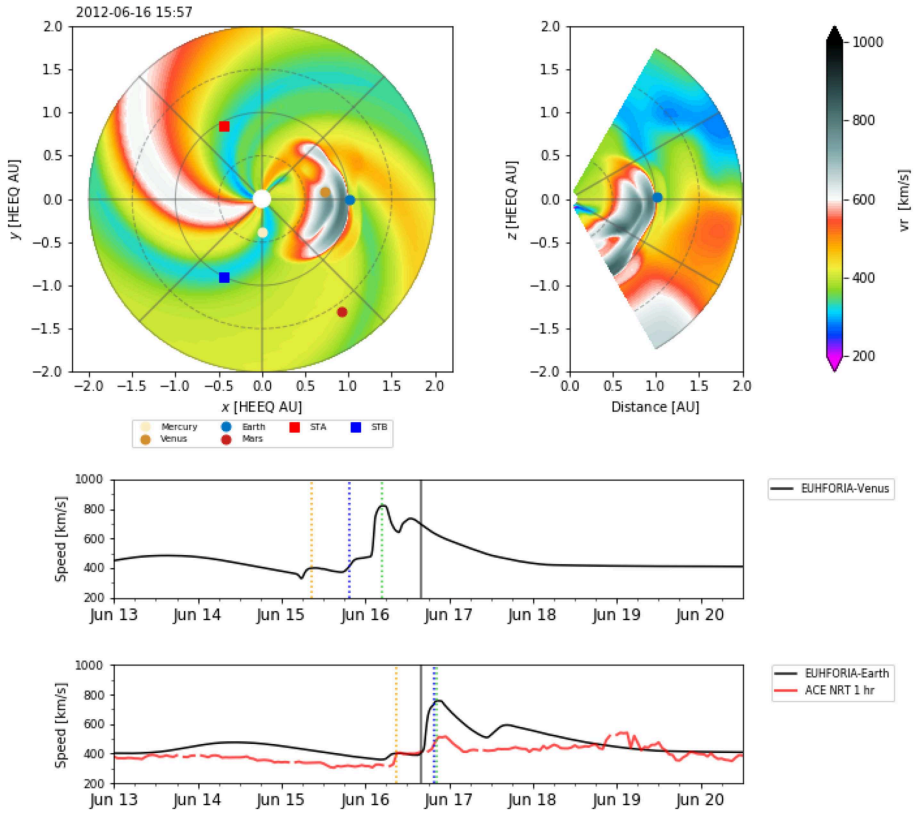

FIGURE 3 | Snapshot of the solar wind speed simulated with EUHFORIA, showing the arrival at Earth of CME3 around June 16, 2012 at 16:00 UT. The heliographic equatorial plane **(Left)** and the meridional plane containing Earth **(Right)** are shown, together with the time series at Venus and Earth **(Bottom)**. The arrival times of the CME-driven shocks taken from *in-situ* data for both locations (analyzed in section 3.3) are indicated in the time series with vertical dashed lines (CME1, orange; CME2, blue; CME3, green).

TABLE 2 | Arrival times of the three CMEs at Venus and Earth based on EUHFORIA results and HELCATS/ARRCAT STEREO/SECCHI/HI-A and -B reconstructions.

Target	**VENUS**			**EARTH**		
CME #	**CME1**	**CME2**	**CME3**	**CME1**	**CME2**	**CME3**
EUHFORIA	6/15 08:00	6/15 18:00	6/16 02:00	6/16 06:00	6/16 18:00	6/16 18:00
ARRCAT–STA	6/15 15:12	–	6/15 22:46	6/16 22:17	–	6/16 13:45
ARRCAT–STB	6/15 14:58	–	6/16 08:25	6/16 13:58	–	6/16 16:57

the three CMEs estimated in the ARRCAT catalog are listed in **Table 2**.

Our simulation results are thus consistent with the information reported in the HELCATS/ARRCAT catalog for the impact of CME1 and CME3 (albeit with significant differences in arrival time) while for CME2 an *in-situ* impact is forecasted by EUHFORIA only. We note that, in the case of CME2, the apex was propagating at a latitude of −35° (from the GCS reconstruction reported in **Table 1**); thus, the fixed CME half-width of 30° assumed in SSEF30 reconstructions may explain why an arrival 'hit' is not predicted. Now considering CME1 and CME3, the discrepancies in arrival times between our EUHFORIA simulation and the ARRCAT results may arise from both the fixed half-angular width and from the circular CME front assumed in the SSEF30 model. In the EUHFORIA model, CMEs are also launched with an initial spherical cross-section, but their fronts flatten with heliocentric distance as a result of solar wind drag (e.g., Vršnak et al., 2013). Furthermore, we note that Srivastava et al. (2018) analyzed time–elongation maps based on HI data and reconstructed the fronts of CME2 and CME3 by applying the two-spacecraft version of the SSE model, i.e., the stereoscopic SSE (SSSE; Davies et al., 2013) fitting, concluding that the two CMEs would have interacted significantly before the orbit of Venus already, at a heliocentric distance of $\sim$ 100 $R_{\odot}$ (i.e., $\sim$ 0.47 AU). We propose a later interaction of the two CMEs (at $\sim$ 0.72 AU), as supported by the EUHFORIA simulation,

heliospheric imagery, and consideration of the eruption times of CME2 and CME3 and their relative speeds. We attribute these discrepancies to the circular CME front assumed in the SSSE model and to the fact that Srivastava et al. (2018) used a CME half-width of 90° for both CME2 and CME3, while we estimated values of 38.6° and 57.0°, respectively (see **Table 1**). Given that CME3 was traveling faster than CME2, both of these factors would yield an earlier CME arrival (and, therefore, interaction) than was found in our EUHFORIA simulation. We further note that our EUHFORIA cone model results are consistent with the EUHFORIA simulation performed by Scolini et al. (2019) using a cone model for CME2 and a spheromak (Verbeke et al., 2019) model for CME3.

3.3. Interplanetary Observations

We now describe the *in-situ* observations from VEX at Venus and the L1 spacecraft (ACE and Wind) in the near-Earth solar wind. **Table 3** lists the observation times of various significant features that we discuss in detail below, including some key shock and ICME ejecta parameters.

3.3.1. Observations at Venus

Figure 4 shows magnetic field measurements, plasma parameters, and proton and electron counts (where available) measured by VEX. The magnetic field components are given in Venus Solar Orbital (VSO) coordinates.

We interpret the increase in the magnetic field magnitude at 08:30 UT on June 15, 2012 as the shock driven by CME1 (hereafter S1). The observation time of S1 matches exactly with the arrival time of CME1 at Venus as predicted by EUHFORIA and is 6–7 h before the estimated CME1 arrival times reported in the ARRCAT catalog (see **Table 2**). The subsequent period with fluctuating magnetic fields represents the sheath region behind S1. On June 15, 2012 at 19:29 UT VEX entered into a flux rope (hereafter FR2) as indicated by smooth and enhanced magnetic field and the start of a steady rotation. A zoom-in around this transition region (see **Supplementary Figure 1**) reveals first a small field decrease on June 15 at 19:09 UT followed by a field increase at 19:22 UT. The field decrease could possibly mark the end of the ejecta related to the weak CME1 (hereafter E1, which cannot be identified robustly due to the lack of consistent plasma data at VEX), while the increase likely represents a developing shock wave (hereafter S2) driven by CME2. We also note that the magnetic field between 19:09 and 19:22 UT resembles that of the ambient solar wind, with a Parker spiral-like (Parker, 1958) configuration.

The FR2 leading edge time coincides almost exactly with the EUHFORIA prediction of the CME2 arrival at Venus (see **Table 2**) and this interpretation is also in agreement with observations at Earth's L1 point (see section 3.3.2). The two top panels of **Figure 4** show that FR2 was characterized by an enhanced and smooth magnetic field and that the field components rotated in a coherent way. The Y-component of the magnetic field (B_Y) in FR2 at VEX rotated from negative to positive, while the Z-component of the field (B_Z) stayed positive (i.e., northward). CME2 likely continued several hours past the FR2 trailing boundary at VEX, i.e., coherent rotation of the magnetic field direction had ceased, but the field magnitude remained enhanced. As discussed by Richardson and Cane (2010) and Kilpua et al. (2013), cases where ICME signatures continue beyond the flux rope boundaries are not uncommon and could arise, e.g., from interaction with the ambient solar wind and/or erosion of the magnetic flux (e.g., Dasso et al., 2007), or represent a CME wake. VEX entered the Venusian induced magnetosphere on June 16 at 02:24 UT. The approximately 2 h interval when VEX was in the magnetosphere, until June 16 UT at 04:16 UT, has been cut out from **Figure 4**. The average magnetic field magnitude at the FR2 leading edge (over the first 30 min) at VEX was 35.4 nT and during the last 30 min of FR2 the field has decreased to 26.7 nT.

Approximately 1 h after VEX had traveled from the magnetosphere to the magnetosheath, the magnetic field magnitude increased abruptly on June 16 at 04:52 UT. Since outbound bow shock (BS) transitions exhibit decreases of the field magnitude rather than increases, we interpret this field jump as the interplanetary shock driven by CME3 (hereafter S3),

TABLE 3 | Observation times of interplanetary shocks (S), ejecta (E) and flux ropes (FR) around Venus (in VEX data) and Earth (in Wind data).

Shocks	**S1**	**S2**	**S3**	
VENUS				
Time [UT]	6/15 0830	6/15 1922	6/16 0452	
EARTH				
Time [UT]	6/16 0858	6/16 1931	6/16 2032	
ΔV [km/s]	44	49	104	
B_u/B_d	1.58	1.87	2.91	
n_u/n_d	1.36	1.74	2.50	
M_{ms}	1.7	1.6	2.6	
V_{sh} [km/s]	451	486	608	
θ_{Bn} [°]	15	60	75	
Ejecta	**E1**	**FR2**	**FR3**	**ES**
VENUS				
Time [UT]	6/15 1305–1909	6/15 1926–2200	6/16 0518–0828	–
ΔT [h]	6.1	3.6	3.2	–
$\langle B_{LE} \rangle$ [nT]	9.4 ± 2.1	35.4 ± 0.5	52.4 ± 2.5	–
$\langle B_{TE} \rangle$ [nT]	16.8 ± 1.7	26.7 ± 1.0	42.9 ± 2.9	–
EARTH				
Time [UT]	6/16 1345–1931	6/16 2215–2340	6/17 0100–1130	6/17 0346–0432
ΔT [h]	5.8	1.5	10.5	0.76
$\langle B_{LE} \rangle$ [nT]	9.9 ± 0.8	38.9 ± 0.9	39.5 ± 0.4	–
$\langle B_{TE} \rangle$ [nT]	8.2 ± 0.2	38.4 ± 1.7	17.8 ± 1.5	–

The column headed "ES" gives the time interval of the embedded substructure observed at Earth's L1 point near the midpoint of the FR3 time series. Shock parameters that are listed include: speed gradient across the shock (ΔV), upstream–to–downstream magnetic field (B_u/B_d) and density ratio (n_u/n_d), magnetosonic Mach number (M_{ms}), shock speed (V_{sh}), and shock angle (θ_{Bn}). Shock parameters are obtained from the Heliospheric Shock Database (http://ipshocks.fi; see also Kilpua et al., 2015). ΔT gives the ejecta, flux rope and substructure durations. $\langle B_{LE} \rangle$ and $\langle B_{TE} \rangle$ give the 30-min average leading and trailing edge magnetic field magnitude for the ejecta and flux ropes. The leading edge field for FR3 at VEX is calculated for the 30-min interval immediately after the spacecraft exited the Venusian magnetosheath and entered the solar wind.

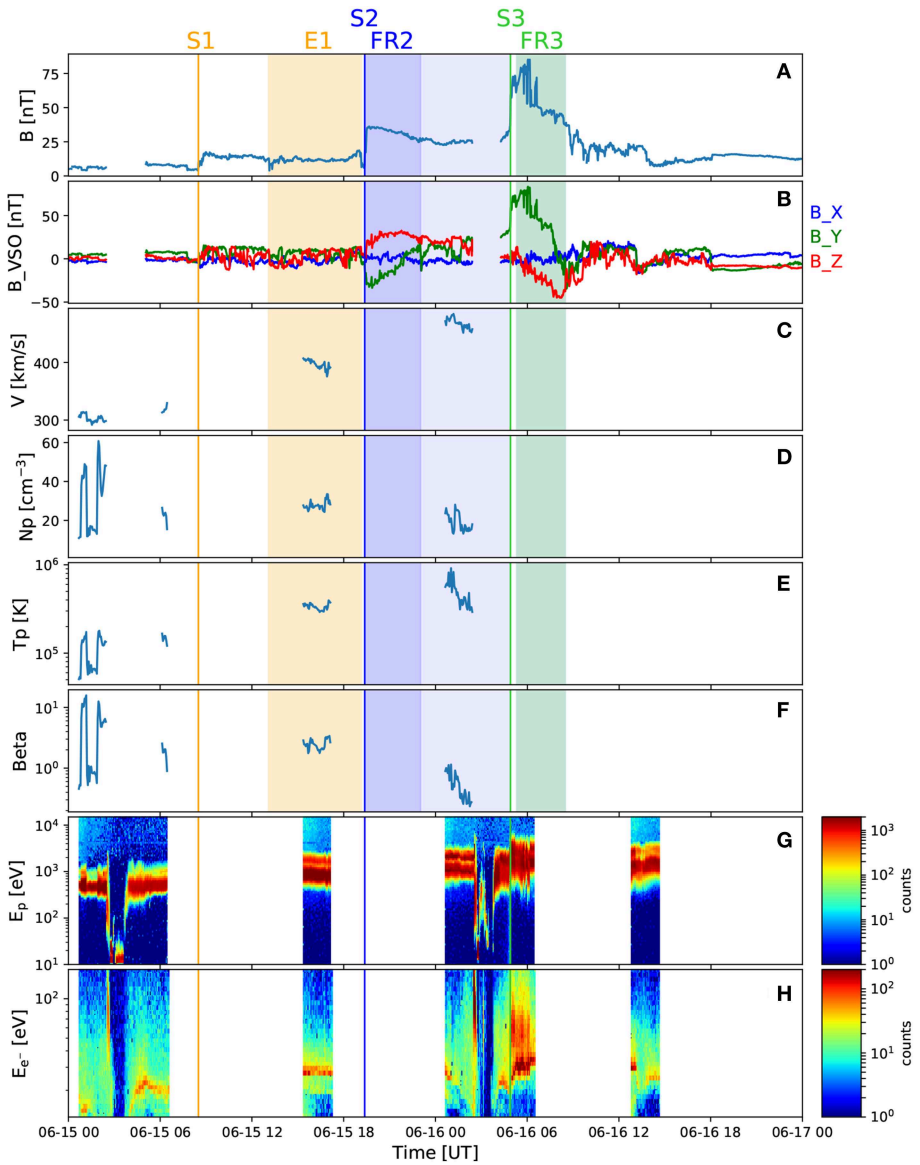

FIGURE 4 | *In-situ* measurements taken by VEX around Venus. The panels show, from top to bottom: **(A)** magnetic field magnitude, **(B)** magnetic field components in VSO coordinates (blue: B_X, green: B_Y, red: B_Z), solar wind **(C)** speed, **(D)** density, **(E)** temperature, and **(F)** plasma beta, and counts for **(G)** protons and **(H)** electrons. The CME-driven shocks (S1, S2, and S3) are marked by vertical lines, while the ejecta and flux ropes (E1, FR2, and FR3) are highlighted with shaded regions. Intervals in the Venusian magnetosphere have been cut out from the magnetic field and plasma data. ASPERA-4, providing electron and proton counts (and from which plasma data are derived), was operational at periapsis and apoapsis only.

similarly to the interpretation given by Kubicka et al. (2016). The detection time of S3 at VEX is also only 2 h later than the arrival time of CME3 predicted by EUHFORIA. The high magnetic fields after S3 represent the sheath driven by CME3 and the following flux rope (hereafter FR3) being compressed in the Venusian magnetosheath. The sharp field variations at the leading edge of FR3 are BS crossings. **Supplementary Figure 2** shows a zoom-in of the VEX magnetic field data around this time. The first outbound BS crossing occurred on June 16 at 05:46 UT and the last outbound crossing at 06:37 UT. The BS crossings were partly beyond the nominal Venusian BS location (see **Figure 1**). We note that Zhang et al. (2008) showed that during a strong CME that impacted Venus on September 10–11, 2006 VEX observed clear BS crossings all along its trajectory even out to 12 Venusian radii. After the last outbound BS crossing, the magnetic field within FR3 is 52 nT and the field decreases to 42.9 nT by the trailing edge of FR3. We define the end boundary of FR3 where the smooth rotation ended and the magnetic field magnitude decreased. At the leading edge of FR3, B_Y was strongly positive and then rotated toward zero by the trailing

edge. B_Z started from small positive values and rotated to large negative values.

3.3.2. Observations Near Earth and Comparison With Venus

Figure 5 shows observations at Earth's Lagrange L1 point; **Figures 5A–C** show interplanetary magnetic field (IMF) observations; the IMF magnitude, IMF components in the GSE coordinate system, and the root-mean-square of the magnetic field vector. **Figures 5D–G** give the solar wind plasma speed, density, temperature, and plasma beta. **Figure 5F** also displays the expected solar wind temperature calculated using three different approaches. The red curve is the expected temperature according to Cane and Richardson (1995) based on the solar wind–temperature relationship derived by Lopez and Freeman (1986), and which has different dependencies for slow and fast wind (break-point at 500 km/s). The light and dark orange curves are from Elliott et al. (2005) who derived a formula separately for solar wind compressions and rarefactions (based on the slopes in the 2 day averaged solar wind speed), respectively, by using a 5 year dataset from ACE and removing all ICME intervals. The solar wind oxygen charge ratio O^{+7}/O^{+6} and average iron charge ratio $\langle Q_{Fe} \rangle$ (2 h cadence) are shown in **Figures 5H,I**, while the bottom **Figure 5J** shows the suprathermal electron 255 eV pitch angle spectrogram. Counterstreaming suprathermal electrons at 0° and 180° pitch angles are generally interpreted as a signature of closed magnetic field configurations where the field lines are connected to the Sun at both ends, while a unidirectional strahl indicates field lines that are open to the heliosphere (e.g., Zwickl et al., 1983; Gosling et al., 1987; Shodhan et al., 2000).

The comparison of **Figures 4**, **5** shows some obvious similarities as well as several differences between the structures detected at Venus and at Earth. Similarly to Venus, the sequence of events at Earth began with shock S1 that was detected on June 16 at 08:58 UT by Wind. This shock time is only 3 h later than the predicted CME1 arrival time at Earth by EUHFORIA, and 5 and 12 h earlier than reported in the HELCATS/ARRCAT catalog for STEREO-A and -B, respectively (see **Table 2**). The plasma data reveal lower temperatures than during the first 4–5 h after the shock and counterstreaming suprathermal electrons starting around June 16, 13:45 UT and continuing until a shock was observed at 19:31 UT on June 16. This interval, shaded in orange in **Figure 5**, likely represents the ejecta related to the weak CME1, i.e., E1. Contrarily to Venus, where CME1 was followed by two separate flux ropes and from which only the latter one drove a well-developed shock, at Earth two close-by shocks were observed followed by one apparently coherent flux rope structure. The first of these shocks (S2) was observed at 19:31 UT and the other shock (S3) only about an hour later at 20:32 UT. **Table 3** shows that of the three shocks detected at L1, S3 was clearly the strongest, being associated with the largest speed jump and shock speed, and the largest upstream–to–downstream magnetic field magnitude and density ratios, and magnetosonic Mach number. It was also the most perpendicular shock, with the shock angle θ_{Bn} being 75°.

The flux rope following S3 featured several classic ICME flux rope signatures (e.g., Zwickl et al., 1983; Richardson and Cane, 2004; Zurbuchen and Richardson, 2006; Kilpua et al., 2017a): enhanced magnetic field magnitude, a coherent rotation of the magnetic field components, some decrease in the field variability, low plasma beta, and enhanced oxygen charge ratio O^{+7}/O^{+6} and average iron charge ratio $\langle Q_{Fe} \rangle$. The measured temperatures were generally high throughout the flux rope structure, being momentarily below only the Elliott et al. (2005) expected temperature curve for compressions. **Figure 5J** shows intervals of counterstreaming suprathermal electrons toward the end of the event.

Our interpretation is that shock S2 at 19:31 UT was driven by CME2 and the closely following shock S3 was driven by CME3, and thus that S3 had propagated through CME2 during the transit from Venus to Earth. In our EUHFORIA simulation run, the arrival of CME2 and CME3 cannot be separated, but their joint arrival time on June 16 at 18 UT corresponds well with the observed shock times. The arrival time of S3 at Wind is also only about 4 h later than CME3 arrival time reported in the ARRCAT catalog for STEREO-B, while the difference is a few hours larger for STEREO-A.

As discussed above, observations following S3 near Earth feature a coherent flux rope and this interval has indeed been interpreted as a single flux rope in previous studies (e.g., Kubicka et al., 2016; Palmerio et al., 2017; Srivastava et al., 2018; Good et al., 2019) and in online ICME catalogs. We suggest, in contrast, that the flux rope structure at L1 consists of two coalesced flux ropes related to CME2 and CME3, i.e., that these CMEs, which at VEX were just about to start interacting, had coalesced into one coherent structure by the time they had reached Earth's orbit. This interpretation is also supported by our EUHFORIA simulation run showing that the fast and prominent CME3 starts overtaking the slower CME2 approximately around the orbit of Venus and then engulfs it (see section 3.2 and **Supplementary Video 1**). We also note that there were no other possible significant CMEs that could have arrived to Venus or Earth during this period.

We have marked the possible intervals featuring the flux ropes related to CME2 and CME3 at Earth's L1 point in **Figure 5** with blue- and green-shaded regions and labeled them FR2 and FR3, respectively. The lighter blue region after FR2 likely represents the part of CME2 that did not contain flux rope signatures, as discussed previously (see section 3.3.1 and **Figure 4**). FR2 was thus compressed from 3.6 h at VEX to 1.5 h at Earth's L1 point and its magnetic field magnitude was higher by a few nanoteslas (see **Table 3**). FR3, in turn, has expanded from 3.2 h at VEX to 10.5 h at Earth's L1 point. Note that the FR3 duration around Venus is underestimated because its front part was compressed in the Venusian magnetosheath. From Venus to Earth, the leading edge field of FR3 had slightly decreased, but the trailing edge field was considerably lower, falling from 42.9 nT to 17.8 nT.

The interface between FR2 and FR3 has been selected to coincide with the end of the high density region and negative–to–positive signature in B_Y. The front part of FR2 also features enhanced temperatures and solar wind speed. However, we note that this interface time is not unambiguous. In order to test our interface identifications, we have applied the mapping technique described by Good et al. (2018) in **Figure 6** for the

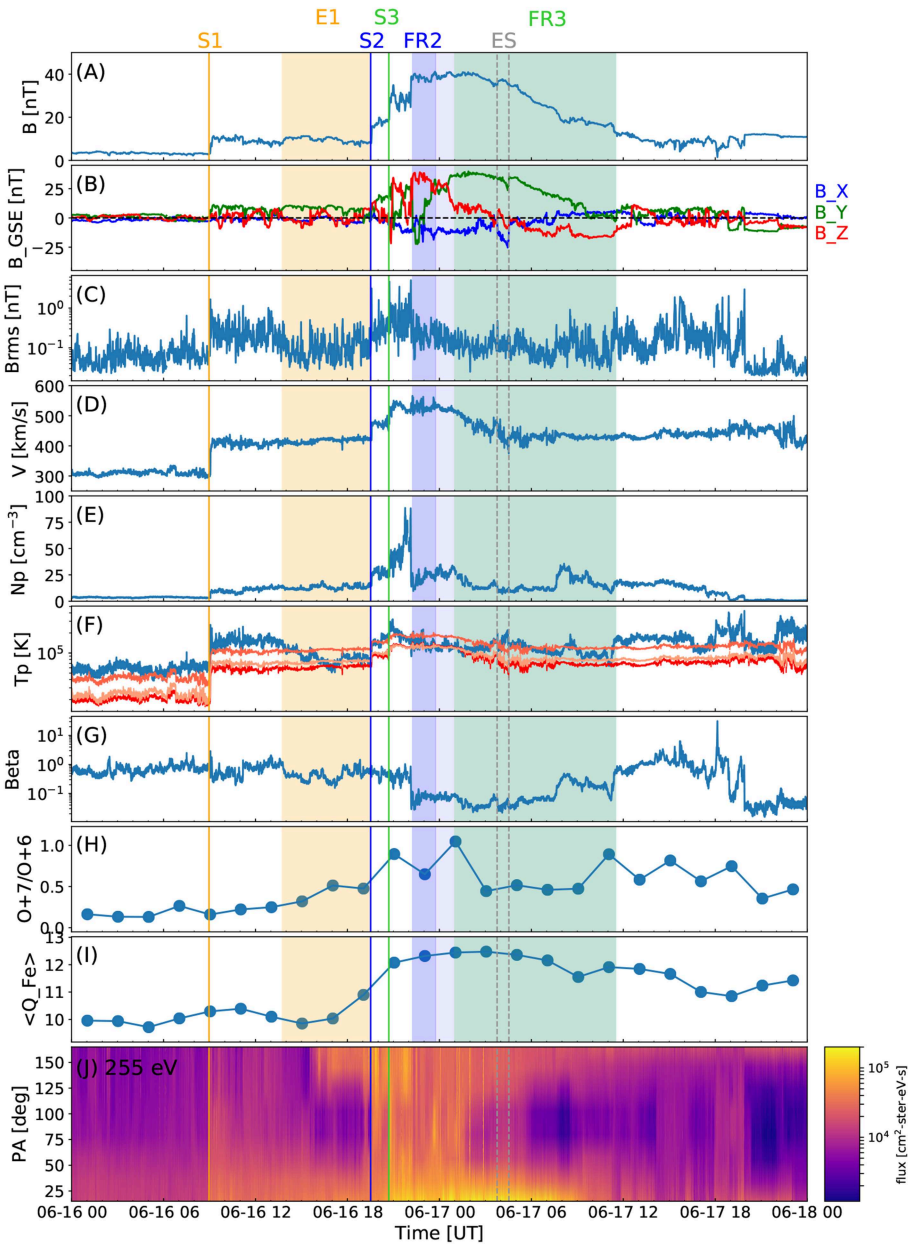

FIGURE 5 | *In-situ* measurements taken at Earth's L1 point. The panels show, from top to bottom: **(A)** magnetic field magnitude, **(B)** magnetic field components in GSE coordinates (blue: B_X, green: B_Y, red: B_Z), **(C)** root-mean-square magnetic field vector (B_{rms}), and solar wind **(D)** speed, **(E)** density, **(F)** temperature (the blue curve is the measured temperature and the red/orange curves indicate the expected temperatures. The red line is from Cane and Richardson (1995), light and dark orange from Elliott et al. (2005) for the rarefactions and compression, respectively; see section 3.3.2 for details), **(G)** plasma beta, **(H)** oxygen charge state ratio, **(I)** average iron charge state, and **(J)** pitch angle spectrogram of suprathermal 255 eV electrons. The 1 m IMF and 3 s solar wind plasma data are from the Wind spacecraft, while the 2 h charge state data are from the ACE spacecraft. Red solid lines show the interplanetary shocks (S1, S2, and S3). Flux rope intervals are indicated by the dark blue and green shaded regions for FR2 and FR3, respectively; though still associated with the CME2 ejecta, the pale blue shaded region is identified as not being part of FR2. The embedded substructure (ES) is bounded by a pair of dashed gray lines.

FR2 and FR3 intervals separately. In outline, the technique maps the magnetic field time series of a flux rope at an inner spacecraft (VEX in the present case) to the radial distance of an outer, aligned spacecraft (Wind) located further away from the Sun. The leading and trailing edges of the mapped profiles are constrained to overlap with the corresponding edges observed at the outer spacecraft, and the field vectors through the flux rope are mapped with a mean linear speed profile derived from the mean propagation speeds of the rope edges. The field vectors of the outer and mapped inner spacecraft profiles are normalized to

the field magnitude to emphasize similarities (or dissimilarities) in the underlying flux rope structure. **Figure 6** shows significant similarities in the flux rope field components and direction angles for FR3, with a more approximate similarity seen in FR2. These mappings give some support for the interface locations identified. We also note that with this interface selection, FR3 features some higher speed and fields at its leading edge. In the end part of FR3 the speed profile is almost steady, signifying the FR3 has relaxed considerably and adjusted to the speed of the trailing solar wind.

The end boundary of FR3 is selected at the point where the plasma beta increased and the most coherent field rotation ended. This boundary coincided with the end of the flux rope included in the Wind ICME list (https://wind.nasa.gov/ICMEindex.php, Nieves-Chinchilla et al., 2018). Again, some ICME-related signatures continued for a few hours after the marked end time; for example, the field magnitude profile was relatively smooth, and O^{+7}/O^{+6} and $\langle Q_{Fe} \rangle$ remained elevated.

We identify a small and distinct substructure within FR3 on June 17 between 03:46 UT and 04:32 UT. This substructure is marked as "ES" in **Figure 5** and its boundaries are indicated by a pair of dashed vertical lines. **Figure 7** shows a zoomed-in view of the substructure, highlighting that it was bounded by a pair of sharp field changes that suggest the presence of current sheets. The magnetic field components are shown here in the minimum variance analysis (MVA, see section 4.1) coordinate system, where the maximum variance component is marked in pink, the intermediate variance component in lime and the minimum variance component in light blue. The MVA has been performed over the substructure interval. Compared to its surroundings, the substructure features a slight enhancement in the magnetic field magnitude and temperature, but lower density and plasma beta. The solar wind speed shows a declining trend throughout the substructure. The intermediate and minimum variance components are relatively steady over the substructure, while the maximum variance component rotates from slightly negative to positive values. Hence, this substructure does not show signatures of a magnetic reconnection exhaust (e.g., Gosling et al., 2005), i.e., a decreased magnetic field magnitude coinciding with enhanced densities and temperatures, and the maximum variance component showing a large change in the field orientation. We also note that the substructure here occurred concurrently with the B_Z component changing sign within FR3. It could thus be similar to substructures studied, e.g., by Dasso et al. (2007) and Steed et al. (2011). They occurred near the centers of CME flux ropes and were interpreted to arise from interaction with the ambient solar wind causing warping of the flux surfaces as, at this point, the spacecraft path is almost tangential to the magnetic flux surfaces of the flux rope.

4. ANALYSIS OF THE *IN-SITU* FLUX ROPES

4.1. Reconstruction Techniques

Minimum variance analysis (MVA), Lundquist fitting (LQF), and Gold-Hoyle fitting (GHF) have been used to determine the orientation of the flux ropes at Venus and Earth. These relatively simple *in-situ* reconstruction techniques allow global parameters of a flux rope to be estimated from local observations made along the spacecraft trajectory.

MVA involves determining the eigenvalues and eigenvectors of the covariance matrix of the magnetic field vector components (Sonnerup and Cahill, 1967). The eigenvector associated with the eigenvalue of intermediate variance ideally corresponds to the flux rope axis direction (Goldstein, 1983). MVA accuracy is greater when the spacecraft intersects the flux rope near its central axis (i.e., a low impact parameter encounter; Gulisano et al., 2007) and when the variance directions are well defined. This latter condition may be assessed through the ratio of the maximum and intermediate eigenvalues, λ_1/λ_2, and the minimum and intermediate eigenvalues, λ_3/λ_2. Ratios of $\lambda_1/\lambda_2 > 1.37$ and $\lambda_3/\lambda_2 < 0.72$ are typically applied as thresholds for well-defined variance directions (Siscoe and Suey, 1972). We note that a recent study by Démoulin et al. (2018) questions the validity of eigenvalue ratios as a measure of MVA accuracy when determining flux rope axis directions.

LQF uses Bessel functions to model the flux rope field structure (Burlaga, 1988; Lepping et al., 1990). The simplest form of LQF models the flux rope as an axisymmetric cylinder with a circular cross section, in which the component of the magnetic field along the cylinder axis, B_z, and the poloidal component, B_ϕ, are given by:

$$B_z^L = B_0 J_0(\alpha r) \tag{1}$$

$$B_\phi^L = H B_0 J_1(\alpha r), \tag{2}$$

respectively, where B_0 is the field strength at the rope axis, J_0 and J_1 are the zeroth- and first-order Bessel functions, respectively, H is the rope handedness (+1 or –1 for a right- or left-handed rope, respectively), r is the radial distance from the axis, and α is a constant. The field component in the radial direction is zero. Following a common convention, we locate the flux rope boundaries at the first zero of J_0; thus the field at the boundaries has no axial component and is purely poloidal.

In GHF (Gold and Hoyle, 1960), the flux rope field components are given by:

$$B_z^G = \frac{B_0}{1 + \tau^2 r^2} \tag{3}$$

$$B_\phi^G = \frac{\tau r B_0}{1 + \tau^2 r^2}, \tag{4}$$

where the twist, τ, gives the number of complete field–line turns per AU. The Gold–Hoyle solutions were first used to fit an interplanetary flux rope by Farrugia et al. (1999). In contrast to the Lundquist rope, in which twist is at a minimum at the axis and infinite at the boundaries, the τ profile across the Gold–Hoyle rope is uniform. As in LQF, the simplest form of GHF assumes a cylindrically symmetric rope geometry with a circular cross section. We locate the rope boundaries at a distance of $1/\tau$ from the rope axis, following the convention of Hood and Priest (e.g., Hood and Priest, 1979).

LQF and GHF are performed with a three-stage, reduced χ^2 minimization of the model field components to the observed,

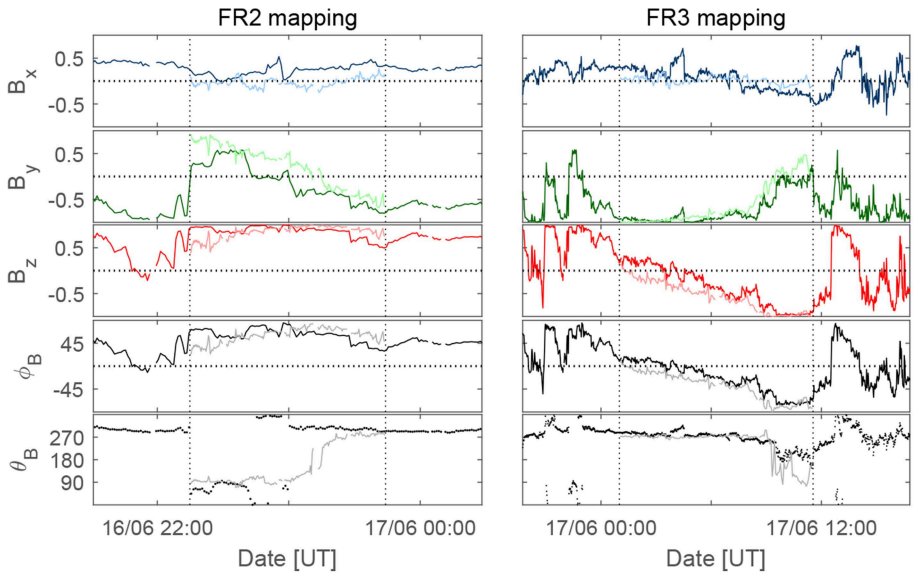

FIGURE 6 | Mapping of the magnetic field data between VEX (pale-colored lines) and Wind (dark-colored lines) for FR2 **(Left)** and FR3 **(Right)**. Details of the technique are given by Good et al. (2018). The panels show the normalized field components in the SCEQ coordinate system and the field latitude and longitude angles. Vertical dashed lines denote the flux rope boundaries.

normalized magnetic field time series. This minimization technique has previously been applied by Good et al. (2019). The flux rope orientation previously obtained from MVA is used as the rope's initial estimate as input for the first minimization of χ^2, which yields fitting F1. The minimization is then repeated with F1 as the initial orientation to give fitting F2, and repeated again with F2 as the initial orientation to give fitting F3. F2 is taken as the final reported fit, and the angle between the F2 and F3 axis orientations, δ, is used as a measure of fit sensitivity to the initialization parameters. Ideally, δ will be zero; non-zero δ values indicate that convergent fits with similar χ^2 values can be obtained for a range of fit parameters, i.e., that there is some elongation to the χ^2 minimum. The value of B_0 is determined separately with the procedure described by Lepping et al. (2003) using the F2 fit parameters.

LQF and GHF provide a range of global flux rope parameters, including the axis direction latitude and longitude angles, θ_0 and ϕ_0, respectively, B_0, H, τ (in GHF), and spacecraft impact parameter, p. The value of p ranges from 0 for spacecraft trajectories intersecting the rope axis to 1 for a skimming intersection at the rope's outer surface. With an estimate of the flux rope diameter, R, and length, L, it is also possible to estimate the magnetic flux content of the ropes. In the Lundquist rope, the axial and poloidal fluxes are approximately given by:

$$F_z^L = 1.4 B_0 R^2 \tag{5}$$

$$F_\phi^L = \frac{B_0}{2.4} RL, \tag{6}$$

and in the Gold-Hoyle rope, the corresponding fluxes are given by:

$$F_z^G = \frac{B_0 \pi \ln\left(1+\tau^2 R^2\right)}{\tau^2} \tag{7}$$

$$F_\phi^G = \frac{B_0 L \ln\left(1+\tau^2 R^2\right)}{2\tau}. \tag{8}$$

Derivations of Equations (5–8) are found in Dasso et al. (2006), and references therein. These expressions are valid for cylindrical ropes with circular cross-sections.

4.2. Reconstruction Results

Fitting results are given in **Table 4**. Fits have been performed that treat FR2 and FR3 as a single flux rope (listed under "FR2+FR3" in **Table 4**) and as separate flux ropes at both Venus and Earth. **Figure 8** displays the LQF and GHF reconstructions (red and blue lines, respectively) of the flux ropes treated separately. The FR2 and FR3 intervals in **Figure 8** are shaded as in previous figures. Fittings have been made to magnetic field data in the Spacecraft–Equatorial (SCEQ) coordinate system; note that **Figures 4**, **5** display data in VSO and GSE coordinates, respectively. At both spacecraft, the flux ropes could be fitted relatively well with both methods. **Table 4** gives two quality-of-fit measures for the GHF and LQF, namely, the δ initiation sensitivity angle and the minimized χ^2 values associated with the fits (see section 4.1); for all fits listed, the δ and χ^2 values are relatively low and consistent with accurate fits. The MVA eigenvalue ratios met the Siscoe and Suey (1972) conditions for well-defined variance directions (see section 4.1).

Fits to the combined FR2+FR3 interval at both spacecraft indicate a rope axis that was directed approximately toward the solar east direction, i.e., $\phi_{FR} \sim 270°$. This was found consistently with all three reconstruction techniques. Axis inclination ϕ_{FR} for all reconstructions was higher at Venus than at Earth, with the difference varying from 31° for GHF to 41° for LQF. Fits to the FR2+FR3 interval at Earth performed in previous studies are consistent with our fit results: Palmerio et al. (2017) applied

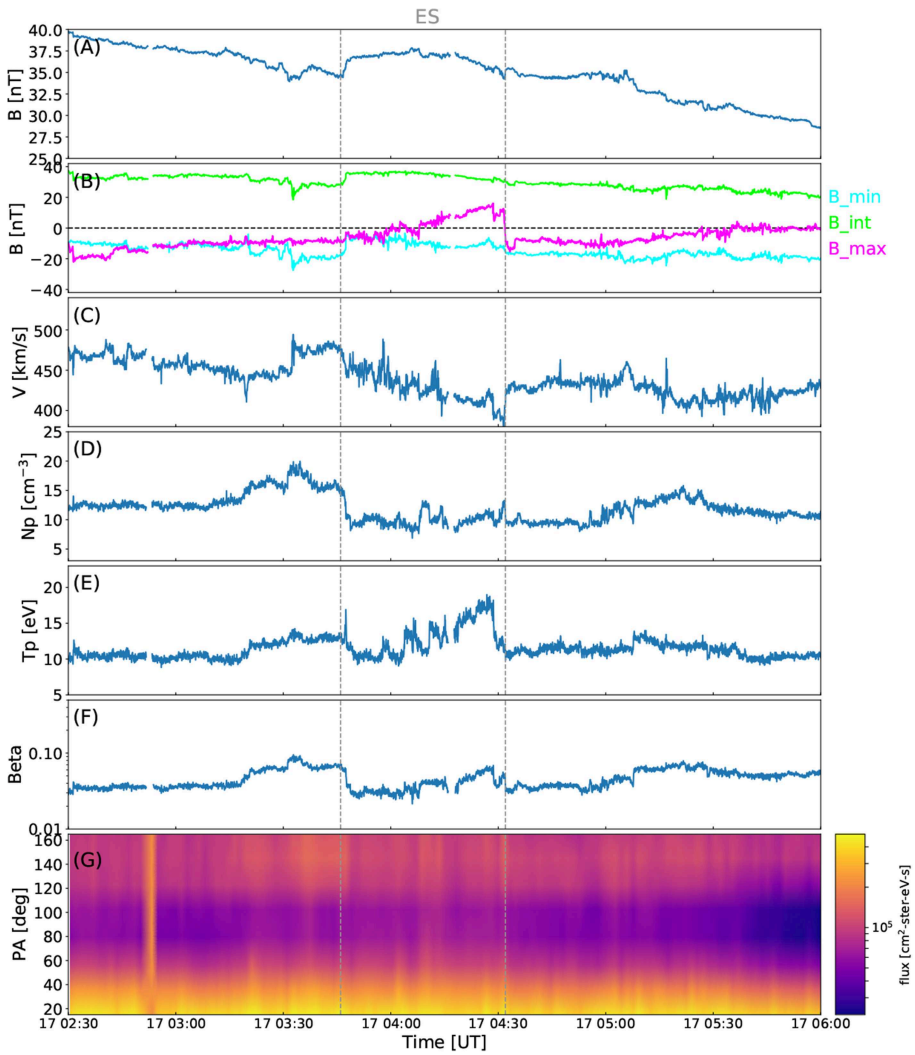

FIGURE 7 | The embedded substructure (ES) in FR3 observed at Earth's L1 point. The ES is bounded by the vertical dashed lines. The panels show, from top to bottom: **(A)** magnetic field magnitude, **(B)** magnetic field components in MVA coordinates (light blue: B_{min}, lime: B_{int}, pink: B_{max}), solar wind **(C)** speed, **(D)** density, **(E)** temperature, **(F)** plasma beta, and **(G)** the pitch angle spectrogram of suprathermal 255 eV electrons. The 3 s IMF and solar wind plasma data are from the Wind spacecraft.

Grad–Shafranov reconstruction (GSR; e.g., Hu and Sonnerup, 2002; Isavnin et al., 2011) obtaining an axis orientation of $\phi_{FR} = 299°$ and $\theta_{FR} = 6°$; Nieves-Chinchilla et al. (2018) used the circular-cylindrical flux rope analytical model (Nieves-Chinchilla et al., 2016) to obtain an axis orientation of $\phi_{FR} = 297°$ and $\theta_{FR} = -3°$. We also note that our fits had a positive chirality (helicity sign) at both Venus and Earth. This is consistent with the analysis of indirect solar proxies (see Section 3.1 and Palmerio et al., 2017), the hemispheric helicity rule (e.g., Seehafer, 1990; Bothmer and Schwenn, 1998; Pevtsov and Balasubramaniam, 2003), and with the presumption of helicity sign conservation (e.g., Woltjer, 1958; Berger, 2005).

Table 4 also lists estimates of the flux rope diameter, S. At Wind, these estimates are derived from the flux rope's passage time and mean proton speed, and take into account the axis orientations and spacecraft impact parameters obtained from the fits. For the FR2+FR3 interval at Wind, the mean proton speed was $\sim$ 439 km/s, yielding $S = 0.140$ AU for LQF and $S = 0.143$ AU for GHF. At VEX, a burst of speed measurements averaging $\sim$ 468 km/s is used to determine S values of 0.147 AU in LQF and 0.138 AU in GHF. The τ, F_z, and F_ϕ values listed in **Table 4** (and discussed below) are functions of $R = S/2$.

We now consider the fits made to FR2 and FR3 separately, as displayed in **Figure 8**. Fitting results for FR2 varied considerably between the different techniques. At Venus, MVA and LQF gave a low inclination axis pointing toward the Sun, while GHF gave a highly (northward) inclined, eastward tilted axis. At Earth, in contrast, MVA and GHF both gave a highly inclined axis tilted toward the east, while LQF gave a low inclination, antisunward-directed axis. At both Venus and Earth,

TABLE 4 | MVA, GHF, and LQF results for FR2 and FR3 treated as a single structure and separately.

	θ_{FR} [°]	ϕ_{FR} [°]	H	λ_1/λ_2	λ_3/λ_2	τ [AU^{-1}]	B_0 [nT]	p	F_z [10^{21} Mx]	F_ϕ [10^{21} Mx]	χ^2	δ [°]	S [AU]
FR2+FR3													
VENUS													
MVA	12	278	+1	1.73	0.21	–	–	–	–	–	–	–	–
LQF	35	274	+1	–	–	–	41	0.02	0.69	1.90	0.10	0	0.147
GHF	30	294	+1	–	–	6.5	48	0.10	1.46	1.02	0.17	0	0.138
EARTH													
MVA	–21	282	+1	2.76	0.12	–	–	–	–	–	–	–	–
LQF	–6	288	+1	–	–	–	38	0.08	0.57	2.31	0.08	2	0.140
GHF	–1	282	+1	–	–	4.2	41	0.01	1.41	0.89	0.15	0	0.143
FR2													
VENUS													
MVA	20	188	+1	15.1	0.56	–	–	–	–	–	–	–	–
LQF	15	177	+1	–	–	–	53	0.74	–	–	0.05	1	–
GHF	75	95	+1	–	–	–	36	0.02	–	–	0.02	0	–
EARTH													
MVA	72	282	+1	17.7	0.37	–	–	–	–	–	–	–	–
LQF	18	351	+1	–	–	–	56	0.63	0.003	0.11	0.05	7	0.008
GHF	70	312	+1	–	–	14.0	42	0.01	0.024	0.029	0.04	0	0.018
FR3													
VENUS													
MVA	–32	285	+1	2.81	0.38	–	–	–	–	–	–	–	–
LQF	–27	310	+1	–	–	–	69	0.86	–	–	0.09	7	–
GHF	–40	271	+1	–	–	–	62	0.01	–	–	0.05	0	–
EARTH													
MVA	–26	236	+1	12.3	0.73	–	–	–	–	–	–	–	–
LQF	–19	312	+1	–	–	–	36	0.29	0.23	1.42	0.11	6	0.090
GHF	–34	272	+1	–	–	3.4	32	0.03	0.68	0.35	0.09	0	0.111

*The flux rope time intervals are given in **Table 3**. The columns show, from left to right: latitude (θ_{FR}) and longitude (ϕ_{FR}) of the flux rope axis, helicity sign (H), maximum–to–intermediate and minimum–to–intermediate eigenvalue ratios from MVA, FR twist (τ), axial magnetic field magnitude (B_0), impact parameter (p), axial (F_z) and poloidal (F_ϕ) magnetic fluxes, minimization parameter (χ^2), initiation sensitivity angle (δ) of GHF and LQF, and flux rope diameter (S). The axis directions are indicated in Spacecraft Equatorial (SCEQ) coordinates.*

LQF estimated considerably higher p and B_0 values than GHF. Some indication of the origin of these differences can be seen in **Figure 8**, which shows quite different reconstructions for B_X between LQF and GHF; the flatter B_X of the GHF better captures the observed profile. However, the large impact parameters found in LQF are consistent with the apex of CME2 propagating toward the south, as seen in remote sensing observations (see **Table 1** and **Supplementary Video 2**) and EUHFORIA modeling (see **Figure 3** and **Supplementary Video 1**). Estimates of S suggest that FR2 was very small in size by the time of arrival at Earth. S has not been determined at Venus for FR2 or FR3 because suitable speed measurements were lacking. The reconstructions presented for FR2 should be considered only as approximations due to the short duration of the event, interactions, and potentially off-centers encounter (e.g., Al-Haddad et al., 2013).

Fitting orientations for FR3 are much more consistent across the different fitting techniques. They all indicate, at both Venus and Earth, an approximately eastward directed rope with a moderate inclination toward the south. It is notable that each technique indicates a slight reduction in inclination (i.e., $|\ \theta_{FR}\ |$ reducing) from Venus to Earth; such reductions with heliocentric distance have been observed previously (e.g., Good et al., 2019). However, p values for LQF and GHF differ significantly; as with FR2, this is partly a result of differences in reconstruction of the B_X component. The diameter S of FR3 was much greater than that of FR2 at Earth.

The magnetic flux content of the ropes have been obtained with Equations 5–8 and parameters from the fits. The axial (F_z) and poloidal (F_ϕ) flux values are listed in **Table 4**. In order to obtain the F_ϕ values, the flux rope length L has been estimated to equal $2\pi\gamma R/180^\circ$, i.e., L spans the arc length defined by the angle

2γ, where γ is the half-angle between the CME legs obtained from the GCS reconstructions (see section 3.1). CME2 and CME3 had γ values of 15° and 27°, respectively; these give L values for FR2 and FR3 of 0.38 AU and 0.68 AU at Venus, and 0.52 and 0.94 AU at Earth, respectively. For the FR2+FR3 interval, the FR3 L values are used. First considering the FR2+FR3 interval, it can be seen that the total flux content at Venus and Earth was comparable in both LQF and GHF. Total flux from the LQF was 2.59×10^{21} Mx at Venus and 2.88×10^{21} Mx at Earth; the corresponding values from GHF were 2.48×10^{21} Mx and 2.30×10^{21} Mx, respectively. The flux is distributed more poloidally than axially in the LQF than in the GHF due to the nature of the respective model fields. Treating the flux ropes separately, both LQF and GHF estimated low flux content in FR2 at Earth, reflecting its small size, while FR3 contained a considerably larger amount of flux.

As discussed in section 3.3.2, FR2 had contracted significantly by the time it reached Earth and, in any case, it represented only a glancing encounter through the northern part of the larger flux rope related to CME2. The resulting fluxes (in particular, $F_\phi = 0.11 \times 10^{21}$ Mx from LQF and $F_\phi = 0.029 \times 10^{21}$ Mx for GHF) are thus small and considerably below (by one to two orders of magnitude) the values derived from solar analysis (see section 3.1, where $F_\phi = 0.5 \times 4.60 \times 10^{21} = 2.30 \times 10^{21}$ Mx from PEA analysis and $F_\phi = 0.5 \times 2.21 \times 10^{21} = 1.11 \times 10^{21}$ Mx from ribbon analysis). For FR3, the poloidal flux values estimated at Wind are equal to $F_\phi = 1.42 \times 10^{21}$ Mx from LQF and $F_\phi = 0.35 \times 10^{21}$ Mx from GHF. The poloidal flux from LQF is thus smaller but of the same order of magnitude as the fluxes estimated from solar observations (see section 3.1, where $F_\phi = 0.5 \times 6.04 \times 10^{21} = 3.02 \times 10^{21}$ Mx and $F_\phi = 0.5 \times 3.88 \times 10^{21} = 1.94 \times 10^{21}$ Mx for PEA and ribbon analyses, respectively), whereas the GHF estimates are an order of magnitude smaller than the solar estimates.

Estimates of magnetic flux in CME flux ropes are subject to large uncertainties. In the case of *in-situ* estimates, uncertainties are related to the length L of the flux rope loop, fitting parameters, distribution of magnetic flux in the flux rope, knowledge of the true cross-sectional shape, and the possible occurrence of erosive reconnection in interplanetary space (e.g., see discussion in Möstl et al., 2008). For example, if CME flux ropes flatten normal to their propagation direction as they travel through interplanetary space, *in-situ* flux values are expected to be underestimated by cylindrical models (Owens, 2008), and thus lower than those obtained from solar observations. Such a discrepancy between solar and *in-situ* estimates has been found in our analysis, and also in several previous works (e.g., Longcope et al., 2007; Qiu et al., 2007; Möstl et al., 2008; Lynch et al., 2010). We further note that estimates for the events analyzed here are complicated by interactions and off-center encounters, particularly for FR2. Recent studies have also emphasized difficulties in the present flux rope fitting techniques, e.g., for detecting writhe (e.g., Al-Haddad et al., 2019). Due to these constraints and the complexity of the events studied, we stress that the flux values are approximate and no firm conclusions should be drawn from them.

5. SUMMARY AND DISCUSSION

In this work, we have analyzed the interplanetary counterparts of three CMEs that erupted from the Sun between June 12 and 14, 2012 using multipoint measurements from VEX at 0.7 AU, and from Wind and ACE at 1 AU. During the investigated period, Venus and Earth were separated by 5.4° in longitude and by 0.2° in latitude, i.e., they very close to radial alignment.

Our analysis of remote-sensing data from the solar disc through the inner heliosphere combined with a careful investigation of *in-situ* measurements supported by 3D heliospheric modeling suggests the following scenario: the first CME (CME1; launched on June 12, 2012 as two sympathetic eruptions that merged close to the Sun) encountered Venus and Earth quite centrally as it propagated along the ecliptic and close to the Sun–Earth line. The most prominent signatures of CME1 detected at Venus and at Earth were a shock and a turbulent sheath. Plasma data also revealed that a magnetic ejecta (E1), featuring lower temperatures and counterstreaming electrons, was likely encountered by Wind. A magnetic cloud structure was likely missing because interaction of the two sympathetic eruptions at the Sun produced a complex ejecta (e.g., Burlaga et al., 2002). The second and third CMEs (CME2 and CME3; launched on June 13, 2012 and June 14, 2012, respectively) arrived in succession at Venus, producing two separate flux rope (FR2 and FR3) intervals. Soon after the passage of FR2, VEX moved into Venus's induced magnetosphere for 2 h. The shock driven by CME3 (S3) and the following FR3 arrived at Venus when VEX was back in the magnetosheath on the nightside; the sheath and the front part of FR3 were thus compressed in the Venusian magnetosheath. Due to solar wind preconditioning provoked by the preceding CMEs, CME3 likely propagated out to Venus's orbit experiencing relatively little solar wind drag, thus maintaining its high speed and magnetic field magnitude (e.g., Liu et al., 2014). Significant interactions occurred between Venus and Earth; the shock driven by CME3 propagated through CME2 and resulted in a closely-based double shock signature before FR2 at Earth's L1 point. Both simulation and observational studies have shown that the shock of a faster CME can propagate through a slower preceding CME and that their shocks may finally merge into a single, stronger shock (e.g., Odstrcil et al., 2003; Farrugia and Berdichevsky, 2004; Wu et al., 2004; Xiong et al., 2007; Lugaz et al., 2013).

Observations at Earth's L1 point showed that CME3 had compressed CME2 to create a structure resembling one coherent flux rope. Compared to measurements at Venus, the flux ropes FR2 and FR3 had mostly maintained their integrity. This is in agreement with the trailing part of FR2 and its wake having had fields directed in a roughly similar direction as those at the leading edge of FR3. Thus, no significant magnetic reconnection is expected to have occurred between these two CMEs.

On average, the magnetic field magnitudes in ICMEs decrease with increasing distance from the Sun as a result of expansion (e.g., Richardson et al., 2006). For example, Leitner et al. (2007) obtained the radial dependence $r_H^{-1.64\pm0.4}$ (where r_H is the radial distance from the Sun) from their analysis of 130 magnetic clouds observed during the Helios era between 0.3 and 1 AU.

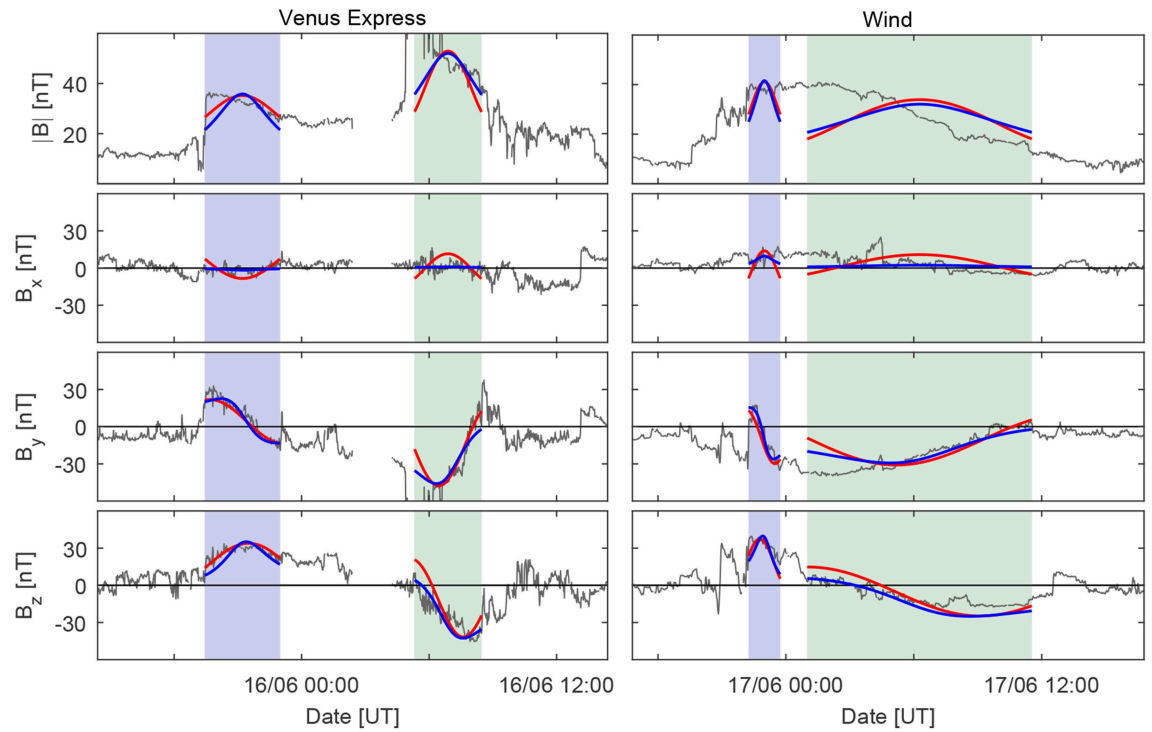

FIGURE 8 | Gold-Hoyle fits (blue lines) and Lundquist fits (red lines) to the magnetic field data at VEX **(Left)** and Wind **(Right)** separately for FR2 (blue-shaded interval) and FR3 (green-shaded interval). Measurements made in the Venusian magnetosphere have been removed. The panels show, from top to bottom, the magnetic field magnitude and the three field components in Spacecraft Equatorial (SCEQ) coordinates. The SCEQ coordinate system is identical to the Heliocentric Earth Equatorial (HEEQ; Thompson, 2006) system at the locations of Earth and the Sun–Earth L1 point.

Using this approximate dependence, the leading edge field of 35.6 nT for FR2 at Venus would have dropped to about 20 nT by the time it had reached Earth's orbit. In the case of FR2, the magnetic fields were now instead slightly higher at Earth than at Venus. The high magnetic fields observed at Earth (∼ 40 nT) were thus partly related to the compression of CME2, i.e., not only to the fast and prominent CME3, which, according to remote-sensing observations, appeared as the most obviously Earth-directed CME. In their simulation study, Schmidt and Cargill (2004) investigated cases where a faster and high-*B* CME and a slower and low-*B* CME interact at their flanks, i.e., in a similar fashion to our case. The two cases studied, one where the interacting CMEs have the same chirality and the other where the CMEs have opposite chirality, are presented in their **Figures 4**, **5**, respectively. Both scenarios result in contraction of the leading CME at the point of interaction and enhancement of the field. Similar cases have also been analyzed e.g. by Lugaz et al. (2013), where contraction of a leading CME and relaxation of a trailing CME were observed. However, the details of CME–CME interaction depend strongly on the specific properties and directions of the interacting CMEs.

As discussed in section 3.3, the combined structure consisting of FR2 and FR3 at Earth has been treated as a single flux rope (linked to CME3) in previous studies. However, when considering observations at Venus, this interpretation is clearly problematic. There are no other CMEs in a suitable time window that could have caused such a strong interplanetary shock to propagate through CME3. In this single-rope scenario, the flux rope would have also had to rotate by about 30–40° between Venus and Earth (see our reconstruction results from **Table 4**), due either to radial evolution or to the flux rope being highly warped over small longitudinal distances. As noted in the Introduction, significant changes in the tilts of flux rope axes have been reported in multi-spacecraft studies, but were mostly connected to cases where the observing spacecraft have been separated by at least a few tens of degrees in longitude.

We emphasize the ambiguity in determining the interface between FR2 and FR3 at Earth due to CME–CME interaction and the interplanetary counterpart of CME2 featuring a wake after FR2 (as discussed in section 3.3.1, the ICME ejecta-like magnetic field signatures continued beyond the FR2 trailing boundary). We note, however, that our selected FR2 and FR3 intervals show clear similarities between Venus and Earth when compared through a direct mapping technique, and this interpretation also better matches with the observed speed profile at Wind. The substructure we identified within FR3 did not show signatures of a reconnection exhaust. We conclude that it either represented a warping of flux surfaces near the center of the flux rope, as suggested by Dasso et al. (2007), or to have been formed spontaneously due to the flux rope kinematic propagation (Owens, 2009). We also note that the solar wind density was high at Earth in FR2 and temperatures were relatively enhanced

throughout the whole FR2 and FR3 interval, particularly during the passage of FR2 and the front part of FR3. The plasma beta, however, was depressed during the passage of both flux ropes, consistent with the findings of Farrugia and Berdichevsky (2004) who analyzed interacting CMEs using *in-situ* observations by Helios and ISEE.

As discussed above, the magnetic field characteristics of FR3 were quite similar at the two observation points. While the flux rope axis orientation matched relatively well (within $\sim$ 10° for LQF and GHF) for FR3 between Venus and Earth, the FR2 reconstruction results were less consistent, possibly due to the significant compression and spacecraft crossings made far from the flux rope axis. Kubicka et al. (2016) concluded that observations at VEX for this CME–CME interaction event yielded a good proxy of the corresponding geomagnetic storm strength at Earth. This likely results from the flux ropes roughly maintaining their integrity despite significant interaction. Were reconnection and drastic merging of the CMEs to have occurred between Venus and Earth, it is likely that the prediction of a storm would have been less accurate. However, the results indicate that, in some interacting CME cases at least, a probe at the distance of Venus could be used successfully for space weather forecasting (see also Lindsay et al., 1999). One possibility to obtain consistent solar wind monitoring closer to the Sun is the placement of identical probes in orbit about the Sun, e.g., at the orbit of Venus (Ritter et al., 2015; Törmä, 2016) or in orbit around Earth in a diamond-like configuration (Cyr et al., 2000). The aim is to have such a large grid of monitors that at least one of them would always encounter any Earth-impacting CME. The accuracy of forecasting using these approaches is, however, significantly influenced by any considerable change over small spacecraft separations (as suggested e.g., by Kilpua et al., 2011; Lugaz et al., 2018; Good et al., 2019) and significant evolution or interaction of CMEs over relatively small radial distances.

In conclusion, we have highlighted in this paper the complexity of interpreting interplanetary observations made during interacting CME events. During the investigated period, remote-sensing observations showed only one clearly Earth-directed CME that was fast and prominent, with a single coherent flux rope being detected *in situ* at Earth. Measurements taken by VEX around Venus were crucial for revealing that this coherent flux rope structure at Earth was actually composed of two coalesced flux ropes, the first being embedded in an edge-encountered CME and compressed by the following CME. Together, they produced the strongest magnetic field magnitudes observed in the near-Earth solar wind during Solar Cycle 24. Although Earth and Venus were almost radially aligned and separated by only 0.28 AU in radial distance, the spacecraft at these locations observed interaction between the two successive CMEs at very different phases: VEX observed the interaction just prior to onset, while the spacecraft at Earth's L1 point made observations when the interaction was almost complete. A considerable interaction thus occurred over a relatively short radial distance. Our study also highlights the importance of heliospheric modeling and imaging for building a comprehensive picture of CMEs and their interactions in interplanetary space.

AUTHOR CONTRIBUTIONS

EK: *in-situ* analysis and interpretation, primary responsibility for drafting the text, and combining different elements of the analysis. SG: *in-situ* analysis and interpretation, flux rope fitting and mapping, and text composition. EP: solar, coronagraph, and heliospheric remote-sensing observations and interpretation, Venus *in-situ* analysis, and text composition. EA: CME reconstructions at the Sun and EUHFORIA simulation. EL: solar observations and estimation of magnetic flux at the Sun. MA-L: earth *in-situ* analysis (substructure). MK, DM, and DP: analysis of solar observations. JP: EUHFORIA simulation, heliospheric evolution. JM and SP: EUHFORIA simulation. YF: Venus *in-situ* data analysis and interpretation. All of the authors read and critically revised the paper, approved the final version, and agreed to be accountable for all aspects of the work.

FUNDING

This work was supported by funding from the SolMAG project (ERC-COG 724391) funded by the European Research Council (ERC) in the framework of the Horizon 2020 Research and Innovation Programme, the BRAIN-be project CCSOM, and the Academy of Finland project SMASH 310445. EK and DP were supported with funding from the Finnish Society of Sciences and Letters and the Ruth och Nils Stenbäcks stipendium. The results presented here have been achieved under the framework of the Finnish Centre of Excellence in Research of Sustainable Space (Academy of Finland grant number 312390), which we gratefully acknowledge.

ACKNOWLEDGMENTS

EUHFORIA is developed as a joint effort between the University of Helsinki and KU Leuven. The validation of solar wind and CME modeling with EUHFORIA throughout the inner heliosphere is being performed within the BRAIN-be project CCSOM (Constraining CMEs and Shocks by Observations and Modeling; http://www.sidc.be/ccsom/). We acknowledge the European Union FP7-SPACE-2013-1 programme for the HELCATS project (#606692). EK and DP acknowledge the Finnish Society of Sciences and Letters and the Ruth och Nils Stenbäcks stipendium. We also acknowledge use of the CDAW SOHO/LASCO event catalog (https://cdaw.gsfc.nasa.gov/CME_list/), which is generated and maintained at the CDAW Data Center by NASA and the Catholic University of America in cooperation with NRL, and the STEREO/SECCHI/COR2 CME catalog (http://solar.jhuapl.edu/Data-Products/COR-CME-Catalog.php) that is generated and maintained by John Hopkins University Applied Physics Laboratory, in collaboration with NRL and the NASA Goddard Space Flight Center. The authors thank the STEREO/SECCHI consortium for providing the data (COR and HI). The SECCHI data used here were produced by an international consortium of the Naval Research Laboratory (USA), Lockheed Martin Solar and Astrophysics Lab (USA), NASA Goddard Space Flight Center (USA), Rutherford Appleton Laboratory (UK), University of Birmingham (UK), Max-Planck-Institut for Solar System Research (Germany),

Centre Spatiale de Liége (Belgium), Institut d'Optique Theorique et Appliquée (France), and Institut d'Astrophysique Spatiale (France). We acknowledge A. Szabo for the Wind/MFI data, K. Ogilvie for the Wind/SWE data, R. Lin/S. Bale for the Wind/3DP data, and G. Gloeckler for the ACE/SWICS data.

SUPPLEMENTARY MATERIAL

The Supplementary Material for this article can be found online at: https://www.frontiersin.org/articles/10.3389/fspas.2019.00050/full#supplementary-material

REFERENCES

Al-Haddad, N., Nieves-Chinchilla, T., Savani, N. P., Möstl, C., Marubashi, K., Hidalgo, M. A., et al. (2013). Magnetic field configuration models and reconstruction methods for interplanetary coronal mass ejections. *Sol. Phys.* 284, 129–149. doi: 10.1007/s11207-013-0244-5

Al-Haddad, N., Poedts, S., Roussev, I., Farrugia, C. J., Yu, W., and Lugaz, N. (2019). The magnetic morphology of magnetic clouds: multi-spacecraft investigation of twisted and writhed coronal mass ejections. *Astrophys. J.* 870:100. doi: 10.3847/1538-4357/aaf38d

Arge, C. N., Luhmann, J. G., Odstrcil, D., Schrijver, C. J., and Li, Y. (2004). Stream structure and coronal sources of the solar wind during the May 12th, 1997 CME. *J. Atmosp. Sol. Terrest. Phys.* 66, 1295–1309. doi: 10.1016/j.jastp.2004.03.018

Barabash, S., Sauvaud, J.-A., Gunell, H., Andersson, H., Grigoriev, A., Brinkfeldt, K., et al. (2007). The Analyser of Space Plasmas and Energetic Atoms (ASPERA-4) for the Venus Express mission. *Planet. Space Sci.* 55, 1772–1792. doi: 10.1016/j.pss.2007.01.014

Berger, M. A. (2005). Magnetic helicity conservation. *Highlights Astron.* 13:85. doi: 10.1017/S1539299600015148

Bothmer, V., and Schwenn, R. (1998). The structure and origin of magnetic clouds in the solar wind. *Ann. Geophys.* 16, 1–24. doi: 10.1007/s00585-997-0001-x

Brueckner, G. E., Howard, R. A., Koomen, M. J., Korendyke, C. M., Michels, D. J., Moses, J. D., et al. (1995). The Large Angle Spectroscopic Coronagraph (LASCO). *Sol. Phys.* 162, 357–402. doi: 10.1007/BF00733434

Burlaga, L., Sittler, E., Mariani, F., and Schwenn, R. (1981). Magnetic loop behind an interplanetary shock: Voyager, Helios, and IMP 8 observations. *J. Geophys. Res.* 86, 6673–6684. doi: 10.1029/JA086iA08p06673

Burlaga, L. F. (1988). Magnetic clouds and force-free fields with constant alpha. *J. Geophys. Res.* 93, 7217–7224. doi: 10.1029/JA093iA07p07217

Burlaga, L. F., Lepping, R. P., and Jones, J. A. (1990). "Global configuration of a magnetic cloud," in *Physics of Magnetic Flux Ropes*, volume 58 of *Geophysical Monograph* eds C. T. Russell, E. R. Priest, and L. C. Lee (Washington, DC: American Geophysical Union), 373–377.

Burlaga, L. F., Plunkett, S. P., and St. Cyr, O. C. (2002). Successive CMEs and complex ejecta. *J. Geophys. Res.* 107:1266. doi: 10.1029/2001JA000255

Cane, H. V., and Richardson, I. G. (1995). Cosmic ray decreases and solar wind disturbances during late October 1989. *J. Geophys. Res.* 100, 1755–1762. doi: 10.1029/94JA03073

Cane, H. V., and Richardson, I. G. (2003). Interplanetary coronal mass ejections in the near-Earth solar wind during 1996–2002. *J. Geophys. Res.* 108:1156. doi: 10.1029/2002JA009817

Cane, H. V., Richardson, I. G., and Wibberenz, G. (1997). Helios 1 and 2 observations of particle decreases, ejecta, and magnetic clouds. *J. Geophys. Res.* 102, 7075–7086. doi: 10.1029/97JA00149

Chen, J. (2017). Physics of erupting solar flux ropes: coronal mass ejections (CMEs), Recent advances in theory and observation. *Phys. Plasmas* 24:090501. doi: 10.1063/1.4993929

Chi, Y., Zhang, J., Shen, C., Hess, P., Liu, L., Mishra, W., et al. (2018). Observational study of an earth-affecting problematic ICME from STEREO. *Astrophys. J.* 863:108. doi: 10.3847/1538-4357/aacf44

Crooker, N. U., Gosling, J. T., and Kahler, S. W. (1998). Magnetic clouds at sector boundaries. *J. Geophys. Res.* 103, 301–306. doi: 10.1029/97JA02774

Cyr, O. C. S., Mesarch, M. A., Maldonado, H. M., Folta, D. C., Harper, A. D., Davila, J. M., et al. (2000). Space weather diamond: a four spacecraft monitoring system. *J. Atmos. Sol. Terrest. Phys.* 62, 1251–1255. doi: 10.1016/S1364-6826(00)00069-9

Dasso, S., Mandrini, C. H., Démoulin, P., and Luoni, M. L. (2006). A new model-independent method to compute magnetic helicity in magnetic clouds. *Astron. Astrophys.* 455, 349–359. doi: 10.1051/0004-6361:20064806

Dasso, S., Nakwacki, M. S., Démoulin, P., and Mandrini, C. H. (2007). Progressive transformation of a flux rope to an ICME. Comparative analysis using the direct and fitted expansion methods. *Sol. Phys.* 244, 115–137. doi: 10.1007/s11207-007-9034-2

Davies, J. A., Harrison, R. A., Perry, C. H., Möstl, C., Lugaz, N., Rollett, T., et al. (2012). A self-similar expansion model for use in solar wind transient propagation studies. *Astrophys. J.* 750:23. doi: 10.1088/0004-637X/750/1/23

Davies, J. A., Perry, C. H., Trines, R. M. G. M., Harrison, R. A., Lugaz, N., Möstl, C., et al. (2013). Establishing a stereoscopic technique for determining the kinematic properties of solar wind transients based on a generalized self-similarly expanding circular geometry. *Astrophys. J.* 777:167. doi: 10.1088/0004-637X/777/2/167

Démoulin, P., Dasso, S., and Janvier, M. (2018). Exploring the biases of a new method based on minimum variance for interplanetary magnetic clouds. *Astron. Astrophys.* 619:A139. doi: 10.1051/0004-6361/201833831

Domingo, V., Fleck, B., and Poland, A. I. (1995). The SOHO mission: an overview. *Sol. Phys.* 162, 1–37. doi: 10.1007/BF00733425

Eastwood, J. P., Biffis, E., Hapgood, M. A., Green, L., Bisi, M. M., Bentley, R. D., et al. (2017). The economic impact of space weather: where do we stand? *Risk Analy.* 37, 206–228. doi: 10.1111/risa.12765

Elliott, H. A., McComas, D. J., Schwadron, N. A., Gosling, J. T., Skoug, R. M., Gloeckler, G., et al. (2005). An improved expected temperature formula for identifying interplanetary coronal mass ejections. *J. Geophys. Res.* 110:A04103. doi: 10.1029/2004JA010794

Eyles, C. J., Harrison, R. A., Davis, C. J., Waltham, N. R., Shaughnessy, B. M., Mapson-Menard, H. C. A., et al. (2009). The heliospheric imagers onboard the STEREO mission. *Sol. Phys.* 254, 387–445. doi: 10.1007/s11207-008-9299-0

Farrugia, C., and Berdichevsky, D. (2004). Evolutionary signatures in complex ejecta and their driven shocks. *Ann. Geophys.* 22, 3679–3698. doi: 10.5194/angeo-22-3679-2004

Farrugia, C. J., Berdichevsky, D. B., Möstl, C., Galvin, A. B., Leitner, M., Popecki, M. A., et al. (2011). Multiple, distant (40°) *in situ* observations of a magnetic cloud and a corotating interaction region complex. *J. Atmos. Sol. Terrest. Phys.* 73, 1254–1269. doi: 10.1016/j.jastp.2010.09.011

Farrugia, C. J., Janoo, L. A., Torbert, R. B., Quinn, J. M., Ogilvie, K. W., Lepping, R. P., et al. (1999). "A uniform-twist magnetic flux rope in the solar wind," in *American Institute of Physics Conference Series, Solar Wind Nine,* eds S. R. Habbal, R. Esser, J. V. Hollweg, and P. A. Isenberg (Melville, NY: American Institute of Physics), 745–748.

Feng, H., Zhao, Y., Zhao, G., Liu, Q., and Wu, D. (2019). Observations on a series of merging magnetic flux ropes within an interplanetary coronal mass ejection. *Geophys. Res. Lett.* 46, 5–10. doi: 10.1029/2018GL080063

Gloeckler, G., Cain, J., Ipavich, F. M., Tums, E. O., Bedini, P., Fisk, L. A., et al. (1998). Investigation of the composition of solar and interstellar matter using solar wind and pickup ion measurements with SWICS and SWIMS on the ACE spacecraft. *Space Sci. Rev.* 86, 497–539. doi: 10.1023/A:1005036131689

Gold, T., and Hoyle, F. (1960). On the origin of solar flares. *Month. Not. R. Astron. Soc.* 120:89. doi: 10.1093/mnras/120.2.89

Goldstein, H. (1983). "On the field configuration in magnetic clouds," in *NASA Conference Publication*, *JPL Solar Wind Five, Vol. 228*, ed M. Neugebauer (Washington, DC: NASA), 731–733

Good, S. W., Forsyth, R. J., Eastwood, J. P., and Möstl, C. (2018). Correlation of ICME magnetic fields at radially aligned spacecraft. *Sol. Phys.* 293:52. doi: 10.1007/s11207-018-1264-y

Good, S. W., Kilpua, E. K. J., LaMoury, A. T., Forsyth, R. J., Eastwood, J. P., and Möstl, C. (2019). Self-Similarity of ICME flux ropes: observations by

radially aligned spacecraft in the inner heliosphere. *J. Geophys. Res.* 124. doi: 10.1029/2019JA026475

Gopalswamy, N., Yashiro, S., Akiyama, S., and Xie, H. (2017). Estimation of reconnection flux using post-eruption arcades and its relevance to magnetic clouds at 1 AU. *Sol. Phys.* 292:65. doi: 10.1007/s11207-017-1080-9

Gosling, J. T. (1990). Coronal mass ejections and magnetic flux ropes in interplanetary space. *Am. Geophys. Union Geophy. Monogr. Ser.* 58, 343–364.

Gosling, J. T., Baker, D. N., Bame, S. J., Feldman, W. C., Zwickl, R. D., and Smith, E. J. (1987). Bidirectional solar wind electron heat flux events. *J. Geophys. Res.* 92, 8519–8535. doi: 10.1029/JA092iA08p08519

Gosling, J. T., McComas, D. J., Phillips, J. L., and Bame, S. J. (1991). Geomagnetic activity associated with earth passage of interplanetary shock disturbances and coronal mass ejections. *J. Geophys. Res.* 96, 7831–7839. doi: 10.1029/91JA00316

Gosling, J. T., Skoug, R. M., McComas, D. J., and Smith, C. W. (2005). Direct evidence for magnetic reconnection in the solar wind near 1 AU. *J. Geophys. Res.* 110:A01107. doi: 10.1029/2004JA010809

Green, L. M., Kliem, B., Török, T., van Driel-Gesztelyi, L., and Attrill, G. D. R. (2007). Transient coronal sigmoids and rotating erupting flux ropes. *Sol. Phys.* 246, 365–391. doi: 10.1007/s11207-007-9061-z

Green, L. M., Török, T., Vršnak, B., Manchester, W., and Veronig, A. (2018). The origin, early evolution and predictability of solar eruptions. *Space Sci. Rev.* 214:46. doi: 10.1007/s11214-017-0462-5

Gulisano, A. M., Dasso, S., Mandrini, C. H., and Démoulin, P. (2007). Estimation of the bias of the Minimum Variance technique in the determination of magnetic clouds global quantities and orientation. *adv. Space Res.*, 40:1881–1890. doi: 10.1016/j.asr.2007.09.001

Hood, A. W., and Priest, E. R. (1979). Kink instability of solar coronal loops as the cause of solar flares. *Sol. Phys.* 64, 303–321. doi: 10.1007/BF00151441

Howard, R. A., Moses, J. D., Vourlidas, A., Newmark, J. S., Socker, D. G., Plunkett, et al. (2008). Sun Earth Connection Coronal and Heliospheric Investigation (SECCHI). *Space Sci. Rev.* 136, 67–115. doi: 10.1007/978-0-387-09649-0-5

Hu, Q., and Sonnerup, B. U. Ö. (2002). Reconstruction of magnetic clouds in the solar wind: Orientations and configurations. *J. Geophys. Res.* 107, SSH 10-1–SSH 10-15. doi: 10.1029/2001JA000293

Huttunen, K. E. J., Koskinen, H. E. J., and Schwenn, R. (2002). Variability of magnetospheric storms driven by different solar wind perturbations. *J. Geophys. Res.* 107, SMP 20-1–SMP 20-8. doi: 10.1029/2001JA900171

Huttunen, K. E. J., Schwenn, R., Bothmer, V., and Koskinen, H. E. J. (2005). Properties and geoeffectiveness of magnetic clouds in the rising, maximum and early declining phases of solar cycle 23. *Ann. Geophys.* 23, 625–641. doi: 10.5194/angeo-23-625-2005

Isavnin, A., Kilpua, E. K. J., and Koskinen, H. E. J. (2011). Grad–Shafranov reconstruction of magnetic clouds: overview and improvements. *Sol. Phys.* 273, 205–219. doi: 10.1007/s11207-011-9845-z

James, A. W., Green, L. M., Palmerio, E., Valori, G., Reid, H. A. S., Baker, D., et al. (2017). On-disc observations of flux rope formation prior to its eruption. *sol. phys.* 292:71. doi: 10.1007/s11207-017-1093-4

James, A. W., Valori, G., Green, L. M., Liu, Y., Cheung, M. C. M., Guo, Y., et al. (2018). An observationally constrained model of a flux rope that formed in the solar corona. *Astrophys. J.* 855:L16. doi: 10.3847/2041-8213/aab15d

Janvier, M., Dasso, S., Démoulin, P., Masías-Meza, J. J., and Lugaz, N. (2015). Comparing generic models for interplanetary shocks and magnetic clouds axis configurations at 1 AU. *J. Geophys. Res.* 120, 3328–3349. doi: 10.1002/2014JA020836

Jian, L., Russell, C. T., Luhmann, J. G., and Skoug, R. M. (2006). Properties of interplanetary coronal mass ejections at one AU during 1995 – 2004. *Sol. Phys.* 239, 393–436. doi: 10.1007/s11207-006-0133-2

Kaiser, M. L., Kucera, T. A., Davila, J. M., St. Cyr, O. C., Guhathakurta, M., and Christian, E. (2008). The STEREO mission: an introduction. *Space Sci. Rev.* 136, 5–16. doi: 10.1007/s11214-007-9277-0

Kazachenko, M. D., Lynch, B. J., Welsch, B. T., and Sun, X. (2017). A database of flare ribbon properties from the solar dynamics observatory. I. Reconnection flux. *Astrophys. J.* 845:49. doi: 10.3847/1538-4357/aa7ed6

Kilpua, E., Koskinen, H. E. J., and Pulkkinen, T. I. (2017a). Coronal mass ejections and their sheath regions in interplanetary space. *Living Rev. Sol. Phys.* 14:5. doi: 10.1007/s41116-017-0009-6

Kilpua, E. K. J., Balogh, A., von Steiger, R., and Liu, Y. D. (2017b). Geoeffective properties of solar transients and stream interaction regions. *Space Sci. Rev.* 212, 1271–1314. doi: 10.1007/s11214-017-0411-3

Kilpua, E. K. J., Isavnin, A., Vourlidas, A., Koskinen, H. E. J., and Rodriguez, L. (2013). On the relationship between interplanetary coronal mass ejections and magnetic clouds. *Ann. Geophys.* 31, 1251–1265. doi: 10.5194/angeo-31-1251-2013

Kilpua, E. K. J., Jian, L. K., Li, Y., Luhmann, J. G., and Russell, C. T. (2011). Multipoint ICME encounters: Pre-STEREO and STEREO observations. *J. Atmos. Sol. Terrest. Phys.* 73, 1228–1241. doi: 10.1016/j.jastp.2010.10.012

Kilpua, E. K. J., Lumme, E., Andreeova, K., Isavnin, A., and Koskinen, H. E. J. (2015). Properties and drivers of fast interplanetary shocks near the orbit of the Earth (1995-2013). *J. Geophys. Res.* 120, 4112–4125. doi: 10.1002/2015JA021138

Klein, L. W., and Burlaga, L. F. (1982). Interplanetary magnetic clouds at 1 AU. *J. Geophys. Res.* 87, 613–624. doi: 10.1029/JA087iA02p00613

Kubicka, M., Möstl, C., Amerstorfer, T., Boakes, P. D., Feng, L., Eastwood, J. P., et al. (2016). Prediction of geomagnetic storm strength from inner heliospheric *in situ* observations. *Astrophys. J.* 833:255. doi: 10.3847/1538-4357/833/2/255

Leitner, M., Farrugia, C. J., MöStl, C., Ogilvie, K. W., Galvin, A. B., Schwenn, R., et al. (2007). Consequences of the force-free model of magnetic clouds for their heliospheric evolution. *J. Geophys. Res.* 112:A06113. doi: 10.1029/2006JA011940

Lemen, J. R., Title, A. M., Akin, D. J., Boerner, P. F., Chou, C., Drake, J. F., et al. (2012). The Atmospheric Imaging Assembly (AIA) on the Solar Dynamics Observatory (SDO). *Sol. Phys.* 275, 17–40. doi: 10.1007/s11207-011-9776-8

Lepping, R. P., Acũna, M. H., Burlaga, L. F., Farrell, W. M., Slavin, J. A., Schatten, K. H., et al. (1995). The Wind magnetic field investigation. *Space Sci. Rev.* 71, 207–229. doi: 10.1007/BF00751330

Lepping, R. P., Berdichevsky, D. B., and Ferguson, T. J. (2003). Estimated errors in magnetic cloud model fit parameters with force-free cylindrically symmetric assumptions. *J. Geophys. Res.* 108:1356. doi: 10.1029/2002JA009657

Lepping, R. P., Jones, J. A., and Burlaga, L. F. (1990). Magnetic field structure of interplanetary magnetic clouds at 1 AU. *J. Geophys. Res.* 95, 11957–11965. doi: 10.1029/JA095iA08p11957

Lin, R. P., Anderson, K. A., Ashford, S., Carlson, C., Curtis, D., Ergun, R., et al. (1995). A three-dimensional plasma and energetic particle investigation for the Wind spacecraft. *Space Sci. Rev.* 71, 125–153. doi: 10.1007/BF00751328

Lindsay, G. M., Russell, C. T., and Luhmann, J. G. (1999). Predictability of Dst index based upon solar wind conditions monitored inside 1 AU. *J. Geophys. Res.* 104, 10335–10344. doi: 10.1029/1999JA900010

Liu, Y. D., Luhmann, J. G., Kajdič, P., Kilpua, E. K. J., Lugaz, N., Nitta, N. V., et al. (2014). Observations of an extreme storm in interplanetary space caused by successive coronal mass ejections. *Nat. Commun.* 5:3481. doi: 10.1038/ncomms4481

Longcope, D., Beveridge, C., Qiu, J., Ravindra, B., Barnes, G., and Dasso, S. (2007). Modeling and measuring the flux reconnected and ejected by the two-ribbon flare/CME event on 7 November 2004. *Sol. Phys.* 244, 45–73. doi: 10.1007/s11207-007-0330-7

Lopez, R. E., and Freeman, J. W. (1986). Solar wind proton temperature-velocity relationship. *J. Geophys. Res.* 91, 1701–1705. doi: 10.1029/JA091iA02p01701

Lugaz, N., Farrugia, C. J., Manchester, W. B. IV, and Schwadron, N. (2013). The interaction of two coronal mass ejections: influence of relative orientation. *Astrophys. J.* 778:20. doi: 10.1088/0004-637X/778/1/20

Lugaz, N., Farrugia, C. J., Winslow, R. M., Al-Haddad, N., Galvin, A. B., Nieves-Chinchilla, T., et al. (2018). On the spatial coherence of magnetic ejecta: measurements of coronal mass ejections by multiple spacecraft longitudinally separated by 0.01 AU. *Astrophys. J. Lett.* 864:L7. doi: 10.3847/2041-8213/aad9f4

Lugaz, N., Temmer, M., Wang, Y., and Farrugia, C. J. (2017). The interaction of successive coronal mass ejections: a review. *Sol. Phys.* 292:64. doi: 10.1007/s11207-017-1091-6

Lynch, B. J., and Edmondson, J. K. (2013). Sympathetic magnetic breakout coronal mass ejections from pseudostreamers. *Astrophys. J.* 764:87. doi: 10.1088/0004-637X/764/1/87

Lynch, B. J., Li, Y., Thernisien, A. F. R., Robbrecht, E., Fisher, G. H., Luhmann, J. G., et al. (2010). Sun to 1 AU propagation and evolution of a slow streamer-blowout coronal mass ejection. *J. Geophys. Res.* 115:A07106. doi: 10.1029/2009JA015099

Martinecz, C., Fränz, M., Woch, J., Krupp, N., Roussos, E., Dubinin, E., et al. (2008). Location of the bow shock and ion composition boundaries at

Venus—initial determinations from Venus Express ASPERA-4. *Planet. Space Sci.* 56, 780–784. doi: 10.1016/j.pss.2007.07.007

Mishra, W., and Srivastava, N. (2014). Morphological and kinematic evolution of three interacting coronal mass ejections of 2011 February 13-15. *Astrophys. J.* 794:64. doi: 10.1088/0004-637X/794/1/64

Möstl, C., Farrugia, C. J., Kilpua, E. K. J., Jian, L. K., Liu, Y., Eastwood, J. P., Harrison, R. A., Webb, D. F., Temmer, M., Odstrcil, D., et al. (2012). Multi-point shock and flux rope analysis of multiple interplanetary coronal mass ejections around 2010 August 1 in the inner heliosphere. *Astrophys. J.* 758:10. doi: 10.1088/0004-637X/758/1/10

Möstl, C., Isavnin, A., Boakes, P. D., Kilpua, E. K. J., Davies, J. A., Harrison, R. A., Barnes, D., Krupar, V., Eastwood, J. P., Good, S. W., et al. (2017). Modeling observations of solar coronal mass ejections with heliospheric imagers verified with the Heliophysics System Observatory. *Space Weather* 15, 955–970. doi: 10.1002/2017SW001614

Möstl, C., Miklenic, C., Farrugia, C. J., Temmer, M., Veronig, A., Galvin, A. B., et al. (2008). Two-spacecraft reconstruction of a magnetic cloud and comparison to its solar source. *Ann. Geophys.* 26, 3139–3152. doi: 10.5194/angeo-26-3139-2008

Nieves-Chinchilla, T., Linton, M. G., Hidalgo, M. A., Vourlidas, A., Savani, N. P., Szabo, A., et al. (2016). A circular-cylindrical flux-rope analytical model for magnetic clouds. *Astrophys. J.* 823:27. doi: 10.3847/0004-637X/823/1/27

Nieves-Chinchilla, T., Vourlidas, A., Raymond, J. C., Linton, M. G., Al-haddad, N., Savani, N. P., et al. (2018). Understanding the internal magnetic field configurations of ICMEs using more than 20 years of Wind observations. *Sol. Phys.* 293:25. doi: 10.1007/s11207-018-1247-z

Odstrcil, D., Vandas, M., Pizzo, V. J., and MacNeice, P. (2003). "Numerical simulation of interacting magnetic flux ropes,". in *Solar Wind Ten*, volume 679 of *American Institute of Physics Conference Series*, eds M. Velli, R. Bruno, F. Malara, and B. Bucci (Melville, NY: American Institute of Physics), 699–702.

Ogilvie, K. W., Chornay, D. J., Fritzenreiter, R. J., Hunsaker, F., Keller, J., Lobell, J., et al. (1995). SWE, a comprehensive plasma instrument for the Wind spacecraft. *Space Sci. Rev.* 71, 55–77. doi: 10.1007/BF00751326

Ogilvie, K. W., and Desch, M. D. (1997). The Wind spacecraft and its early scientific results. *Adv. Space Res.* 20, 559–568. doi: 10.1016/S0273-1177(97)00439-0

Owens, M. J. (2008). Combining remote and *in situ* observations of coronal mass ejections to better constrain magnetic cloud reconstruction. *J. Geophys. Res.* 113:A12102. doi: 10.1029/2008JA013589

Owens, M. J. (2009). The formation of large-scale current sheets within magnetic clouds. *Sol. Phys.* 260, 207–217. doi: 10.1007/s11207-009-9442-6

Owens, M. J., Lockwood, M., and Barnard, L. A. (2017). Coronal mass ejections are not coherent magnetohydrodynamic structures. *Sci. Rep.* 7:4152. doi: 10.1038/s41598-017-04546-3

Palmerio, E., Kilpua, E. K. J., James, A. W., Green, L. M., Pomoell, J., Isavnin, A., et al. (2017). Determining the intrinsic CME flux rope type using remote-sensing solar disk observations. *Sol. Phys.* 292:39. doi: 10.1007/s11207-017-1063-x

Palmerio, E., Kilpua, E. K. J., Möstl, C., Bothmer, V., James, A. W., Green, L. M., et al. (2018). Coronal magnetic structure of earthbound CMEs and *in situ* comparison. *Space Weather* 16, 442–460. doi: 10.1002/2017SW001767

Parker, E. N. (1958). Dynamics of the interplanetary gas and magnetic fields. *Astrophys. J.* 128:664. doi: 10.1086/146579

Pesnell, W. D., Thompson, B. J., and Chamberlin, P. C. (2012). The Solar Dynamics Observatory (SDO). *Sol. Phys.* 275, 3–15. doi: 10.1007/s11207-011-9841-3

Pevtsov, A. A., and Balasubramaniam, K. S. (2003). Helicity patterns on the Sun. *Adv Space Res.* 32, 1867–1874. doi: 10.1016/S0273-1177(03)90620-X

Pomoell, J., Lumme, E., and Kilpua, E. (2019). Time-dependent data-driven modeling of active region evolution using energy-optimized photospheric electric fields. *Sol. Phys.* 294:41. doi: 10.1007/s11207-019-1430-x

Pomoell, J., and Poedts, S. (2018). EUHFORIA: European heliospheric forecasting information asset. *J. Space Weather Space Clim.* 8:A35. doi: 10.1051/swsc/2018020

Pulkkinen, T. (2007). Space weather: terrestrial perspective. *Living Rev. Sol. Phys.* 4:1. doi: 10.12942/lrsp-2007-1

Qiu, J., Hu, Q., Howard, T. A., and Yurchyshyn, V. B. (2007). On the magnetic flux budget in low-corona magnetic reconnection and interplanetary coronal mass ejections. *Astrophys. J.* 659, 758–772. doi: 10.1086/512060

Richardson, I. G., and Cane, H. V. (2004). Identification of interplanetary coronal mass ejections at 1 AU using multiple solar wind plasma composition anomalies. *J. Geophys. Res.* 109:A09104. doi: 10.1029/2004JA010598

Richardson, I. G., and Cane, H. V. (2010). Near-earth interplanetary coronal mass ejections during solar cycle 23 (1996 - 2009): catalog and summary of properties. *Sol. Phys.* 264, 189–237. doi: 10.1007/s11207-010-9568-6

Richardson, I. G., and Cane, H. V. (2012). Solar wind drivers of geomagnetic storms during more than four solar cycles. *J. Space Weather Space Cilmate* 2:A01. doi: 10.1051/swsc/2012001

Richardson, J. D., Liu, Y., Wang, C., and Burlaga, L. F. (2006). ICMES at very large distances. *Adv. Space Res.* 38, 528–534. doi: 10.1016/j.asr.2005.06.049

Ritter, B., Meskers, A. J. H., Miles, O., Rußwurm, M., Scully, S., Roldán, A., et al. (2015). A space weather information service based upon remote and *in-situ* measurements of coronal mass ejections heading for Earth. A concept mission consisting of six spacecraft in a heliocentric orbit at 0.72 AU. *J. Space Weather Space Clim.*, 5:A3. doi: 10.1051/swsc/2015006

Ruffenach, A., Lavraud, B., Owens, M. J., Sauvaud, J.-A., Savani, N. P., Rouillard, A. P., Démoulin, P., Foullon, C., Opitz, A., Fedorov, A., et al. (2012). Multispacecraft observation of magnetic cloud erosion by magnetic reconnection during propagation. *J. Geophys. Res.* 117:A09101. doi: 10.1029/2012JA017624

Schmidt, J., and Cargill, P. (2004). A numerical study of two interacting coronal mass ejections. *Ann. Geophys.* 22, 2245–2254. doi: 10.5194/angeo-22-2245-2004

Schou, J., Scherrer, P. H., Bush, R. I., Wachter, R., Couvidat, S., Rabello-Soares, M. C., et al. (2012). Design and ground calibration of the Helioseismic and Magnetic Imager (HMI) instrument on the Solar Dynamics Observatory (SDO). *Sol. Phys.* 275, 229–259. doi: 10.1007/s11207-011-9842-2

Schrijver, C. J., Kauristie, K., Aylward, A. D., Denardini, C. M., Gibson, S. E., Glover, A., et al. (2015). Understanding space weather to shield society: a global road map for 2015-2025 commissioned by COSPAR and ILWS. *Adv. Space Res.* 55, 2745–2807. doi: 10.1016/j.asr.2015.03.023

Scolini, C., Rodriguez, L., Mierla, M., Pomoell, J., and Poedts, S. (2019). Observation-based modelling of magnetised coronal mass ejections with EUHFORIA. *Astron. Astrophys.* 626:A122. doi: 10.1051/0004-6361/201935053

Scolini, C., Verbeke, C., Poedts, S., Chané, E., Pomoell, J., and Zuccarello, F. P. (2018). Effect of the initial shape of coronal mass ejections on 3-D MHD simulations and geoeffectiveness predictions. *Space Weather* 16, 754–771. doi: 10.1029/2018SW001806

Seehafer, N. (1990). Electric current helicity in the solar atmosphere. *Sol. Phys.* 125, 219–232. doi: 10.1007/BF00158402

Shodhan, S., Crooker, N. U., Kahler, S. W., Fitzenreiter, R. J., Larson, D. E., Lepping, R. P., et al. (2000). Counterstreaming electrons in magnetic clouds. *J. Geophys. Res.* 105, 27261–27268. doi: 10.1029/2000JA000060

Siscoe, G. L., and Suey, R. W. (1972). Significance criteria for variance matrix applications. *J. Geophys. Res.* 77, 1321–1322. doi: 10.1029/JA077i007p01321

Sonnerup, B. U. O., and Cahill, L. J. Jr. (1967). Magnetopause structure and attitude from explorer 12 observations. *J. Geophys. Res.* 72:171–183. doi: 10.1029/JZ072i001p00171

Srivastava, N., Mishra, W., and Chakrabarty, D. (2018). Interplanetary and geomagnetic consequences of interacting CMEs of 13 - 14 June 2012. *Sol. Phys.* 293:5. doi: 10.1007/s11207-017-1227-8

Steed, K., Owen, C. J., Démoulin, P., and Dasso, S. (2011). Investigating the observational signatures of magnetic cloud substructure. *J. Geophys. Res.* 116:A01106. doi: 10.1029/2010JA015940

Stone, E. C., Frandsen, A. M., Mewaldt, R. A., Christian, E. R., Margolies, D., Ormes, J. F., et al. (1998). The Advanced Composition Explorer. *Space Sci. Rev.* 86, 1–22. doi: 10.1023/A:1005082526237

Svedhem, H., Titov, D. V., McCoy, D., Lebreton, J. P., Barabash, S., Bertaux, J. L., et al. (2007). Venus Express—The first European mission to Venus. *Planet. Space Sci.* 55, 1636–1652. doi: 10.1016/j.pss.2007.01.013

Thernisien, A. (2011). Implementation of the graduated cylindrical shell model for the three-dimensional reconstruction of coronal mass ejections. *Astrophys. J. Suppl. Ser.* 194:33. doi: 10.1088/0067-0049/194/2/33

Thernisien, A., Vourlidas, A., and Howard, R. A. (2009). Forward modeling of coronal mass ejections using STEREO/SECCHI data. *Sol. Phys.* 256, 111–130. doi: 10.1007/s11207-009-9346-5

Thernisien, A. F. R., Howard, R. A., and Vourlidas, A. (2006). Modeling of flux rope coronal mass ejections. *Astrophys. J.* 652, 763–773. doi: 10.1086/508254

Thompson, W. T. (2006). Coordinate systems for solar image data. *Astron. Astrophys.* 449, 791–803. doi: 10.1051/0004-6361:20054262

Törmä, O. (2016). *Laser communication concept for space weather forecasting CubeSat fleet mission*. (Ph.D. thesis), Aalto University.

Török, T., Panasenco, O., Titov, V. S., Mikić, Z., Reeves, K. K., Velli, M., et al. (2011). A model for magnetically coupled sympathetic eruptions. *Astrophys. J. Lett.* 739:L63. doi: 10.1088/2041-8205/739/2/L63

Tripathi, D., Bothmer, V., and Cremades, H. (2004). The basic characteristics of EUV post-eruptive arcades and their role as tracers of coronal mass ejection source regions. *Astron. Astrophys.* 422, 337–349. doi: 10.1051/0004-6361:20035815

Verbeke, C., Pomoell, J., and Poedts, S. (2019). The evolution of coronal mass ejections in the inner heliosphere: implementing the spheromak model with EUHFORIA. *Astron. Astrophys.* 627:A111. doi: 10.1051/0004-6361/201834702

Vourlidas, A., Balmaceda, L. A., Stenborg, G., and Dal Lago, A. (2017). Multi-viewpoint coronal mass ejection catalog based on STEREO COR2 observations. *Astrophys. J.* 838:141. doi: 10.3847/1538-4357/aa67f0

Vourlidas, A., Lynch, B. J., Howard, R. A., and Li, Y. (2013). How many CMEs have flux ropes? Deciphering the signatures of shocks, flux ropes, and prominences in coronagraph observations of CMEs. *Sol. Phys.* 284, 179–201. doi: 10.1007/s11207-012-0084-8

Vršnak, B., Žic, T., Vrbanec, D., Temmer, M., Rollett, T., Möstl, C., Veronig, A., et al. (2013). Propagation of interplanetary coronal mass ejections: the drag-based model. *Sol. Phys.* 285, 295–315. doi: 10.1007/s11207-012-0035-4

Wang, W., Zhu, C., Qiu, J., Liu, R., Yang, K. E., and Hu, Q. (2019). Evolution of a magnetic flux rope toward eruption. *Astrophys. J.* 871:25. doi: 10.3847/1538-4357/aaf3ba

Webb, D. F., Cliver, E. W., Crooker, N. U., Cry, O. C. S., and Thompson, B. J. (2000). Relationship of halo coronal mass ejections, magnetic clouds, and magnetic storms. *J. Geophys. Res.* 105, 7491–7508. doi: 10.1029/1999JA000275

Webb, D. F., and Howard, T. A. (2012). Coronal mass ejections: observations. *Living Rev. Sol. Phys.* 9:3. doi: 10.12942/lrsp-2012-3

Woltjer, L. (1958). A theorem on force-free magnetic fields. *Proc. Natl. Acad. Sci. U.S.A.* 44, 489–491. doi: 10.1073/pnas.44.6.489

Wu, C.-C., Wu, S. T., and Dryer, M. (2004). Evolution of fast and slow shock interactions in the inner heliosphere. *Sol. Phys.* 223, 259–282. doi: 10.1007/s11207-004-1108-9

Xiong, M., Zheng, H., Wu, S. T., Wang, Y., and Wang, S. (2007). Magnetohydrodynamic simulation of the interaction between two interplanetary magnetic clouds and its consequent geoeffectiveness. *J. Geophys. Res.* 112:A11103. doi: 10.1029/2007JA012320

Zhang, J., Richardson, I. G., Webb, D. F., Gopalswamy, N., Huttunen, E., Kasper, J. C., et al. (2007). Solar and interplanetary sources of major geomagnetic storms (Dst ≤ -100 nT) during 1996-2005. *J. Geophys. Res.* 112:A10102. doi: 10.1029/2007JA012321

Zhang, T. L., Baumjohann, W., Delva, M., Auster, H.-U., Balogh, A., Russell, C. T., et al. (2006). Magnetic field investigation of the Venus plasma environment: Expected new results from Venus Express. *Planet. Space Sci.* 54, 1336–1343. doi: 10.1016/j.pss.2006.04.018

Zhang, T. L., Pope, S., Balikhin, M., Russell, C. T., Jian, L. K., Volwerk, M., et al. (2008). Venus Express observations of an atypically distant bow shock during the passage of an interplanetary coronal mass ejection. *J. Geophys. Res.* 113:E00B12. doi: 10.1029/2008JE003128

Zurbuchen, T. H., and Richardson, I. G. (2006). *In-situ* solar wind and magnetic field signatures of interplanetary coronal mass ejections. *Space Sci. Rev.* 123, 31–43. doi: 10.1007/978-0-387-45088-9-3

Zwickl, R. D., Asbridge, J. R., Bame, S. J., Feldman, W. C., Gosling, J. T., and Smith, E. J. (1983). "Plasma properties of driver gas following interplanetary shocks observed by ISEE-3." in *NASA Conference Publication*, *JPL Solar Wind Five*, *Vol 228,* ed M. Neugebauer (Washington, DC: NASA), 711–717.

Conflict of Interest Statement: The authors declare that the research was conducted in the absence of any commercial or financial relationships that could be construed as a potential conflict of interest.

frontiers in Physics

ORIGINAL RESEARCH
published: 04 October 2019
doi: 10.3389/fphy.2019.00151

Coalescence of Magnetic Flux Ropes Within Interplanetary Coronal Mass Ejections: Multi-cases Studies

Yan Zhao [1,2], Hengqiang Feng [1,2], Qiang Liu [1,2] and Guoqing Zhao [1,2]*

[1] Institute of Space Physics, Luoyang Normal University, Luoyang, China, [2] Henan Key Laboratory of Electromagnetic Transformation and Detection, Luoyang, China

Coronal mass ejections (CMEs) are intense solar explosive eruptions and have significant impact on geomagnetic activities. It is important to understand how CMEs evolve as they propagate in the solar-terrestrial space. In this paper, we studied the coalescence of magnetic flux ropes embedded in five interplanetary coronal mass ejections (ICMEs) observed by both ACE and Wind spacecraft. The analyses show that coalescence of magnetic flux ropes could persist for hours and operate in scale of hundreds of earth radii. The two merging flux ropes could be very different in the axial orientation and the plasma density and temperature, which should complicate the progress of coalescence and have impact on the merged structures. The study indicates that coalescence of magnetic flux ropes should be an important factor in changing the magnetic topology of ICMEs.

Keywords: interplanetary coronal mass ejection, magnetic flux rope, coalescence, magnetic reconnection, magnetic clouds

OPEN ACCESS

Edited by:
Rui Liu,
University of Science and Technology of China, China

Reviewed by:
Qiang Hu,
University of Alabama in Huntsville, United States
Fang Shen,
National Space Science Center (CAS), China

****Correspondence:***
Hengqiang Feng
fenghq9921@163.com

Specialty section:
This article was submitted to Space Physics, a section of the journal Frontiers in Physics

Received: *29 June 2019*
Accepted: *19 September 2019*
Published: *04 October 2019*

Citation:
Zhao Y, Feng H, Liu Q and Zhao G (2019) Coalescence of Magnetic Flux Ropes Within Interplanetary Coronal Mass Ejections: Multi-cases Studies. Front. Phys. 7:151. doi: 10.3389/fphy.2019.00151

KEY POINTS

1. Coalescence of magnetic flux ropes within five interplanetary coronal mass ejections was studied.
2. The process of coalescence could be steady and large-scaled.
3. The process of coalescence is an important factor in changing the magnetic topology of interplanetary coronal mass ejections.

INTRODUCTION

Coronal mass ejections (CMEs) are large-scale solar explosive eruptions and their counterparts in the interplanetary space, interplanetary coronal mass ejections (ICMEs), are known to be an important cause of intense geomagnetic disturbances [1–3]. The geomagnetic effectiveness of ICMEs has strongly relation with their magnetic structures. For example, Magnetic Clouds (MCs), a subset of ICMEs, are found to be more effective than non-MC ICMEs in causing intense geomagnetic storms [4]. CMEs are thought to originally be of magnetic flux rope structures (e.g., [5–7]). However, ICMEs appearing as flux rope (i.e., MCs) only account for 30−40% of ICMEs observed at 1 AU [8, 9]. Therefore, understanding how CMEs evolve as they propagate in the solar-terrestrial space is very important for the space weather forecasting.

As an ICME propagates in the interplanetary space, its interaction with ambient solar wind or being caught up by other ICMEs from behind can cause the change of its magnetic topology [10–17]. Multiple rope-like substructures have been detected within ICMEs [18–22]. Feng et al. [22] reported observations of three merging flux ropes within an ICME and they thought that the coalescence would lead to the

formation of a bigger rope. However, the potential of coalescence of flux ropes in altering the magnetic topology (e.g., the scale of coalescence in space and time) is still unclear.

Phan et al. [23] made a statistical study of extended reconnection X-lines in the solar wind at 1 AU with the combined observations of ACE and Wind spacecraft. In the work presented here, we surveyed the reconnection current sheet listed in Phan et al. [23] and found five of them were formed during coalescence of magnetic flux ropes embedded in ICMEs. The analyses show that the operation of coalescence can extend hundreds of earth radii and persist for several hours. The two merging flux ropes could be very different in some aspects. We think that coalescence of flux ropes should play important roles in the evolution of ICMEs.

DATA

The data used in this paper are obtained from several instruments onboard ACE and Wind spacecraft. Wind magnetic field data and plasma data with time resolution of 3 s are taken from the Fluxgate Magnetometer experiment and the 3DP instrument, respectively [24, 25]. ACE magnetic field data (1 and 16 s resolution) are from MAG and plasma data (64 s resolution) are from SWEPAM instrument [26, 27]. If not specified, the GSE coordinate system (the Geocentric Solar Ecliptic coordinate system in which the x-axis directs from the Earth to the Sun, the z-axis points north, perpendicular to the ecliptic plane, the y-axis completes the right-handed coordinate system) is used in this paper.

OBSERVATIONS

In this section we first show one example to illustrate the identification of ICMEs and the merging flux ropes, then the procedure for estimating the X-line length formed during the coalescence progress and the other four cases are presented.

Figure 1 shows observations made by ACE (black) and Wind (red) from Oct. 3rd, 2000 to Oct. 5th, 2000. For clarity, the time series of ACE are shifted 110 min forward. During the whole interval showed in **Figure 1**, the data curves of the magnetic field and plasma at the two spacecraft were generally similar. From ∼12:00 on Oct. 3rd (the first vertical line), the magnetic field became smoother and its strength gradually increased (**Figures 1a–d**). In the meantime, the proton temperature and the plasma beta values dropped (**Figures 1i,j**). At ∼03:00 on Oct. 5th (the second vertical line), the speed of the plasma, the proton temperature and the plasma beta values suddenly increased (**Figures 1e,i,j**). Based on the above observations, we think the spacecraft encountered an ICME during the interval bounded by the two dashed vertical lines.

During the two intervals covered by the orange color, the magnetic field rotated. For the first orange region, B_z gradually increased from −2 nT to 7 nT (**Figure 1d**). For the second orange region, B_y gradually increased from −6 to 15 nT (**Figure 1c**) and B_z first increased to 15 nT, then decreased to −8 nT (**Figure 1d**). Along with the rotation, the strength of the magnetic

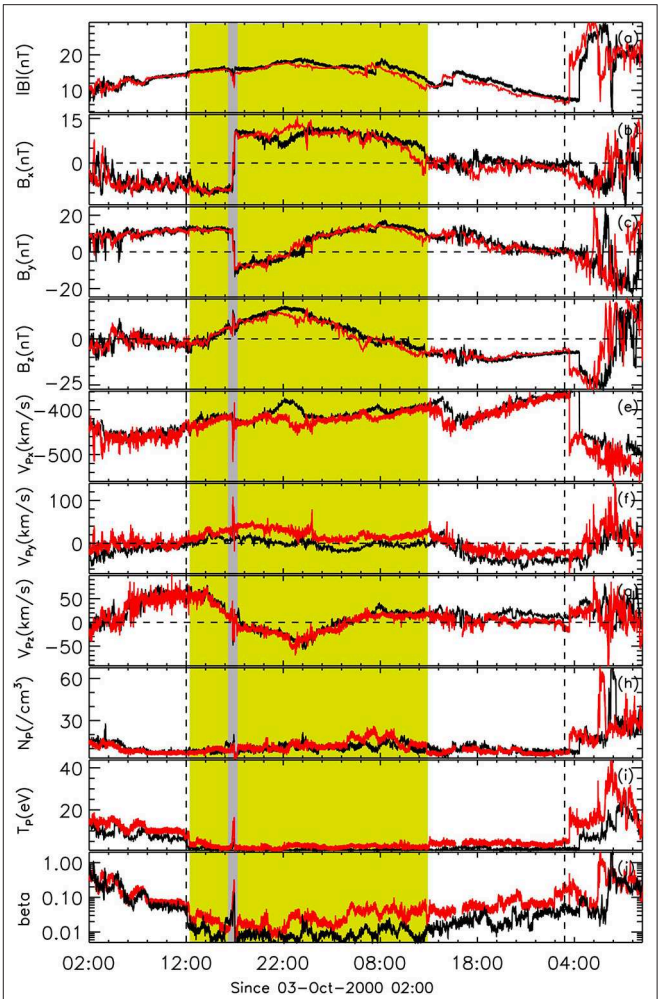

FIGURE 1 | Measurements of ACE (black) and Wind (red) from 02:00 UT on Oct 03 to 11:00 UT on Oct 05, 2000. The observations of ACE have been shifted 110 min for forward. **(a–d)** Magnitude and three components of the magnetic field. **(e–g)** Three components of plasma velocity. **(h–j)** Proton density, temperature and proton plasma beta values. The two vertical dashed lines indicates the boundary of the ICME. the two orange regions denote the two merging flux ropes. The shadow region denotes the reconnection current sheet intermediating the calescence.

field enhanced. The rotation of the magnetic field and the concurrent enhancement in its strength indicated that the two orange regions corresponded to crossing of two flux ropes. With the assumption of two dimension and quasi-steady state, the axis of a flux rope can be determined by Grad-Shafranov (G-S) reconstruction method [28]. According to the G-S equation, the thermal pressure and the magnetic pressure are constant along one magnetic field line in the plane perpendicular to the axial direction [28]. Applying the G-S reconstruction method to the data of the two orange regions, the obtained axis of the two flux ropes was ($\varphi = 116.08, \theta = 19.45$) for the earlier, and ($\varphi = 1.82, \theta = 29.88$) for the latter, where φ and θ are the longitude and latitude with respect to the ecliptic plane.

In the intermediate region (the shadow region) between the two magnetic flux ropes, the spacecraft detected steep

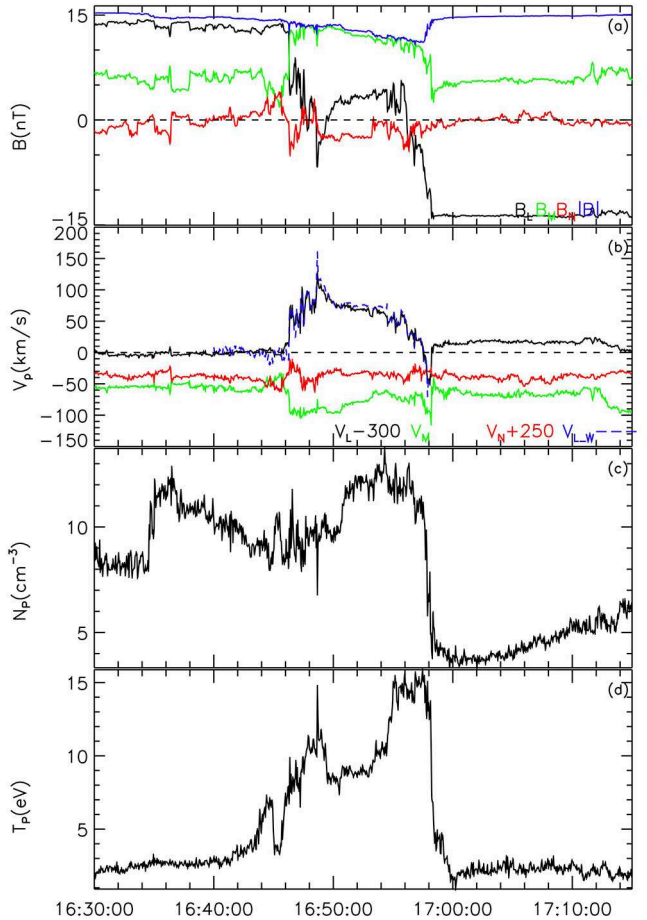

FIGURE 2 | The enlarged vision of current sheet (the shadow region in **Figure 1**) in the *LMN* coordinate system. **(a)** Magnitude (blue) and three components of the magnetic field, *L* (black), *M* (green), and *N* (red). **(b)** Three components of plasma velocity. The dashed blue line represent the velocity predicted by walen relation. Note that the origin data curves have been shifted up or down for clarity. **(c–d)** The proton density and temperature.

changes in B_x and B_y with B_x jumping from −9 to 11 nT and B_y dropping from 12 to −10 nT (**Figures 1b,c**). Meanwhile, the plasma velocity in the V_x and V_y component locally peaked (**Figures 1e,f**). The proton temperature and the plasma beta values also showed a local peak (**Figures 1i,j**). The above observations indicated that the spacecraft might cross exhaust of magnetic reconnection, which can be more clearly in **Figure 2**.

In **Figure 2**, all vectors are presented in a local *LMN* coordinate system, where *L* was assumed to be along the reconnection outflow direction, *M* along the X-line direction and *N* along the normal direction of the reconnection current sheet. *N* was determined by minimum variance analysis of the magnetic field across the current sheet [29] and that *M* was chose so that the *M* components of the in-plane asymptotical magnetic field in both sides of the current sheet are same [30]. $L = M \times N$ forms the right-hand coordinate system. The most remarkable feature of the magnetic field is the two-step decrease in B_L (**Figure 2a**), which corresponded to a bifurcated current sheet. Within the current sheet, the proton temperature increased (**Figure 2d**). The changes in V_L (**Figure 2b**) during the crossing of the current sheet were consistent with these predicted (the dashed lines) by walén relation, which were calculated from the following equation [31, 32]:

$$V_{predicted} = V_{reference} \pm (1 - \alpha_{reference})^{1/2} (1 - \mu_0 \rho_{reference})^{-1/2} (B\rho_{reference}/\rho - B_{reference})$$

Note that the pressure anisotropy factor, α, was assumed to be zero. Therefore, we thought that the spacecraft crossed exhaust of magnetic reconnection [33]. Detection of the reconnection current sheet between two flux ropes indicated that the two flux ropes were merging [22].

Adopting a similar procedure as that in Phan et al. [32], the extent of the X-line associated with the coalescence was estimated. The reconnection current sheet intermediating the coalescence was assumed to be planar and its normal direction obtained by minimum variance analysis was ($\varphi = 41.19, \theta = -17.41$). The separation of the two ships was [193, 223, −3.8] R_E in GSE. Using this normal direction and the planar assumption, the predicted temporal delay from ACE to Wind was 103 min which was close to the observed temporal delay, 110 min. This agreement indicated that the obtained normal direction and the planar assumption were valid. The direction of the X-line, *M* was ($\varphi = 52.55, \theta = 72.26$) [30]. With the knowledge of *N*, *M* and the separation of the two ships, the distance along the X-line between the locations where the two ships intersected the current sheet was calculated to be 14 R_E, which meant that the extend of the coalescence in space was at least 14 R_E. The temporal delay between the two ships was ∼110 min and the interval covered by the reconnection current sheet was ∼12 min. Therefore, the progress of coalescence at least operated for 122 min.

With similar procedure, another four events of coalescence of flux ropes within an ICME were analyzed. The four events and the reconnection current sheet intermediating the coalescence are, respectively, presented in **Figures 3**, **4**. Some of the five ICMEs have been studied by other researches [21, 22]. The details of the five cases are listed in **Table 1**. These cases were different in some aspects. The interval of the two merging flux ropes only occupied a small portion (∼23%) of the whole duration of the ICME in Apr. 2000 (**Figure 3B**). However, for the other four cases, the two merging flux ropes occupied most of the ICME that they were embedded in **Figures 1**, **3A,C,D**. The angle formed by the axes of the two merging flux ropes varied from case to case with a range from ∼70° to ∼160° (**Table 1**, in column Fr2-to-fr1). The plasma carried by the merging flux ropes could also be different in temperature and density (**Figures 3Ah,Ci,Dh**). For example, the plasma density was much higher in the latter flux ropes than that in the former one for the case in Mar. 1998 (**Figure 3Ah**). There were also significant differences in the estimated mini duration of the magnetic reconnection and length of X-line associated

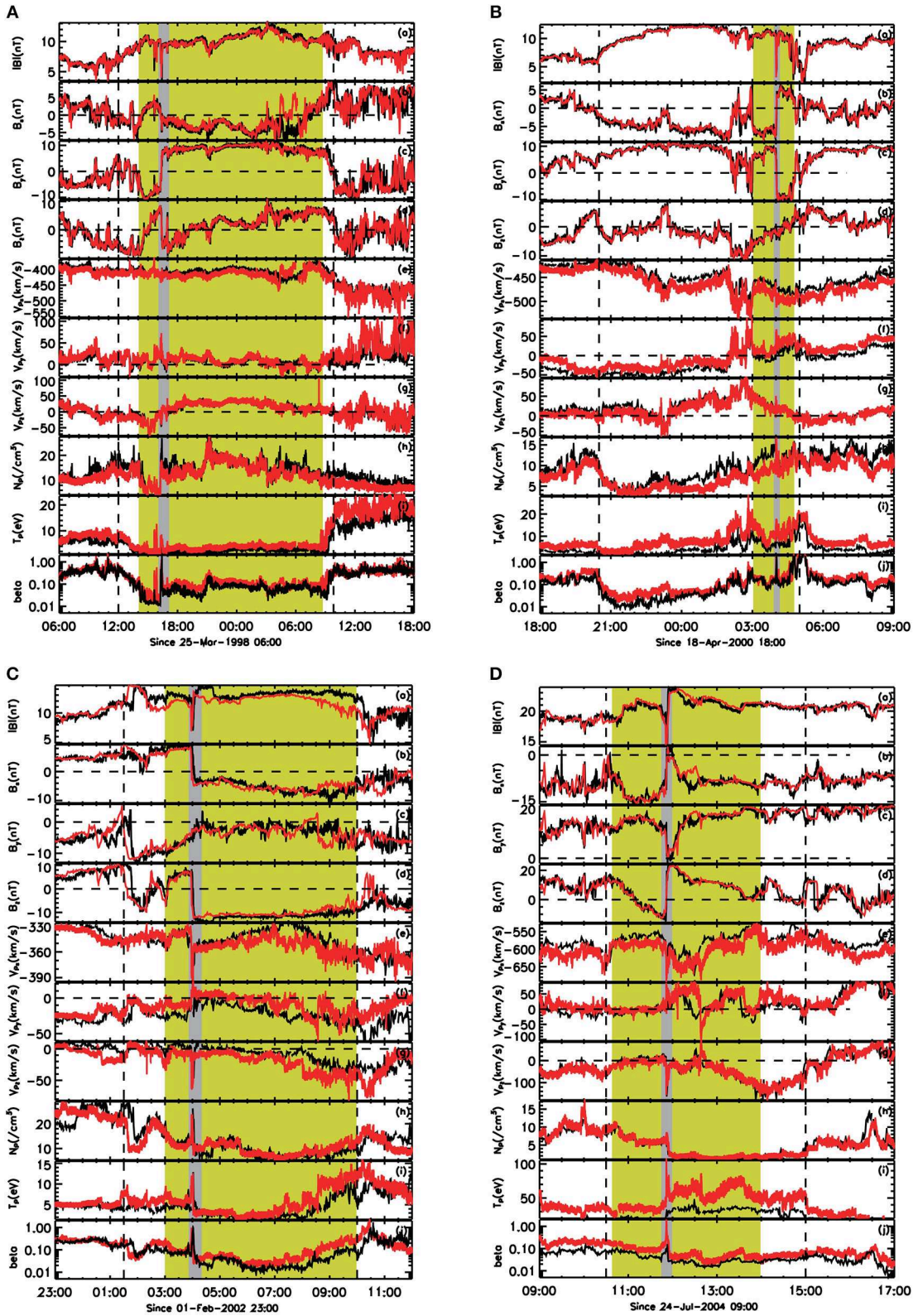

FIGURE 3 | The other four ICMEs in Mar. 1998 **(A)**, Apr. 2000 **(B)**, Feb. 2002 **(C)**, and Jul. 2004 **(D)**. The observations of ACE have been shifted 5 min for case **A** (28 min for case **B**, 147 min for case **C**, −13 min for case **D**) forward. For each case, the figure format is similar to **Figure 1**.

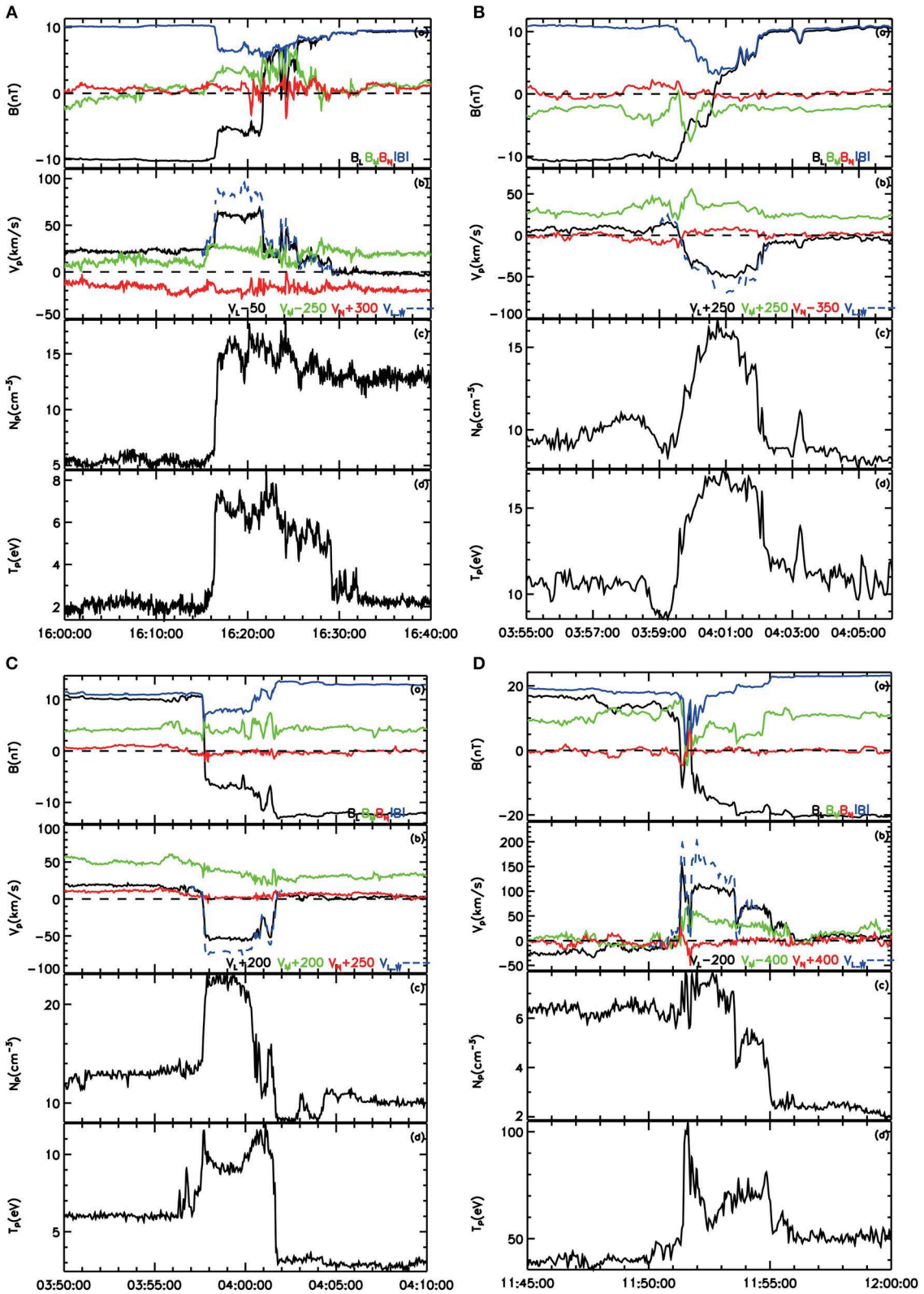

FIGURE 4 | The reconnection current sheet intermediating the coalescence of flux ropes in ICME **(A–D)**. For each case, the figure format is similar to **Figure 2**.

with the coalescence (**Table 1**, in columns len and dur). For example, the duration and the length were 34 min and 8 R_E, respectively, for the case in Apr. 2004, while for the case in Feb. 2002, the values were 150 min and 393 R_E, respectively. Finally, the density and temperature of plasma were not symmetric on both side of the reconnection current sheet in some cases (e.g., **Figures 4Ac,Cd,Dc**).

DISCUSSION AND CONCLUSION

ICMEs consisting of multiple flux ropes have been reported [20, 21]. Recently, Feng et al. [22] reported observations of an ICME within which a series of merging flux ropes was detected. They thought the coalescence would lead to the formation of bigger ropes in the ICME. However, if the magnetic reconnection intermediating the coalescence is patchy and transient, the change made by coalescence in the magnetic topology of ICMEs will be localized in space. The cases presented here shows that coalescence of magnetic flux ropes can operate in scale of hundreds of Earth radii and persist for hundreds of minutes. Note that the presented values in scale and duration of coalescence were likely to be much underestimated. Therefore, the progress of coalescence should be an important factor in the evolution of CMEs, If CMEs originally are of magnetic flux rope structures.

Simulations show that coalescence of magnetic flux ropes with same axis direction will end up with one bigger rope [14, 34]. The case in the real interplanetary space shall be more complex. In Feng et al. [22], the axis of the first two merging flux ropes had nearly opposite directions, which they thought the coalescence may lead to the formation of a bigger rope with weak axial field. For the five case reported here, the axes of the two merging flux ropes were not parallel but formed an angle ranging from $\sim 70^\circ$ to $\sim 160^\circ$. The direction of the X-line also formed big angles with the ropes' axis (the last column in **Table 1**). The relative attitude of the two merging flux ropes should have significant impact on the structures formed by the process of coalescence. Awasthi et al. [35] reported a non-MC ICME whose pre-eruptive structure consisted of multiple-braided flux ropes with different degrees and they thought reconnection occurring between these flux ropes was responsible for the complex structure of the ICME. The presented results are consistent with the observations in Awasthi et al. [35]. The difference in the plasma (e.g., in the temperature and density) carried by the merging flux ropes could cause asymmetric conditions at both side of the reconnection current sheet (**Figures 4Ac,Cd,Dc**), which may further complicate the progress of coalescence.

In summary, we reported five ICMEs observed by both ACE and Wind spacecraft, within which merging flux ropes were detected. The coalescence of magnetic flux ropes could be steady and large scale. The two merging ropes could be different in the axial orientation and the plasma density and temperature. The results showed here indicates that coalescence of magnetic flux ropes is an important factor for understanding of the evolution of CMEs.

TABLE 1 | A list of the parameters of the five ICMEs.

Case	Year	ICME		Fr1				Fr2				CS			X-line			
		sta	end	sta	end	lon	lat	sta	end	lon	lat	to-fr1	time	lon	lat	lon	lat	len	dur	to-fr1
1	1998	03/25 12:00	03/26 09:50	03/25 14:00	03/25 16:00	260	−10	03/25 16:40	03/26 09:20	96	19	162.10	03/25 16:16:16	32.66	22.30	141.31	37.94	17	18	118.66
2	2000	04/18 20:30	04/19 05:00	04/19 03:00	04/19 03:56	140.67	−13.08	04/19 04:07	04/19 04:40	278.65	5.32	137.86	04/19 03:59:19	210.80	32.78	23.73	57.02	8	34	115.47
3	2000	10/03 12:00	10/05 02:00	10/03 12:15	10/03 16:20	116.08	19.45	10/03 17:17	10/04 13:00	1.82	29.88	99.79	10/03 16:45:35	41.19	−17.41	52.55	72.26	14	122	63.56
4	2002	02/02 01:30	02/02 10:00	02/02 03:00	02/02 03:50	332.67	25.4	02/02 04:17	02/02 10:00	306.49	−71.77	98.85	02/02 03:57:10	40.20	−21.70	300.75	−22.99	393	150	57.48
5	2004	07/24 10:30	07/24 15:00	07/24 10:40	07/24 11:43	123.06	−15.21	07/24 11:58	07/24 14:00	88.29	49.66	71.75	07/24 11:51:19	46.22	−4.02	134.71	20.58	55	19	37.57

Fr1, the first flux rope encountered by spacecraft within the ICME; Fr2, the second flux rope encountered by spacecraft within the ICME; CS, the reconnection current sheet detected between Fr1 and Fr2; sta, the start date and time of the structure; end, the end date and time of the structure; lon, the longitude of the axis of the flux rope (/normal of the current sheet/ the direction of X-line) with respect to the ecliptic plane, in degrees; lat, the latitude of the axis of the flux rope (/normal of the current sheet/ the direction of X-line) with respect to the ecliptic plane, in degrees; t-fr1, the angle of the direction of the axis of Fr2 (X-line) to the axis of Fr1, in degrees; time, the time when cs was observed; len, the estimated length of x-line, in earth radii; dur, minimum duration of reconnection, in minutes.

AUTHOR CONTRIBUTIONS

YZ drafted the manuscript and led the observational analysis. HF provided heuristic advice and revised the manuscript. QL and GZ conducted the G-S reconnection. All authors contributed to the interpretation of the results and helped draft the manuscript.

ACKNOWLEDGMENTS

We acknowledge supports from NSFC under grant Nos. 41674170, 41804162, and 41974197. We thank NASA/GSFC for the use of data from the Wind. These data can obtain freely from the Coordinated Data Analysis Web (http://cdaweb.gsfc.nasa.gov/cdaweb/istp_public/).

REFERENCES

1. Tsurutani BT, Gonzalez WD, Tang F, Akasofu SI, Smith EJ. Origin of interplanetary southward magnetic fields responsible for major magnetic storms near solar maximum (1978–1979). *J Geophys Res.* (1988) **93**:8519–31. doi: 10.1029/JA093iA08p08519
2. Gonzalez WD, Tsurutani BT, Clúa de Gonzalez AL. Interplanetary origin of magnetic storms. *Space Sci Rev.* (1999) **88**:529–62. doi: 10.1023/A:1005160129098
3. Zhang J, Dere KP, Howard RA. Identification of Solar Sources of Major Geomagnetic Storms between 1996 and 2000. *Astrophys J.* (2008) **582**:520. doi: 10.1086/344611
4. Gonzalez WD, Echer E, Clua-Gonzalez AL, Tsurutani BT. Interplanetary origin of intense geomagnetic storms (Dst<-100 nT) during solar cycle 23. *Geophys Res Lett.* (2007) **34**:L06101. doi: 10.1029/2006GL028879
5. Rust DM, Kumar A. Evidence for helically kinked magnetic flux ropes in solar eruptions. *Astrophys J.* (2009) **464**:L199. doi: 10.1086/310118
6. Liu R, Chang L, Wang S, Na D, Wang H. Sigmoid-to-flux-rope transition leading to a loop-like coronal mass ejection. *Astrophys J Lett.* (2010) **725**:L84–90. doi: 10.1088/2041-8205/725/1/L84
7. Zhang J, Cheng X, Ding M. Observation of an evolving magnetic flux rope before and during a solar eruption. *Nat. Commun.* (2012) **3:**747. doi: 10.1038/ncomms1753
8. Gosling J. Coronal mass ejections and magnetic flux ropes in interplanetary space. *Phys Magn Flux Ropes.* (1990) **A92–31201**:12–75. doi: 10.1029/GM058p0343
9. Mulligan T, Russell CT, Gosling J. On interplanetary coronal mass ejection identification at 1AU. In: *AIP Conference Proceedings*. Melville, NY: AIP (1999). p. 693–6. doi: 10.1063/1.58659
10. Farrugia C, Berdichevsky D. Evolutionary signatures in complex ejecta and their driven shocks. *Ann Geophys.* (2004) **22**:3679–98. doi: 10.5194/angeo-22-3679-2004
11. Feng HQ, Wu DJ, Wang JM, Chao JK. Magnetic reconnection exhausts at the boundaries of small interplanetary magnetic flux ropes. *Astron Astrophys.* (2011) **527**:A67. doi: 10.1051/0004-6361/201014473
12. Gopalswamy N, Yashiro S, Kaiser ML, Howard RA, Bougeret JL. Radio signatures of coronal mass ejection interaction: coronal mass ejection cannibalism?. *Astrophy J.* (2001) **548**:L91–4. doi: 10.1086/318939
13. Gopalsamy N, Yashiro S, Kaiser ML, Howard RA, Bougeret JL. Interplanetary radio emission due to interaction between two coronal mass ejections. *Geophys Res Lett.* (2002) **29**:1265–8. doi: 10.1029/2001GL013606
14. Odstrcil D, Vandas M, Pizzo VJ, MacNeice P. Numerical simulation of interacting magnetic flux ropes. In: Velli M, Bruno R, Malara F, editors. *SOLARWIND 10, AIP Conference Proceedings*. Melville, NY: AIP (2003). p. 699–702. doi: 10.1063/1.1618690
15. Temmer M, Vrsnak B, Amerstorfer T, Bein B. Characteristics of kinematics of a coronal mass ejection during the 2010 August 1 CME-CME interaction event. *Astrophys J.* (2012) **749**:57. doi: 10.1088/0004-637X/749/1/57
16. Liu YD, Yang Z, Wang R, Luhmann JG, Richardson JD, Lugaz N. Sun-to-Earth characteristics of two coronal mass ejections interacting near 1 au: formation of a complex ejecta and generation of a two-step geomagnetic storm. *Astrophys J.* (2014) **793**:L41–6. doi: 10.1088/2041-8205/793/2/L41
17. Ruffenach A, Lavraud B, Farrugia CJ, Demoulin P, Dasso S, Owens MJ, et al. Statistical study of magnetic cloud erosion by magnetic reconnection. *J Geophys Res.* (2015) **120**:43–60. doi: 10.1002/2014JA020628
18. Fainberg J, Osherovich VA, Stone RC, MacDowall RJ. Ulysses observations of electron and proton components in a magnetic cloud and related wave activity. In: Winterhalter D, Gosling JT, Habbal SR, Kurth WS, Neugebauer M, editors. *Proceeding Solar Wind 8 Conference, Dana Point*. Melville, NY: AIP (1996). p. 554–7. doi: 10.1063/1.51513
19. Osherovich VA, Fainberg J, Stone RG. Multi-tube model for interplanetary magnetic clouds. *Geophys Res Lett.* (1999) **26**:401–4. doi: 10.1029/1998GL900306
20. Hu Q, Smith CW, Ness NF, Skoug RM. Multiple flux rope magnetic ejecta in the solar wind. *J Geophys Res.* (2004) **109**:A03102. doi: 10.1029/2003JA010101
21. Chian AC-L, Feng HQ, Hu Q, Loew MH, Miranda RA, Muñoz PR, et al. Genesis of interplanetary intermittent turbulence: a case study of rope-rope magnetic reconnection. *Astrophys J.* (2016) **832**:179. doi: 10.3847/0004-637X/832/2/179
22. Feng H, Zhao Y, Zhao G, Liu Q, Wu D. Observations on a series of merging magnetic flux ropes within an interplanetary coronal mass ejection. *Geophys Res Lett.* (2019) **146**:5–10. doi: 10.1029/2018GL080063
23. Phan TD, Gosling JT, Davis MS. Prevalence of extended reconnection X-lines in the solar wind at 1 AU. *Geophys Res Lett.* (2009) **36**:L09108. doi: 10.1029/2009GL037713
24. Lepping RP, Acuna MH, Burlaga LF, Farrell WM, Slavin JA, Schatten KH, et al. The wind magnetic field investigation, edited by Russell, C. T. *Space Sci Rev.* (1995) **71**:207–29. doi: 10.1007/BF00751330
25. Lin RP, Anderson KA, Ashford S, Carlson C, Curtis D, Ergun R, et al. A three-dimensional plasma and energetic particle investigation for the wind spacecraft. *Space Sci Rev.* (1995) **71**:125–53. doi: 10.1007/BF00751328
26. Mccomas DJ, Bame SJ, Barker P, Feldman WC, Phillips JL, Riley P, et al. Solar wind Electron Proton Alpha Monitor (SWEPAM) for the advanced composition explorer. *Space Sci Rev.* (1998) **86**:563–612. doi: 10.1023/A:1005040232597
27. Smith CW, L'Heureux JL, Ness NF, Acuña MH, Burlaga LF, Scheifele J. The ace magnetic fields experiment. *Space Sci. Rev.* (1998) **86**:613–32. doi: 10.1007/978-94-011-4762-0_21
28. Hu Q, Sonnerup BUÖ. (2002). Reconstruction of magnetic clouds in the solar wind: orientation and configuration. *J Geophys Res.* **107**:10–5. doi: 10.1029/2001JA000293
29. Sonnerup BUÖ, Cahill LJ. Magnetopause structure and attitude from explorer 12 observations. *J Geophys Res.* (1967) **72**:171–83. doi: 10.1029/JZ072i001p00171
30. Sonnerup BUÖ. Magnetopause reconnection rate. *J Geophys Res.* (1974) **79**:1546–9. doi: 10.1029/JA079i010p01546
31. Paschmann G, Papamastorakis I, Baumjohann W, Sckopke N, Carlson CW, Sonnerup BUÖ, et al. The magnetopause for large magnetic shear: AMPTE/IRM observations. *J Geophys Res.* (1986) **91**:11099–115. doi: 10.1029/JA091iA10p11099

32. Phan TD, Gosling JT, Davis MS, Skoug RM, Øieroset M, Lin RP, et al. A magnetic reconnection X-line extending more than 390 Earth radii in the solar wind. *Nature*. (2006) **439**:175. doi: 10.1038/nature04393
33. Gosling JT, Skoug RM, McComas DJ, Smith CW. Direct evidence for magnetic reconnection in the solar wind near 1 AU. *J Geophys Res.* (2005) **110**:A01107. doi: 10.1029/2004JA010809
34. Schmidt J, Cargill P. A numerical study of two interacting coronal mass ejections. *Ann Geophys.* (2004) **22**:2245–54. doi: 10.5194/angeo-22-2245-2004
35. Awasthi AK, Liu R, Wang H, Wang Y, Shen C. Pre-eruptive magnetic reconnection within a multi-flux-rope System in the Solar Corona. *Astrophys J.* (2018) **857**:124. doi: 10.3847/1538-4357/aab7fb

Conflict of Interest: The authors declare that the research was conducted in the absence of any commercial or financial relationships that could be construed as a potential conflict of interest.

frontiers in Astronomy and Space Sciences

ORIGINAL RESEARCH
published: 09 October 2019
doi: 10.3389/fspas.2019.00063

Reconstruction of a Highly Twisted Magnetic Flux Rope for an Inter-active-region X-Class Solar Flare

Chaowei Jiang[1]*, *Aiying Duan*[2], *Xueshang Feng*[3], *Peng Zou*[1], *Pingbing Zuo*[1] and *Yi Wang*[1]

[1] Institute of Space Science and Applied Technology, Harbin Institute of Technology, Shenzhen, China, [2] School of Atmospheric Sciences, Sun Yat-sen University, Zhuhai, China, [3] SIGMA Weather Group, State Key Laboratory for Space Weather, National Space Science Center, Chinese Academy of Sciences, Beijing, China

Solar eruptions are manifestation of explosive release of magnetic energy in the Sun's corona. Large solar eruptions originate mostly within active regions, where strong magnetic fields concentrate on the solar surface. Here we studied the magnetic field structure for an exception, which is a peculiar GOES X1.2 flare accompanied with a very fast coronal mass ejection taking place between two active regions, where the magnetic field is relatively weak. The pre-flare magnetic field is reconstructed from the SDO/HMI vector magnetogram, using a non-linear force-free field extrapolation method. It is found that prior to the flare, there is a highly twisted magnetic flux rope with magnetic field lines winding over 6 turns, which connects the border of a leading sunspot of one active region and the following polarity of the neighboring active region. The basic configuration of the flux rope is consistent with the observed sigmoidal coronal loops and filament channels by SDO/AIA. It resides rather low-lying between the active regions such that the torus instability is not able to be triggered. Thus, it is likely that, due to the strong magnetic twist, the kink instability of the flux rope triggers the eruption.

Keywords: magnetic fields, methods: numerical, sun: corona, sun: flares, sun: filaments

OPEN ACCESS

Edited by:
Rui Liu,
University of Science and Technology of China, China

Reviewed by:
Satoshi Inoue,
Nagoya University, Japan
Yingna Su,
Purple Mountain Observatory (Chinese Academy of Sciences), China

***Correspondence:**
Chaowei Jiang
chaowei@hit.edu.cn

Specialty section:
This article was submitted to Stellar and Solar Physics, a section of the journal Frontiers in Astronomy and Space Sciences

Received: *26 June 2019*
Accepted: *19 September 2019*
Published: *09 October 2019*

Citation:
Jiang C, Duan A, Feng X, Zou P, Zuo P and Wang Y (2019) Reconstruction of a Highly Twisted Magnetic Flux Rope for an Inter-active-region X-Class Solar Flare. Front. Astron. Space Sci. 6:63. doi: 10.3389/fspas.2019.00063

1. INTRODUCTION

The catastrophic energy-conversion phenomena, such as solar flares and coronal mass ejections (CMEs) from the sun can heavily influence the space weather and human activities in modern society. Now it is well-recognized that the Sun's magnetic field plays a key role in such solar explosive transients (Forbes et al., 2006; Chen, 2011; Shibata and Magara, 2011; Cheng et al., 2017; Guo et al., 2017), thus it is paramount to understand the underlying magnetic field structure for a reliable forecast of solar eruptions. Strong flares and CMEs originated mostly from solar active regions (ARs), where high concentrations of magnetic field clusters (Toriumi and Wang, 2019). In particular, major flares (e.g., those above GOES X-class) occurred predominantly from the site of magnetic polarity inversion lines (PILs) at the photosphere which possess strong magnetic shear as well as high magnetic gradient. Such PILs are often found in δ-sunspot groups (that is, two sunspots with inverse signs of magnetic polarity share the same penumbra), possibly as a result of colliding of magnetic flux tubes during their emergence from right below the photosphere (Fang and Fan, 2015).

However, there are exceptions, although rather few. By surveying the flare events above GOES M5 with 45° from the disk center between 2010 and 2016 (Toriumi et al., 2017), it is found that, out of a total number of 51 flares, there are 2 events that took place between ARs where the PIL is in a relatively weak field without significant magnetic shear and gradient. Among them is an X1.2 flare, and this inter-AR flare produced an extremely fast CME (above 1,800 km/s). From a space weather perspective, this is an important event as forecasters expected a significant impact (a G3 class geomagnetic storm or higher) on the Earth, yet it did not occur. Thus, attentions have been attracted in many papers to study the CME propagation, attempting to reveal why it is significantly deflected from the solar disk center to the Mars by a longitude of over 40° (Mays et al., 2015; Möstl et al., 2015; Wang et al., 2015; Zheng et al., 2016; Zagainova and Fainshtein, 2018). Nevertheless, it is still not clear what is the source magnetic field structure that triggers the eruption. Why such a weak field region can produce such strong flare and fast CME?

In this paper, using a coronal magnetic field reconstruction method, we reveal that prior to the flare, there is a highly twisted magnetic flux rope (MFR) with magnetic twist number reaching over 6 turns. Overall, the configuration of MFR is consistent with the observed sigmoidal coronal loops and filament channels, and it is likely the source structure leading to the eruption of the flare and CME through kink instability. The rest of the paper is organized as follows: section 2 present the observations; section 3 gives a brief description of the coronal magnetic reconstruction method; section 4 shows the reconstructed MFR, and finally conclusions are made in section 5.

2. OBSERVATIONS

The X1.2 flare occurred between two neighboring ARs, numbered as NOAA 11944 and 11943, on 2014 January 7, associated with a very fast halo CME with linear speed of ∼1,830 km/s. **Figure 1** shows the source region and the flare loops observed by the *Solar Dynamics Observatory* (*SDO*), as well as the CME observed by STEREO. The flare started at 18:04 UT, peaked at 18:32 UT and ended at 18:58 UT. As shown in **Figure 1**, the flare site (or the CME source region) is located at S12W08, which is close to the disk center, between the ARs 11944 (S09W01) and 11943 (S11W19).

In **Figure 2**, we further show the source region with *SDO*/HMI magnetogram. Three ARs cluster forming a complicate system, which is usually very active for eruptions because of the underlying complex magnetic topology. There are mainly four polarities of two pairs forming the ARs 11944 and 11943, respectively. The leading sunspot of AR 11944 has a positive polarity (P1, which has a field strength up to ∼3,000 G), and a high-gradient PIL divides it with its following sunspot of polarity N1. However, the X1.2 flare did not take place along this strong-gradient PIL. Rather, it occurred mainly along the relatively weak-gradient PIL dividing P1 and the negative polarity (N2) of the neighboring AR, 11943, thus the negative polarity (N1) of AR 11944 barely contributed to the flare. Furthermore, there are secondary flare ribbons extending along the PIL of AR 11943 (N2-P2), as it seems that N2 is surrounded by P1 and P2.

There are several pieces of evidences indicating the existence of a long MFR between the two ARs prior to the flare. Firstly, there is a sigmoidal coronal loop connecting P1 and N2 (**Figures 2B,C**), which has a length of at least 300 arcsec. The west elbow is more prominent, roughly following the PIL between polarities N2 and P2. Secondly, almost co-aligned with the sigmoidal loop, there is a filament observed in AIA images (see **Figure 2C**). Last, a filament channel, which is relatively dark, can be clearly seen in the AIA 171 Å image a few hours before the flare (**Figure 2D**). Overall its structure is complex and rather segmented, but the major part of the filament channel has a very similar S shape as the sigmoidal loops. Wang et al. (2015) has performed a NLFFF reconstruction for this region using the Wiegelmann (2004)'s NLFFF code. Although they also conjectured that an MFR

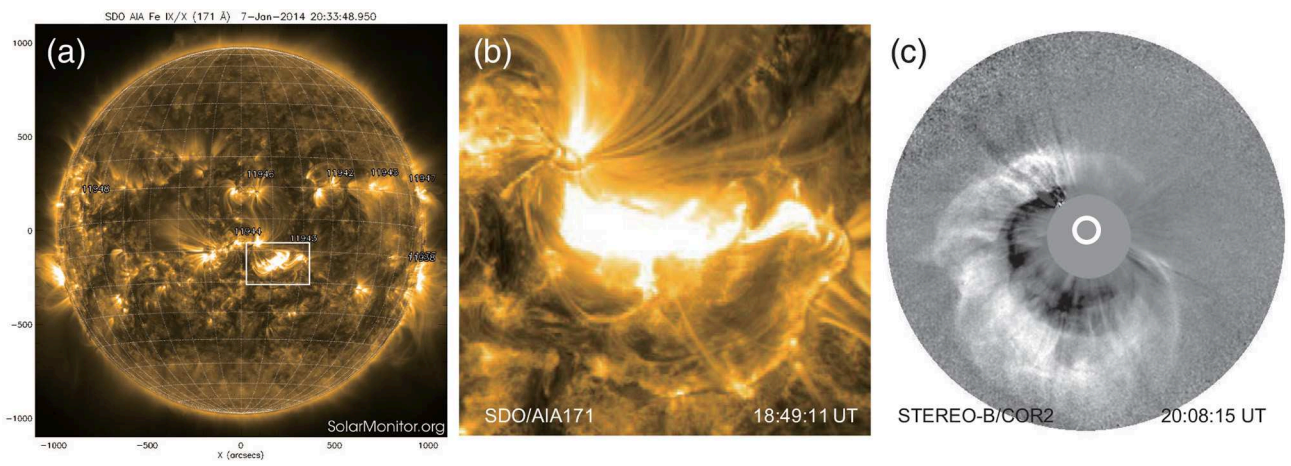

FIGURE 1 | (a) Location of the flare site in a full-disk *SDO*/AIA 171 Å image. The number of the ARs are labeled, and the boxed region denotes the flare site. **(b)** Enlarged view of the flaring loops during the X1.2 flare. **(c)** A running difference image of the CME from the flare region observed by STEREO-B/COR2.

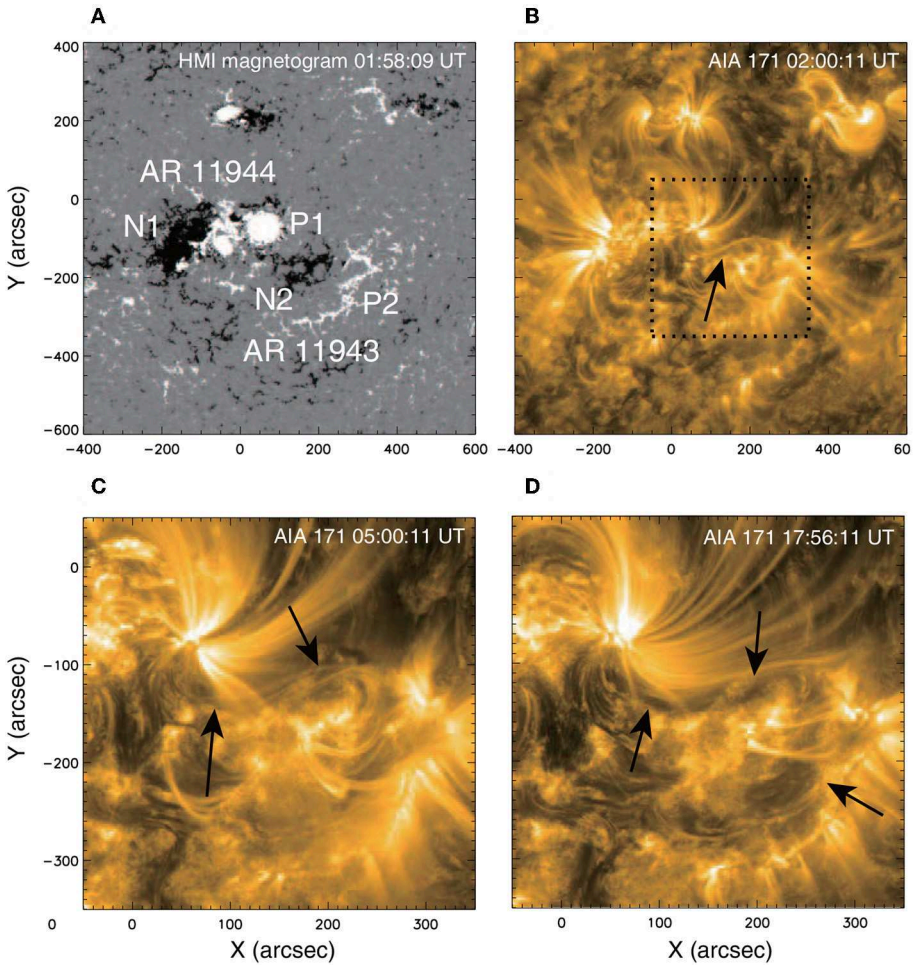

FIGURE 2 | (A) *SDO*/HMI magnetogram showing the distribution of magnetic polarities around the flare site. The main polarities are labeled as N1 and P1, which constitute AR 11944, and N2 and P2, which constitute AR 11943. The flare occurred mainly in association with P1 and N2. **(B)** *SDO*/AIA 171 Å image of the same field view of **(A)**. The arrow remarks a sigmoidal coronal loop in the flare site. **(C)** Enlarged view of the sigmoid as well as a filament as denoted by the arrows. **(D)** The filament channels as denoted by the arrows.

exists in the flare site, but the NLFFF code failed to reproduce such an MFR.

3. CORONAL MAGNETIC FIELD RECONSTRUCTION

We carried out 3D magnetic field reconstruction for the pre-flare corona from the *SDO*/HMI vector magnetograms using the CESE–MHD–NLFFF code (Jiang and Feng, 2013). In particular, we used the data product of the Space-weather HMI Active Region Patch (SHARP, Bobra et al., 2014), in which the 180° ambiguity has been resolved by using the minimum energy method, the coordinate system has been modified via the Lambert method, and the projection effect has been corrected. Here the magnetogram is taken at the time of 17:48 UT, about 20 min before the flare. The CESE–MHD–NLFFF code is based on an MHD-relaxation method which seeks approximately force-free equilibrium. It solves a set of modified zero-β MHD equations with a friction force using an advanced conservation-element/solution-element (CESE) space-time scheme on a non-uniform grid with parallel computing (Jiang et al., 2010; Duan et al., 2018). The code also utilizes adaptive mesh refinement and a multi-grid algorithm to optimize the relaxation process. This model has been tested by different benchmarks including a series of analytic force-free solutions (Low and Lou, 1990) and numerical MFR models (Titov and Démoulin, 1999). The results of extrapolation reproduced from *SDO*/HMI are in good agreement with corresponding observable features like filaments, coronal loops, and sigmoids (Jiang and Feng, 2013; Jiang et al., 2014). Especially, among the NLFFF methods that use solely vector magnetograms as input, it seems that only the CESE–MHD–NLFFF code can reconstruct MFR in a weak field region, for example, Jiang et al. (2014) successfully reconstructed a large-scale MFR corresponding to an intermediate filament in the boundary of the AR 11283. In this paper, we applied the same

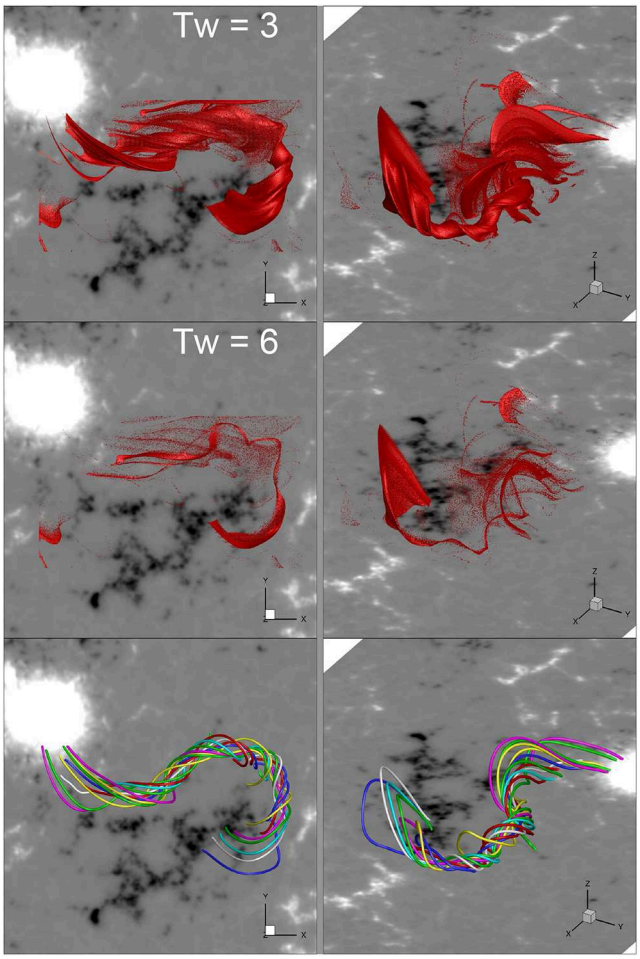

FIGURE 3 | Top: iso-surface of magnetic twist number $T_w = 3$ in two different angles of view. **Middle**: iso-surface of magnetic twist number $T_w = 6$. **Bottom**: sampled magnetic field lines of the MFR in different views. Note that the lines colored in white represent the axis of the rope, i.e., the one that possesses the maximum value of $T_w = 6.5$.

code to the inter-AR region producing the X1.2 flare. It should be noted that there are other ways for modeling MFR in such weak-field region, for instance, the flux-rope insertion method (Su and van Ballegooijen, 2012) can also reconstruct MFR matching observations by inserting an MFR following observed filament channel into a background potential field. In particular, an MFR was also reconstructed in a weak field region between two ARs (Zhou et al., 2019) using the flux-rope insertion method.

4. THE MFR

From the reconstructed field, MFR can be precisely located by calculating the magnetic twist number T_w in the whole computation volume, which is defined by

$$T_w = \int_L \frac{(\nabla \times B) \cdot B}{4\pi B^2} dl \qquad (1)$$

where the integral is taken along the length L of the magnetic field line from one footpoint on the photosphere to the other (Liu et al., 2016). We find a right-handed, significantly twisted MFR, indicating a positive helicity. In **Figure 3**, we show the iso-surfaces with $T_w = 3$ and $T_w = 6$, which are the surfaces of a flux volume with field-line winding number above 3 and 6 turns, respectively. Although interrupted by many small-scale structures, the volume of the strong twisted flux is coherent, forming a forward S shape, in agreement with the sigmoidal loops seen in AIA 171 Å image as well as the filament channel seen in the AIA 304 Å image. The maximum value of T_w in the MFR reaches ∼6.5, and the corresponding field line can be a proxy of the axis of the rope, as suggested by Liu et al. (2016). In the bottom panels, we show sampled magnetic field lines of the rope with different colors, and the rope axis is colored in white. As can be seen, the field lines start from the penumbra of the big sunspot of AR 11944, wind tightly around the axis, run very lowly above the bottom surface in the central part, and finally end in the negative polarity (N2) of AR 11943.

With the data of magnetic field, we can search the location where the filament material can likely be sustained. Such place are magnetic dips where the magnetic field lines concave upward such that the magnetic tension points upward to support the heavy cold filament mass. The magnetic dips are defined as locations where $\vec{B} \cdot \nabla B_z > 0$ and $B_z = 0$. In **Figure 4**, we show the magnetic dips. There is clearly a spine of magnetic dips, which extend to a height of ∼7 Mm above the photosphere, and overall the shape looks co-spatial with the filament observed in AIA 171 Å image in **Figure 2C**.

We further study the ideal MHD instabilities of the MFR. There are two kinds of ideal instabilities that prevail in the study of eruption of coronal MFRs. One is the torus instability (TI) which occurs if the strapping field that stabilizing the MFR decreases with height too fast, and the control parameter is its decay index (Kliem and Török, 2006). The decay index n is defined as

$$n = \frac{d\log(B)}{d\log(h)} \qquad (2)$$

where B denotes the strapping field stabilizing the MFR and h is the height. Theoretically derived threshold for the decay index is found in the range of 1–2 (Kliem and Török, 2006; Fan and Gibson, 2007; Török and Kliem, 2007; Aulanier et al., 2010; Démoulin and Aulanier, 2010). In **Figure 5**, we show the MFR and its strapping flux, which is approximated by the potential field model based on the vertical component of the magnetogram. As can be seen the magnetic flux connecting the big sunspot of P1 and the negative polarity N2 plays the main role in confining the MFR. In the right panel of **Figure 5**, we show an iso-surface of decay index $n = 0.5$, above which the decay index is larger than 0.5. As can be clearly seen, the main body of the MFR situated below the iso-surface. Regarding that the TI threshold is mostly above 1, we concluded that this MFR is far below such threshold and the TI cannot be the trigger of the eruption.

Then we consider the other instability, the kink instability (KI, Török and Kliem, 2005). If the MFR is twisted too much, KI occurs with the rope axis experiences an eruptive deformation.

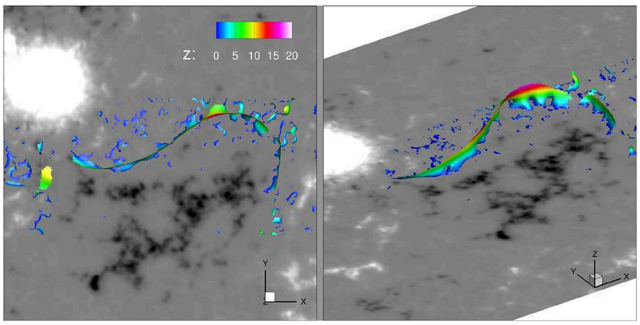

FIGURE 4 | Two different views of distribution of magnetic dips, which is shown by the colored structures, and the colors represent the heights of the dips.

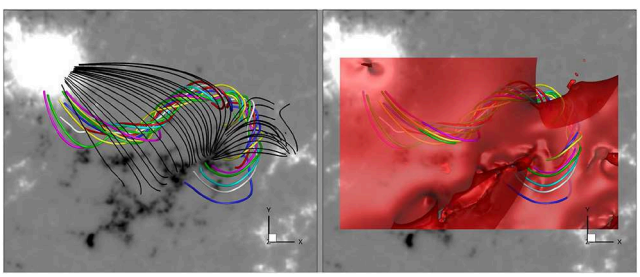

FIGURE 5 | Left: the color lines represent the MFR, while the black lines show sampled field lines of the strapping field overlying the MFR. These field lines are plotted using the potential field model extrapolated from the vertical component of the magnetogram. **Right**: the red, transparent surface is the iso-surface with magnetic decay index $n = 0.5$, and as can be seen, the significant part of the MFR is below the surface.

Unfortunately, there seems to be no unique value for the threshold of KI, since it depends on many details of the MFR, for example, the overall shape, the distribution of magnetic twist, the aspect ratio, etc. Theoretical and numerical investigations have shown the KI threshold, which is a critical value of the magnetic twist number, seems to reside in the range of 1.25–2.5 turns (Fan and Gibson, 2003; Török et al., 2004; Török and Kliem, 2005). However, since these results are derived using a simple and idealized MFR models, for example, a half-circle current torus (Titov and Démoulin, 1999), while the MFRs reconstructed from the real data often show very different configurations with strong asymmetry and non-uniform magnetic twist, thus it is not easy to apply directly the theoretical values to the reconstructed solution. Here the reconstructed MFR has a very large magnetic twist as well as a rather complex configuration. Considering the strong twist, the KI is most likely the candidate of the eruption trigger. We should also remind the readers that cautions are needed here because different coronal field reconstruction methods might give very different results with the same magnetogram. Further analysis of the formation and growth of the MFR is necessary to see how the magnetic twist evolves before the eruption. Also the magnetic-reconnection trigger cannot be excluded here because of the complex magnetic topology of the flare site. It has been found that the MFR's overlying magnetic field has a null-point-like magnetic topology (Wang et al., 2015), and the flare has a large, almost circular-shaped weak ribbon. Thus, the breakout reconnection model might also play a role in triggering the flare. A further investigation is deserved for studying the background magnetic topology as well as its evolution associated with the development of the MFR.

5. CONCLUSIONS

In this paper, we studied the coronal magnetic field for a peculiar inter-AR, X-class eruptive flare which occurred in a relatively weak-field region between two ARs. Using the CESE–MHD–NLFFF code and the *SDO*/HMI vector magnetogram, we reconstructed a highly twisted MFR before the flare, which is not found in previous NLFFF extrapolations (e.g., Wang et al., 2015). The existence of such pre-flare MFR is indicated by several pieces of evidences, such as the sigmoidal coronal loops, the filament and filament channel, and the overall configuration of the reconstructed MFR resembles well with all these observed features. The MFR has a maximum magnetic twist number of 6.5, but resides rather low-lying between the ARs such the TI is not able to be triggered. It is likely that, due to the strong magnetic twist, the KI of the MFR triggers the eruption.

Thus we can provide an answer to the question as arised in section 1: why such a weak field region can produce such strong flare and fast CME? Although the flare occurred in the weak-field region as indicated by the magnetogram, overlying the weak-field region is a highly twisted MFR which connects the penumbra of a leading sunspot of one active region and the following polarity of the neighboring active region. Thus, the magnetic field of the MFR is actually not weak, and more importantly, its high twist and large size indicate that lots of non-potential energy is accumulated in the large volume. It can provide free magnetic energy to power the flare and meanwhile it offers a mechanism for trigger the eruption by, possibly, KI of the MFR. Last, it should be noted that the existence of a highly twisted MFR in such a weak-field region seems unusual since the magnetogram shows no significant magnetic shear. Further investigation on the existence of the MFR in different time and particularly on how it was formed will be carried out in the near future.

DATA AVAILABILITY STATEMENT

All datasets generated for this study are included in the manuscript/supplementary files.

AUTHOR CONTRIBUTIONS

All authors listed have made a substantial, direct and intellectual contribution to the work, and approved it for publication.

FUNDING

This work was jointly supported by National Natural Science Foundation of China (NSFC 41822404, 41731067, 41574170,

41531073), the Fundamental Research Funds for the Central Universities (Grant No. HIT.BRETIV.201901), the China Postdoctoral Science Foundation (2018M641812), and Shenzhen Technology Project JCYJ20180306171748011. Data from observations are courtesy of NASA *SDO*/AIA and the HMI science teams.

REFERENCES

Aulanier, G., Török, T., Démoulin, P., and DeLuca, E. E. (2010). Formation of torus-unstable flux ropes and electric currents in erupting sigmoids. *Astrophys. J.* 708, 314–333. doi: 10.1088/0004-637X/708/1/314

Bobra, M. G., Sun, X., Hoeksema, J. T., Turmon, M., Liu, Y., Hayashi, K., et al. (2014). The helioseismic and magnetic imager (HMI) vector magnetic field pipeline: SHARPs–space-weather HMI active region patches. *Sol. Phys.* 289, 3549–3578. doi: 10.1007/s11207-014-0529-3

Chen, P. F. (2011). Coronal mass ejections: Models and their observational basis. *Liv. Rev. Sol. Phys.* 8:1. doi: 10.12942/lrsp-2011-1

Cheng, X., Guo, Y., and Ding, M. (2017). Origin and structures of solar eruptions I: magnetic flux rope. *Sci. China Earth Sci.* 60, 1383–1407. doi: 10.1007/s11430-017-9074-6

Démoulin, P., and Aulanier, G. (2010). Criteria for flux rope eruption: non-equilibrium versus torus instability. *Astrophys. J.* 718, 1388–1399. doi: 10.1088/0004-637X/718/2/1388

Duan, A. Y., Zhang, H., and Lu, H. Y. (2018). 3D MHD simulation of the double-gradient instability of the magnetotail current sheet. *Sci. China Technol. Sci.* 61, 104–111. doi: 10.1007/s11431-017-9158-7

Fan, Y., and Gibson, S. E. (2003). The emergence of a twisted magnetic flux tube into a preexisting coronal arcade. *Astrophys. J.* 589, L105–L108. doi: 10.1086/375834

Fan, Y., and Gibson, S. E. (2007). Onset of coronal mass ejections due to loss of confinement of coronal flux ropes. *Astrophys. J.* 668, 1232–1245. doi: 10.1086/521335

Fang, F., and Fan, Y. (2015). δ-sunspot formation in simulation of active-region-scale flux emergence. *Astrophys. J.* 806:79. doi: 10.1088/0004-637X/806/1/79

Forbes, T. G., Linker, J. A., Chen, J., Cid, C., Kóta, J., Lee, M. A., et al. (2006). CME theory and models. *Space Sci. Rev.* 123, 251–302. doi: 10.1007/s11214-006-9019-8

Guo, Y., Cheng, X., and Ding, M. (2017). Origin and structures of solar eruptions II: magnetic modeling. *Sci. China Earth Sci.* 60, 1408–1439. doi: 10.1007/s11430-017-9081-x

Jiang, C., and Feng, X. (2013). Extrapolation of the solar coronal magnetic field from SDO/HMI magnetogram by a CESE-MHD-NLFFF code. *Astrophys. J.* 769:144. doi: 10.1088/0004-637X/769/2/144

Jiang, C., Wu, S. T., Feng, X., and Hu, Q. (2014). Nonlinear force-free field extrapolation of a coronal magnetic flux rope supporting a large-scale solar filament from a photospheric vector magnetogram. *Astrophys. J. Lett.* 786:L16. doi: 10.1088/2041-8205/786/2/L16

Jiang, C. W., Feng, X. S., Zhang, J., and Zhong, D. K. (2010). AMR simulations of magnetohydrodynamic problems by the CESE method in curvilinear coordinates. *Sol. Phys.* 267, 463–491. doi: 10.1007/s11207-010-9649-6

Kliem, B., and Török, T. (2006). Torus instability. *Phys. Rev. Lett.* 96:255002. doi: 10.1103/PhysRevLett.96.255002

Liu, R., Kliem, B., Titov, V. S., Chen, J., Wang, Y., Wang, H., et al. (2016). Structure, stability, and evolution of magnetic flux ropes from the perspective of magnetic twist. *Astrophys. J.* 818:148. doi: 10.3847/0004-637X/818/2/148

Low, B. C., and Lou, Y. Q. (1990). Modeling solar force-free magnetic fields. *Astrophys. J.* 352, 343–352. doi: 10.12942/lrsp-2012-5

Mays, M. L., Thompson, B. J., Jian, L. K., Colaninno, R. C., Odstrcil, D., Möstl, C., et al. (2015). Propagation of the 7 January 2014 CME and resulting geomagnetic non-event. *Astrophys. J.* 812:145. doi: 10.1088/0004-637X/812/2/145

Möstl, C., Rollett, T., Frahm, R. A., Liu, Y. D., Long, D. M., Colaninno, R. C., et al. (2015). Strong coronal channelling and interplanetary evolution of a solar storm up to Earth and Mars. *Nat. Commun.* 6:7135. doi: 10.1038/ncomms8135

Shibata, K., and Magara, T. (2011). Solar flares: magnetohydrodynamic processes. *Liv. Rev. Sol. Phys.* 8:6. doi: 10.12942/lrsp-2011-6

Su, Y., and van Ballegooijen, A. (2012). Observations and magnetic field modeling of a solar polar crown prominence. *Astrophys. J.* 757:168. doi: 10.1088/0004-637X/757/2/168

Titov, V. S., and Démoulin, P. (1999). Basic topology of twisted magnetic configurations in solar flares. *Astron. Astrophys.* 351, 707–720.

Toriumi, S., Schrijver, C. J., Harra, L. K., Hudson, H., and Nagashima, K. (2017). Magnetic properties of solar active regions that govern large solar flares and eruptions. *Astrophys. J.* 834:56. doi: 10.3847/1538-4357/834/1/56

Toriumi, S., and Wang, H. (2019). Flare-productive active regions. *Liv. Rev. Sol. Phys.* 16:3. doi: 10.1007/s41116-019-0019-7

Török, T., and Kliem, B. (2005). Confined and ejective eruptions of kink-unstable flux ropes. *Astrophys. J. Lett.* 630, L97–L100. doi: 10.1086/462412

Török, T., and Kliem, B. (2007). Numerical simulations of fast and slow coronal mass ejections. *Astron. Nachr.* 328, 743–746. doi: 10.1002/asna.200710795

Török, T., Kliem, B., and Titov, V. S. (2004). Ideal kink instability of a magnetic loop equilibrium. *Astron. Astrophys.* 413, L27–L30. doi: 10.1051/0004-6361:20031691

Wang, R., Liu, Y. D., Dai, X., Yang, Z., Huang, C., and Hu, H. (2015). The role of active region coronal magnetic field in determining coronal mass ejection propagation direction. *Astrophys. J.* 814:80. doi: 10.1088/0004-637X/814/1/80

Wiegelmann, T. (2004). Optimization code with weighting function for the reconstruction of coronal magnetic fields. *Sol. Phys.* 219, 87–108. doi: 10.1023/B:SOLA.0000021799.39465.36

Zagainova, Y. S., and Fainshtein, V. G. (2018). Comparison of features of the generation of coronal mass ejections with variable velocity in the field of view of LASCO coronagraphs. *Geomag. Aeron.* 58, 966–972. doi: 10.1134/S0016793218070253

Zheng, R., Chen, Y., and Wang, B. (2016). Slipping magnetic reconnections with multiple flare ribbons during an X-class solar flare. *Astrophys. J.* 823:136. doi: 10.3847/0004-637X/823/2/136

Zhou, G. P., Tan, C. M., Su, Y. N., Shen, C. L., Tan, B. L., Jin, C. L., et al. (2019). Multiple magnetic reconnections driven by a large-scale magnetic flux rope. *Astrophys. J.* 873:23. doi: 10.3847/1538-4357/ab01cf

Conflict of Interest: The authors declare that the research was conducted in the absence of any commercial or financial relationships that could be construed as a potential conflict of interest.

The handling editor declared a past co-authorship with the authors CJ and AD.

frontiers in Physics

ORIGINAL RESEARCH
published: 13 December 2019
doi: 10.3389/fphy.2019.00218

Mass Motion in a Prominence Bubble Revealing a Kinked Flux Rope Configuration

Arun Kumar Awasthi[1,2]* *and Rui Liu*[1,2]*

[1] CAS Key Laboratory of Geospace Environment, Department of Geophysics and Planetary Sciences, University of Science and Technology of China, Hefei, China, [2] CAS Center for Excellence in Comparative Planetology, Hefei, China

Prominence bubbles are cavities rising into quiescent prominences from below. The bubble-prominence interface is often the active location for the formation of plumes, which flow turbulently into quiescent prominences. Not only the origin of prominence bubbles is poorly understood, but most of their physical characteristics are still largely unknown. Here, we investigate the dynamical properties of a bubble, which is observed since its early emergence beneath the spine of a quiescent prominence on 20 October 2017 in the Hα line-center and in $\pm$0.4 Å line-wing wavelengths by the 1-m New Vacuum Solar Telescope. We report the prominence bubble to be exhibiting a disparate morphology in the Hα line-center compared to its line-wings' images, indicating a complex pattern of mass motion along the line-of-sight. Combining Doppler maps with flow maps in the plane of sky derived from a Nonlinear Affine Velocity Estimator, we obtained a comprehensive picture of mass motions revealing a counter-clockwise rotation inside the bubble; with blue-shifted material flowing upward and red-shifted material flowing downward. This sequence of mass motions is interpreted to be either outlining a kinked flux rope configuration of the prominence bubble or providing observational evidence of the internal kink instability in the prominence plasma.

Keywords: quiescent prominences, prominence: bubble, prominence: magnetic field, prominence: instability, kinked flux rope, internal kink instability

OPEN ACCESS

Edited by:
Xueshang Feng,
National Space Science Center (CAS), China

Reviewed by:
Yeon-Han Kim,
Korea Astronomy and Space Science Institute, South Korea
Xin Cheng,
Nanjing University, China

***Correspondence:**
Arun Kumar Awasthi
arun.awasthi.87@gmail.com
Rui Liu
rliu@ustc.edu.cn

Specialty section:
This article was submitted to Stellar and Solar Physics, a section of the journal Frontiers in Physics

Received: *30 August 2019*
Accepted: *28 November 2019*
Published: *13 December 2019*

Citation:
Awasthi AK and Liu R (2019) Mass Motion in a Prominence Bubble Revealing a Kinked Flux Rope Configuration. Front. Phys. 7:218. doi: 10.3389/fphy.2019.00218

1. INTRODUCTION

It is crucial to understand the dynamical characteristics and magnetic field configuration of the solar prominences primarily due to their association with the solar eruptions. Prominences are believed to be a visible manifestation of the cool material suspended in the corona on the dips of the nearly horizontal magnetic field lines spanned across the polarity inversion line [1–3]. Although a long-term observational history of solar filaments enabled the general characterization of its formation and evolution [4–6], high-resolution observations unveiled obscure features, for example, the prominence bubbles. Bubbles are observed as a void region located just above the spicule height emerging underneath the quiescent prominences [7, 8]. Bubbles are known to be the active locations for the formation of "plumes" which are a probable source of mass supply into the prominence [9] countering the observed drainage of the prominence material due to the gravitation pull. Therefore, it is crucial to determine the physical mechanisms responsible for the formation, uprise, and expansion of the bubbles.

It is unclear what is inside the prominence bubble. Is it a void region or filled with low-density cool plasma? The earliest observation of the prominence bubble in Ca 8542 Å spectra [7] revealed the absence of line emission in the bubble to be due to its absorption by the cool plasma, and not due to the "off-band effect" of the filter. Heinzel et al. [10] compared the EUV and X-ray intensities observed from prominence with the bubble, determining the opacity of the bubble (and hence the hydrogen column density) to be approximately one-sixth of that of the prominence. Similarly, Labrosse et al. [11] obtained the intensity of the coronal Fe xii line in the bubble to be larger than that in the prominence, however lower than the corona. They speculated the absorption to be due to the optically thin prominence plasma which, however, is not clearly visible in the Hα images. Berger et al. [8] determined the temperature of the plasma inside the bubble to be ranging between $2.5–12\times10^5$ kelvin, and that it is 25–120 times hotter than the surrounding prominence material. Of particular interest was the observation of a hot rising structure (logT$\approx$6.0) within a prominence bubble investigated in Berger et al. [8], which was argued to play a crucial role in the formation and expansion of the bubble through pushing the cooler prominence material upwards. They further inferred "magneto-thermal convection" process to be responsible for the expansion of the prominence bubble. Similarly, Shen et al. [12] also found higher temperature inside the bubble ($< T >= 6.83$MK) compared to the surrounding prominence material ($< T >= 5.53$MK). On the other hand, Dudík et al. [13] rejected the presence of any kind of hot material inside the bubble based on the investigation of a prominence bubble in the EUV 193 Å wavelength. Further, the emission inside the prominence bubble and the prominence cavity region was found to be of similar magnitude. In agreement to this, Gunár et al. [14] interpreted the apparent brightening in the bubble region (particularly in the 171 Å images) to be due to the material corresponding to the prominence-corona-transition-region (PCTR) in the foreground or the background of the bubble based on the observational evidence that the bubble appeared as a void region in Hα images but not distinctly separable in the contemporaneous optically thick EUV 304 Å images. Therefore, it is evident that the consensus on the composition of the bubble interior is yet to be reached.

Highly structured ambient and background magnetic field on the top of low emitting bubbles makes it very difficult to determine the magnetic field strength and configuration of the prominence bubble. Dudík et al. [13] modeled prominence bubble through the inclusion of an emerging parasitic bipole beneath the prominence where the arcade field lines of the bipole correspond to the boundary of the bubble. They further argued that bubbles are devoid of any material and just the "gaps or windows" in the prominence due to the absence of dips in the bubble field lines. Moreover, the reconnection between the arcade field lines of the bubble and that of the overlying prominence may explain the generation of plumes. Shen et al. [12] interpreted the enhanced temperature inside the investigated bubble using the aforesaid scheme of reconnection. The magnetic field strength of two different prominence bubbles estimated using the *THEMIS/MTR* polarimetric observations revealed a higher magnetic field inside the bubble compared to the prominence [15], which is indicative of emerging magnetic flux at the location of the prominence bubble. Observational evidences of flux emergence beneath the prominence can be found in Chae et al. [16]. Based on these observations, the role of Lorentz force has been proposed to explain the emergence and uprise of the prominence bubbles.

Quiescent prominences exhibit irregular motion persistently over the entire structure which is generally attributed to the fundamental plasma instabilities. Ryutova et al. [17] investigated several cases of prominence with bubbles and plumes and suggested the presence of both the Kelvin–Helmholtz (K–H) and Rayleigh–Taylor (R–T) instabilities. K–H instability is attributed to driving the ripples (perturbations) at the bubble boundary to form a single large plume whereas self-similar multiple plumes are suggested to be due to the R–T instability. Further, they characterized the bubble to be a "growing coronal cavity" underneath the prominence and suggested the screw-pinch instability [18] to be the formation mechanism of the bubble. K-H instability is one among the most commonly observed instabilities [19] and occurs at the surface of discontinuity of the two fluids which propagate with different speeds, however, possess sufficient enough shear so as to overcome the surface tension force. Berger et al. [20] attributed the coupled KH–RT instability to be responsible for the development and growth of ripples at the boundary of a prominence bubble as they were located at the density inversion layer. Similarly, Mishra and Srivastava [21] found the magnetic R-T (MRT) instability to drive regular formation and development of plumes originating from small-scale cavities developed within the prominence whereas the collapse of a plume was attributed to K-H instability. Thus, probing the dynamical behavior of the prominence material leads to the identification of associated plasma instabilities, and in turn, offers insights into the physics of formation and stability of the quiescent prominence.

Therefore, it is evident that the physics of the formation and evolution of prominence bubbles is still debated. Thanks to high spatial-resolution Hα images of a prominence recorded by New Vacuum Solar Telescope (NVST), we distinctly characterize the mass motions within a prominence bubble (section 3) in this work. A crucial finding of our analysis is the presence of disparate mass distribution within the bubble in the co-temporal Hα line-center and in line-wing images. An interesting feature in the EUV observations of the prominence is the presence of a "bright compact region" within the bubble. The morphological and thermodynamical evolution of the blob is made to discuss its origin in the context of bubble or from PCTR. Finally, Doppler analysis from the Hα line-wing observations is employed to infer the magnetic skeleton of the prominence bubble in section 4.

2. INSTRUMENTS AND DATA

In order to investigate the mass motion in a quiescent prominence, we primarily use the images acquired by a ground-based 1-m New Vacuum Solar Telescope (NVST; [22]) in the Hα line center and in $\pm$0.4 Å wings, during 07:27–09:28 UT. NVST raw data-set has been further subjected to the alignment

as well as speckle reconstruction, resulting in the pixel scale and the temporal cadence of the final Hα images to be 0″.136 and 28 s, respectively. While the NVST field-of-view could only capture the southern section of the prominence (**Figures 1a–c**), the full context of the prominence has been obtained using full-disk extreme ultra-violet (EUV) images in the 211, 171, and 193 Å wavelengths, recorded by the Atmospheric Imaging Assembly (AIA; [23]) onboard *Solar Dynamics Observatory* (SDO; [24]) with a pixel scale of 0″.6 and a temporal cadence of 12 s. Full-disk Hα images acquired by the *Kanzelhöhe Solar Observatory (KSO)* and *Global Oscillation Network Group (GONG)* with the pixel scale of 1″ have also been utilized to study the long-term evolution of the prominence.

3. OBSERVATIONAL RESULTS

We investigate the mass motion in a quiescent prominence of October 20, 2017, located at the north-east limb of the solar disk (N24E87). In particular, dynamical characteristics intrinsic to a prominence bubble (marked by yellow arrows in the of **Figures 1a–c**), that is situated beneath the spine of the prominence, have been investigated. The bubble is seen in the form of a dark cavity in the Hα line center whereas the same appears bright surrounded by dark threads in the EUV observations. From the NVST Hα images, it is evident that the cavity region has a distinctively sharp boundary (**Figure 1c**), a typical feature attributed to the prominence bubbles. Further, the bubble interior is composed of fine structures and appears to be filled partially with the material of relatively lesser brightness than the prominence itself. The prominence structure corresponds to a typical "hedgerow" shape, suggesting that the prominence main body spans obliquely with respect to the line-of-sight [17]. This can be further confirmed by the Hα images of the prominence acquired on the subsequent days where the prominence is visible in absorption against the bright disk and spans along the north-south direction (**Figures 1d,e**). Such configuration allows a clear view of the prominence material as the effect of the sky-plane projection of the background and foreground activities remain minimal [25]. As follows we characterize the small-scale mass motion within the prominence bubble.

3.1. Morphological Evolution of the Prominence Bubble in Hα

The evolutionary sequence of the prominence bubble since its formation has been investigated using the NVST Hα line-center and line-wing images (**Figure 2** and available online as **Supplementary Movie**). Prominence bubble originated in the form of an ellipse-shaped void with its major axis having the span of ∼13" (∼9 Mm) and acutely tilted toward the solar limb (**Figure 2a**). After 90 minutes of evolution, the bubble enlarged [∼35" (25 Mm)] and became more vertically arranged (**Figure 2k**). Several interesting features have been identified in the bubble interior and at the boundary in the course of its evolution, discussed as follows and in the section 3.3.

Since the bubble formation, counter-clockwise shear flows are persistently observed along its boundary (**Figure 2b**). Further, as the bubble uplifts, its visually topmost boundary exhibits excess in emission compared to the prominence brightness (**Figure 2d**). This manifests the accumulation of ambient prominence material on the bubble boundary during its uprising process [17].

3.2. Doppler Map and Flow Field in the Prominence Bubble

We investigate the dynamical characteristics of the prominence material by analyzing the images acquired by NVST in the Hα line center as well as in the H$\alpha\pm$0.4 Å wings. It is interesting to note that mass distribution in the bubble interior as seen in the Hα line-center images differs remarkably from that appearing in the respective Hα blue and red wing images (**Figure 3**). For instance, while the prominence bubble is imaged in the form of a cavity in the Hα line-center wavelength at 08:52:37 UT (**Figure 3b2**), the co-temporal Hα line-wing images (**Figures 3a2,c2**) indicate that the mass motion inside the bubble along the line-of-sight (LOS) has a complex pattern. Therefore, multi-wavelength observations are crucial in making a comprehensive assessment of the dynamical characteristics of prominence bubbles, as conducted in the present study.

In order to quantify the mass motion inside the bubble as well as on its boundaries, we employ the nonlinear affine velocity estimator (NAVE) technique [26] to derive the flow-map from the NVST images acquired in the Hα line-center, blue and red-wing wavelengths. The flow-map has been derived over a grid of uniform spacing of 5 pixels (∼0.5 Mm) and 50 × 65 pixels span. The continuity equation, a default solver in the NAVE procedure, is used for an FWHM of 30 pixels. An important input to the NAVE procedure is the noise level, which is determined using the relationship $\sigma_d/\sqrt{2}$, where σ_d is determined as the standard deviation of the absolute difference of two consecutive images corresponding to a region enclosing a quiet and dark area above the prominence. In parallel, in order to deduce plasma motion along the LOS, doppler maps have been constructed using the following relationship [27].

$$D = \frac{B - R}{B + R} \tag{1}$$

where B and R refer to the pixel intensities in the Hα blue and red-wing images, respectively.

The overlay of flow maps, derived using the Hα line-wing images [pink (cyan) vectors in **Figures 3d1–d3** corresponds to the red (blue) wing of the Hα line profile], onto the co-temporal doppler maps [background images in the (**Figures 3d1–d3**) with the blue (red) color representing the positive (negative) doppler index] revealed the material inside the bubble to be rotating in a counter-clockwise sense. It is further observed that the red-shifted material is predominately exhibiting a downflow (toward the solar disk), whereas a definitive trend of upward motion was seen in the blue-shifted material (**Figure 3d3**). The rotational motion remained persistent during the entire period of investigation (07:27–09:27 UT), however with a varying speed ranging between 5 and 38 km/s. The flow of the red-shifted material has been mainly constrained either at the top of the bubble or at its left side. Similarly, the blue-shifted

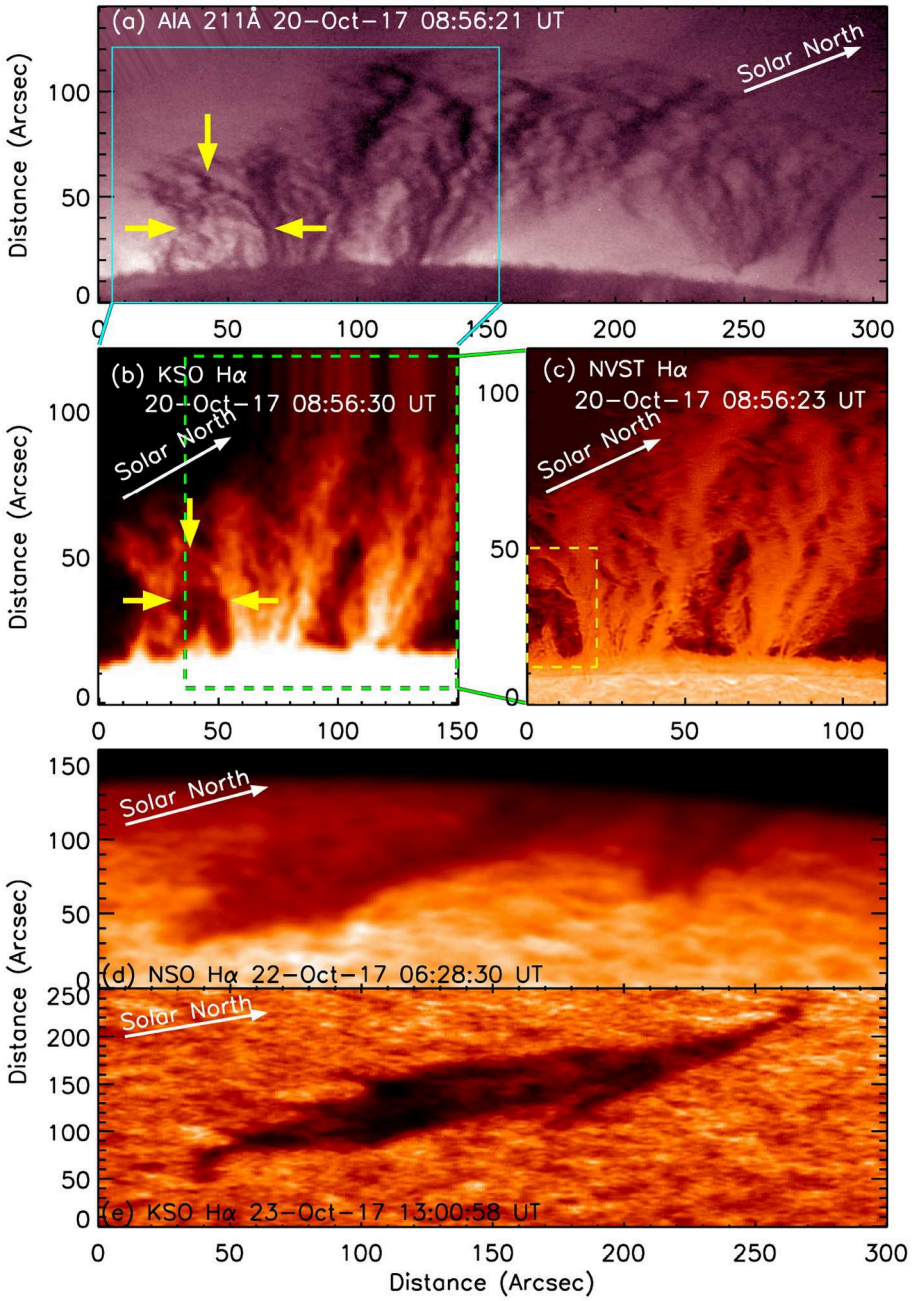

FIGURE 1 | Multi-wavelength overview of the quiescent prominence, located at the northeast limb of the solar disk on October 20, 2017 (N24E87). All the images have been rotated clockwise by 65° for presenting an upright view of the prominence. **(a)** AIA 211 Å image showing the entire prominence spanning across approximately 250" on the limb. The Cyan rectangle represents the field of view of the Hα image acquired by the Kanzelhoehe Solar Observatory (KSO), shown in **(b)**. The green square region in **(b)** indicates the field-of-view of the Hα image recorded by NVST, shown in panel **(c)**. Prominence bubble, investigated in this paper is outlined in yellow in **(a–c)**. **(d,e)** Prominence as observed on 22 and 23 October 2017 from the *National Solar Observatory (NSO)* and *KSO*, respectively. It is clear that the prominence morphology has not altered significantly.

material appears to be flowing predominately at the bottom or at the right side of the bubble (directions correspond to the vertically upright view of the bubble as a reference, see **Figure 3**).

3.3. Plasma Instabilities in the Prominence Bubble

Mass motion inside the bubble and along its boundary reveals several interesting features associated with the plasma

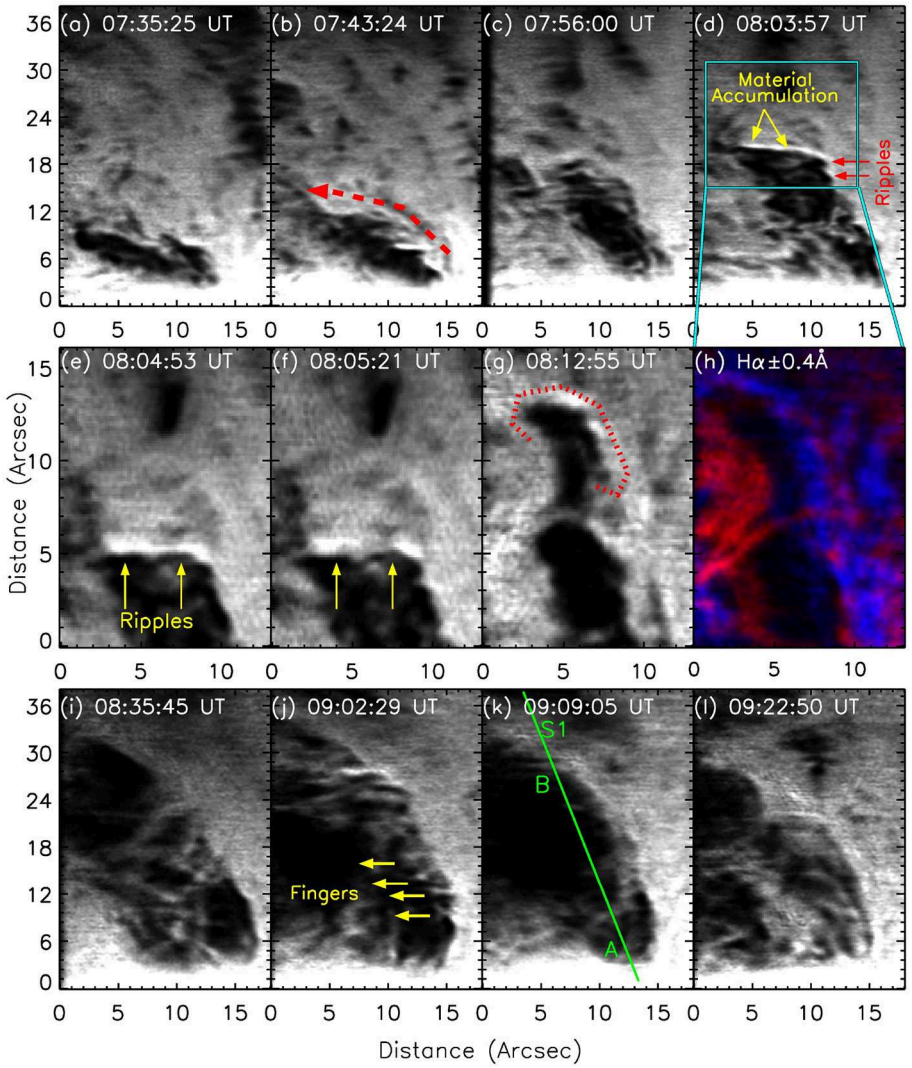

FIGURE 2 | Dynamical evolution of a prominence bubble since its formation as seen in the Hα line-center and line-wing image sequence, acquired by *NVST* telescope. Crucial dynamical activities exhibited by the material flowing in the bubble interior and at the boundary include; anti-clockwise shear flow at the bubble boundary **(a–b)**, brightened section of the bubble boundary indicating the plasma accumulation as bubble uplifts **(c–d)**; rippling boundary followed by the generation of a mushroom-head plume (**e–g** in Hα line-center). Hα line-wing images of the plume show dissimilar line-of-sight flow pattern across the rising plume which comprises of blue-shifted material at the head of the plume while red-shifted material is predominant at its left leg **(h)**. A clear instance of the formation of finger-shaped structures, extending out from the right boundary of the bubble, is shown in **(j)**. Constantly altering mass distribution in the bubble interior **(i–l)** is indicative of the highly dynamical nature of the investigated bubble. (A movie covering the entire evolutionary sequence of the bubble in the Hα line-center as well as in the line-wings, and in various EUV wavelengths is made available online as a **Supplementary Material**).

instabilities. For instance, at least two distinctively clear small-amplitude (0.5 Mm) ripples are observed at the right boundary of the bubble (shown by red arrows in **Figure 2d**). Subsequently, the top boundary of the bubble also exhibits a clear signature of rippling motions (**Figure 2e**). While there is no significant increase in the amplitude of the rippling motion until the image acquired at 08:05:21 UT (**Figure 2f**), the perturbations increased significantly later, leading to the generation of a typical mushroom-head plume (**Figure 2g**). Interestingly, only a single episode of the plume generation (average uplift speed ∼13 km/s) was observed. This indicates the nonlinear explosive phase of the K–H instability to be the most possible mechanism for the investigated plume [17]. To further understand, we have derived the growth rate of explosive instability using Equation (2) [17] for our case of plume evolution.

$$v_{explosive} \simeq \alpha \frac{\tilde{\nu}_{ei}}{ln(|W|/|W_0|)} \tag{2}$$

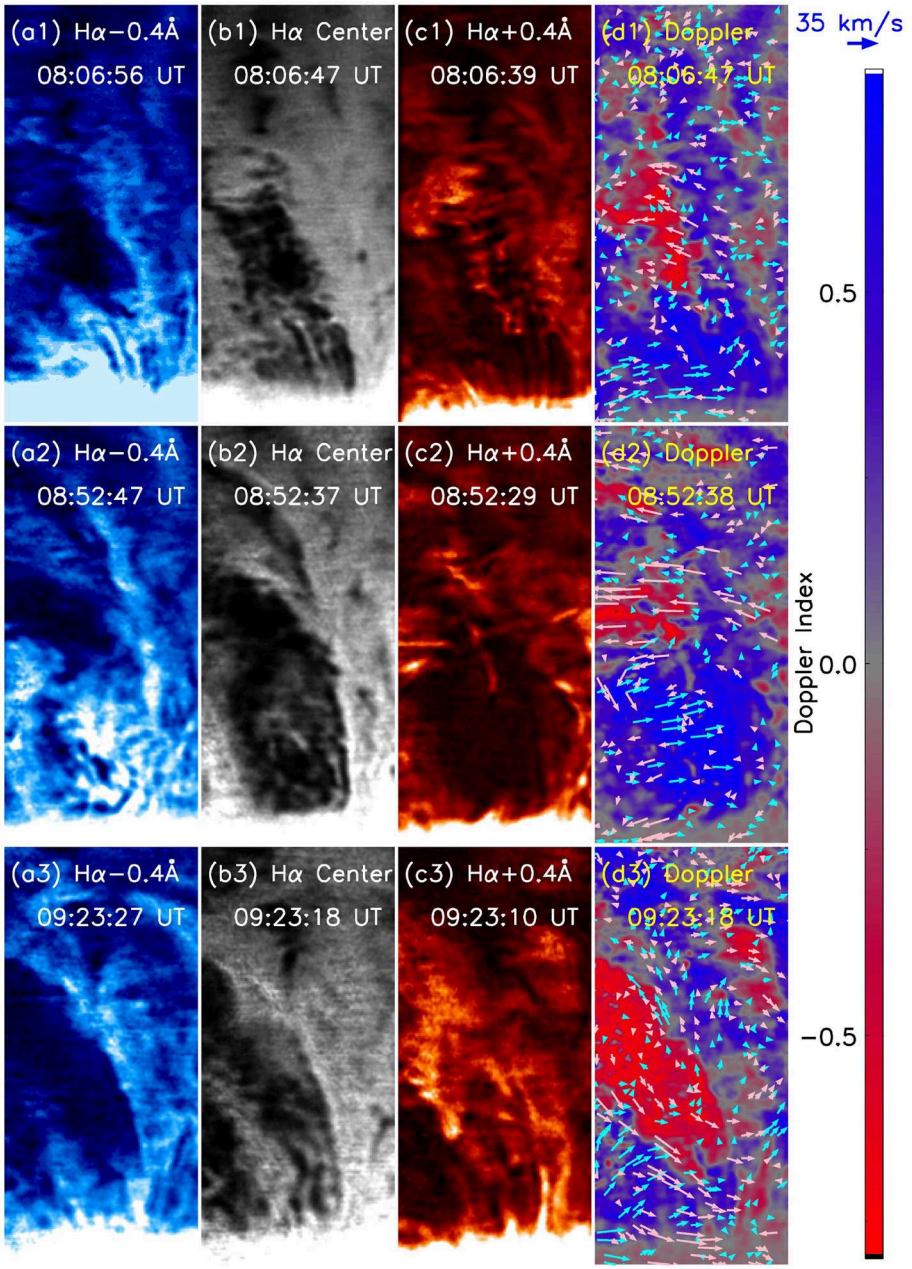

FIGURE 3 | Bubble dynamics quantified using the flow maps derived using NAVE procedure and Doppler maps. A sequence of images in the Hα-0.4 Å, Hα line-center, and Hα+0.4 Å are shown in the first three columns **(a–c)**, respectively. **(d1–d3)** The flow map derived from the Hα blue- and red-wing images is plotted in cyan and pink, respectively, on the respective Doppler maps. The blue (red) color in the doppler map represents the mass motion toward (away from) the line-of-sight. The LOS refers to the direction pointing away and orthogonal to the image plane.

where the parameter α is considered equal to unity. $\tilde{\nu}_{ei}$ is the rate of inverse slowing down of the particles due to electron-ion collision. Considering the temperature and density of the particles to be 1 MK and 5×10^{10} cm^{-3}, respectively, $\tilde{\nu}_{ei}$ takes a value of 2.7×10^{-2} s^{-1}. It has been further shown in Ryutova et al. [17] that the ratio of energy increased ($|W|/|W_0|$) can be approximated to the ratio of the square of the initial and final perturbation amplitudes, which are determined to be 0.5" and 4.5", respectively, in our case (*cf.* **Figures 2f,g**). With the aforesaid values and equation 2, the rate of growth of the explosive instability is determined to be 9.34×10^{-3} s^{-1}, similar to that deduced in Ryutova et al. [17]. Another possible mechanism for the plume generation can be the coupled KH–RT instability [20], however limited spatial resolution restricts the definitive determination of the growth rate of the ripples in their pre-explosive evolution phase (on or before 08:05:21 UT;

see **Figures 2e–f**) which makes it difficult to test this scenario. Hα line-wing images ($\pm$0.4 Å) of the plume reveal the blue-shifted emission to be dominant at the plume head whereas the red-shifted material prevails along its left trail (**Figures 2i–l**). This is a possible indication of generation of sheared flow at the plume boundary as the plume ascends.

In addition to the counter-clockwise flow of material, clockwise mass motion along the right boundary of the bubble is also found at the early onset phase of the bubble evolution, particularly during 07:35–07:43 UT (**Figure 4**; also refer to the movie associated with the **Figure 2**). These oppositely directed flows may provide favorable conditions for the generation of K–H instability. Using the NAVE technique on the Hα images, we determined the flow speed along the right boundary region of the bubble to be varying in the range of 2–10 km/s, in agreement to that deduced in Berger et al. [20]. Further definitive characterization of K-H instability may be difficult here due to limited spatial resolution of the NVST images.

Another interesting feature of the bubble evolution is the development of finger structures at the bubble boundary. One such evidently clear instance is reported in **Figure 2j** where the average separation between the fingers is 1.1 Mm ($\sim$1.5"). Usually, finger-like break-up structures are believed to be generated due to R–T instability taking place at the boundary of plasma layers of different densities [28]. However, since the fingers are not oriented along the direction of solar gravity, these extrusions may be the K–H vortices generated due to shearing flows.

3.4. EUV Perspective and Thermal Diagnostics of the Prominence Bubble and Bright Blob

Extreme Ultraviolet (EUV) images obtained from the *SDO*/AIA instrument have been analyzed in order to determine the morphological and thermodynamic evolution of the prominence bubble (**Figure 5**). Prominence bubble interior in the 211 Å EUV image sequence (**Figure 5a**; also refer to the **Supplementary Movie** associated with the **Figure 2**) appears to be highly structured and dynamic in nature, similar to that observed in the Hα images.

A distinctively clear bright blob-like feature appeared inside the bubble at 08:59 UT in the EUV images (**Figure 5b**). The evolution of EUV emission corresponding to the bubble is quantified by taking an average of the emission from a small circular region-of-interest (ROI), selected so as to cover the change in intensity from both the bubble interior as well as the bright blob. Similarly, the respective background fluctuations are estimated by averaging the brightness of the pixels corresponding to an ROI away from the prominence, but the same in terms of geometrical parameters (area and radial distance from the limb) of the bubble ROI. The resulted EUV intensity profiles from both the bubble (full lines) and the background (dotted lines) are plotted in **Figure 5i**. We also prepare a time-distance map from the Hα image sequence (**Figure 5k**) along a virtual slit crossing the bubble (slit "S1" is shown in the **Figure 2k**) in order to compare the bubble evolution in the EUV and Hα wavelengths. Since the earliest formation of the bubble in Hα, a slight enhancement in the EUV emission compared to that at earlier times is evidenced. In addition to several small-scale perturbations, EUV intensity profile also exhibits a "maximum" at 09:04 UT, corresponding to the bright blob within the bubble. It is crucial to note that the EUV emission corresponding to the blob is always slightly lower than the background emission in the respective wavelengths. This is indicative of the presence of material either in the blob or along its line of sight. On the other hand, the blob appears dark in the Hα wavelengths as also seen from the time-distance images during 09:00–09:15 UT (indicated in **Figure 5k**).

To characterize the thermodynamical nature of the blob, we prepared emission measure (EM) maps by employing the method presented in Su et al. [29], which is a modified version of the sparse inversion technique for thermal diagnostics developed by Cheung et al. [30]. This technique makes use of the pixel intensity from the six EUV wavelengths obtained from *SDO*/AIA namely 94, 131, 171, 193, 211, and 335Å to derive the EM[T] distribution. We have prepared the EM maps corresponding to the temperature range 0.5–15 MK with a bin size LogT = 0.05. The evolution of emission measure derived by taking an average of the estimated EM[T] distribution over the region corresponding to the bubble and the background ROI are plotted in **Figure 5j**. The uncertainty is calculated using the Monte-Carlo method, implemented in the EM diagnostics technique of Su et al. [29]. We find the EM values only within the temperature range logT = 6.0–6.6 to be reliable as the derived EM for temperature values beyond this range possess very large uncertainties (**Figure 5j**). Therefore, we estimate the EM-weighted average temperature ($< T >_{EM}$) using the Equation 3 (adopted from [31]) only within the aforesaid temperature range.

$$< T >_{EM} = \frac{\sum EM \times T}{\sum EM} \tag{3}$$

The $< T >_{EM}$ of the blob results to be 1.99 MK, similar to that of the background corona (1.97 MK). Therefore, this analysis remains inconclusive in untangling the thermodynamical characteristics of bright blob within the bubble from that of the foreground/background corona.

4. DISCUSSION AND CONCLUSION

Our investigation of mass motion of a prominence targets the evolutionary phase of a bubble since its earliest appearance in the Hα and EUV observations. We find several new morphological and dynamical characteristics of the prominence bubble as discussed following.

The bubble interior is observed to replete with dynamic mass (**Figures 2**, **3**). This suggests that during the formation stage, prominence bubbles do not always possess an obvious cavity-like morphology as usually identified in the existing literature [8, 13]. Besides, we have been unable to identify any

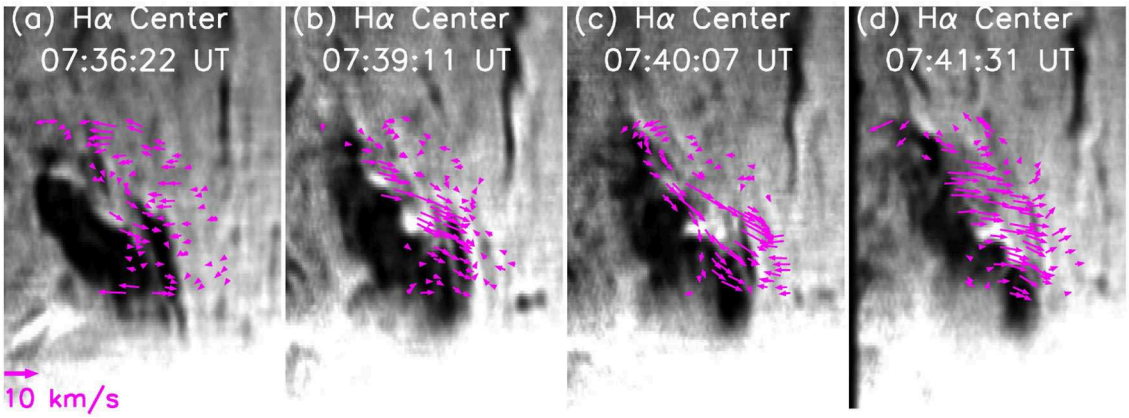

FIGURE 4 | Sheared flow along bubble boundary as seen in the early evolution phase of the bubble. **(a–d)** Sequence of images in the Hα line-center along with the flow-map, derived using NAVE procedure, show the oppositely directed flows along the right boundary of the bubble.

distinct morphological difference between the bubble location and ambient prominence prior to the formation of the bubble. Therefore, the formation mechanism of the bubble may not require any preferential magnetic field configuration of the pre-existing prominence. The observed disparate mass distribution in the Hα line-center compared to that in the co-temporal line-wing ($\pm$0.4 Å) images indicate a highly dynamical nature of the mass motions inside the bubble (**Figure 3**). To better understand, a comprehensive dynamical characteristic of the prominence bubble is derived by preparing doppler maps and flow-maps from the line-wing images. This revealed a counter-clockwise rotational motion of the material in the bubble interior, which is composed predominately of the blue-shifted material exhibiting upward flow while red-shifted material undergoes a downward flow. Doppler maps further reveal that the red-shifted material is primarily observed in the top as well as at the left portion of the bubble whereas the bottom and the right sections of the bubble are filled with the blue-shifted material (**Figures 3d1–d3**). We interpret this sequence of mass motion to be outlining a kinked flux rope configuration of the magnetic field inside the prominence bubble (**Figures 6a1,a2**). Liu et al. [32] obtained a similar doppler-shift pattern in a pre-eruptive active-region prominence and inferred it as the signature of a kink-unstable configuration. This concurs with the hypothesis of an emerging flux complex to be the magnetic field structure of the prominence bubble, conceived in Berger et al. [20].

Internal kink instability [33–35] can provide an alternate interpretation of the dynamical characteristics exhibited by the prominence bubble investigated in this work. From the counter-streaming mass motions [36] in a magnetic field configuration which is resulted from the internal kink instability with higher mode values (m$\geq$2) ([37]; refer to **Figure 6b**), it is possible to envisage a similar Doppler pattern that is shown by the prominence bubble (**Figures 3d1–d3**). Mei et al. [38] performed isothermal numerical magneto-hydrodynamic (MHD) simulations in a finite plasma-β environment to parameterize the role of internal and external kink instabilities in a magnetic flux rope (MFR). They found both kinds of instabilities to be competing to drive a complex evolution of MFR through the process of reconnection within and around the MFR. However, since the internal kinks are known to possess a smaller growth rate and tend to be energetically benign, which may explain the absence of any obvious signs of heating within the bubble, it can be a preferred mechanism compared to the external kink in the case of prominence bubbles. Further, internal kinks are local and confined in nature, hence their impact on the external field is limited which can help the bubbles in maintaining their shape and boundary for a longer period of time.

Since the earliest appearance of the bubble, we find the signatures of rapid rotational motion within the bubble with a speed much faster relative to the intrinsic motions exhibited by the prominence material. These flows are found to be present within the bubble (**Figure 2**) as well as along its boundary (**Figure 4**) and can be characterized as shear flows [20]. During the uprise and expansion phase of the bubble, prominence material gets accumulated on the boundary of the bubble. When the shear flow interacts with these dense bubble boundaries, ripples of 0.5–1 Mm amplitude are generated. The amplitude of the ripples rapidly increases in time, leading to generating a large typical mushroom-headed plume. While the ripples are understood to be the signatures of linear phase of instability, its rapid growth rate leading to the generation of a plume is attributed to the non-linear explosive stage of K–H instability [17]. In addition, finger-shaped structures are also observed on the bubble boundary. Although such structures are generally associated with the R–T instability [28], we believe that these extrusions may be the K–H vortices as the fingers are not oriented along the direction of solar gravity. Therefore, the generation of K–H instability can be understood as the intrinsic dynamical characteristic of the prominence bubble during its evolution and expansion.

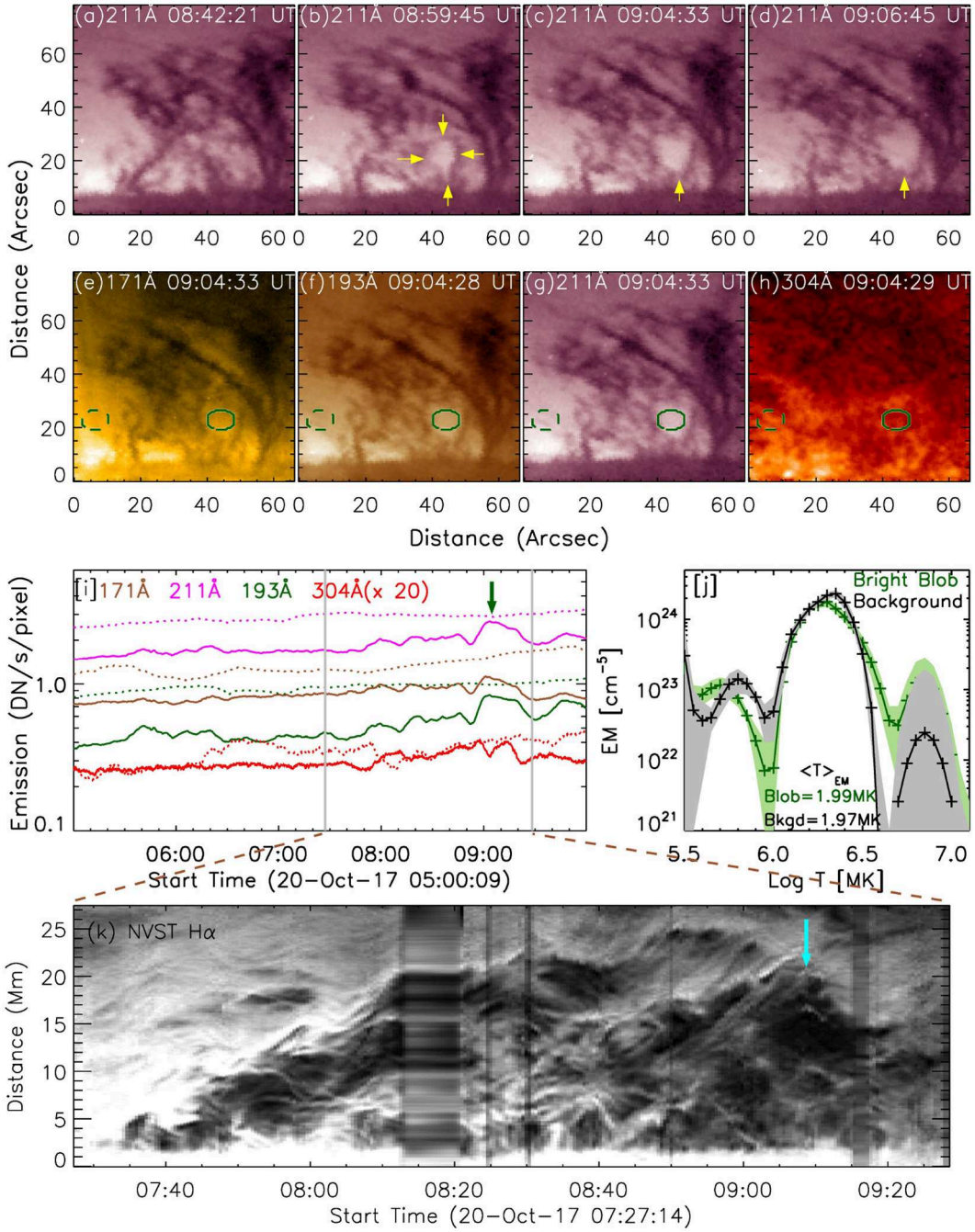

FIGURE 5 | EUV perspective of the prominence bubble and thermodynamical evolution of a bright blob within the bubble. **(a–d)** Similar to the Hα observations, the bubble interior appears highly structured throughout its evolution. The formation and expansion of an interesting bright blob-like feature within the bubble, indicated by yellow color arrows in the top panel of the figure. **(e–h)** EUV images showing the multi-wavelength perspective of the blob at 09:04 UT. **(i)** Mean EUV intensity profile within a region-of-interest (ROI) representing the blob (green; full line) during 05:00 UT–10:00 UT. Background intensity evolution in respective wavelengths as derived from a ROI away from the prominence [dotted green region in panels **(e–h)**] is also plotted. **(j)** Emission measure distribution within the selected ROIs corresponding to bright blob (green) and background (black) is plotted along with the respective errors. **(k)** Time-distance map prepared from the Hα line-center image sequence over a virtual slit "S1" along the direction A to B (see **Figure 2k**).

In order to probe the signatures of heating within the bubble, we estimate the EUV emission originating within the bubble region. During the bubble expansion, slight increase in the EUV emission is found inside the bubble (particularly in the 171, 193, 211, and 304Å wavelengths), but the peak emission in the respective wavelengths has always remained lower than

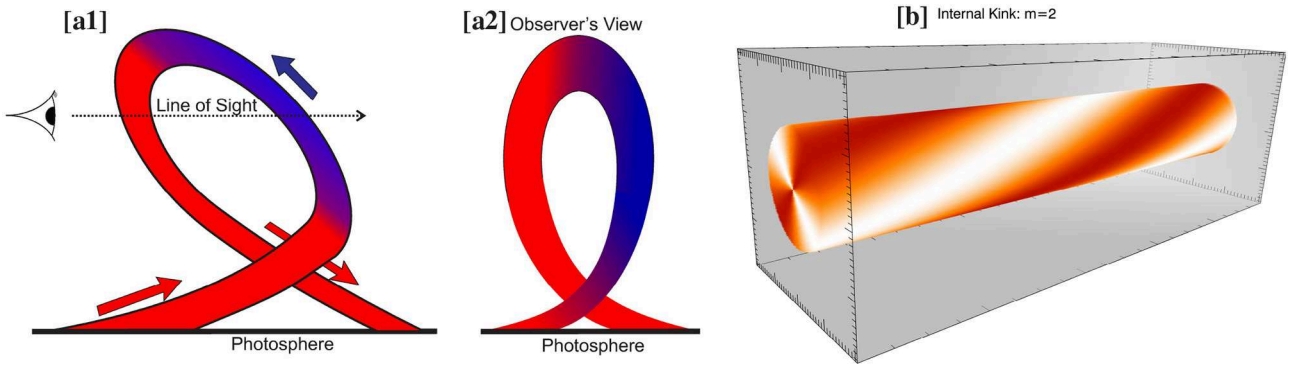

FIGURE 6 | Inferences on the magnetic structure of the prominence bubble as revealed by mass motions. **(a1,a2)** Schematic representation of a kinked flux-rope as the magnetic field configuration of the bubble, drawn from two perspectives. Material flowing toward (away from) the observer is denoted in blue (red) color. **(b)** Internal kink instability in a cylindrical flux-rope corresponding to mode (m) = 2.

that resulting from the background corona (**Figure 5i**). An in-depth investigation further revealed an interesting episode of the formation of a localized blob within the bubble, which appears bright in all of the aforementioned EUV wavelength channels. Similar EUV emission characteristics have been exhibited by a compact region within the prominence bubble investigated in Berger et al. [39], who derived its temperature to be of the order of 1 MK. In agreement, the EM-weighted mean temperature of the blob in our case is derived to be∼1.99 MK. However, since ambient corona is also estimated to have similar temperature as that of the blob, it is difficult to infer whether the emission corresponds to the "hot compact region" within the bubble [39] or from the foreground/background prominence-corona-transition-region (PCTR) [14]. Intriguingly, the blob is observed to push the material toward the bubble boundaries during the course of its evolution, which appears to result in the upward expansion of the bubble.

To conclude, high-resolution observation of the prominence not only offers insights into its magnetic field configuration, but it also provides a platform to characterize the generation and growth of the instabilities in the magnetohydrodynamic fluids. Intrinsic mass motions in the prominence (not necessarily leading to its eruption) are an outstanding indirect probe of the physical conditions, as demonstrated in this study where they outline a kinked flux rope configuration of the prominence bubble or provide a new observational signature of the internal kink instability in the prominence. This work also provides physical constraints in the form of morphological characteristics, growth rate, and thermodynamical characteristics of the bubble, which can be used to drive realistic numerical simulations.

DATA AVAILABILITY STATEMENT

Hα observations from NVST, analyzed in this work, can be requested through the URL http://fso.ynao.ac.cn/datashow.aspx?id=1782. Data from *SDO* and *GONG* Hα network are archived at the respective instruments' URLs and freely available for download.

AUTHOR CONTRIBUTIONS

AA conducted the data analysis and wrote the manuscript under the guidance of RL. RL led the interpretation of the results.

FUNDING

AA acknowledges the support from the Chinese Academy of Science (CAS) as well as the International Postdoctoral Program of the University of Science and Technology of China. RL acknowledges the support from NSFC 41474151, 41774150, and 41761134088.

ACKNOWLEDGMENTS

This investigation primarily made use of the data acquired from the New Vacuum Solar Telescope under a guest observation program. NVST is operated by the Yunnan Astronomical Observatory, Kunming, China. AA acknowledges the hospitality offered by the staff of Fuxian Lake Solar Observatory during his stay for the observing period and for carrying out the post-processing of the raw data in terms of the alignment and application of speckle-reconstruction technique. RL thank Prof. Jongchul Chae for providing the NAVE code. Dr. Yang Su and Dr. Mark Cheung are acknowledged for the code used to derive the thermodynamical properties of the plasma bubble from the EUV images. Authors also acknowledge the reviewers for their constructive comments which improved the scientific clarity of the work.

SUPPLEMENTARY MATERIAL

The Supplementary Material for this article can be found online at: https://www.frontiersin.org/articles/10.3389/fphy.2019.00218/full#supplementary-material

Associated with **Figure 2**, a supplementary movie covering the entire evolutionary sequence of the bubble in the Hα line-center as well as in the line-wings, and in various EUV wavelengths is made available online.

REFERENCES

1. Leroy JL, Bommier V, Sahal-Brechot S. New data on the magnetic structure of quiescent prominences. *Astron Astrophys.* (1984) **131**:33–44.
2. Aulanier G, DeVore CR, Antiochos SK. Prominence magnetic dips in three-dimensional sheared arcades. *Astrophys J Lett.* (2002) **567**:L97–101. doi: 10.1086/339436
3. Ariste, AL. Magnetometry of prominences. In: Vial JC, Engvold O, Editors. *Solar Prominences. Astrophysics and Space Science Library*, Vol. 415. Cham: Springer International Publishing (2015). p. 179–203. doi: 10.1007/978-3-319-10416-4_8
4. Martin SF, Echols CR. *An Observational and Conceptual Model of the Magnetic Field of a Filament*. Dordrecht: Springer Netherlands (1994). p. 339–346.
5. Mackay DH, Karpen JT, Ballester JL, Schmieder B, Aulanier G. Physics of solar prominences: II magnetic structure and dynamics. *Space Sci Rev.* (2010) **151**:333–99. doi: 10.1007/s11214-010-9628-0
6. Parenti S. Solar prominences: observations. *Liv Rev Solar Phys.* (2014) 11:1. doi: 10.12942/lrsp-2014-1
7. Stellmacher G, Wiehr E. Observatino of an instability in a "Quiescent" prominence. *Astron Astrophys.* (1973) **24**:321.
8. Berger TE, Liu W, Low BC. SDO/AIA detection of solar prominence formation within a coronal cavity. *Astrophys J Lett.* (2012) **758**:L37. doi: 10.1088/2041-8205/758/2/L37
9. Berger TE, Shine RA, Slater GL, Tarbell TD, Title AM, Okamoto TJ, et al. Hinode SOT observations of solar quiescent prominence dynamics. *Astrophys J Lett.* (2008) **676**:L89. doi: 10.1086/587171
10. Heinzel P, Schmieder B, Fárník F, Schwartz P, Labrosse N, Kotrč P, et al. Hinode, TRACE, SOHO, and Ground-based Observations of a Quiescent Prominence. *Astrophys J.* (2008) **686**:1383–96. doi: 10.1086/591018
11. Labrosse N, Schmieder B, Heinzel P, Watanabe T. EUV lines observed with EIS/Hinode in a solar prominence. *Astron Astrophys.* (2011) **531**:A69. doi: 10.1051/0004-6361/201015064
12. Shen Y, Liu Y, Liu YD, Chen PF, Su J, Xu Z, et al. Fine magnetic structure and origin of counter-streaming mass flows in a quiescent solar prominence. *Astrophys J Lett.* (2015) **814**:L17. doi: 10.1088/2041-8205/814/1/L17
13. Dudík J, Aulanier G, Schmieder B, Zapiór M, Heinzel P. Magnetic Topology of Bubbles in Quiescent Prominences. *Astrophys J.* (2012) **761**:9. doi: 10.1088/0004-637X/761/1/9
14. Gunár S, Schwartz P, Dudík J, Schmieder B, Heinzel P, Jurčák J. Magnetic field and radiative transfer modelling of a quiescent prominence. *Astron Astrophys.* (2014) **567**:A123. doi: 10.1051/0004-6361/201322777
15. Levens PJ, Schmieder B, López Ariste A, Labrosse N, Dalmasse K, Gelly B. Magnetic field in atypical prominence structures: bubble, tornado, and eruption. *Astrophys J.* (2016) **826**:164. doi: 10.3847/0004-637X/826/2/164
16. Chae J, Martin SF, Yun HS, Kim J, Lee S, Goode PR, et al. Small magnetic bipoles emerging in a filament channel. *Astrophys J.* (2001) **548**:497–507. doi: 10.1086/318661
17. Ryutova M, Berger T, Frank Z, Tarbell T, Title A. Observation of plasma instabilities in quiescent prominences. *Solar Phys.* (2010) **267**:75–94. doi: 10.1007/s11207-010-9638-9
18. Sakurai T. Magnetohydrodynamic interpretation of the motion of prominences. *Pub Astron Soc Japan* (1976) **28**:177–98.
19. Zhelyazkov I, Chandra R, Srivastava AK. Kelvin-Helmholtz instability in an active region jet observed with Hinode. *Astrophys Space Sci.* (2016) **361**:51. doi: 10.1007/s10509-015-2639-2
20. Berger T, Hillier A, Liu W. Quiescent prominence dynamics observed with the hinode solar optical telescope. II. Prominence bubble boundary layer characteristics and the onset of a coupled Kelvin-Helmholtz Rayleigh-Taylor instability. *Astrophys J.* (2017) **850**:60. doi: 10.3847/1538-4357/aa95b6
21. Mishra SK, Srivastava AK. The Evolution of magnetic Rayleigh-Taylor unstable plumes and hybrid KH-RT instability into a loop-like eruptive prominence. *Astrophys J.* (2019) **874**:57. doi: 10.3847/1538-4357/ab06f2
22. Liu Z, Xu J, Gu BZ, Wang S, You JQ, Shen LX, et al. New vacuum solar telescope and observations with high resolution. *Res Astron Astrophys.* (2014) **14**:705–18. doi: 10.1088/1674-4527/14/6/009
23. Lemen JR, Title AM, Akin DJ, Boerner PF, Chou C, Drake JF, et al. The Atmospheric Imaging Assembly (AIA) on the Solar Dynamics Observatory (SDO). *Solar Phys.* (2012) **275**:17–40. doi: 10.1007/s11207-011-9776-8
24. Pesnell WD, Thompson BJ, Chamberlin PC. The Solar Dynamics Observatory (SDO). *Solar Phys.* (2012) **275**:3–15. doi: 10.1007/978-1-4614-3673-7-2
25. Berger TE, Slater G, Hurlburt N, Shine R, Tarbell T, Title A, et al. Quiescent prominence dynamics observed with the hinode solar optical telescope. I. Turbulent upflow plumes. *Astrophys J.* (2010) **716**:1288–307. doi: 10.1088/0004-637X/716/2/1288
26. Chae J, Sakurai T. A test of three optical flow techniques-LCT, DAVE, and NAVE. *Astrophys J.* (2008) **689**:593–612. doi: 10.1086/592761
27. Langangen Ø, Rouppe van der Voort L, Lin Y. Measurements of plasma motions in dynamic fibrils. *Astrophys J.* (2008) **673**:1201–8. doi: 10.1086/524057
28. Innes DE, Cameron RH, Fletcher L, Inhester B, Solanki SK. Break up of returning plasma after the 7 June 2011 filament eruption by Rayleigh-Taylor instabilities. *Astron Astrophys.* (2012) **540**:L10. doi: 10.1051/0004-6361/201118530
29. Su Y, Veronig AM, Hannah IG, Cheung MCM, Dennis BR, Holman GD, et al. Determination of differential emission measure from solar extreme ultraviolet images. *Astrophys J.* (2018) **856**:L17. doi: 10.3847/2041-8213/aab436
30. Cheung MCM, Boerner P, Schrijver CJ, Testa P, Chen F, Peter H, et al. Thermal diagnostics with the atmospheric imaging assembly on board the solar dynamics observatory: a validated method for differential emission measure inversions. *Astrophys J.* (2015) **807**:143. doi: 10.1088/0004-637X/807/2/143
31. Cheng X, Zhang J, Saar SH, Ding MD. Differential emission measure analysis of multiple structural components of coronal mass ejections in the inner corona. *Astrophys J.* (2012) **761**:62. doi: 10.1088/0004-637X/761/1/62
32. Liu R, Alexander D, Gilbert HR. Kink-induced Catastrophe in a Coronal Eruption. *Astrophys J.* (2007) **661**:1260–71. doi: 10.1086/513269
33. Mikic Z, Schnack DD, van Hoven G. Dynamical evolution of twisted magnetic flux tubes. I - Equilibrium and linear stability. *Astrophys J.* (1990) **361**:690–700.
34. Hood AW, Browning PK, van der Linden RAM. Coronal heating by magnetic reconnection in loops with zero net current. *Astron Astrophys.* (2009) **506**:913–25. doi: 10.1051/0004-6361/200912285
35. Keppens R, Guo Y, Makwana K, Mei Z, Ripperda B, Xia C, et al. Ideal MHD instabilities for coronal mass ejections. *arXiv e-prints* (2019) arXiv:1910.12659
36. Zirker JB, Engvold O, Martin SF. Counter-streaming gas flows in solar prominences as evidence for vertical magnetic fields. *Nature.* (1998) **396**:440–1.
37. Cap FF. *Handbook on Plasma Instabilities. Vol 1*. New York, NY: Academic Press Inc. (1976). doi: 10.1016/B978-0-12-159101-4.X5001-3
38. Mei ZX, Keppens R, Roussev II, Lin J. Parametric study on kink instabilities of twisted magnetic flux ropes in the solar atmosphere. *Astron Astrophys.* (2018) **609**:A2. doi: 10.1051/0004-6361/201730395
39. Berger T, Testa P, Hillier A, Boerner P, Low BC, Shibata K. et al. Magneto-thermal convection in solar prominences. *Nature* (2011) **472**:197–200. doi: 10.1038/nature09925

Conflict of Interest: The authors declare that the research was conducted in the absence of any commercial or financial relationships that could be construed as a potential conflict of interest.

frontiers in Astronomy and Space Sciences

ORIGINAL RESEARCH
published: 30 January 2020
doi: 10.3389/fspas.2020.00001

Probing the Thermodynamic State of a Coronal Mass Ejection (CME) Up to 1 AU

Wageesh Mishra[1]*, *Yuming Wang*[2], *Luca Teriaca*[1], *Jie Zhang*[3] and *Yutian Chi*[2]

[1] Max Planck Institute for Solar System Research, Göttingen, Germany, [2] CAS Key Laboratory of Geospace Environment, Department of Geophysics and Planetary Sciences, University of Science and Technology of China, Hefei, China, [3] Department of Physics and Astronomy, George Mason University, Fairfax, VA, United States

Several earlier studies have attempted to estimate some of the thermodynamic properties of Coronal Mass Ejections (CMEs) either very close to the Sun or at 1 AU. In the present study, we attempt to extrapolate the internal thermodynamic properties of 2010 April 3 flux rope CME from near the Sun to 1 AU. For this purpose, we use the flux rope internal state (FRIS) model which is constrained by the kinematics of the CME. The kinematics of the CME is estimated using the *STEREO*/COR and HI observations in combination with drag based model (DBM) of CME propagation. Using the FRIS model, we focus on estimating the polytropic index of the CME plasma, heating/cooling rate, entropy changing rate, Lorentz force and thermal pressure force acting inside the CME. Our study finds that the polytropic index of the selected CME ranges between 1.7 and 1.9. This implies that the CME is in the heat-releasing state (i.e., entropy loss) throughout its journey from the Sun to Earth. The hindering role of Lorentz force and contributing role of thermal pressure force in governing the expansion of the CME is also identified. On comparing the estimated properties of the CME flux rope from the FRIS model with the *in situ* observations of the CME taken at 1 AU, we find relevant discrepancies between the results predicted by the model and the observations. We outline the approximations made in our study of probing the internal state of the CME during its heliospheric evolution and discuss the possible causes of the observed discrepancies.

Keywords: sun, corona, coronal mass ejections, solar wind, kinematics, thermodynamics, polytropic index

OPEN ACCESS

Edited by:
Dipankar Banerjee, Indian Institute of Astrophysics, India

Reviewed by:
Alessandro Bemporad, Osservatorio Astrofisico di Torino (INAF), Italy
Keiji Hayashi, Northwest Research Associates, United States

***Correspondence:**
Wageesh Mishra
mishra@mps.mpg.de

Specialty section:
This article was submitted to Stellar and Solar Physics, a section of the journal Frontiers in Astronomy and Space Sciences

Received: *26 September 2019*
Accepted: *08 January 2020*
Published: *30 January 2020*

Citation:
Mishra W, Wang Y, Teriaca L, Zhang J and Chi Y (2020) Probing the Thermodynamic State of a Coronal Mass Ejection (CME) Up to 1 AU. Front. Astron. Space Sci. 7:1. doi: 10.3389/fspas.2020.00001

1. INTRODUCTION

Coronal mass ejections (CMEs) are the large-scale transients arising from the Sun and, being energetic plasma phenomena, they are the main driver of disturbances in the terrestrial space environment (Tousey, 1973; Hundhausen et al., 1984; Schwenn, 2006; Zhang et al., 2007; Baker, 2009; Chen, 2011; Webb and Howard, 2012). CMEs moving outside the field of view of coronagraphs are often referred to as interplanetary coronal mass ejections (ICMEs). Based on the *in situ* observations of ICMEs, a subset of them are named Magnetic clouds (MCs) as they show large and coherent rotation of the magnetic field vector, larger magnetic field, and a low plasma beta (Burlaga et al., 1981; Marubashi and Lepping, 2007; Wang et al., 2018). Such MCs are understood as flux ropes expanding during their heliospheric evolution while keeping their magnetic connection to the Sun (Larson et al., 1997; Gulisano et al., 2010). Solar-terrestrial physics studies have improved our understanding of different forces acting on the different parts of a CME, their kinematic

evolution and space weather effects by using remote sensing and *in situ* spacecraft observations for several decades. However, the physical processes behind the formation of CMEs/ICMEs associated flux ropes, their acceleration and heating have not yet been understood completely (Forsyth et al., 2006; Chen, 2011; Webb and Howard, 2012; Harrison et al., 2018).

The heating and acceleration of the solar wind have been investigated extensively since the seminal work of Parker (1960). However, a majority of studies on CMEs that make use of white light imaging observations which only provide information on the plasma density, have not focused on understanding the thermodynamics of the CMEs. Near the Sun, some information on the thermodynamic state of a CME is obtained using the EUV spectral observations from the Ultraviolet Coronagraph Spectrometers (UVCS), Coronal Diagnostic Spectrometer (CDS), and Solar Ultraviolet Measurements of Emitted Radiation (SUMER) instruments aboard the *SOlar and Heliospheric Observatory* (SOHO) spacecraft (Akmal et al., 2001; Raymond, 2002; Ciaravella et al., 2003; Kohl et al., 2006; Bemporad and Mancuso, 2010). These studies suggested that there is a deposition of thermal energy into CMEs in the inner corona where they have a higher temperature than the ambient solar wind. To understand the dominant physical mechanism responsible for heating/cooling of expanding plasmoids in the heliosphere, it is necessary to probe the CME thermodynamic state at different distances from the Sun. The thermodynamic evolution of CMEs is often understood by using a polytropic approximation. The different value of the polytropic index for the CME plasma implies different rates of heating, which leads to a different evolution of the CME. An empirical determination of the polytropic index using *in situ* observations is possible if a CME can be observed by several radially-aligned spacecraft (Phillips et al., 1995). The global MHD modeling of ICMEs based on a polytropic approximation to the energy equation has been published by Riley et al. (2003) and Manchester et al. (2004). The combined information of density, temperature and ionization state of CMEs can be used to understand the physical processes within CME plasma.

Over the years, *in situ* measurements of ICMEs have been made using several spacecraft located over a range of heliocentric distances from the Sun. The studies on the thermodynamic treatment of ICMEs between 0.3 and 30 AU have been carried out using *in situ* observations of *Voyagers*, *Ulysses*, *Helios*, *WIND*, *ACE,* and *STEREO* spacecraft (Osherovich et al., 1993; Phillips et al., 1995; Wang and Richardson, 2004; Liu et al., 2006a). The studies have confirmed that CMEs have a lower temperature than that in the ambient solar wind (Burlaga et al., 1981; Richardson and Cane, 1993), and they have highly elevated ionic charge states (Lepri et al., 2001; Zurbuchen et al., 2003). The elevated charge states which freeze in relatively close to the Sun during the CME expansion are indicative of strong heating at CME source relative to the ambient solar wind. The occasional presence of singly charged helium and relatively low ionic charge states in ICMEs is found to be associated with low-temperature filament material on the Sun (Burlaga et al., 1998; Gruesbeck et al., 2012). Since the two spacecraft rarely get well co-aligned radially for recurrent observations of the plasma properties of the same CME at different distances (Skoug et al., 2000). Therefore, in general, *in situ* measurements do not allow us to examine the evolution of an individual CME as it travels away from the Sun. However, using a large amount of *in situ* observations of CMEs over different distances, one can adopt a statistical method to understand their thermodynamic evolution. Such a statistical approach assumes that an average of observed plasma parameters over many CMEs represents the properties of a typical CME. Using such approach, it has been statistically shown that both the density and magnetic field decrease faster in ICMEs than in the solar wind, but the temperature decreases slower in ICMEs than in the solar wind, and the expansion of an ICME is more like an isothermal process than an adiabatic one (Wang and Richardson, 2004; Liu et al., 2005, 2006a; Wang et al., 2005). Recently, using *in situ* observations of ICMEs at different distances between 0.3 and 1 AU, it was shown that there is a good correlation between the ejecta and sheath speeds, but low correlation between the magnetic field magnitudes in the sheath and ejecta (Janvier et al., 2019).

Although a few earlier studies have investigated the thermodynamic state of CMEs using remote sensing observations close to the Sun and *in situ* observations very far from the Sun. Thus, these studies provide CME thermal parameters only at a certain heliocentric distance and/or at a certain time. The pioneering attempt to investigate the internal state of an individual CME during its propagation in the outer corona (i.e., 2–70 $R_{\odot}$) was done by Wang et al. (2009) by developing a Flux Rope Internal State (FRIS) model. The model was further improved by Mishra and Wang (2018) and they applied it to the coronagraphic observations of a slow CME to understand the internal forces and thermodynamic properties (polytropic index, heating rate, entropy change, etc.). The use of coronagraphic observations in combination with the FRIS model allowed to track the thermodynamic evolution of a specific CME with distance from the Sun. This approach differs from earlier studies which provided a statistical result, over a large amount of data, on the variation of a few thermodynamic parameters with distance. The FRIS model is extremely advantageous as it probes the evolution of the CMEs thermodynamic state in terms of CMEs kinematics which can be accurately derived from available imaging observations. It is expected that CMEs with different kinematic characteristics may show different thermodynamic evolution in the heliosphere. Therefore, it would be an obvious next step to apply the FRIS model to different CMEs and understand their thermodynamic evolution.

In the present study, we attempt to apply the FRIS model to a fast CME of 3 April 2010. The CME did not decelerate much during it interplanetary propagation and could be identified as the fastest ICME to arrive near the Earth since the 2006 December 13 event (Liu et al., 2008, 2011). The 3 April 2010 CME had also caused a prolonged geomagnetic storm leading to a breakdown of a *Galaxy 15* satellite for about 6 months. This CME has been extensively studied for its solar and interplanetary signatures, however its thermodynamic properties were so far not explored. Importantly, we estimate the thermodynamic properties of the selected CME up to 1 AU and compare the model extrapolated results with the *in situ* observations of the

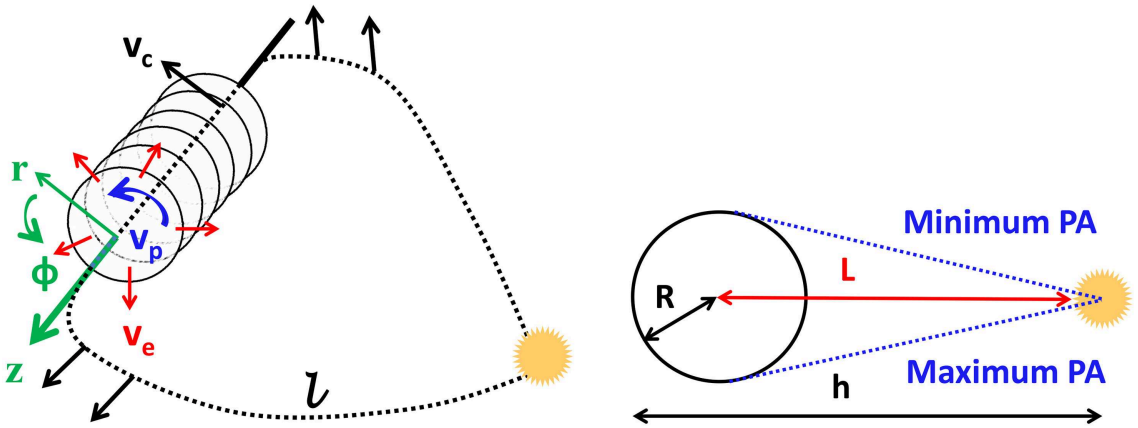

FIGURE 1 | Left: A representative picture of a CME flux rope. The black dashed line indicates the looped axis of the flux rope with the axial length as *l*. A cylindrical coordinate system (i.e., *r*, ϕ, *z*) is attached to the axis of the flux rope (in green). **Right**: A representative picture for the cross-section of the CME flux rope. The radius of the flux rope is *R*, the distance from the flux rope axis to the solar surface is *L*, the distance of the CME leading edge from the Sun's center is *h*, and the minimum and the maximum position angles (PA) are shown with dotted blue lines (adapted from Mishra and Wang, 2018).

CME near the Earth. For the completeness, we briefly introduce the improved FRIS model and the parameters which can be derived using the model in section 2. The application of the model to the coronagraphic observations of the selected CME is made in section 3. The extrapolation of the CME kinematics and estimated thermodynamic properties is described in section 4. The results obtained from the observations with the aid of the FRIS model and their discussion are summarized in section 5.

2. FLUX ROPE INTERNAL STATE (FRIS) MODEL FOR CME

The flux rope internal state (FRIS) model was first developed by Wang et al. (2009) and later by Mishra and Wang (2018). To better define the basis of the present study, we briefly describe the FRIS model here. The FRIS model treats the CME as an axisymmetric cylinder in the local scale with self-similar expansion during its heliospheric propagation (**Figure 1**). The model considers three global motions for a CME's flux rope characterized by linear propagation speed (υ_c), expansion speed (υ_e), and poloidal speed (υ_p) which are represented in the figure with black, red, and blue arrows respectively. Thus, under self-similar expansion and considering that magnetic field lines are frozen-in with the plasma flows, the density in the flux rope CME would have a fixed distribution. Further, the mass and angular momentum of the CME are assumed to be conserved. Thus, the average density in the flux rope would change with time as CME propagates away from the Sun. Under the assumption that the axial length of a CME flux rope is proportional to the distance (L) between the axis of the flux rope and the solar surface, the average density can be expressed in terms of L and radius (R) of the cross-section of the flux rope.

Further, using the laws of thermodynamics for a polytropic process, one can express the evolution of a thermodynamic variable, such as a change in entropy, in terms of average density and polytropic index (Γ). The FRIS model investigates the expanding propagation of a flux rope CME under thermal pressure force, Lorentz force from the axis to the boundary of the flux-rope, and centrifugal force due to the poloidal motion of the plasma. Therefore, one can derive the expressions for various forces by measuring the kinematics (i.e., L, R, and their derivatives) of a CME flux rope. The derivation of dynamic and thermodynamic variables is possible by involving several unknown constants dependent on the plasma and magnetic field parameters (e.g., distributions of density, poloidal speed, and magnetic vector potential, length of the flux rope, equivalent heat source and coefficient of conductivity, etc.) inside the flux rope CME. Therefore, in the model, the evolution of several thermodynamic parameters of the CME is expressed in terms of a time-dependent variable (λ) that can further be expressed in terms of the observed kinematic parameters of the CME and on several unknown coefficients introduced in the model. These introduced unknown coefficients (c_{1-5}) could be derived from the observed kinematics of the CMEs. The expressions for the coefficients depend on other unknown constants and their interpretation is given in the middle and bottom panels of **Table 1**. It is also evident that once the values of λ, its derivative, the coefficients, and CME kinematics are estimated, the expressions in the top panel of the table can be used to estimate several thermodynamic parameters of the CME.

$$
\begin{aligned}
(LR^2)^{\gamma-1} &= L^{\gamma-1}R^{\gamma-1}\Big[c_5a_e + \{(\gamma-1)c_4a_e\nu_c - c_3c_5L^{-1} \\
&+c_4\frac{da_e}{dt}L\}R^{-1} \\
&+\{(2-\gamma)c_3c_4\nu_cL^{-1} + (\gamma-1)c_4a_e\nu_eL\}R^{-2} \\
&+\{(2-\gamma)c_3c_4\nu_e - c_2c_5L - c_1c_5\}R^{-3} \\
&+\{(1-\gamma)c_1c_4\nu_c - \gamma c_2c_4\nu_cL\}R^{-4} \\
&+\{(4-\gamma)c_1c_4\nu_eL + (4-\gamma)c_2c_4\nu_eL^2\}R^{-5}\Big] \qquad (1)
\end{aligned}
$$

TABLE 1 | List of the derived internal thermodynamic parameters, constants, and coefficients from FRIS model.

Internal thermodynamic parameters derived from the model

Quantities	Factors	Values	SI units
Lorentz force ($\bar{f}_{em}$)	$\frac{k_2 M}{k_7}$	$c_2 R^{-5} + c_3 L^{-2} R^{-3}$	Pa m^{-1}
Thermal pressure force ($\bar{f}_{th}$)	$\frac{k_2 M}{k_7}$	$\lambda L^{-\gamma} R^{-\gamma-1}$	Pa m^{-1}
Centrifugal force ($\bar{f}_p$)	$\frac{k_2 M}{k_7}$	$c_1 R^{-5} L^{-1}$	Pa m^{-1}
Proton number Density ($\overline{n_p}$)	$\frac{M}{k_7}$	$\frac{1}{\pi m_p}(LR^2)^{-1}$	m^{-3}
Thermal pressure ($\overline{p}$)	$\frac{k_2 k_8 M}{k_4 k_7}$	$\lambda (LR^2)^{-\gamma}$	Pa
Temperature ($\overline{T}$)	$\frac{k_2 k_8}{k_4}$	$\frac{\pi\sigma}{\gamma-1}\lambda (LR^2)^{1-\gamma}$	K
Changing rate of entropy ($\frac{ds}{dt}$)		$\frac{1}{\sigma\lambda}\frac{d\lambda}{dt}$	J K^{-1} kg^{-1} s^{-1}
Heating rate ($\overline{\kappa}$)	$\frac{k_2 k_8}{k_4}$	$\frac{\pi}{\gamma-1}(LR^2)^{1-\gamma}\frac{d\lambda}{dt}$	J kg^{-1} s^{-1}
Thermal energy (E_i)	$\frac{k_2 k_8 M}{k_4}$	$\frac{\pi}{\gamma-1}\lambda (LR^2)^{1-\gamma}$	J
Magnetic energy (E_m)		$E_{m1} + E_{m2}$	J
E_{m1}	$\frac{k_9}{k_7}$	$\frac{\pi}{\mu_0} L^{-1}$	J
E_{m2}	$k_7 k_{10}$	$\frac{\pi}{\mu_0} LR^{-2}$	J
Polytropic index (Γ)		$\gamma + \frac{\ln \frac{\lambda(t)}{\lambda(t+\Delta t)}}{\ln\left\{\frac{L(t+\Delta t)}{L(t)}\left[\frac{R(t+\Delta t)}{R(t)}\right]^2\right\}}$	

All the constants (k_{1-12}) introduced in the model

Constants	Interpretations
k_1	Scale the magnitude of the poloidal motion
$k_{2-6,8-10}$	Integrals of distributions of density, poloidal speed and magnetic vector potential
k_7	Ratio of the length of the flux rope *l* to the distance *L*
k_{11}	Coefficient of equivalent conductivity
k_{12}	Aspect ratio, i.e., the ratio of the radius of the flux rope *R* to the distance *L*

All the coefficients (c_{0-5}) introduced in the model

Coefficients	Expressions
c_0	$\frac{k_4 M^{\gamma-1}}{k_2 k_7^{\gamma-1}}$
c_1	$\frac{k_1^2 k_3 L_A^2}{k_2 M^2} \geq 0$
c_2	$\frac{-k_5 k_7}{\mu_0 k_2 M}$
c_3	$\frac{-k_6}{\mu_0 k_2 k_7 M} \leq 0$
c_4	$\frac{k_2 k_8 M}{(\gamma-1) k_4 k_7 k_{11} T_a}$
c_5	$\frac{\pi\sigma k_2 k_8}{(\gamma-1) k_4 T_a}$

Top: The estimated thermodynamic parameters are scaled by the factors, i.e., Quantity = Factor × Value. We note that the variable, $\lambda = L^{\gamma-1}R^{\gamma-1}(a_e - c_1 R^{-3} - c_2 LR^{-3} - c_3 L^{-1}R^{-1})$. The values of L and R of the flux rope can be measured from the imaging observations, and consequently the value of λ can be derived. γ is the adiabatic index (5/3 for monoatomic ideal gas), μ_0 is the magnetic permeability of free space, M is the total mass of a CME, and $\sigma = \frac{(\gamma-1)m_p}{2k}$, where m_p is the proton mass and k is the Boltzmann constant. Middle: The constants $k_{2,7,8,11} > 0$ while $k_{3,6,9,10} \geq 0$. These constants cannot be estimated from the FRIS model alone. Bottom: The coefficients (c_{0-5}) are also constants which can be estimated from the model. L_A is the total angular momentum of a flux rope CME and T_a is the equivalent temperature of the ambient solar wind around the CME.

The relation between the unknown coefficients and the measurements of a CME flux rope is expressed in Equation (1). In the equation, *L*, *R*, υ_c, υ_e, a_e, and $\frac{da_e}{dt}$ are the measurements of distance between the axis of the flux rope and the solar surface, the radius of the flux rope, propagation speed, expansion speed, expansion acceleration, and rate of change of expansion acceleration of the flux rope, respectively. γ is the heat capacity ratio (i.e., adiabatic index) which is 5/3 for monoatomic ideal gases. From the equation, it is clear that if we have the measurements *L*, *R*, and their time derivatives, the value of all the unknown coefficients c_{1-5} can be estimated by fitting the Equation (1) to the measurements of the CME flux rope. Once the values of c_{1-5} and λ is obtained from the model, several thermodynamic parameters of the CME can be estimated as evident from **Table 1**. From the table, we also note the presence of unknown factors which scale the estimated thermodynamic parameters. These factors forbid us to estimate the absolute value of most of the thermodynamic parameters of the CME, but allow to show their trend with time or heliocentric distance.

Using the FRIS model, we can infer the evolution of thermodynamic properties and internal forces of CMEs using the estimated kinematics of the CMEs as inputs in the model. Using multiple viewpoints observations, such as white light coronagraphic and heliospheric imaging observations from the twin *STEREO* spacecraft, and 3D reconstruction methods, it is possible to accurately estimate the CMEs deprojected kinematics as they propagate farther out from the Sun (Inhester, 2006; Thernisien et al., 2009; Mierla et al., 2010; Davies et al., 2013; Mishra et al., 2014; Harrison et al., 2018). If a CME could not be tracked continuously in imaging observations at larger distances from the Sun, one can implement the drag-based model (DBM) (Vršnak et al., 2013) and/or MHD models (Pomoell and Poedts, 2018) to derive the speed of the CME at those distances.

3. APPLICATION OF THE FRIS MODEL TO THE CME OF 3 APRIL 2010

The CME of 3 April 2010 was associated with the disappearance of a filament, coronal dimming, and a B7.4 long-duration flare from NOAA Active Region (AR) 1059 (Liu et al., 2011). The CME was observed as a halo by SOHO/LASCO-C2, in the SE quadrant by *STEREO*/COR1-A and in the SW quadrant by *STEREO*/COR1-B coronagraphs. To implement the FRIS model, as described in section 2, we require the radius of cross-section of the flux rope CME (*R*), the distance of the axis of the flux rope from the solar surface (*L*) and their derivatives.

3.1. Observations and Measurements From Imaging Observations

To derive the 3D kinematics (*L*, *R*, directions, etc.) of the selected CME, we used the Graduated Cylindrical Shell (GCS) model (Thernisien et al., 2006, 2009). The details about derivable parameters from GCS forward fitting model and procedures for its correct application have been discussed thoroughly in the literature (Lynch et al., 2010; Thernisien, 2011; Vourlidas et al., 2013; Wang et al., 2014; Mishra et al., 2015). The GCS model is applied first to the COR2 observations of the CME. We manually adjusted all the six free parameters of the GCS model to closely match the modeled flux rope geometry with the observed

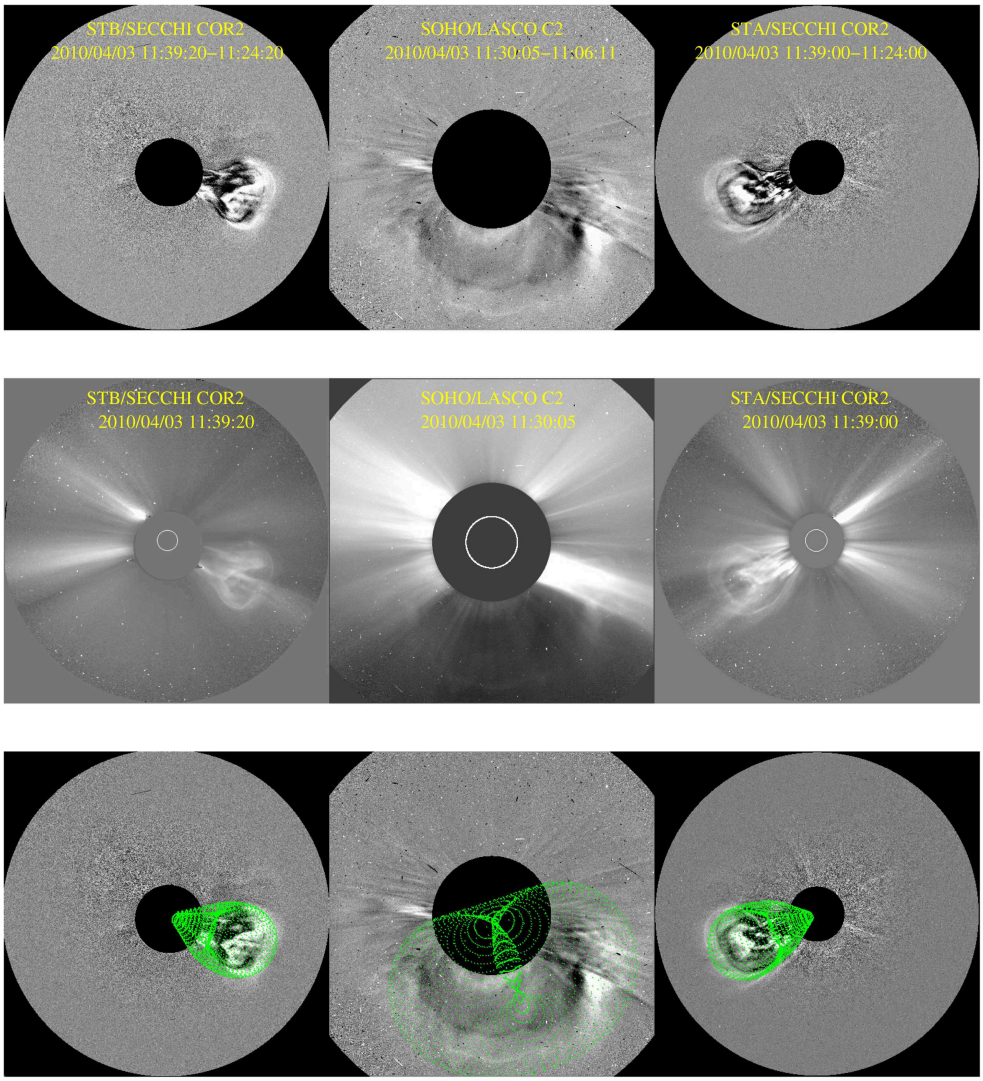

FIGURE 2 | The observation of 3 April 2010 CME from three different viewing angles. The triplet of concurrent images are taken from *STEREO*/COR2-B **(left)**, SOHO/LASCO-C2 **(middle)**, and *STEREO*/COR2-A **(right)** around 11:39 UT on 3 April 2010. The top, middle and bottom panels show the running difference images, direct images, running difference images having GCS model wire-frame overlaid with green, respectively.

CME flux rope. The GCS fitted wireframe contour obtained after the application of the GCS model to the contemporaneous coronagraphic images of the CME from the three viewpoints are shown in **Figure 2**. However, it is difficult to apply the GCS model to HI images due to the faint structure of CMEs at large distances from the Sun. Despite the ambiguous tracking of the CME flux rope in HI1 field of view, we applied the GCS model to the HI1 observations and derived the GCS modeled parameters. The GCS fitted wireframe contour to the contemporaneous images of HI1-A, LASCO-C3, and HI1-B are shown in **Figure 3**. The obtained longitude, latitude, tilt angle, aspect ratio (a) and half-angle of the CME are 1°, -20°, 20° (i.e., anti-clockwise from the ecliptic plane), 0.43 and, 20°, respectively when the leading edge of the CME was at the height (h) of 54 $R_\odot$ from the Sun. On comparing the GCS parameters in COR2 and HI1 field of view, we find that the CME smoothly deflected toward the Sun-Earth line by $\sim 7^\circ$ and toward the ecliptic by $\sim 6^\circ$ during its propagation from 4 $R_\odot$ to 35 $R_\odot$ while other GCS parameters were unchanged.

We used the precise measurements of CME's aspect ratio (a) and the height of its leading edge (h), obtained from GCS forward model, to derive the radius of the flux rope as $R = (\frac{a}{1+a})h$. The distance (L) of the center of the flux rope from the solar surface is given as, $L = D - 1\ R_\odot$, where D is the heliocentric distance of the CME's center and is given by, $D = h - R$. The value of D, R, their first-order time derivative as propagation and expansion speeds (υ_c & υ_e), and their second-order time derivatives as propagation and expansion accelerations (a_c & a_e) are shown in **Figure 4**. The figure also shows the vertical error bars at each data point considering arbitrary uncertainties of 0.5 $R_\odot$ and 1 $R_\odot$ in the measurements of the distance from COR2

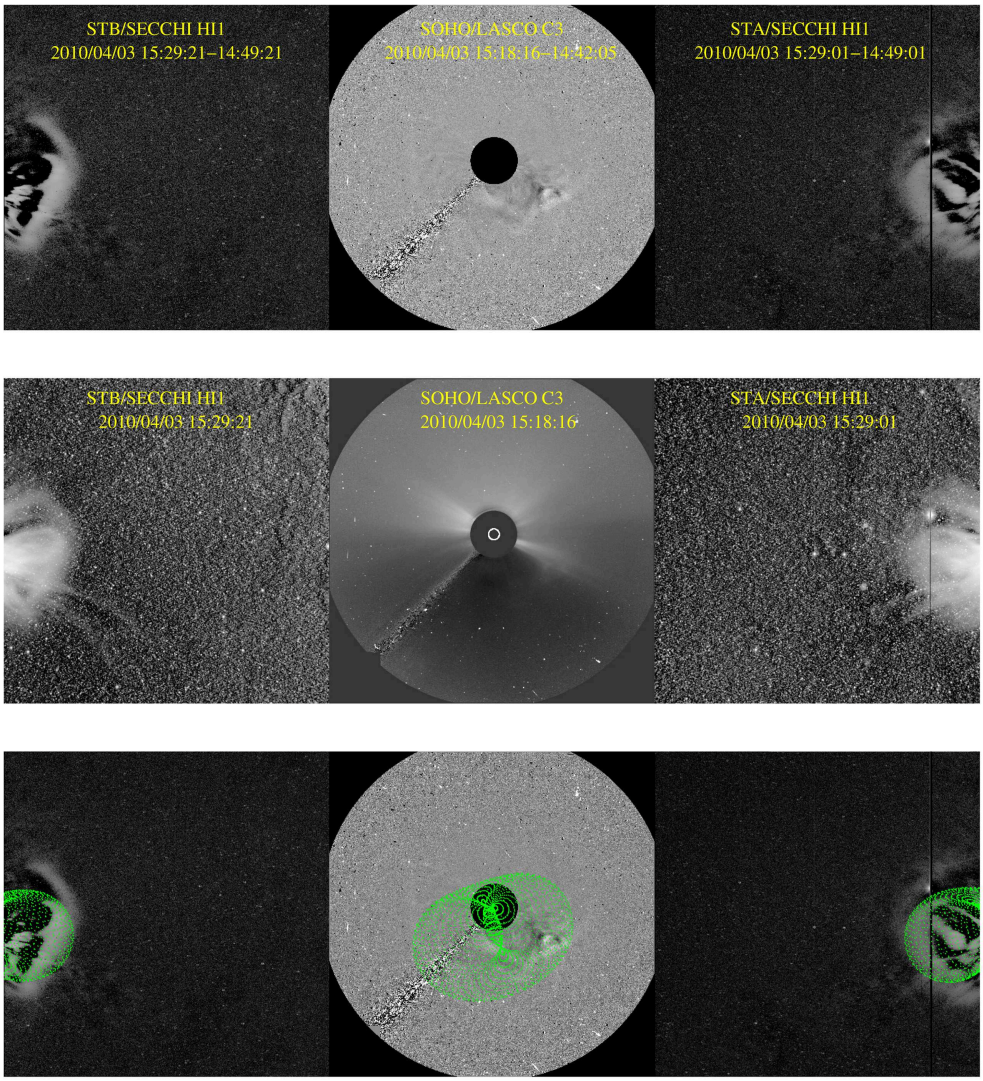

FIGURE 3 | Same as in **Figure 2**. In this case, however, the triplet of concurrent images are taken from *STEREO*/HI1-B **(left)**, SOHO/LASCO-C3 **(middle)**, and *STEREO*/HI1-A **(right)** around 15:29 UT on 3 April 2010.

and HI1 observations, respectively. The relative uncertainties in the acceleration is larger than that in the speed. This implies that uncertainties in the measurements of R and D will be amplified in its second-order derivatives. Therefore, we smooth the measured D and R before taking their derivatives. In the smoothing process, each observed data point is replaced with the value obtained after a linear fitting of a few neighboring data points within a moving boxcar. The FRIS model involves the acceleration of the CME flux rope and therefore the uncertainties in the measured kinematics of the CME will propagate into the derived model results. In the figure, a measurements gap in the kinematics separates the values derived from COR2 and HI1 observations. The measurement gap appeared because of difficulty in tracking the CME continuously during its transition from the COR2 field of view to the HI1 field of view. Such a situation often arises as CME flux rope becomes faint near the exit edge of COR2 and is not observed as a fully developed structure at the entrance of HI1. The COR2 observations allowed the tracking of the CME from $D = 2.5\ R_\odot$ to 8.6 $R_\odot$ and the HI1 observations enabled us to track the CME farther from $D = 15\ R_\odot$ to 42 $R_\odot$ from the Sun. During the evolution of the CME from $D = 2.5$ to 42 $R_\odot$, the radius of the flux rope expanded from $R = 1.1$ to 18.2 $R_\odot$.

From **Figure 4**, the propagation speed of the CME is found to rise in the beginning from 540 km s^{-1} at $D = 2.5\ R_\odot$ to 680 km s^{-1} at $D = 15\ R_\odot$, which slowly declines to be 580 km s^{-1} at $D = 42\ R_\odot$. Similarly, the expansion speed of the CME flux rope rises from 231 to 293 km s^{-1} which then smoothly declines to 250 km s^{-1}. We also note a change in the trend of CME acceleration for the measurements in COR2 and HI1. This is possible due to the use of observations from different instruments (i.e., COR2 and HI1) which have different sensitivity, making difficult the tracking of the same feature from COR2 to

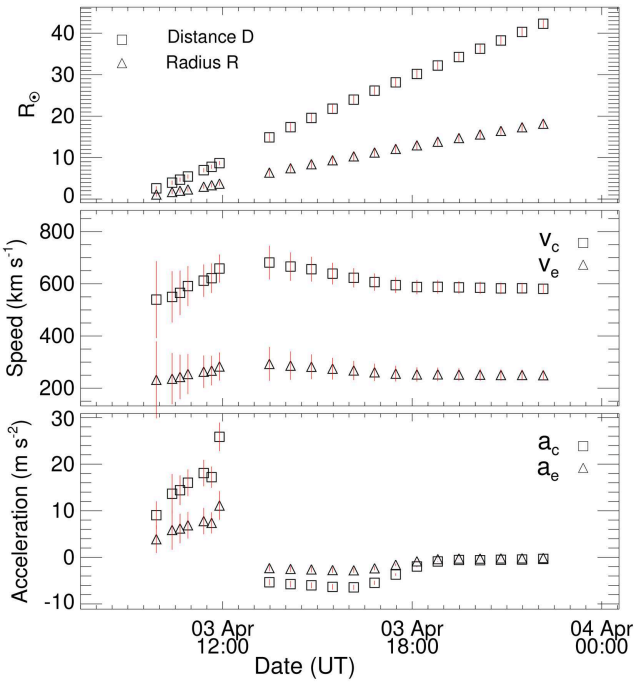

FIGURE 4 | The top panel shows the variations of the heliocentric distance (*D*) of the center of flux rope CME and its radius (*R*) with time. The data points before and after the measurements gap correspond to estimates from the COR2 and HI1 observations, respectively. The first-order derivative of *D* and *R* as the propagation speed (v_c) and expansion speed (v_e) is shown in the middle panel. The bottom panel shows the propagation acceleration (a_c) and expansion acceleration (a_e) as the first-order derivative of v_c and v_e, respectively. The vertical lines at each data point show the error bars which are derived from the arbitrary assumption of the uncertainties of 0.5 $R_\odot$ and 1 $R_\odot$ in the measurements of *D* from COR2 and HI1 observations, respectively.

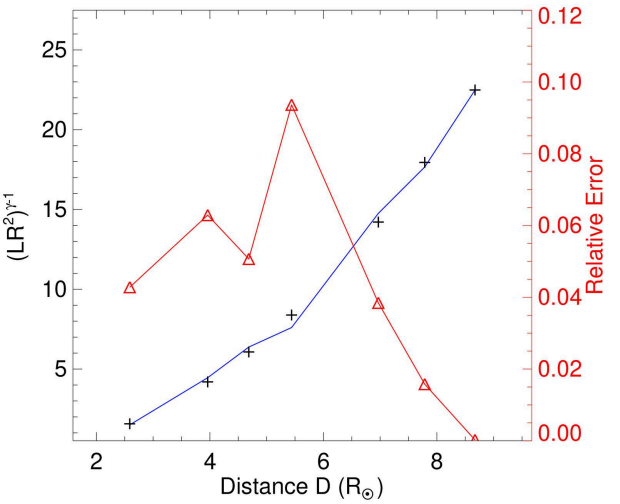

FIGURE 5 | The variations in $(LR^2)^{\gamma-1}$ from the measurements (black), the modeled result for this parameter (blue), and the relative error (red) in the model results are shown.

HI1. However, the deceleration of the CMEs within few solar radii in the coronagraphic field of view, followed by a phase of residual acceleration, has been noted in earlier studies (Zhang and Dere, 2006; Vršnak and Žic, 2007). The effect of tracking uncertainties between COR2 and HI1 may be minimal on the CME thermodynamics which is obtained by the separate run of the FRIS model for the observations of COR2 and HI1, as explained in section 3.3. The kinematics of this CME has also been investigated extensively in earlier studies using different 3D reconstruction techniques on *STEREO*/COR and HI observations in conjunction with drag based and MHD models (Möstl et al., 2010; Liu et al., 2011; Rollett et al., 2012; Mishra and Srivastava, 2013; Mishra et al., 2014). These studies tracked the density enhanced feature in the shock-sheath region of the CME by constructing the *J*-maps (Davies et al., 2009). Although our present study derived the kinematics of the CME flux rope using the GCS model instead of tracking the density feature in the J-maps, we find that our estimates of kinematic parameters are in fair agreement to those in earlier studies within 10%. Once the kinematics of the CME flux rope is obtained, it can be used to constrain the FRIS model and probe the internal state of the CME.

3.2. Implementing the FRIS Model

The FRIS model derives the thermodynamic parameters of a CME by using the estimates of the kinematics of the CME, the unknown coefficients (c_{1-5}), and the time-dependent variable λ in the model. To implement the FRIS model, we follow the following three main steps: (i) To determine the best set of unknowns coefficients which can represent the observed characteristics of the flux rope, we fitted the measured values of $(LR^2)^{\gamma-1}$ in the left-hand side of Equation (1) with the model derived expression in the right-hand side of the equation. The fitting is performed using *MPFITFUN* routine of IDL which can fit a user-supplied model to a set of user-supplied measured data (Markwardt, 2009). On using the distance in unit of $R_\odot$ and time in unit of hr for observed data points of the CME characteristics derived from COR2 observations, the values of the coefficients, i.e., c_1, c_2, c_3, c_4, and c_5 are obtained as 0, −25.6, −75.8, 1.8, and 1.0, respectively. The goodness of the fit can be examined based on the values of $(LR^2)^{\gamma-1}$ derived from the measurements (Q_m) and its values derived from fitting (Q_f) model expression. The relative error (δ) in the fitted result compared to the measured results is represented by $\delta = |Q_m - Q_f|/Q_m$, which when multiplied by 100 gives its percentage value. We find that the relative error in the model results to the measurements is always within 10% at any data point in COR2 as shown in **Figure 5**. This represents a reasonably accurate fitting as the model results match well with the measurements for the selected CME. (ii) We used the obtained values of the coefficients and observed kinematic parameters to determine the value of λ. (iii) Finally, once the values of λ, its derivative, and the coefficients are known, the expressions in **Table 1** are used to estimate several thermodynamic parameters of the CME. We note that the obtained values of the coefficients c_{1-5} are assumed to also represent the evolution of the CME derived from HI observations. Such an assumption helps in mutually comparing

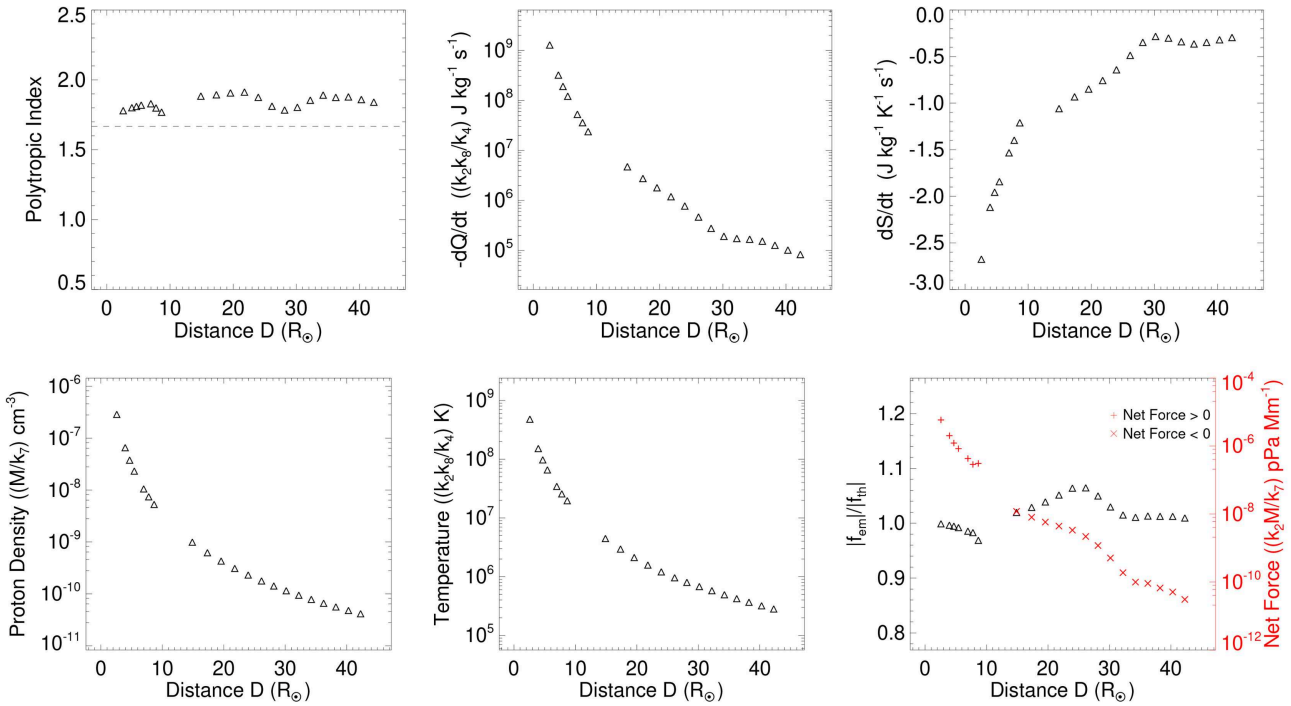

FIGURE 6 | Top: The variation of the polytropic index (Γ), cooling rate (-dQ/dt), and rate of change of entropy (ds/dt) of the CME with the heliocentric distance of the CME's center (D) are shown in the left, central, and right panels, respectively. **Bottom**: The average proton number density ($\overline{n_p}$) and Temperature ($\overline{T}$) of the CME, and different forces acting on the CME with the heliocentric distance of its center (D) is shown in the left, central, and right panel, respectively. The bottom-right panel shows the ratio of absolute values of Lorentz and thermal force ($|\bar{f}_{em}|/|\bar{f}_{th}|$) (on left Y-axis) and the net force (on right Y-axis) acting inside the CME.

the estimates of the CME thermodynamic parameters in COR2 and HI field of view. This is because the estimates of the CME thermodynamic parameters are scaled by the factors involving the coefficients.

3.3. Thermodynamic Processes in a CME

We examine the evolution of several thermodynamic parameters using the FRIS model for the selected CME of 3 April 2010. The estimated polytropic index, cooling rate, rate of change of entropy, density, temperature, and various forces are shown in **Figure 6**. It is noted that we could only estimate the absolute value of the polytropic index and rate of change of entropy. The estimates of other parameters are relative values because they are scaled by factors listed in **Table 1** and mentioned along the Y-axes of the various panels in the figure. From the top-left panel of the figure, it is found that although there is a small fluctuation in the value of the polytropic index, its value range between 1.7 and 1.9 as the CME is evolving from the inner to the outer corona. Thus, the value of the polytropic index is almost constant during the evolution of the CME. The estimated value of the polytropic index greater than 1.66 implies that CME is releasing the heat into the surrounding.

The top-central panel of **Figure 6** shows that the value of the cooling rate per unit mass (-dQ/dt) which is always positive for the CME of 3 April 2010. However, the value of cooling rate is decreasing continuously as the CME is moving away from $D = 2.5\ R_\odot$ to $D = 42\ R_\odot$. The positive value of cooling rate implies that thermal energy is being released out from the CME into the surrounding. The top-right panel of the figure shows the rate of change of entropy (ds/dt) per unit mass. The value of rate of change of entropy was about –2.7 J kg^{-1} K^{-1} s^{-1} at the beginning of $D = 2.5\ R_\odot$ and continuously increased to become –0.3 J kg^{-1} K^{-1} s^{-1} at $D = 42\ R_\odot$. This implies that the rate of loss of the entropy is getting smaller as the CME is moving away from the Sun. It is also noted that the release of entropy from the CME and its cooling rate are larger near the Sun (i.e, within $D = 8.6\ R_\odot$) than those at larger distances from the Sun.

The bottom-left and bottom-central panels of **Figure 6** shows the estimated variations in the average proton density and temperature of the CME with the heliocentric distance of its center, respectively. We note a decrease in average CME density and temperature with the distance which implies a decrease in thermal pressure inside the CME. This is expected as the CME is continuously expanding while moving away from the Sun. The decrease in the proton density and temperature is much faster when the CME is near the Sun (i.e, observed in COR2 within $D = 8.6\ R_\odot$), and the rate of decrease becomes slower tending toward its asymptotic values as the CME moves away from the Sun. This is expected as the expansion acceleration (a_e) is positive (with increase in υ_e from 231 to 283 km s^{-1}) corresponding to COR2 observations and it has negative values (with decrease in υ_e from 293 to 250 km s^{-1}) corresponding to HI1 observed data points (**Figure 4**).

As described in section 3.2, the value of the coefficient c_1 is estimated to be zero from the fitting of Equation (1). c_1 is related to the poloidal motion of the plasma, and thus the centrifugal force is found to be absent for the CME of 3 April 2010. This is expected as there is no strong evidence of significant poloidal motion in CMEs near the Sun. However, recent works has suggested the presence of poloidal plasma motion inside the CMEs near 1 AU possibly due to local mechanisms rather than a global cause (Wang et al., 2015; Zhao et al., 2017a,b). In the present study, we found that the dynamics of the selected CME is governed by the Lorentz force ($\bar{f}_{em}$) and thermal pressure force ($\bar{f}_{th}$). The evolution of the ratio of the absolute value of average Lorentz to thermal forces and the net force ($\bar{f}$) inside the CME is shown in the bottom-right panel of **Figure 6**. From the figure, it can be noted that the ratio of the two forces is slightly smaller than unity near the Sun (i.e, within $D = 8.6\ R_\odot$) while it becomes slightly larger than unity at larger distances from the Sun in HI1 field of view. Thus, the magnitude of the thermal force is larger than the Lorentz force near the Sun. The net force inside the CME (i.e., Lorentz force + thermal pressure force) is found to be positive near the Sun, within $D = 8.6\ R_\odot$, after which the net force is negative at a larger distance. This implies that the directions of the two forces are opposite. Further, it is noted from **Figure 4** that the expansion acceleration is positive (i.e., $a_e = 3$–$11\ m\ s^{-2}$) below $D = 8.6\ R_\odot$ and beyond this distance its value becomes negative (i.e., $a_e = -2.3$ to $-0.2\ m\ s^{-2}$). Thus, we find that the Lorentz force ($\bar{f}_{em}$) acting toward the center of the CME prohibits it from free expansion. The thermal pressure force ($\bar{f}_{th}$) acting away from the center of the CME is the actual internal cause of the CME expansion. It is evident that the absolute values of both the $\bar{f}_{em}$ and $\bar{f}_{th}$ forces are getting very close to each other at the last few data points where the expansion acceleration is also close to zero.

4. EXTRAPOLATION OF CME INTERNAL STATE UP TO 1 AU

4.1. Estimation of CME Kinematics

The internal thermodynamic parameters of the CME can be estimated up to 1 AU if the measured propagation and expansion speed profiles of the CME to be used as inputs in the FRIS model (Mishra and Wang, 2018) could be measured up to 1 AU. However, we could not unambiguously identify CME flux rope using GCS forward fitting model (Thernisien et al., 2009) beyond $D = 42\ R_\odot$, as explained in section 3.1. To derive the CME speed from the distances beyond $D = 42\ R_\odot$ to near the Earth at L1, we implemented the drag based model (DBM) (Vršnak et al., 2013). The DBM assumes that beyond a distance of $20R_\odot$, the acceleration of a CME is governed by the interaction between the CME and the ambient solar wind via aerodynamic drag (Cargill, 2004). The quadratic form of the instantaneous drag acceleration is, $a_d = -K_d\ (v - w)\ |(v - w)|$, where v, w, and K_d are the instantaneous speed of the CME, ambient solar wind speed, and the drag parameter, respectively. The analytical solution to the equation of motion of a CME under the drag acceleration with the approximation of $K_d(r) =$ constant and $w(r) =$ constant, can be written as Equation (2). In the equation, the sign $\pm$ depends on deceleration/acceleration regime, i.e., it is plus for $\upsilon_0 > w$, and minus for $\upsilon_0 < w$.

$$r(t) = \pm\frac{1}{K_d}\ln[1 \pm K_d(\upsilon_0 - w)t] + wt + r_0 \qquad (2)$$

From Equation (2), we can find the time taken by a CME to travel from an initial radial distance (i.e., r_0 at $t = t_0$) to a final distance (i.e., r at t) for a given initial take-off speed of υ_0. The estimation of the drag parameter (K_d) for an individual CME depends on the cross-sectional areas of CME, solar wind density and CME mass. The large uncertainties in the estimation of the CME mass using coronagraphic observations from single and multiple viewpoints has been discussed in earlier studies (Vourlidas et al., 2000; Colaninno and Vourlidas, 2009; Mishra et al., 2014). Because of the limited accuracy in the estimation of variables on which the drag parameter depends, we take its value from a statistical study of a large number of events in Vršnak et al. (2013).

The study of Vršnak et al. (2013) shows that the drag parameter (K_d) often lies in the range 0.2×10^{-7} to $2.0 \times 10^{-7}\ km^{-1}$. They also showed that the ambient solar wind speed should be chosen to lie between 300 and 400 km s^{-1} for a slow solar wind environment, and between 500 and 600 km s^{-1} for fast solar wind environment created by a coronal hole in the vicinity of the source region of the CME. We note that the study of Vršnak et al. (2013) represents the drag parameter with the symbol γ while we have reserved this symbol for the adiabatic index. The selected CME is propagating at least partly through a high-speed solar wind stream as confirmed in earlier studies (Möstl et al., 2010; Liu et al., 2011; Rollett et al., 2012). For such cases, it is suggested in Vršnak et al. (2013) that a higher value of the solar-wind speed should be combined with a lower value of drag parameter. In this way, we took a straightforward option to choose the drag parameter and extrapolate the CME kinematics beyond the HI field-of-view where the CME could not be tracked unambiguously.

The Earth was found to be immersed in high-speed solar wind from a coronal hole located at a geoeffective location on the Sun during the arrival of this CME at 1 AU. It is most likely that high-speed wind has partly influenced the kinematics of this fast CME. Several studies have established the moderate deceleration of a CME during its journey from the Sun to 1 AU because of aerodynamic drag by the ambient high-speed (Möstl et al., 2010; Liu et al., 2011; Rollett et al., 2012; Mishra and Srivastava, 2013). In such a case, we extrapolated the obtained kinematics of the CME from GCS fitting (**Figure 4**) up to 1 AU by implementing the DBM (Vršnak et al., 2013). Using the last data point from GCS fitting, we find the heliocentric distance of the leading edge (i.e., $h = D + R$) of the CME at 60.5 $R_\odot$ with the speed (i.e., propagation speed + expansion speed) of 830 km s^{-1} at 22:10 UT on 3 April 2010. These characteristics of the CME leading edge such as radial distance, speed and time are used as initial inputs in Equation (2). Further, we used a high value of $w = 550$ km s^{-1} combined with a low value of $K_d = 0.2 \times 10^{-7}$ as the high-speed solar wind is characterized by low density and high speed. Once the time variations of h is estimated, we derived other kinematic parameters up of the CME up to 1 AU (**Figure 7**) to be used in

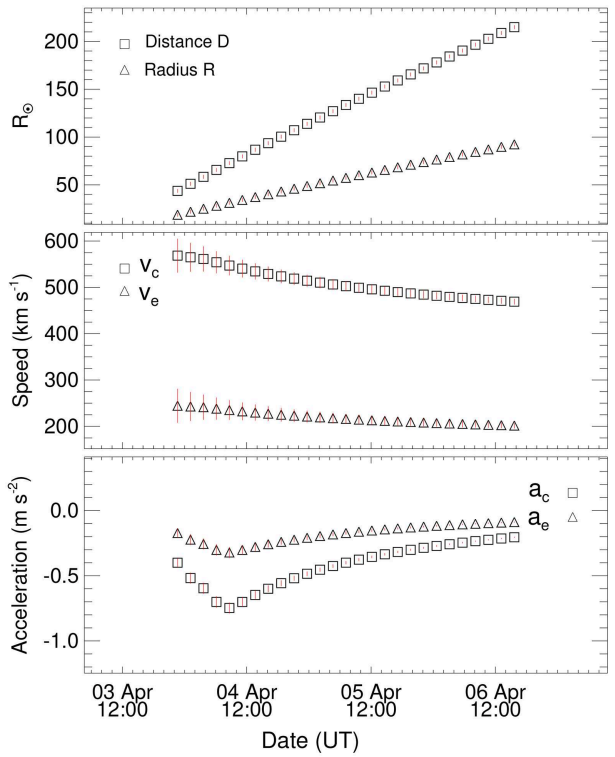

FIGURE 7 | The kinematics of 3 April 2010 CME as obtained by using the drag based model (DBM) is shown. Top panel shows the estimated heliocentric distances (*D*) of the center of flux rope CME and its radius (*R*). The first-order derivative of *D* and *R* as the propagation speed (v_c) and expansion speed (v_e), respectively, are shown in the middle panel. The bottom panel shows the propagation acceleration (a_c) and expansion acceleration (a_e) as the first-order derivative of v_c and v_e, respectively. The vertical lines at each data point show the error bars. The errors are derived from the arbitrary assumption of the uncertainties of 2 $R_\odot$ in the estimates of *D*.

the FRIS model. To estimate the values of *R* corresponding to *h*, it is assumed that the aspect ratio (*a*) of the CME flux rope remains the same as derived from the GCS model using COR2 observations. The validity of the assumption of constant aspect ratio is discussed in section 5.

The estimates of kinematics for the CME using the DBM from $D = 44\ R_\odot$ to 1 AU is shown in **Figure 7**. From the figure, it can be seen the estimated arrival time of the center of the CME flux rope at L1 at about 15:30 UT on 6 April with a transit speed (υ_c) of 470 km s^{-1}. At this distance, the radius of the flux rope is 90 $R_\odot$ having an expansion speed (υ_e) of 200 km s^{-1}. From the obtained latitude and longitude of the CME using GCS model in section 3.1, the CME is found to be heading toward the Earth, and an interplanetary counterpart of the CME should be observed by the spacecraft near the Earth. Using the *in situ* observations taken by *WIND* spacecraft (Ogilvie et al., 1995), Figure 14 in Mishra and Srivastava (2013) shows the arrival of a CME at the L1 point as a magnetic cloud (Klein and Burlaga, 1982; Lepping et al., 1990). Since the magnetic cloud is known to be a flux rope structure, the observed properties of the magnetic cloud can be compared with the properties of the flux rope estimated from the DBM as it will be explained in section 5. Once we could estimate the propagation and expansion characteristics of the CME up to 1 AU, they can be used as inputs in the FRIS model to extrapolate the CME thermodynamic parameters.

4.2. Estimation of CME Thermodynamics

We used the expressions from **Table 1** and derived the CME thermodynamic parameters which are shown in **Figure 8**. It is noted that the value of the fitted coefficients (i.e., c_{1-5}) as used with COR2 and HI observed CME parameters are assumed to represent the evolution of the CME estimated from the DBM. From the top-left panel of **Figure 8**, it is seen that the polytropic index of the CME plasma remains constant at about 1.9 up to the moment the center of the CME reached 1 AU. The value of the polytropic index implies that the CME is continuously releasing heat into its surrounding during its heliospheric journey up to near the Earth. From the top-central panel of the figure, it is clear that the cooling rate (i.e, heat release out from the CME) is much faster at a smaller distance and becomes slower at the distances larger than $D = 80\ R_\odot$. The top-right panel shows that there is a loss of entropy (i.e., the release of entropy) from the CME throughout its heliospheric journey. However, the rate of loss of entropy became smaller beyond the distance $D = 80\ R_\odot$.

The bottom-left panel of **Figure 8** shows the decrease in the average proton density of the CME implying its continuous expansion up to 1 AU. The expansion is seen from the middle panel of **Figure 7**. The bottom-central panel of **Figure 8** shows a decrease in the average temperature of the CME implying the work done by the CME in the process of expansion. The result suggests that the CME originated from hotter source region on the Sun and cools down during its expanding propagation. Looking **Figures 6**, **8** together, we note that the decrease of density and temperature of the CME is faster at lower distances and tends toward its asymptotic values. Our analysis suggests that the expansion of the CME has not been sufficient before the CME reaches the Earth and, therefore, the CME is found to release heat and entropy into the surrounding.

The bottom-right panel of **Figure 8** shows the ratio of absolute values of the Lorentz ($|\bar{f}_{em}|$) to thermal pressure forces ($|\bar{f}_{th}|$) and the net force acting inside the CME. From the figure, we note that the value of $|\bar{f}_{em}|/|\bar{f}_{th}|$ is around 1.01 in the beginning at $D = 44\ R_\odot$ and increases slowly to become around 1.17 at $D = 1$ AU. We also note that the net force which is the vector sum of Lorentz and thermal pressure force is always negative from $D = 44\ R_\odot$ to 1 AU. It implies that the Lorentz force is larger in magnitude than the thermal pressure force, and the direction of both the forces are opposite to each other. The Lorentz force prohibiting the free expansion of the CME leads to the expected negative net force which also corresponds to the negative expansion acceleration of the CME as shown in the bottom panel of **Figure 7**.

4.3. Comparison of Model Results With *in situ* Observations at 1 AU

The selected CME in our study is found to arrive at Earth and its identification in the *in situ* observations at the L1 point has

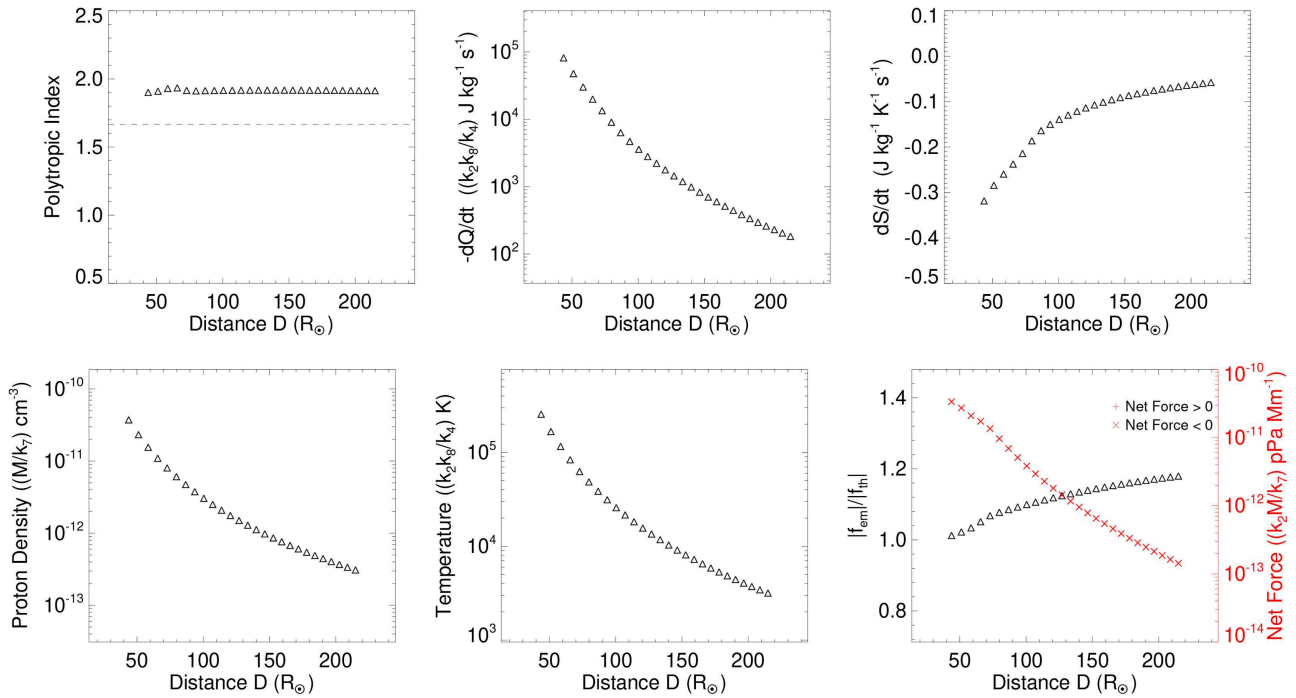

FIGURE 8 | Top: The variation of the polytropic index (Γ), cooling rate (-dQ/dt), and rate of change of entropy (ds/dt) of the CME with the heliocentric distance of the CME's center (D) is shown in the left, central, and right panels, respectively. **Bottom**: The average proton number density ($\overline{n_p}$) and Temperature ($\overline{T}$) of the CME, and different forces acting on the CME with the heliocentric distance of its center (D) is shown in the left, central, and right panel, respectively. The bottom-right panel shows the ratio of absolute values of Lorentz and thermal force ($|\bar{f}_{em}|/|\bar{f}_{th}|$) (on left Y-axis) and the net force (on right Y-axis) acting inside the CME.

been made in earlier studies (Möstl et al., 2010; Mishra and Srivastava, 2013). Using the FRIS model, in the present study, we could estimate the absolute value of the rate of change of entropy (ds/dt). The absolute value of heating rate per unit mass of the CME plasma can be written as, $dQ/dt = ds/dt \times \mathrm{T}$, where T is the average temperature of the CME plasma. Thus, the absolute value of the heating rate per unit mass of the CME plasma can also be estimated if the real temperature was known. Figure 14 in Mishra and Srivastava (2013) shows that the selected CME is identified as a magnetic cloud near the Earth and its average temperature [i.e., $(\mathrm{T}_p+\mathrm{T}_e)/2$] is noted as 4×10^4 K. The value of rate of change of entropy obtained from FRIS model at $D = 1$ AU is -5.8×10^{-2} J kg^{-1} K^{-1} s^{-1}. Therefore, the absolute value of heating rate of the CME plasma at $D = 1$ AU is estimated as -2.3×10^3 J kg^{-1} s^{-1}. The negative value of heating rate implies the cooling, i.e., the release of heat from the CME. The release of thermal energy from the CME is also confirmed from the value of the polytropic index which is about 1.9 at $D = 1$ AU.

Using the FRIS model, the average temperature of the CME at 1 AU is estimated as 3.17×10^3 K with a scale factor of $\mathrm{k_2k_8/k_4}$. From the *in situ* observations, the average temperature of the CME near 1 AU is noted as 4×10^4 K. On comparing the model-derived temperature with *in situ* observed temperature, the value of the factor $\mathrm{k_2k_8/k_4}$ is estimated as 12.6. The value of the factor depends on the coefficients c_{1-5} fitted from the model which is assumed to be the same during the entire journey of the CME. Therefore, if the value of the factor $\mathrm{k_2k_8/k_4}$ is assumed to be the same near the Sun as at 1 AU, the temperature of the CME would be 10^9 K at the distance of a few solar radii from the Sun. Clearly, the FRIS model overestimates the temperature near the Sun while underestimated its value near the Earth.

Further, it is evident from **Table 1** that if the absolute value of the proton number density is obtained by other means independent of the model, one can derive the unknown factor $\mathrm{M/k_7}$. In this factor, M is the mass of the CME and $\mathrm{k_7}$ is an important proportionality constant between the axial length (l) of the flux rope and the distance of the center of the flux rope from the solar surface, i.e., $l = \mathrm{k_7}\ L$, as derived in Mishra and Wang (2018). The model derived the proton number density of the CME at 1 AU is $3.09 \times 10^{-13} \times \mathrm{M/k_7}$ cm^{-3} while the *in situ* observed proton density of the magnetic cloud is 2 cm^{-3}. On comparing the model derived and observed density, the value of the factor $\mathrm{M/k_7}$ is found as 6.4×10^{12} kg. The value of true mass (M) for the CME of 3 April 2010 is estimated as 3.16×10^{12} kg in an earlier study of Bein et al. (2013). This mass is estimated using the method developed by Colaninno and Vourlidas (2009) where they use the two viewpoints of *STEREO*. From the mass estimates, the value of $\mathrm{k_7}$ is estimated as around 0.5 which is too small to be realistic. In fact, the value of $\mathrm{k_7}$ is found to be around 2.57 in earlier studies (Wang et al., 2015, 2016).

The small value of $\mathrm{k_7}$ suggests the underestimation of the proton number density from the FRIS model near 1 AU and/or underestimation of CME mass. The underestimation of CME mass by a factor of two is noted in the mass estimation method

which assumes the CME propagating in the plane of sky of the observer (Vourlidas et al., 2000). In the mass estimation method using coronagraph observations from multiple viewpoints of *STEREO* (Colaninno and Vourlidas, 2009), one can find the 3D direction of CME improving on the plane of sky assumption but still, the true width of the CME along the line of sight remains unknown. This unknown width of the CME and assumption that CME mass lies in a plane can lead to an underestimation of CME mass by up to 15% (Vourlidas et al., 2000). We also note that while comparing the model results with the observations at 1 AU, we used the mass estimates from near-Sun coronagraph observations. However, far from the Sun, the measured CME mass is found to increase due to piled-up mass of solar wind plasma around the CME, called the snow plough effect (Tappin, 2006; DeForest et al., 2013). We think that the extrapolation of CME thermodynamic parameters up to a large distance from the Sun, i.e., 1 AU have larger uncertainties due to limited accuracy in the input parameters of the model. Further insight can be made if the *in situ* observations of CME density and temperature are derived at other closer distances from the Sun. Further, we can see from **Table 1** that if the constant k_2 can be obtained, the absolute value of forces acting inside the CME can be estimated. The present study did not discuss each constant but rather focused on demonstrating the potential of the FRIS model for estimating the thermodynamic parameters of the CME from the Sun to 1 AU.

5. RESULTS AND DISCUSSION

Our present study estimates the thermodynamic parameters of the 3 April 2010 CME from near the Sun to the Earth using the Flux rope internal state (FRIS) model. Thus the model is efficient in probing the CME internal state at distances often inaccessible by the *in situ* spacecraft which usually provide the information on CME thermodynamics. The input for the model is the estimated kinematics of the CME which is derived using the *SOHO*/LASCO and *STEREO*/COR white-light observations in combination with the drag based model (DBM). The white-light observations enabled the identification of the CME flux rope to be fitted from the GCS model from $D = 2.5$ to 42 $R_\odot$, and thereafter the DBM is used up to $D = 1$ AU. The estimated thermodynamic parameters of the CME is shown in **Figures 6**, **8**. From both figures, we note that the polytropic index of the CME plasma ranged between 1.7 and 1.9 up to $D = 42$ $R_\odot$, and beyond this distance, the value of polytropic index remains constant as 1.9 up to $D = 1$ AU. A value of the polytropic index greater than 1.66 suggests that there is a release of heat out from the CME throughout its journey from near the Sun to Earth.

The obtained value of the polytropic index is not in agreement with earlier studies of Liu et al. (2006a) where they have reported a value of the polytropic index ranging between 1.1 and 1.3. However, they used *in situ* observations of ICMEs between 0.3 AND 20 AU and derived their result statistically. In a recent study, using the FRIS model, Mishra and Wang (2018) shows that the polytropic index for a CME (12 December 2008 event) decreases from 1.8 to 1.3 between $D = 6$ and 15 $R_\odot$. We, in the present study, find no systematic variation in the polytropic index despite tracking the CME up to much larger distances. It means that the CME of 3 April 2010 is always in heat releasing state unlike the CME shown in Mishra and Wang (2018) that was initially releasing heat before reaching an adiabatic state and then started acquiring heat from the ambient medium. We note that the CME of 12 December 2008 was having a slower speed while the CME selected for the present study is a fast CME showing only a moderate deceleration from the Sun to 1 AU. The moderate deceleration of the CME is expected as it is being pushed from the back by the high-speed wind which contributed to the CME's propagation speed but prohibited the CME from expansion. It has been shown that an interaction between the high-speed stream and the preceding magnetic cloud can compress the preceding structure (Fenrich and Luhmann, 1998; Gopalswamy et al., 2009). Thus, the insufficient expansion might not have allowed the CME to be cool enough to depart from the heat releasing state to an adiabatic state with the ambient surrounding.

It is expected that the heating of plasma in the open magnetic field configuration of the solar wind and in the closed magnetic field configuration of CMEs would be different. Thus, it is interesting to compare the magnitude of the estimated polytropic index of the selected CME with that of the solar wind plasma. The estimation of the polytropic index for the solar wind has been the subject of many studies (Parker, 1960; Feldman et al., 1978; Sittler and Scudder, 1980; Totten et al., 1995; Nicolaou et al., 2014). In the polytropic solar wind theory of Parker (1960), the polytropic index is suggested to be smaller than 1.5 to obtain an accelerated wind solution. This implies that the solar wind acceleration would become negative for the value of the polytropic index larger than 1.5, and no real wind-type solution exists. In Feldman et al. (1978) study, the value of electron polytropic index was determined to be 1.45 while Sittler and Scudder (1980) obtained its empirical value to be as 1.18. Further, Totten et al. (1995) empirically estimated the proton polytropic index and found its value to be 1.46. Recently, Nicolaou et al. (2014) determined that the average value of proton polytropic index to be around 1.8. Thus, there are mutually differing results on the behavior of solar wind whether it is more like that of an isothermal gas than an adiabatic one. In our study, the polytropic index of the ICME is around 1.8 which is clearly larger than the value for solar wind reported in most of the earlier studies. However, we expect that the selected Earth-directed CME of 3 April 2010 to be a unique case which is continuously being pushed by the high-speed stream emanating from a coronal hole located at a geoeffective location on the Sun (Möstl et al., 2010; Liu et al., 2011).

From the ratio of Lorentz and thermal pressure forces and the resultant direction of the net force as shown in **Figures 6**, **8**, it is evident that the Lorentz force is acting toward the center of the CME flux rope while the thermal pressure force is acting away from the center. The magnitude of both forces decreases as the CMEs moves out away from the Sun, however, the decrease in thermal pressure force is faster than the Lorentz force. This is evident as the net force is acting outward from the CME center in the beginning before $D = 8.6$ $R_\odot$ and beyond this distance, the net force is found to have the direction toward the center of the CME. Further, the expansion acceleration has the positive value

($a_e > 0$) before $D = 8.6\ R_\odot$ and after its value becomes negative ($a_e < 0$). The consistency in the direction of the net force and expansion acceleration suggests that the thermal pressure drives the expansion of the CME while the Lorentz force prohibits the CME from expansion. The direction of the Lorentz force is decided by the distribution of the B_z in the cross-section of the CME flux rope as described in Mishra and Wang (2018). The ratio of the magnitude of the Lorentz to thermal force is ranging between 0.99 and 0.96 before $D = 8.6\ R_\odot$, and beyond this distance it ranges between 1.01 and 1.17. This clearly shows that even a small difference between these two forces can change the expansion acceleration by a few m s^{-2}. Surprisingly, the CME is found to be in heat releasing state throughout its journey irrespective of the sign of the expansion acceleration and the net force.

In the process of heat release from the CME, we note a loss of entropy during the propagation of the CME from the Sun to Earth. The rate of loss of entropy is -2.7 J kg^{-1} K^{-1} s^{-1} at $D = 2.5\ R_\odot$ which reduced to be -0.58 J kg^{-1} K^{-1} s^{-1} at $D = 1$ AU. The rate of loss of the entropy is much faster before $D = 8.6\ R_\odot$ when the expansion acceleration and the net force are found to be positive. The cooling rate of the CME is consistent with the rate of loss of entropy throughout the CME journey. This is possible if the CME has higher heat content than the surrounding medium due to its compression by the high-speed wind stream from behind. We would like to point out that because of simplicity, the polytropic law has been employed in several studies. However, the polytropic approximation is a gross simplification of the real energy transport equation. There are various processes such as turbulence, magnetic field dissipation, conduction of heat from solar atmosphere, heat exchange with ambient medium, etc. which can lead to heating/cooling of the CMEs. Thus, using the FRIS model, the identification of the process responsible for the reported cooling of the CME remains unsolved, and further studies are required in this direction.

Interestingly, the CME is identified as a magnetic cloud in *in situ* observations at L1. The center of the magnetic cloud arrived at 02:50 UT on 6 April 2010 preceded by the arrival of a shock at 8:28 UT on 5 April 2010. The magnetic cloud, from its leading to trailing edge, took around 26.4 hr to cross the L1 point. The average propagation speed (υ_c) of the cloud is observed as 650 km s^{-1} while its expansion speed (υ_e) as 115 km s^{-1} at L1. From the *in situ* observed speeds at L1, the aspect ratio of the CME is measured to be around 0.20 which is around half of the aspect ratio derived from the GCS model on COR2 and HI-1 observations. It is clear that our assumption of constant aspect ratio for the CME, beyond the HI-1 observed last data point, breaks down before its arrival at L1. It is expected that the assumption would be broken gradually as the CME propagates away from the Sun in the radially expanding solar wind. Because of this, the estimates of radius, expansion speed, and expansion acceleration, determined using the combination of aspect ratio and heights of the CME obtained from DBM, would also have uncertainties. A correction factor to the aspect ratio of the CME, based on the near-Sun and near-Earth observations of the CME, may be introduced for examining its time variation. In another study, we plan to estimate the uncertainties in the thermodynamic parameters derived from the FRIS model due to uncertainties in the expansion characteristics which is used as inputs in the model.

From the *in situ* observations at L1, the radius of the cloud is measured to be around 89 $R_\odot$. The observed arrival time of the center of the cloud at L1 is around 12.6 hr early than estimated from DBM in section 4.1. Although the estimates of the radius of the cloud from the DBM and *in situ* observations are almost equal, the DBM estimates of propagation and expansion speed are 180 km s^{-1} smaller and 90 km s^{-1} larger, respectively, than the observed values. The underestimation of the propagation speed of the CME flux rope (i.e., magnetic cloud) from the DBM is consistent with the estimation of its delayed arrival near the 1 AU. However, the overestimation of expansion speed from the DBM may arise because of neglecting the flattening of the CME's front (i.e., constant aspect ratio assumption), the interaction of the CME with the high-speed wind, and/or trajectory of *in situ* spacecraft through the flank of the magnetic cloud (Möstl et al., 2010). It appears that when compressing a CME by high-speed wind from its back, the radial extent of the CME may not decrease but its expansion may slow down. This is most likely if the compression happens for a certain duration after which the CME may overexpand to return to its expected size.

It is also noted that the drag-based model assumes that the CME is propagating into an isotropic ambient solar wind. However, the CME has a 3D structure spanning over different longitudes and latitudes. Therefore, it is possible that parts of the CME at different latitudes and longitudes are influenced by solar wind of different speeds. It is expected that the high-speed wind from coronal holes may strongly affect the part of the CME at higher latitudes than that at lower latitudes (Heinemann et al., 2019). The CME can also experience solar wind of different speeds during the different segments of its heliospheric journey (Temmer et al., 2012; Mishra et al., 2014). However, the drag-based model employed in our study using a typical value for solar wind speed has been validated (Vršnak et al., 2013) to estimate the CME arrival time with typical errors of only around 0.5 day which can be further reduced by improving the drawbacks of the simplified drag-based model. Thus,the effect of several assumptions in the DBM (Vršnak et al., 2013), FRIS model (Mishra and Wang, 2018), and the observational path of the *in situ* spacecraft is not evaluated in the present study.

The cooling rate of the CME is found to change by an order of 10^6 during its propagation from near the Sun to 1 AU. We also note that the density and temperature of the CME changed by an order of 10^5 from near the Sun to 1 AU. It seems that the FRIS model overestimates the value of temperature near the Sun while underestimates near the Earth. This may arise if the measured expansion acceleration is overestimated near the Sun and underestimated at far distances. The values obtained from the FRIS model need further verification from the observations at different distances from the Sun. We expect that the *in situ* observations from *Parker Solar Probe* (PSP) and upcoming *Solar Orbiter* (SolO) would help to understand CMEs parameters at various distances by repeatedly probing the region closer to the Sun. The measurements of CME electron density at various distances from the Sun using polarimetric

remote sensing observations can help to validate the model results. Thus, a comparison of results from independent methods has the potential to better interpret the evolution of the CME thermodynamics. We also emphasize that some of the unknown constants in the FRIS model can be constrained to a reasonable value if some properties (e.g., density, temperature, etc.) of the CMEs are measured independently at different distances from the Sun.

We note that there have been observations that proton temperature in a direction perpendicular ($T_{\perp p}$) to the magnetic field is larger than that parallel ($T_{\parallel p}$) to the field in the region of ICMEs sheath, solar wind, and planetary magnetosheath (Marsch et al., 1982; Fuselier et al., 1994; Liu et al., 2006b). Such a temperature anisotropy, i.e., $T_{\perp p}/T_{\parallel p} > 1$, is found to be a direct consequence of the magnetic field line draping and plasma depletion in planetary magnetosheaths and around a fast ICMEs driving a shock (Crooker and Siscoe, 1977; Gosling and McComas, 1987). The anisotropic ion distributions exceeding certain thresholds for instabilities may induce proton cyclotron waves and mirror mode waves in ICMEs sheath, but unlikely inside the ICMEs characterized by low plasma beta (Gary, 1992; Liu et al., 2006b; Ala-Lahti et al., 2018). The heating effects of these waves are not investigated in our study, rather we assumed an average plasma temperature and pressure for describing the CME thermodynamic evolution.

Furthermore, since the FRIS model incorporates the total pressure from electron and proton populations in terms of expansion speed of the flux rope, it is worth comparing the polytropic index from FRIS model to the estimates of proton and electron polytropic index from *in situ* observations at a specific distance from the Sun. The electron polytropic index is often reported to be smaller than unity ($\Gamma\sim0.5$) while the proton polytropic index is larger than unity ($\Gamma\sim1.2$) in CMEs (Osherovich et al., 1993; Sittler and Burlaga, 1998). This implies that energy transport for the electrons and protons can be approximated by two different polytropes. However, it is complex to understand the electron polytropic index because of the core and halo components and their anisotropy. The solar wind electron characteristics inside and outside CMEs have been investigated in earlier studies (Sittler and Burlaga, 1998; Skoug et al., 2000). Future studies in this direction would be relevant as the energy transport (thermal equilibrium and evolution) for the electrons from the Sun may be more effective than that of the protons for the same temperature.

The mass of the CME is an input parameter in the FRIS model as the expressions for thermodynamic parameters (e.g., density, forces, etc.) have scaling factors involving the CME mass and other unknown constants (**Table 1**). The mass of the CME also partly contributes to the value of the drag parameter used in the drag-based model of CME propagation. Thus, the CME's mass, the estimation of which involves large uncertainties (Vourlidas et al., 2000; Colaninno and Vourlidas, 2009), can influence the thermodynamic and kinetic evolution of the CME. However, in our study, we showed the trend of variation in the derived thermodynamic parameters instead of deriving their absolute magnitudes. Further, we did not estimate a specific value of drag parameter for the selected CME rather we used its value as suggested by Vršnak et al. (2013) based on a statistical sample of events. Therefore, we did not require the exact magnitude of CME mass in our study to find the trend of variations in the density and forces as shown in **Figures 6**, **8** with scaling factors.

It is known that CMEs interacts with the solar wind during its heliospheric propagation. Such interaction leads to momentum exchange between the CME and solar wind due to drag force (Cargill et al., 1996), restricts the free expansion of the CME due to solar wind pressure (Klein and Burlaga, 1982), and causes flattening or pancaking of the CME due to solar wind stretching effect (Riley and Crooker, 2004). The FRIS model indirectly includes solar wind drag force and restricting effect on expansion by indirectly measuring the distance of CME flux rope (L) and the radius (R) of its cross-section. However, the solar wind stretching effect by radially expanding solar wind which distorts the circular cross-section of the flux rope is not taken into account in our model. This implies that in our study radius and expansion speed of the CME is overestimated while the distance of CME flux rope from the Sun and propagation speed is underestimated. Since these kinematic parameters of the flux rope are used as inputs in the model, we admit that the model results are affected by the assumptions on the flux rope structure. The extent of underestimation and overestimation would be increasingly larger at distances away from the Sun as the distortion of the CME flux rope is less severe at smaller distances. The effect of this as an underestimation of thermal pressure and Lorentz force is discussed in earlier studies (Wang et al., 2009; Mishra and Wang, 2018). Further, the FRIS model has not considered the curvature of the axis of the flux rope and thus an additional component of Lorentz force driving the CME is neglected. This would further cause an underestimation of the Lorentz force from the model.

Also, the FRIS model assumes a self-similar expansion for the CME during its propagation. This assumption breaks gradually as the CME moves away from the Sun and its obvious evidence is flattening of CME due to solar wind stretching effect (Riley and Crooker, 2004). However, it has been suggested that the self-similar expansion of CMEs remains a valid approximation when the CME is nearly force-free and within tens of solar radii from the Sun (Low, 1982; Chen et al., 1997; Démoulin and Dasso, 2009; Subramanian et al., 2014). Thus, we emphasize that the uncertainties in model thermodynamic parameters may come from the assumptions in the FRIS model and also from the uncertainties in the CME measurements. The extent of such uncertainties would be different at different distances from the Sun and their evaluation require a separate in-depth study. The present study focused on extrapolating the thermodynamic parameters of 3 April 2010 CME from near the Sun to 1 AU, and shows the potential of FRIS model. The findings from the present study regarding the evolution of CME internal state is in contrast to earlier studies (Liu et al., 2006a; Mishra and Wang, 2018). Therefore, using the FRIS model, it is worth examining several cases of CMEs having different kinematic characteristics to better understand the physical processes responsible for the thermodynamic evolution of the CMEs.

We finally note that the kinematics of the CME derived from the methods such as the GCS forward fitting model (Thernisien et al., 2009) and drag-based model (DBM) (Vršnak et al., 2013)

would also have some uncertainties. This is possible because of an ideal assumption of graduated cylindrical shell geometry for flux rope structure in the GCS fitting model and negligence of Lorentz force in the DBM. The uncertainties in the kinematics would lead to further uncertainties in the thermodynamic parameters derived from the FRIS model, even if all the assumptions in the FRIS model is found to be perfectly valid. To assess the effect of these uncertainties, it would require to re-run the FRIS model corresponding to new kinematic profiles accounting for the error bars therein. The re-run of the FRIS model means the estimation of a new set of fitting coefficients introduced in the model by fitting the observations with the model derived expressions. Based on our attempts, we find that the new fitting coefficients would be completely different due to the highly non-linear and sensitive fitting equation involved in the FRIS model. Since the model derived thermodynamic parameters are scaled by the fitting coefficients, the estimated thermodynamic parameters using completely different sets of coefficients cannot be directly compared with each other. However, we plan to tackle this issue and perform a separate in-depth analysis assessing the effects of the uncertainties in CME kinematics on the thermodynamic evolution of the CME.

DATA AVAILABILITY STATEMENT

The datasets generated for this study are available on request to the corresponding author.

AUTHOR CONTRIBUTIONS

WM and YW contributed to the initial conception of the paper. WM wrote the main draft having discussion on analysis with LT, JZ, and YC. All of the authors have read the paper and approved its final version.

FUNDING

YW is supported by the National Natural Science Foundation of China (NSFC) grant nos. 41574165, 41774178, and 41761134088.

ACKNOWLEDGMENTS

We acknowledge the UK Solar System Data Center (UKSSDC) for providing the *STEREO*/COR2 and HI data.

REFERENCES

Akmal, A., Raymond, J. C., Vourlidas, A., Thompson, B., Ciaravella, A., Ko, Y.-K., et al. (2001). SOHO observations of a coronal mass ejection. *Astrophys. J.* 553, 922–934. doi: 10.1086/320971

Ala-Lahti, M. M., Kilpua, E. K. J., Dimmock, A. P., Osmane, A., Pulkkinen, T., and Souček, J. (2018). Statistical analysis of mirror mode waves in sheath regions driven by interplanetary coronal mass ejection. *Ann. Geophys.* 36, 793–808. doi: 10.5194/angeo-36-793-2018

Baker, D. N. (2009). What does space weather cost modern societies? *Space Weather* 7:02003. doi: 10.1029/2009SW000465

Bein, B. M., Temmer, M., Vourlidas, A., Veronig, A. M., and Utz, D. (2013). The height evolution of the "True" coronal mass ejection mass derived from STEREO COR1 and COR2 observations. *Astrophys. J.* 768:31. doi: 10.1088/0004-637X/768/1/31

Bemporad, A., and Mancuso, S. (2010). First complete determination of plasma physical parameters across a coronal mass ejection-driven shock. *Astrophys. J.* 720, 130–143. doi: 10.1088/0004-637X/720/1/130

Burlaga, L., Fitzenreiter, R., Lepping, R., Ogilvie, K., Szabo, A., Lazarus, A., et al. (1998). A magnetic cloud containing prominence material - January 1997. *J. Geophys. Res.* 103:277. doi: 10.1029/97JA02768

Burlaga, L., Sittler, E., Mariani, F., and Schwenn, R. (1981). Magnetic loop behind an interplanetary shock - Voyager, Helios, and IMP 8 observations. *J. Geophys. Res.* 86, 6673–6684. doi: 10.1029/JA086iA08p06673

Cargill, P. J. (2004). On the aerodynamic drag force acting on interplanetary coronal mass ejections. *Solar Phys.* 221, 135–149. doi: 10.1023/B:SOLA.0000033366.10725.a2

Cargill, P. J., Chen, J., Spicer, D. S., and Zalesak, S. T. (1996). Magnetohydrodynamic simulations of the motion of magnetic flux tubes through a magnetized plasma. *J. Geophys. Res.* 101, 4855–4870. doi: 10.1029/95JA03769

Chen, J., Howard, R. A., Brueckner, G. E., Santoro, R., Krall, J., Paswaters, S. E., et al. (1997). Evidence of an erupting magnetic flux rope: LASCO coronal mass ejection of 1997 April 13. *Astrophys. J. Lett.* 490, L191–L194. doi: 10.1086/311029

Chen, P. F. (2011). Coronal mass ejections: models and their observational basis. *Living Rev. Solar Phys.* 8:1. doi: 10.12942/lrsp-2011-1

Ciaravella, A., Raymond, J. C., van Ballegooijen, A., Strachan, L., Vourlidas, A., Li, J., et al. (2003). Physical parameters of the 2000 February 11 coronal mass ejection: ultraviolet spectra versus white-light images. *Astrophys. J.* 597, 1118–1134. doi: 10.1086/381220

Colaninno, R. C., and Vourlidas, A. (2009). First determination of the true mass of coronal mass ejections: a novel approach to using the two STEREO viewpoints. *Astrophys. J.* 698, 852–858. doi: 10.1088/0004-637X/698/1/852

Crooker, N. U., and Siscoe, G. L. (1977). A mechanism for pressure anisotropy and mirror instability in the dayside magnetosheath. *J. Geophys. Res.* 82:185. doi: 10.1029/JA082i001p00185

Davies, J. A., Harrison, R. A., Rouillard, A. P., Sheeley, N. R., Perry, C. H., Bewsher, D., et al. (2009). A synoptic view of solar transient evolution in the inner heliosphere using the Heliospheric Imagers on STEREO. *Geophys. Res. Lett.* 36:L02102. doi: 10.1029/2008GL036182

Davies, J. A., Perry, C. H., Trines, R. M. G. M., Harrison, R. A., Lugaz, N., Möstl, C., et al. (2013). Establishing a stereoscopic technique for determining the kinematic properties of solar wind transients based on a generalised self-similarly expanding circular geometry. *Astrophys. J.* 776:1. doi: 10.1088/0004-637X/777/2/167

DeForest, C. E., Howard, T. A., and McComas, D. J. (2013). Tracking coronal features from the low corona to earth: a quantitative analysis of the 2008 December 12 coronal mass ejection. *Astrophys. J.* 769:43. doi: 10.1088/0004-637X/769/1/43

Démoulin, P., and Dasso, S. (2009). Causes and consequences of magnetic cloud expansion. *Astron. Astrophys.* 498, 551–566. doi: 10.1051/0004-6361/200810971

Feldman, W. C., Asbridge, J. R., Bame, S. J., Gosling, J. T., and Lemons, D. S. (1978). Electron heating within interaction zones of simple high-speed solar wind streams. *J. Geophys. Res.* 83, 5297–5304. doi: 10.1029/JA083iA11p05297

Fenrich, F. R., and Luhmann, J. G. (1998). Geomagnetic response to magnetic clouds of different polarity. *Geophys. Res. Lett.* 25, 2999–3002. doi: 10.1029/98GL51180

Forsyth, R. J., Bothmer, V., Cid, C., Crooker, N. U., Horbury, T. S., Kecskemety, K., et al. (2006). ICMEs in the inner heliosphere: origin, evolution and propagation effects. Report of Working Group G. *Space Sci. Rev.* 123, 383–416. doi: 10.1007/s11214-006-9022-0

Fuselier, S. A., Anderson, B. J., Gary, S. P., and Denton, R. E. (1994). Inverse correlations between the ion temperature anisotropy and plasma beta in the Earth's quasi-parallel magnetosheath. *J. Geophys. Res.* 99, 14931–14936. doi: 10.1029/94JA00865

Gary, S. P. (1992). The mirror and ion cyclotron anisotropy instabilities. *J. Geophys. Res.* 97, 8519–8529. doi: 10.1029/92JA00299

Gopalswamy, N., Mäkelä, P., Xie, H., Akiyama, S., and Yashiro, S. (2009). CME interactions with coronal holes and their interplanetary consequences. *J. Geophys. Res.* 114:A00A22. doi: 10.1029/2008JA013686

Gosling, J. T., and McComas, D. J. (1987). Field line draping about fast coronal mass ejecta: a source of strong out-of-the-ecliptic interplanetary magnetic fields. *Geophys. Res. Lett.* 14, 355–358. doi: 10.1029/GL014i004p00355

Gruesbeck, J. R., Lepri, S. T., and Zurbuchen, T. H. (2012). Two-plasma model for low charge state interplanetary coronal mass ejection observations. *Astrophys. J.* 760:141. doi: 10.1088/0004-637X/760/2/141

Gulisano, A. M., Démoulin, P., Dasso, S., Ruiz, M. E., and Marsch, E. (2010). Global and local expansion of magnetic clouds in the inner heliosphere. *Astron. Astrophys.* 509:A39. doi: 10.1051/0004-6361/200912375

Harrison, R. A., Davies, J. A., Barnes, D., Byrne, J. P., Perry, C. H., Bothmer, V., et al. (2018). CMEs in the heliosphere: I. A statistical analysis of the observational properties of CMEs detected in the heliosphere from 2007 to 2017 by STEREO/HI-1. *Solar Phys.* 293:77. doi: 10.1007/s11207-018-1297-2

Heinemann, S. G., Temmer, M., Farrugia, C. J., Dissauer, K., Kay, C., Wiegelmann, T., et al. (2019). CME-HSS interaction and characteristics tracked from sun to earth. *Solar Phys.* 294:121. doi: 10.1007/s11207-019-1515-6

Hundhausen, A. J., Sawyer, C. B., House, L., Illing, R. M. E., and Wagner, W. J. (1984). Coronal mass ejections observed during the solar maximum mission - Latitude distribution and rate of occurrence. *J. Geophys. Res.* 89, 2639–2646. doi: 10.1029/JA089iA05p02639

Inhester, B. (2006). Stereoscopy basics for the STEREO mission. *arXiv:astro-ph/0612649*.

Janvier, M., Winslow, R. M., Good, S., Bonhomme, E., Démoulin, P., Dasso, S., et al. (2019). Generic magnetic field intensity profiles of interplanetary coronal mass ejections at mercury, venus, and earth from superposed epoch analyses. *J. Geophys. Res.* 124, 812–836. doi: 10.1029/2018JA025949

Klein, L. W., and Burlaga, L. F. (1982). Interplanetary magnetic clouds at 1 AU. *J. Geophys. Res.* 87, 613–624. doi: 10.1029/JA087iA02p00613

Kohl, J. L., Noci, G., Cranmer, S. R., and Raymond, J. C. (2006). Ultraviolet spectroscopy of the extended solar corona. *Astron. Astrophys. Rev.* 13, 31–157. doi: 10.1007/s00159-005-0026-7

Larson, D. E., Lin, R. P., McTiernan, J. M., McFadden, J. P., Ergun, R. E., McCarthy, M., et al. (1997). Tracing the topology of the October 18-20, 1995, magnetic cloud with 0.1-10^2 keV electrons. *Geophys. Res. Lett.* 24, 1911–1914. doi: 10.1029/97GL01878

Lepping, R. P., Burlaga, L. F., and Jones, J. A. (1990). Magnetic field structure of interplanetary magnetic clouds at 1 AU. *J. Geophys. Res.* 95, 11957–11965. doi: 10.1029/JA095iA08p11957

Lepri, S. T., Zurbuchen, T. H., Fisk, L. A., Richardson, I. G., Cane, H. V., and Gloeckler, G. (2001). Iron charge distribution as an identifier of interplanetary coronal mass ejections. *J. Geophys. Res.* 106, 29231–29238. doi: 10.1029/2001JA000014

Liu, Y., Luhmann, J. G., Bale, S. D., and Lin, R. P. (2011). Solar source and heliospheric consequences of the 2010 April 3 coronal mass ejection: a comprehensive view. *Astrophys. J.* 734:84. doi: 10.1088/0004-637X/734/2/84

Liu, Y., Luhmann, J. G., Müller-Mellin, R., Schroeder, P. C., Wang, L., Lin, R. P., et al. (2008). A comprehensive view of the 2006 December 13 CME: from the sun to interplanetary space. *Astrophys. J.* 689, 563–571. doi: 10.1086/592031

Liu, Y., Richardson, J. D., and Belcher, J. W. (2005). A statistical study of the properties of interplanetary coronal mass ejections from 0.3 to 5.4 AU. *Planet. Space Sci.* 53, 3–17. doi: 10.1016/j.pss.2004.09.023

Liu, Y., Richardson, J. D., Belcher, J. W., Kasper, J. C., and Elliott, H. A. (2006a). Thermodynamic structure of collision-dominated expanding plasma: Heating of interplanetary coronal mass ejections. *J. Geophys. Res.* 111:A01102. doi: 10.1029/2005JA011329

Liu, Y., Richardson, J. D., Belcher, J. W., Kasper, J. C., and Skoug, R. M. (2006b). Plasma depletion and mirror waves ahead of interplanetary coronal mass ejections. *J. Geophys. Res.* 111:A09108. doi: 10.1029/2006JA011723

Low, B. C. (1982). Self-similar magnetohydrodynamics. I - The gamma = 4/3 polytrope and the coronal transient. *Astrophys. J.* 254, 796–805. doi: 10.1086/159790

Lynch, B. J., Li, Y., Thernisien, A. F. R., Robbrecht, E., Fisher, G. H., Luhmann, J. G., et al. (2010). Sun to 1 AU propagation and evolution of a slow streamer-blowout coronal mass ejection. *J. Geophys. Res.* 115:A07106. doi: 10.1029/2009JA015099

Manchester, W. B., Gombosi, T. I., Roussev, I., Ridley, A., de Zeeuw, D. L., Sokolov, I. V., et al. (2004). Modeling a space weather event from the Sun to the Earth: CME generation and interplanetary propagation. *J. Geophys. Res.* 109:A02107. doi: 10.1029/2003JA010150

Markwardt, C. B. (2009). "Non-linear Least-squares Fitting in IDL with MPFIT," in *Astronomical Data Analysis Software and Systems XVIII Vol. 411 of Astronomical Society of the Pacific Conference Series*, eds D. A. Bohlender, D. Durand, and P. Dowler (Québec City, QC: Astronomical Society of the Pacific), 251.

Marsch, E., Schwenn, R., Rosenbauer, H., Muehlhaeuser, K. H., Pilipp, W., and Neubauer, F. M. (1982). Solar wind protons: three-dimensional velocity distributions and derived plasma parameters measured between 0.3 and 1 AU. *J. Geophys. Res.* 87, 52–72. doi: 10.1029/JA087iA01p00052

Marubashi, K., and Lepping, R. P. (2007). Long-duration magnetic clouds: a comparison of analyses using torus- and cylinder-shaped flux rope models. *Ann. Geophys.* 25, 2453–2477. doi: 10.5194/angeo-25-2453-2007

Mierla, M., Inhester, B., Antunes, A., Boursier, Y., Byrne, J. P., Colaninno, R., et al. (2010). On the 3-D reconstruction of Coronal Mass Ejections using coronagraph data. *Ann. Geophys.* 28, 203–215. doi: 10.5194/angeo-28-203-2010

Mishra, W., and Srivastava, N. (2013). Estimating the arrival time of earth-directed coronal mass ejections at *in situ* spacecraft using COR and HI observations from STEREO. *Astrophys. J.* 772:70. doi: 10.1088/0004-637X/772/1/70

Mishra, W., Srivastava, N., and Davies, J. A. (2014). A comparison of reconstruction methods for the estimation of coronal mass ejections kinematics based on SECCHI/HI observations. *Astrophys. J.* 784:135. doi: 10.1088/0004-637X/784/2/135

Mishra, W., Srivastava, N., and Singh, T. (2015). Kinematics of interacting CMEs of 25 and 28 September 2012. *J. Geophys. Res.* 120:10. doi: 10.1002/2015JA021415

Mishra, W., and Wang, Y. (2018). Modeling the thermodynamic evolution of coronal mass ejections using their kinematics. *Astrophys. J.* 865:50. doi: 10.3847/1538-4357/aadb9b

Möstl, C., Temmer, M., Rollett, T., Farrugia, C. J., Liu, Y., Veronig, A. M., et al. (2010). STEREO and wind observations of a fast ICME flank triggering a prolonged geomagnetic storm on 5-7 April 2010. *Geophys. Res. Lett.* 37:L24103. doi: 10.1029/2010GL045175

Nicolaou, G., Livadiotis, G., and Moussas, X. (2014). Long-term variability of the polytropic index of solar wind protons at 1 AU. *Solar Phys.* 289, 1371–1378. doi: 10.1007/s11207-013-0401-x

Ogilvie, K. W., Chornay, D. J., Fritzenreiter, R. J., Hunsaker, F., Keller, J., Lobell, J., et al. (1995). SWE, a comprehensive plasma instrument for the wind spacecraft. *Space Sci. Rev.* 71, 55–77. doi: 10.1007/BF00751326

Osherovich, V. A., Farrugia, C. J., Burlaga, L. F., Lepping, R. P., Fainberg, J., and Stone, R. G. (1993). Polytropic relationship in interplanetary magnetic clouds. *J. Geophys. Res.* 98:15. doi: 10.1029/93JA01012

Parker, E. N. (1960). The hydrodynamic theory of solar corpuscular radiation and stellar winds. *Astrophys. J.* 132:821. doi: 10.1086/146985

Phillips, J. L., Feldman, W. C., Gosling, J. T., and Scime, E. E. (1995). Solar wind plasma electron parameters based on aligned observations by ICE and ULYSSES. *Adv. Space Res.* 16, 95–100.

Pomoell, J., and Poedts, S. (2018). EUHFORIA: European heliospheric forecasting information asset. *J. Space Weather Space Clim.* 8:A35. doi: 10.1051/swsc/2018020

Raymond, J. C. (2002). "Spectroscopic diagnostics of CME material," in *From Solar Min to Max: Half a Solar Cycle with SOHO*, ed A. Wilson (Davos: ESA Publications Division), 421–430.

Richardson, I. G., and Cane, H. V. (1993). Signatures of shock drivers in the solar wind and their dependence on the solar source location. *J. Geophys. Res.* 98:15295. doi: 10.1029/93JA01466

Riley, P., and Crooker, N. U. (2004). Kinematic treatment of coronal mass ejection evolution in the solar wind. *Astrophys. J.* 600, 1035–1042. doi: 10.1086/379974

Riley, P., Linker, J. A., Mikić, Z., Odstrcil, D., Zurbuchen, T. H., Lario, D., et al. (2003). Using an MHD simulation to interpret the global context of a coronal mass ejection observed by two spacecraft. *J. Geophys. Res.* 108:1272. doi: 10.1029/2002JA009760

Rollett, T., Möstl, C., Temmer, M., Veronig, A. M., Farrugia, C. J., and Biernat, H. K. (2012). Constraining the kinematics of coronal mass ejections in the inner heliosphere with *in-situ* signatures. *Solar Phys.* 276, 293–314. doi: 10.1007/s11207-011-9897-0

Schwenn, R. (2006). Space weather: the solar perspective. *Living Rev. Solar Phys.* 3:2. doi: 10.12942/lrsp-2006-2

Sittler, E. C., and Burlaga, L. F. (1998). Electron temperatures within magnetic clouds between 2 and 4 AU: Voyager 2 observations. *J. Geophys. Res.* 103, 17447–17454. doi: 10.1029/98JA01289

Sittler, J., E. C., and Scudder, J. D. (1980). An empirical polytrope law for solar wind thermal electrons between 0.45 and 4.76 AU: Voyager 2 and Mariner 10. *J. Geophys. Res.* 85, 5131–5137. doi: 10.1029/JA085iA10p05131

Skoug, R. M., Feldman, W. C., Gosling, J. T., McComas, D. J., Reisenfeld, D. B., Smith, C. W., et al. (2000). Radial variation of solar wind electrons inside a magnetic cloud observed at 1 and 5 AU. *J. Geophys. Res.* 105, 27269–27276. doi: 10.1029/2000JA000095

Subramanian, P., Arunbabu, K. P., Vourlidas, A., and Mauriya, A. (2014). Self-similar expansion of solar coronal mass ejections: implications for Lorentz self-force driving. *Astrophys. J.* 790:125. doi: 10.1088/0004-637X/790/2/125

Tappin, S. J. (2006). The deceleration of an interplanetary transient from the sun to 5 Au. *Solar Phys.* 233, 233–248. doi: 10.1007/s11207-006-2065-2

Temmer, M., Vršnak, B., Rollett, T., Bein, B., de Koning, C. A., Liu, Y., et al. (2012). Characteristics of kinematics of a coronal mass ejection during the 2010 August 1 CME-CME interaction event. *Astrophys. J.* 749:57. doi: 10.1088/0004-637X/749/1/57

Thernisien, A. (2011). Implementation of the graduated cylindrical shell model for the three-dimensional reconstruction of coronal mass ejections. *Astrophys. J. Suppl.* 194:33. doi: 10.1088/0067-0049/194/2/33

Thernisien, A., Vourlidas, A., and Howard, R. A. (2009). Forward modeling of coronal mass ejections using STEREO/SECCHI data. *Solar Phys.* 256, 111–130. doi: 10.1007/s11207-009-9346-5

Thernisien, A. F. R., Howard, R. A., and Vourlidas, A. (2006). Modeling of flux rope coronal mass ejections. *Astrophys. J.* 652, 763–773. doi: 10.1086/508254

Totten, T. L., Freeman, J. W., and Arya, S. (1995). An empirical determination of the polytropic index for the free-streaming solar wind using HELIOS 1 data. *J. Geophys. Res.* 100, 13–17. doi: 10.1029/94JA02420

Tousey, R. (1973). "The solar corona," in *Space Research XIII*, eds M. Rycroft and S. Runcorn (Berlin: Akademie-Verlag), 713–730.

Vourlidas, A., Lynch, B. J., Howard, R. A., and Li, Y. (2013). How many CMEs have flux ropes? Deciphering the signatures of shocks, flux ropes, and prominences in coronagraph observations of CMEs. *Solar Phys.* 284, 179–201. doi: 10.1007/s11207-012-0084-8

Vourlidas, A., Subramanian, P., Dere, K. P., and Howard, R. A. (2000). Large-angle spectrometric coronagraph measurements of the energetics of coronal mass ejections. *Astrophys. J.* 534, 456–467. doi: 10.1086/308747

Vršnak, B., and Žic, T. (2007). Transit times of interplanetary coronal mass ejections and the solar wind speed. *Astron. Astrophys.* 472, 937–943. doi: 10.1051/0004-6361:20077499

Vršnak, B., Žic, T., Vrbanec, D., Temmer, M., Rollett, T., Möstl, C., et al. (2013). Propagation of interplanetary coronal mass ejections: the drag-based model. *Solar Phys.* 285, 295–315. doi: 10.1007/s11207-012-0035-4

Wang, C., Du, D., and Richardson, J. D. (2005). Characteristics of the interplanetary coronal mass ejections in the heliosphere between 0.3 and 5.4 AU. *J. Geophys. Res.* 110:A10107. doi: 10.1029/2005JA011198

Wang, C., and Richardson, J. D. (2004). Interplanetary coronal mass ejections observed by Voyager 2 between 1 and 30 AU. *J. Geophys. Res.* 109:A06104. doi: 10.1029/2004JA010379

Wang, Y., Shen, C., Liu, R., Liu, J., Guo, J., Li, X., et al. (2018). Understanding the twist distribution inside magnetic flux ropes by anatomizing an interplanetary magnetic cloud. *J. Geophys. Res.* 123, 3238–3261. doi: 10.1002/2017JA024971

Wang, Y., Wang, B., Shen, C., Shen, F., and Lugaz, N. (2014). Deflected propagation of a coronal mass ejection from the corona to interplanetary space. *J. Geophys. Res.* 119, 5117–5132. doi: 10.1002/2013JA019537

Wang, Y., Zhang, J., and Shen, C. (2009). An analytical model probing the internal state of coronal mass ejections based on observations of their expansions and propagations. *J. Geophys. Res.* 114:A10104. doi: 10.1029/2009JA014360

Wang, Y., Zhou, Z., Shen, C., Liu, R., and Wang, S. (2015). Investigating plasma motion of magnetic clouds at 1 AU through a velocity-modified cylindrical force-free flux rope model. *J. Geophys. Res.* 120, 1543–1565. doi: 10.1002/2014JA020494

Wang, Y., Zhuang, B., Hu, Q., Liu, R., Shen, C., and Chi, Y. (2016). On the twists of interplanetary magnetic flux ropes observed at 1 AU. *J. Geophys. Res.* 121, 9316–9339. doi: 10.1002/2016JA023075

Webb, D. F., and Howard, T. A. (2012). Coronal mass ejections: observations. *Living Rev. Solar Phys.* 9:3. doi: 10.12942/lrsp-2012-3

Zhang, J., and Dere, K. P. (2006). A statistical study of main and residual accelerations of coronal mass ejections. *Astrophys. J.* 649, 1100–1109. doi: 10.1086/506903

Zhang, J., Richardson, I. G., Webb, D. F., Gopalswamy, N., Huttunen, E., Kasper, J. C., et al. (2007). Solar and interplanetary sources of major geomagnetic storms (Dst <= -100 nT) during 1996-2005. *J. Geophys. Res.* 112:A10102. doi: 10.1029/2007JA012321

Zhao, A., Wang, Y., Chi, Y., Liu, J., Shen, C., and Liu, R. (2017a). Main cause of the poloidal plasma motion inside a magnetic cloud inferred from multiple-spacecraft observations. *Solar Phys.* 292:58. doi: 10.1007/s11207-017-1077-4

Zhao, A., Wang, Y., Liu, J., Zhou, Z., Shen, C., Liu, R., et al. (2017b). The role of viscosity in causing the plasma poloidal motion in magnetic clouds. *Astrophys. J.* 845:109. doi: 10.3847/1538-4357/aa8093

Zurbuchen, T. H., Fisk, L. A., Lepri, S. T., and von Steiger, R. (2003). "The composition of interplanetary coronal mass ejections," in *Solar Wind Ten*, eds M. Velli, R. Bruno, F. Malara, and B. Bucci (Pisa: AIP Conference Proceedings), 604–607. doi: 10.1063/1.1618667

Conflict of Interest: The authors declare that the research was conducted in the absence of any commercial or financial relationships that could be construed as a potential conflict of interest.

frontiers in Astronomy and Space Sciences

ORIGINAL RESEARCH
published: 12 May 2020
doi: 10.3389/fspas.2020.00017

Two Successive Type II Radio Bursts Associated With B-Class Flares and Slow CMEs

Suli Ma[1]* *and Huadong Chen*[1,2]

[1] CAS Key Laboratory of Solar Activity, National Astronomical Observatories, Chinese Academy of Sciences, Beijing, China,
[2] School of Astronomy and Space Science, University of Chinese Academy of Sciences, Beijing, China

From 2018 Oct 12 to 13, three successive solar eruptions (E1–E3) with B-class flares and poor white light coronal mass ejections (CMEs) occurred from the same active region NOAA AR 12724. Interestingly, the first two eruptions are associated with Type II radio bursts but the third is not. Using the soft X-ray flux data, radio dynamic spectra and dual perspective EUV intensity images, we comparatively investigate the three events. Our results show that their relevant flares are weak (B2.1, B7.9, and B2.3) and short-lived (13, 9, and 14 min). The main eruption directions of E1 and E2 are along ∼45° north of their radial directions, while E3 primarily propagated along the radial direction. In the EUV channels, the early speeds of the first two CMEs have apparent speeds of ∼320 and ∼380 km s^{-1}, which could exceed their respective local Alfvén speeds of ∼300 and ∼350 km s^{-1}. However, the CME in the third eruption possesses a much lower speed of ∼160 km s^{-1}. These results suggest that the observed Type II radio bursts in the eruptions E1 and E2 are likely triggered by their associated CMEs and the direction of eruption and the ambient plasma and magnetic environments may take an important place in producing Type II radio burst or shock as well.

Keywords: radio radiation, coronal mass ejections (CMEs), UV radiation, flares, corona, filaments, shock waves, magnetic topology

OPEN ACCESS

Edited by:
Dipankar Banerjee,
Indian Institute of Astrophysics, India

Reviewed by:
Mingde Ding,
Nanjing University, China
Debi Prasad Choudhary,
California State University, Northridge, United States

***Correspondence:**
Suli Ma
sma@nao.cas.cn

Specialty section:
This article was submitted to Stellar and Solar Physics, a section of the journal Frontiers in Astronomy and Space Sciences

Received: *03 June 2019*
Accepted: *07 April 2020*
Published: *12 May 2020*

Citation:
Ma S and Chen H (2020) Two Successive Type II Radio Bursts Associated With B-Class Flares and Slow CMEs. Front. Astron. Space Sci. 7:17. doi: 10.3389/fspas.2020.00017

1. INTRODUCTION

Solar Type II radio bursts were first reported by Payne-Scott et al. (1947) and named by Wild and McCready (1950). Usually, a Type II burst appeared as a slowly drifting, from high to low frequencies, narrow frequency band patterns in radio dynamic spectra (e.g., Nelson and Melrose, 1985). It is generally believed that type II bursts are excited by magnetohydrodynamics (MHD) shocks in the solar atmosphere (e.g., Nelson and Melrose, 1985; Cliver et al., 1999; Nindos et al., 2008, 2011; Vršnak and Cliver, 2008, and references therein).

Since the first discovery of Type II bursts, they have been found to be closely related to both flares (e.g., Wild et al., 1954; Maxwell and Thompson, 1962; Dodge, 1975) and high-velocity ejections (e.g., Dodson et al., 1953; Giovanelli and Roberts, 1958; Swarup et al., 1960). The blast wave initiated by flares and piston-driven mechanism associated with coronal mass ejections (CMEs) have become the two main competitors of the triggering mechanism of the Type II bursts as reviewed by the papers (e.g., Cliver et al., 1999; Vršnak and Cliver, 2008; Nindos et al., 2011) and also suggested by some recent studies (e.g., Zheng et al., 2018; Eselevich et al., 2019; Frassati et al., 2019). In the piston-driven mechanism, besides CME front, some other triggers, such as soft X-ray jet, erupting coronal loop and eruptive magnetic flux rope are also proposed to explain the

production of shock or Type II burst (e.g., Klein et al., 1999; Klassen et al., 2003; Dauphin et al., 2006; Su et al., 2015; Eselevich et al., 2017; Grechnev et al., 2018).

In theory, the occurrence of a coronal shock requires the introduction of a sudden disturbance in the corona, which should travel with a speed faster than the local Alfvén velocity. Early studies (e.g., Gosling et al., 1976) indicate that the velocities of CMEs with type II bursts would exceed 400–550 km s^{-1}. However, Gopalswamy et al. (2001) made a statistical study and found that 50% of limb CMEs associated Type II bursts during 1995–1997 have speeds lower than 500 km s^{-1} and the lower cutoff of these CMEs' speeds may reach $\sim$ 250 km s^{-1}. So far, detailed case studies about Type II radio bursts with slow CMEs and weak flares (below C-class) have been very rare.

In this paper, we present a case study about two successive Type II bursts associated with B-class flares and CMEs with slow speeds below $\sim$400 km s^{-1} in the period of solar activity minimum. Our comparative investigations suggest that these Type II radio bursts are likely triggered by their associated CMEs and we also discuss the influence from the ambient coronal magnetic structures on the eruptions.

2. OBSERVATIONS

From 2018 Oct 12 to 13, three eruptions orderly took place in the active region (AR) NOAA 12724. AR 12724 is near the solar east limb in the field of view (FOV) of the ground-based telescopes (spectrographs) or space-based telescopes on geosynchronous satellites, such as the Solar and Heliospheric Observatory *SOHO* and the Solar Dynamics Observatory (SDO, Pesnell et al., 2012). The Solar Terrestrial Relations Observatory (STEREO, Kaiser et al., 2008) consists of two space-based observatories—one ahead of Earth in its orbit (*STA*), the other trailing behind (*STB*, lost communications since 2014 Oct 1). The *STA* orbits the Sun with a radius slightly smaller than 1AU and the separation angle between *STA* and the Earth was about 105° during the three events. The host AR is located on the disk in the view of *STA*.

We use the dynamic spectrum data from the radio spectrograph ORFEES (Observation Radio Frequence pour l'Etude des Eruptions Solaires) observing between 140 and 1,000 MHz, Learmonth solar radio spectrograph covering a frequency range of 25–180 MHz (LEAR, Kennewell and Steward, 2003), and the CALLISTO spectrometer (Benz et al., 2009) at the Greenland Observatory. Intensity images provided by the Atmospheric Imaging Assembly (AIA, Lemen et al., 2012) on SDO and the EUV Imager (EUVI, Wuelser et al., 2004) in the Sun Earth Connection Coronal and Heliospheric Investigation (*SECHHI*; Howard et al., 2008) on *STA* are also utilized to study the early stages of the eruptions. The observation from the Large Angle and Spectrometric Coronagraph (LASCO; Brueckner et al., 1995) on-board SOHO with a FOV of 2–6.0 $R_\odot$ help us to check the associated CMEs.

3. RESULTS

3.1. Overview of the Events

The general information of the three successive eruption events (E1–E3) are listed in **Table 1**. All the three events originated from the same active region (AR) NOAA 12724 and each of them involved a filament eruption, a B-class flare and a slow poor white light (WL) CME. Type II radio bursts only appeared in E1 and E2. The detailed magnitude and the start, peak, and end time of each flare are given in the "Flare Class" and "Flare Time" column, respectively. The central locations of the relevant filaments (F1–F3) in the FOV of AIA are presented in the "Filament Center" column. The CMEs' angular widths (AWs) and their quadratic speeds (obtained by performing second-order polynomial fittings to the height-time measurements) at the final height measurements are placed in the "CME AW" and "CME Speed" columns, respectively.

3.2. Filaments

The AIA 304 Å (left column) and EUVI A 195 Å (right column) images in **Figure 1** show the morphologies of the AR 12724, the erupting filaments (F1–F3) and their corresponding flares (Flare1–Flare3). In the 304 Å images, it can be seen that F1 and F2 almost have a north-south orientation, while F3 runs from east to west. According to the EUVI A 195 Å observations, Flare1 and Flare2 were located in the northwest of AR 12724, while Flare3 mainly lay in the AR's southeast. To the east of AR 12724, a small emerging active region labeled "New" appeared to have nothing to do with the eruptions.

3.3. Flares and Radio Bursts

The GOES X-ray fluxes and radio dynamic spectrums associated with E1, E2 and E3 are shown in the panels (a) and (b) of **Figures 2–4**, respectively. **Figure 2a** displays the short-lived B2.1 Flare1. In **Figure 2b**, a type II radio burst can be found in the Learmonth's radio dynamic spectrum, suggesting that a shock (Shock1) was generated during E1. The type II radio burst, including a fundamental band (F) and a harmonic band (H) with two splitting lanes (H_L and H_U), started from $\sim$01:52 UT, when Flare1 has entered its descending phase. After $\sim$02:00 UT, it gradually disappeared. The frequencies along F, H_L and H_U change from about 40, 78, and 80 MHz to 26, 54, and 64 MHz, respectively. Their average frequency drift rates are -0.086, -0.087, and -0.109 MHz s^{-1}. We adopt the frequency values represented by the black (F), red (H_L), and blue (H_U) dashed curves to measure local plasma densities and further derive the speeds of Shock1 (see section 3.6).

It is generally believed that the band-splitting is caused by the emission from the upstream and downstream shock regions and the downstream/upstream density jump (X) could provide an estimate of the coronal Alfvén speed (e.g, Smerd et al., 1974; Mann et al., 1995; Vršnak, 2001). The density jump can be described as

$$X = \frac{n_2}{n_1} = (\frac{f_U}{f_L})^2 \quad (1)$$

(Vršnak et al., 2002). Here, n_1 and n_2 are the electron densities of the plasma at the frequency f_L in the lower frequency branch and at the frequency f_U in the upper frequency branch of the harmonic bands, respectively. For the Type II radio burst in E1, we take $f_U = 77.5$ and $f_L = 64.5$ at 01:54:32 UT (indicated by the vertical line in **Figure 2b**) and obtain $X = 1.44$, indicating that Shock1 is a weak shock. Under the quasi-perpendicular shock

TABLE 1 | General information of the eruptions.

Event	Date	Flare class	Flare time (UT) (start peak end)	Radio burst	Filament center	CME AW (°)	CME Speed (km/s)
E1	2018 Oct 12	B2.1	01:43 01:50 01:56	II	−900″, −150″	46	333
E2	2018 Oct 12	B7.1	14:04 14:08 14:13	II, IIIs, IV	−850″, −160″	44	492
E3	2018 Oct 13	B2.3	13:28 13:34 13:42	III	−800″, −240″	38	133

approximation and a plasma beta $\beta - > 0$, the Alfvén Mach number M_A is related to the compression X as

$$M_A = \sqrt{\frac{X(X+5)}{2(4-X)}} \quad (2)$$

Then, M_A around 1.35 can be derived for Shock1.

The GOES X-ray flux of the B7.1-class flare (Flare2) and the composite dynamic spectrum from ORFEES (144–400 MHz) and Greenland (25–105 MHz) associated with E2 are displayed in the top and bottom panels of **Figure 3**, respectively. A variety of radio bursts, such as a group of type III bursts (IIIs), a relatively strong short-lived type IV burst and a weak type II burst, can be found in the composite dynamic spectrum. The Type III bursts occurred in the initial and impulsive phase of Flare2. Some of them show negative frequency drifts which probably result from energetic electron beams propagating outward along open coronal magnetic field (e.g., Yan et al., 2006; Huang et al., 2011), while others show positive drifts which may be caused by energetic electron beams propagating downward from where they are accelerated (likely the reconnection region) (e.g., Reid and Ratcliffe, 2014; Ning, 2016; Tan et al., 2016). The type IV burst appeared after the peak of Flare2 and lasted for about 2 min. It is probably excited by the energetic electrons trapped within the erupting magnetic structures (e.g., Smerd and Dulk, 1971; Vlahos et al., 1982; Stewart, 1985).

At around 14:15 UT on Oct 12, the type II burst appeared with obvious fundamental (F) and second harmonic bands (splitting into two lanes H_L and H_U) in the observation of Greenland. Similar to E1, it likely indicates a shock (Shock2) induced during the eruption E2. Along H_L, the frequency varies from 90 to 74 MHz with a mean frequency drift of −0.099 MHz s^{-1} and that decreases from 98 MHz to 83 MHz with a mean frequency drift of −0.113 MHz s^{-1} along H_U. In addition, a very faint third harmonic band (3H) seems to appear in the dynamic spectrum of ORFEES. Using the same method described above (see Equation 1), we obtained the density jump of Shock2 at 14:15:54 UT (marked by the vertical line in **Figure 3b**, when the H_U is 98 MHz and H_L is 86 MHz), which is about 1.30. The corresponding shock Mach number was deduced as 1.23.

Figure 4 shows the GOES X-ray flux of the flare (top panel) and the dynamic spectra (bottom panel) during E3. A B2.3-class flare (Flare3) correlated with E3. Taking advantage of the joint observations from ORFEES and Greenland, we found that only a very weak type III burst and no sign of type II burst appeared in this event.

3.4. White Light CMEs

The running difference intensity images of LASCO C2 and AIA at 193 Å are composited and shown in **Figure 5**, displaying the coronal changes during E1, E2, and E3. Three faint stream-like CMEs (CME1–CME3) can be separately identified in the three eruptions. They are indicated by the arrows in the left, middle and right column of **Figure 5**, respectively. According to the LASCO CME catalog (see https://cdaw.gsfc.nasa.gov/CME_list), CME1–CME3 only appear in the FOV of C2 ($2\sim6R_\odot$) and belong to "poor CMEs." They separately have an angular width of about 46, 44, and 38°, and a 2nd-order speed at the time of final height measurement of 333, 492, and 133 km s^{-1} (see **Table 1**). The times of their first appearance in the LASCO C2's FOV are around 02:48 UT (Oct 12), 15:12 UT (Oct 12), and 14:36 UT (Oct 13), respectively. Obviously, the Type II bursts in E1 and E2 had already formed before their corresponding CMEs came into the C2 FOV. No relevant CME can be found from the observations of COR 1 (inner coronagraph) and COR 2 (outer coronagraph) on-board *STA*. This may be related to the on-disk perspective of *STA* and the weak magnitudes of the eruptions.

3.5. Eruptions in EUV

The AIA 193 Å (**Figure 6**) and EUVI 195 Å (**Figure 7**) intensity images display the early evolutions of E1–E3 from different perspectives. The original images in the left columns of **Figures 6**, **7** are utilized as references to get the base difference images in the middle and right columns. The AIA 193 Å data clearly exhibit the dome-like structures of CME1 and CME2 with distinct leading edges (LE1 and LE2) in their early stages, while CME3 had a tenuous leading edge (LE3). Comparing the main eruption directions of E1–E3 (indicated by the yellow arrows in **Figure 6**) with the radial directions (denoted by the purple arrows in **Figure 6**), it can be found that CME1 and CME2 primarily propagated northeast, whereas CME3 was ejected approximately along the radial direction.

In the EUVI observations, three diffusing EUV waves (W1–W3) can be observed, as indicated by the orange arrows in **Figure 7**. EUV waves are also called "EIT waves" or global coronal waves, which are large-amplitude waves initially driven by the rapid lateral expansion of a CME in the low corona and later propagating freely (cf. Long et al., 2017). Ma et al. (2009) showed the evidence that EUV wave front includes contribution from its associated CME at the early stage. More information about the "EUV waves" could be seen in the recent reviews (Liu and Ofman, 2014; Warmuth, 2015; Chen, 2016; Long et al., 2017). The propagation directions of W1 and W2 are similar and mainly toward the north from their eruption centers, while

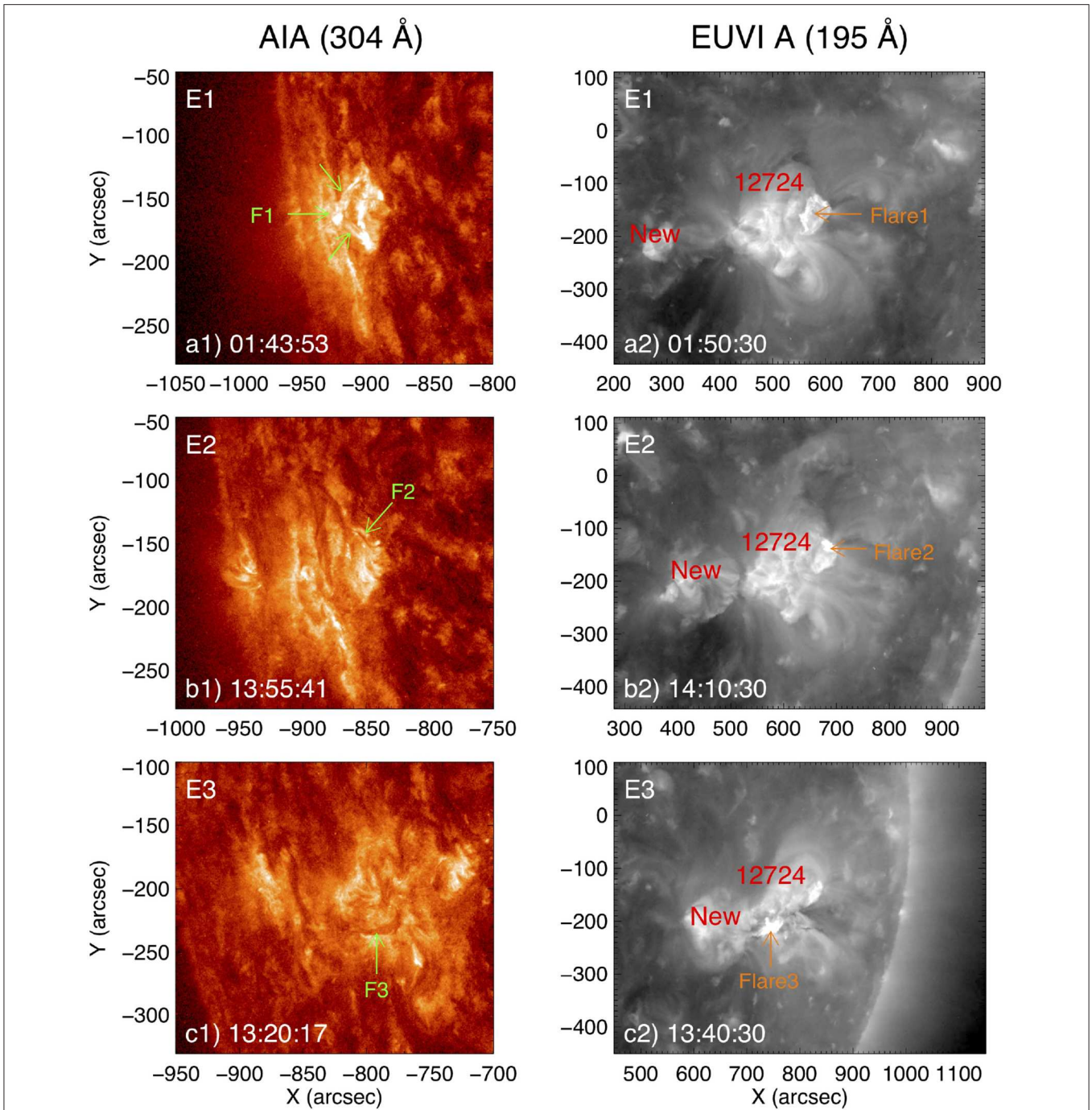

FIGURE 1 | Observations in EUV passbands displaying the morphology of the host active region NOAA 12724 during the occurrences of E1, E2, and E3. **(a1,b1)** and **(c1)** show the AIA observation at 304 Å during E1, E2 and E3, respectively, and the green arrows point to the locations of filament1 (F1), filament2 (F2), and filament3 (F3). **(a2,b2)** and **(c2)** are EUVI images at 195 Å during E1, E2 and E3, respectively, and the orange arrows direct the positions of Flare1, Flare2, and Flare3.

the traveling of W3 has no obvious preference. Combining the AIA and EUVI observations with a separation angle of 105°, we estimate that the eruption directions of E1 and E2 are alike along the ∼45° north of their radial directions and E3 basically erupted radially.

Interestingly, a special brightening area ("SBA," **Figures 6b2**, **7b2**) was observed at the north border of AR 12724 when the north flank of CME2 swept there (from ∼14:09 to ∼14:11 UT on Oct 12). It showed as an arc structure in the AIA images and a brow-like brightening in the EUVI images. The

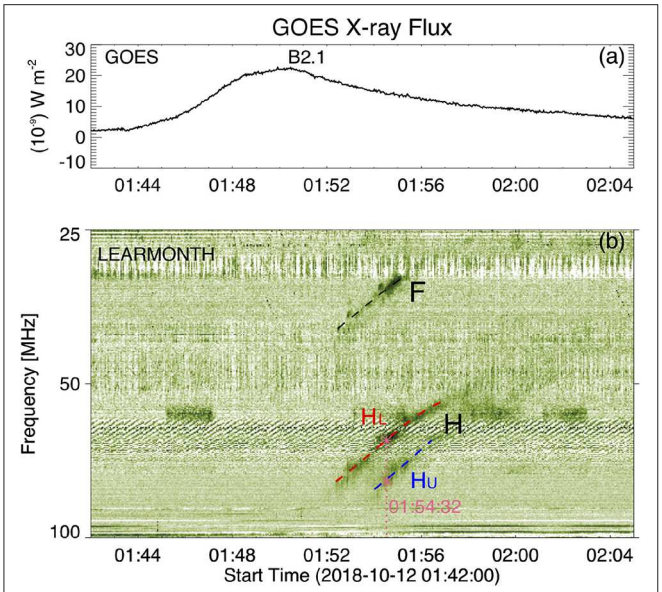

FIGURE 2 | GOES soft X-ray flux during Flare1 in 1–8 Å **(a)** and a radio dynamic spectrum from Learmonth showing the information about the associated Type II radio burst **(b)**. "F" indicates the fundamental frequency band and "H" mark the harmonic frequency band with the lower ("H_L") and higher ("H_U") splitting branches. The three curves along the fundamental (black), lower (red), and higher (blue) harmonic splitting bands are used to measure the frequency drifts and the height and speed of Shock1. The vertical line in **(b)** indicate the time at 01:54:32 UT. The two pink asterisks mark the frequencies which are applied to calculate the density compression of Shock1.

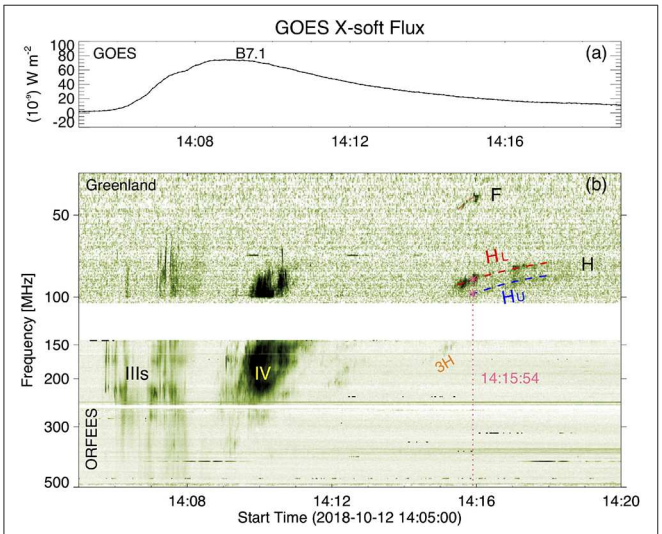

FIGURE 3 | GOES soft X-ray flux during Flare2 in 1–8 Å **(a)** and the composite radio dynamic spectrum from Greenland (25–105 MHz) and ORFEES (144–400 MHz) displaying the complicated radio bursts during E2 **(b)**. Along the red and blue dashed curves in **(b)** we will measure the frequency drift of the Type II radio burst and derive the height and speed of the associated shock (Shock2). The vertical line in **(b)** indicate the time at 14:15:54 UT. The two pink in **(b)** asterisks mark the frequencies which are used to calculate the density compressions of Shock2.

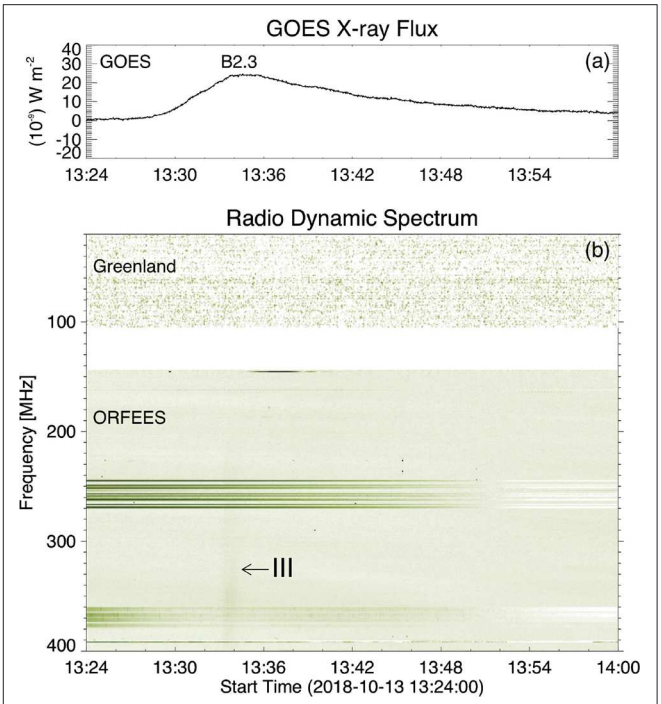

FIGURE 4 | GOES soft X-ray flux in 1–8 Å during Flare3 **(a)** and a composite radio dynamic spectrum from Greenland (25–105 MHz) and ORFEES (144–400 MHz) during E3 **(b).**

SBA may be caused by the interaction of CME or EUV waves with some coronal structures. Later, another expanding dome-like structure and a propagating diffusing wave front can be detected to propagate forward through SBA in the AIA and EUVI intensity images, which are indicated by the blue arrows with "2ND" in **Figures 6b3,b4**, **7b3**, respectively. It is probably a secondary wave.

3.6. Kinetics of the CMEs and Shocks

In order to explore the relationship between the CMEs and their associated Type II radio bursts, we studied the kinetics of CME1–CME3 and Shock1–Shock2, which are presented in **Figure 8**. For convenience, the identical colors represent the same bands or slits in **Figures 2**, **3**, **6**, **8**. Because there is no associated radioheliograph observation to be available, the exact locations of Type II burst sources are hard to be determined. Assuming that the electron density of the corona varies with heliocentric distance and the shock propagates along the radial direction, we first deduced the local plasma densities (n) of Shock1 and Shock2 from the observed frequency (f_p indicated by the black dashed line in **Figure 2** or $2f_p$ indicated by the red and blue dashed lines in **Figures 2**, **3**) in the light of their relationship

$$f_p = 8.98 \times 10^3 \sqrt{n} \tag{3}$$

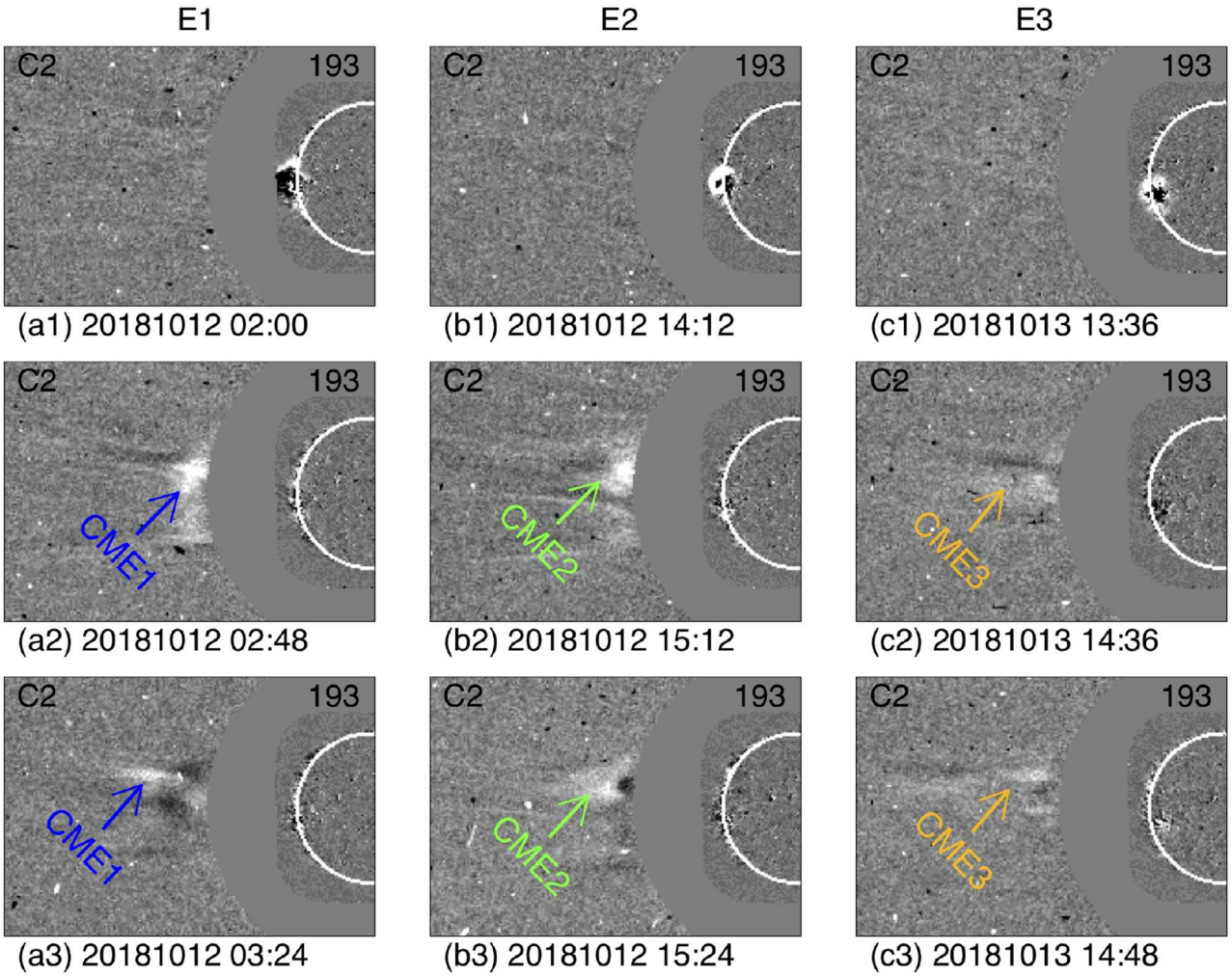

FIGURE 5 | The composite images of LASCO C2 WL and AIA 193 Å running difference images show the propagations of the three faint CMEs. **(a1–a3)** for CME1, **(b1–b3)** for CME2, and **(c1–c3)** for CME3.

The results are shown in **Figures 8a2,a3**. In order to further calculate the heights of Shock1 and Shock2 from the derived local plasma densities n, we apply the coronal plasma density model of Sittler and Guhathakurta (1999) (see also **Figure 8a1**),

$$n(z) = n_0\, a_1\, z^2\, e^{a_2\, z}[1 + a_3\, z + a_4\, z^2 + a_5\, z^3] \qquad (4)$$

$$z = 1/(1+y), a_1 = 0.001292, a_2 = 4.8039,$$

$$a_3 = 0.29696, a_4 = -7.1743, a_5 = 12.321,$$

where y is the height above the solar surface in solar radii and n_0 is the electron number density at the solar surface. We choose n_0 as 6.0×10^8 cm^{-3} considering the events under this study occurring in the period of solar activity minimum, which is similar to the value used in Ma et al. (2011). The time distance profiles of Shock1 and Shock2 calculated from the different splitting bands in the radio dynamic spectra are presented in the panels (c1) and (c2) of **Figure 8**, respectively. It can be seen that the heights of Shock1 and Shock2 approximately change from 1.45 $R_\odot$ to 1.60 $R_\odot$ and from 1.37 $R_\odot$ to 1.46 $R_\odot$, respectively.

The leading edges (LE1–LE3) of CME1–CME3 can be tracked in the AIA running difference images at 193 Å. For each event, we chose three different slits (s1a–s1c, s2a–s2c, and s3a–s3c in **Figure 6**) to make the time-distance slit images, which display the propagations of the leading edges along different directions. As examples, three time-distance diagrams from s1b, s2b and s3b are plotted in the panels (b1–b3) of **Figure 8**. According to the tracks or stripes in the slit images, we calculated the heights of LE1–LE3 and derived their speeds, which are shown by the diamonds in **Figures 8c1–c3,d1–d3**, respectively.

From **Figure 8c1**, it can be seen that although LE1 had moved out of the AIA's FOV when Shock1 began to appear, the development trend of the LE1's heights and the height variation of Shock1 suggest a high degree correlation between them.

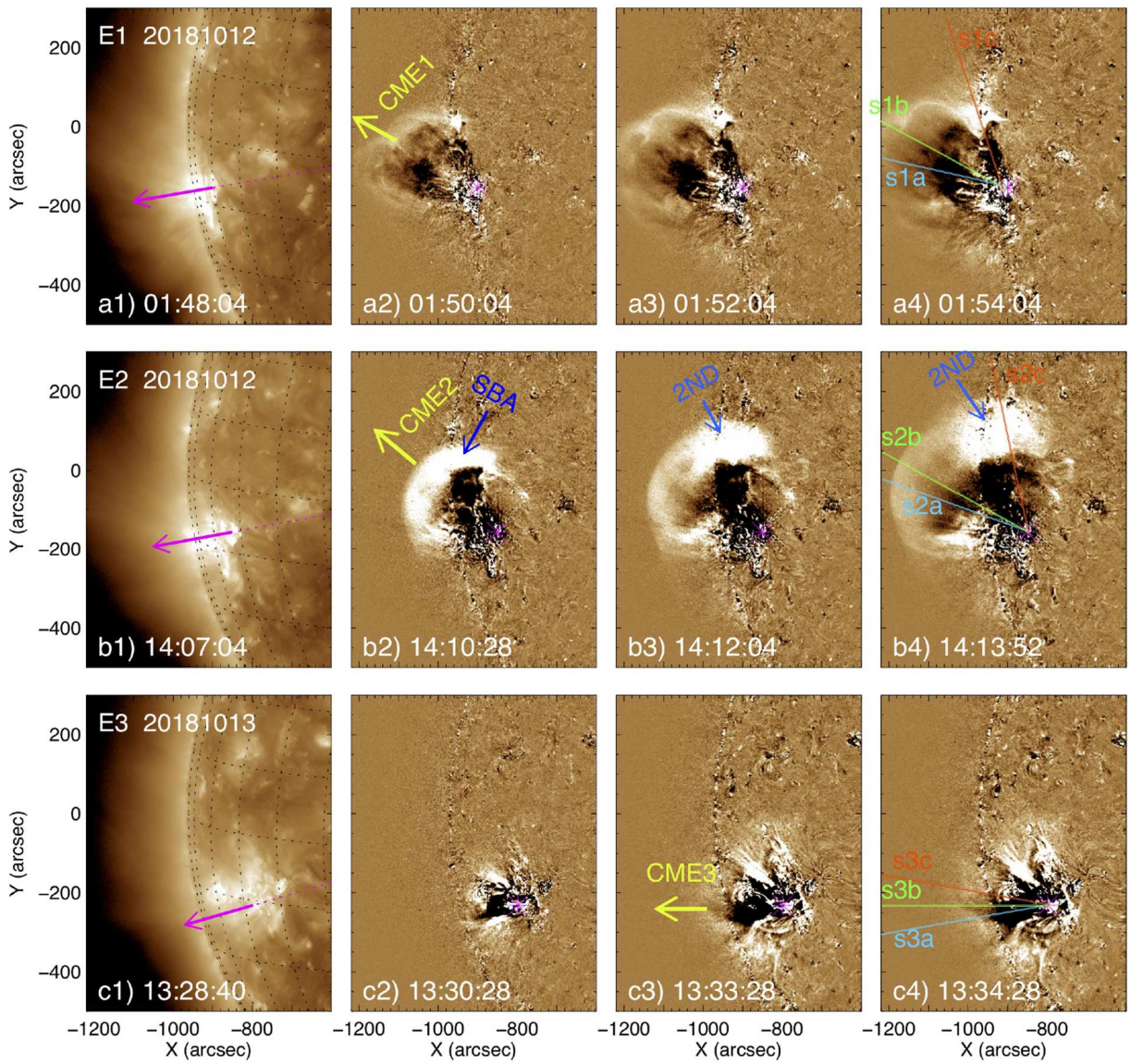

FIGURE 6 | The AIA 193 Å intensity images display the early evolutions of E1 (top), E2 (middle), and E3 (bottom). The panels in left column **(a1,b1,c1)** are original images and the rest panels **(a2–a4, b2–b4,c2–c4)** are base difference images. The pink arrows in **(a1–a3)** denote the heliocentric radial directions that passing through the eruption centers of E1, E2, and E3, respectively. The pink asterisks in panels **(a2–a4, b2–b4,c2–c4)** mark the centers of the eruptions. The yellow arrows in **(a2,b2,c3)** show the main eruption directions of CME1, CME2, and CME3, respectively. "SBA" **(b2)** and "2ND" **(b3–b4)** refer to a special brightening area and a secondary disturbance during E2. The lines in **(a4,b4,c4)** indicate the position of slits s1a–s1c, s2a–s2c, and s3a–s3c, respectively.

Figure 8c2 indicates a similar situation for LE2 and Shock2. Thus, it is likely that the two shocks corresponding to the two Type II radio bursts in E1 and E2 were separately triggered by the expanding of the leading edges of CME1 and CME2. In **Figures 8d1,d2**, it can be found that LE1 and LE2 have various speeds along different propagation directions. LE1 has the largest velocity of ∼320 km s^{-1} (azure diamonds in **Figure 8d1**) along s1a (azure line in **Figure 6a4**). The fastest speed of LE2 is ∼380 km s^{-1} (red diamonds in **Figure 8d2**), which was calculated along the slit s2c (red line in **Figure 6b4**).

The speeds of Shock1 and Shock2 derived from their heights are given in **Figures 8d1,d2**, respectively. It can be found that the shocks' speeds calculated along the different Type II bursts bands are also different. These different speeds represent the speeds of the downstream (blue pluses) and upstream (red and black pluses) shock regions, which might be distinct from each other.

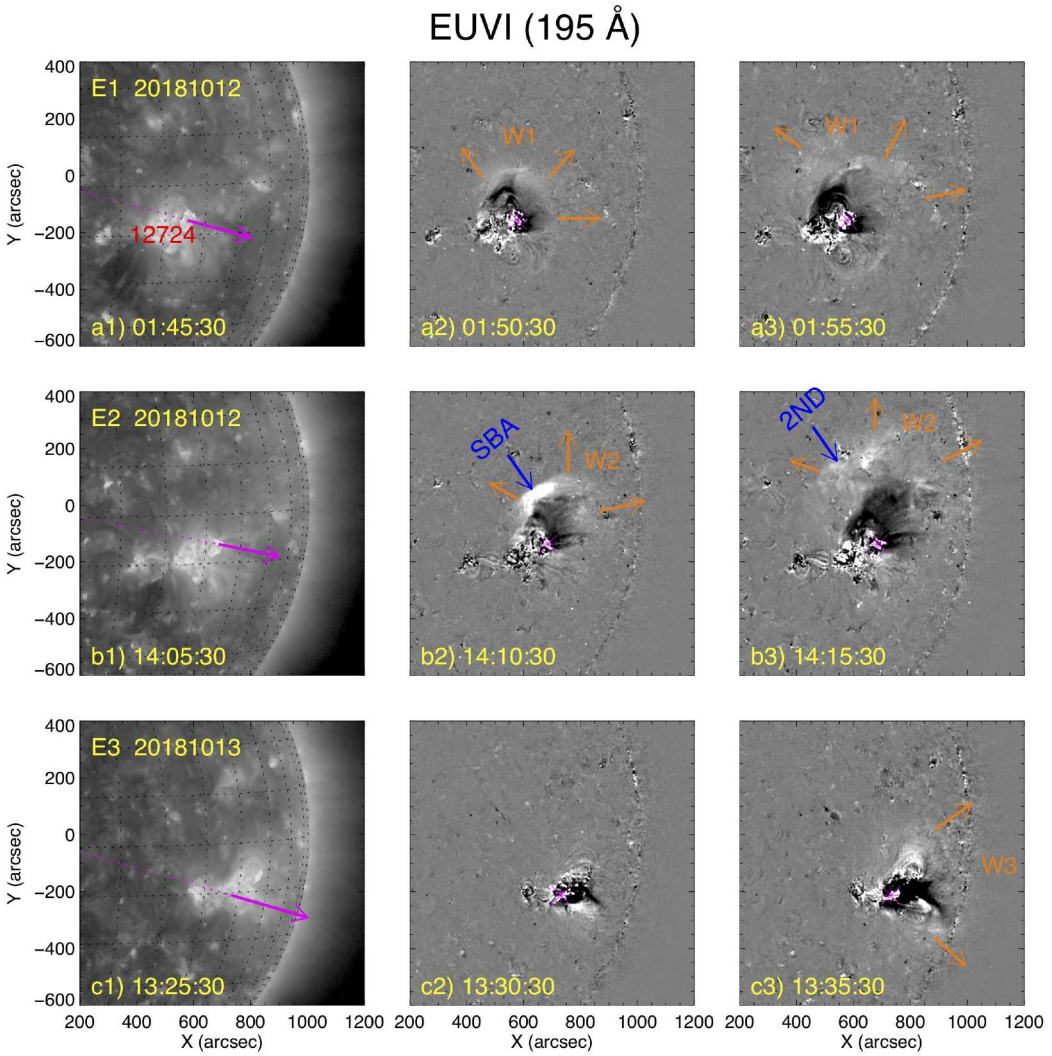

FIGURE 7 | The EUVI 195 Å intensity images show the evolutions of E1 **(a1–a3)**, E2 **(b1–b3)**, and E3 **(c1–c3)** from on-disk perspective. The left column **(a1,b1,c1)** are the original images and the rest panels give the base difference images. Same to **Figure 6**, the pink arrows in the left column images **(a1,b1,c1)** show the heliocentric radial directions through each eruption centers (pink asterisks) The orange arrows indicate the propagation directions of the associated EUV wave "W1" **(a2,a3)**, "W2" **(b2,b3)**, and "W3" **(c3)**.

In addition, the discrepancies of the speeds are also probably caused by the measurement errors. On average, Shock1 has an initial speed of ∼400 km s^{-1} and that of Shock2 is ∼430 km s^{-1}. According to the relationship between the shock's speed (V_s) and the local Alfvén speed V_A, i.e.,

$$M_A = \frac{V_s}{V_A} \tag{5}$$

the Alfvén speeds at the early phases of Shock1 (01:54:32 UT, indicated by the vertical line in **Figures 2b**, **8d1**) and Shock2 (14:15:54 UT, indicated by the vertical line in **Figures 3b**, **8d2**) can be deduced as ∼300 and ∼350 km s^{-1}, respectively. Compared with the fastest speeds of LE1 (∼320 km s^{-1}) and LE2 (∼380 km s^{-1}), the local Alfvén speeds are smaller. These results are in agreement with the scenario of piston-driven shock, supporting our conjecture that the CMEs in E1 and E2 excited their relevant shocks and Type II radio bursts. **Figure 8d3** shows that the leading edge of CME3 had a relatively slower speed (∼160 km s^{-1}) than LE1 and LE2. It is likely less than the local Alfvén speed, which might be the reason why Type II radio burst or shock is absent in E3.

3.7. Background Fields From PFSS Extrapolation

To probe the background field structures surrounding the eruption source area and their relationship with the eruptions, an extrapolation was performed using the potential field source surface (PFSS) model (e.g., Schatten et al., 1969; Schrijver and De Rosa, 2003) with a starting radius of 1.01 $R_\odot$. For better reliability, one HMI longitudinal magnetogram on 2018 Oct 13

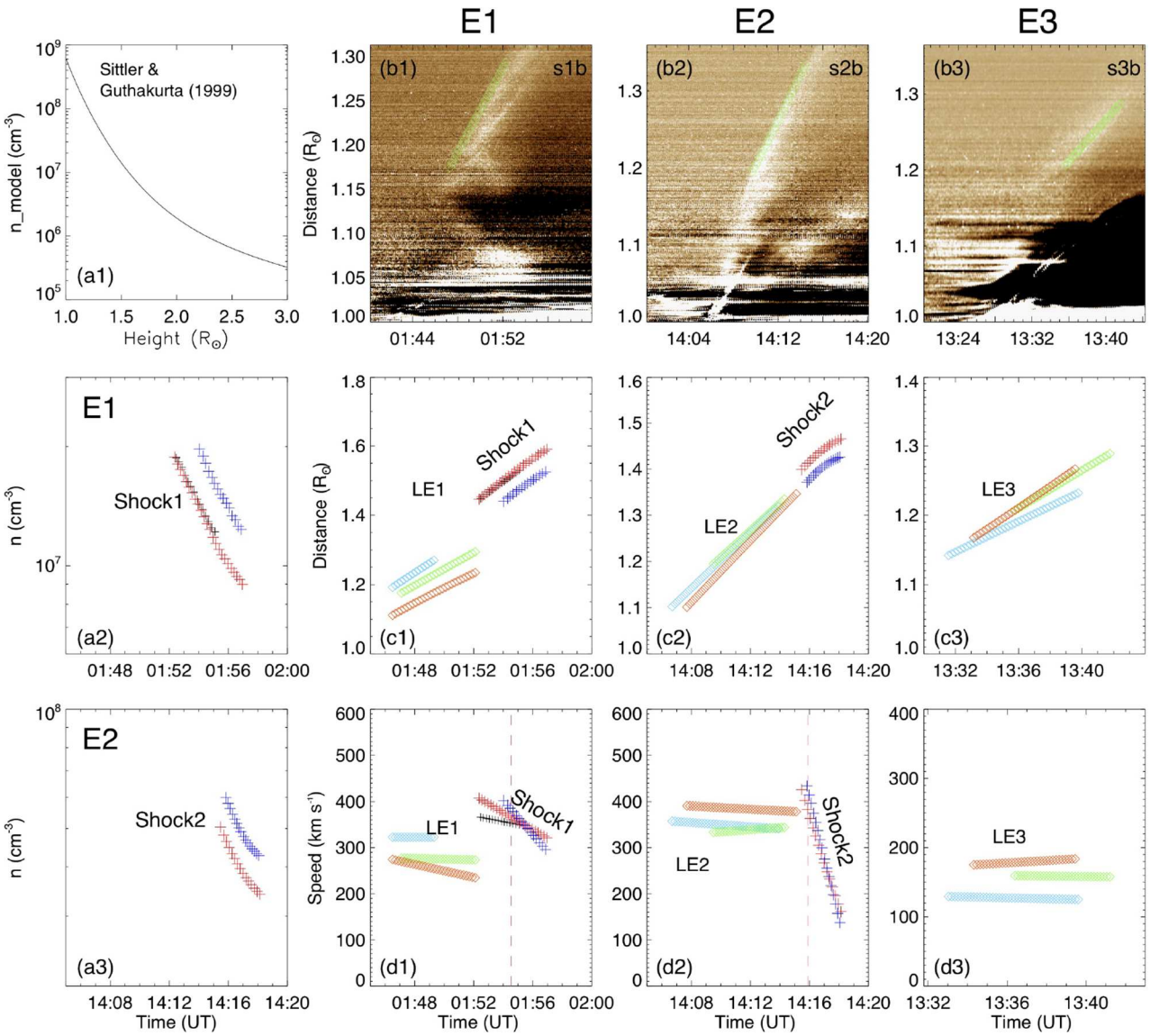

FIGURE 8 | (a1) Shows the electron density changing with the height base on the model of Sittler and Guhathakurta (1999). **(a2,a3)** Display the local plasma electron densities of Shock1 and Shock2 calculated from the observations of their associated Type II radio bursts. **(b1–b3)** Are the time-slit images showing the motions of LE1, LE2, and LE3 along the slits s1b, s2b, and s3b, respectively. **(c1–c3)** Display the heliocentric distances of LE1 (diamonds) and Shock1 (pluses), LE2 (diamonds) and Shock2 (pluses), and LE3 (diamonds), respectively. **(d1–d3)** Are the same to **(c1–c3)**, but for the speeds of LE1–LE3 and Shock1–Shock2. The identical colors in this figure represent the same bands or slits in **Figures 2**, **3**, **6**.

was applied to extrapolate the potential field. The magnetic field lines from the extrapolation are overlaid on the AIA 171 Å, EUVI 195 Å intensity images, HMI and rotated HMI magnetograms, as displayed by **Figures 9a–d**.

The HMI magnetogram in **Figure 9d** shows that AR 12724 mainly consists of the leading positive flux "P" and following negative flux "N," with some surrounding parasitic magnetic elements, such as the fluxes "n" and "p." In this panel, we also overlaid the profiles of the three filaments F1–F3, which are indicated by the red curves. It can be seen that F1 and F2 are located at the northwest of the AR and aligned along the magnetic neutral lines between N and p, while F3 lies in the AR's southeast region between the opposite polarity fluxes P and n. The spine directions of F1 and F2 are approximately from north to south, opposite to the east-west orientation of F3.

At the remote region to the north of AR 12724, we found some different magnetic loop systems, which are represented by the short dark blue field lines. Between these magnetic systems and the magnetic loops inside AR 12724, the magnetic quasi-separatrix layer (indicated by the yellow dashed line) may exist. That area is consistent with the place where the special brightening region SBA in E2 appeared. It is likely that SBA was

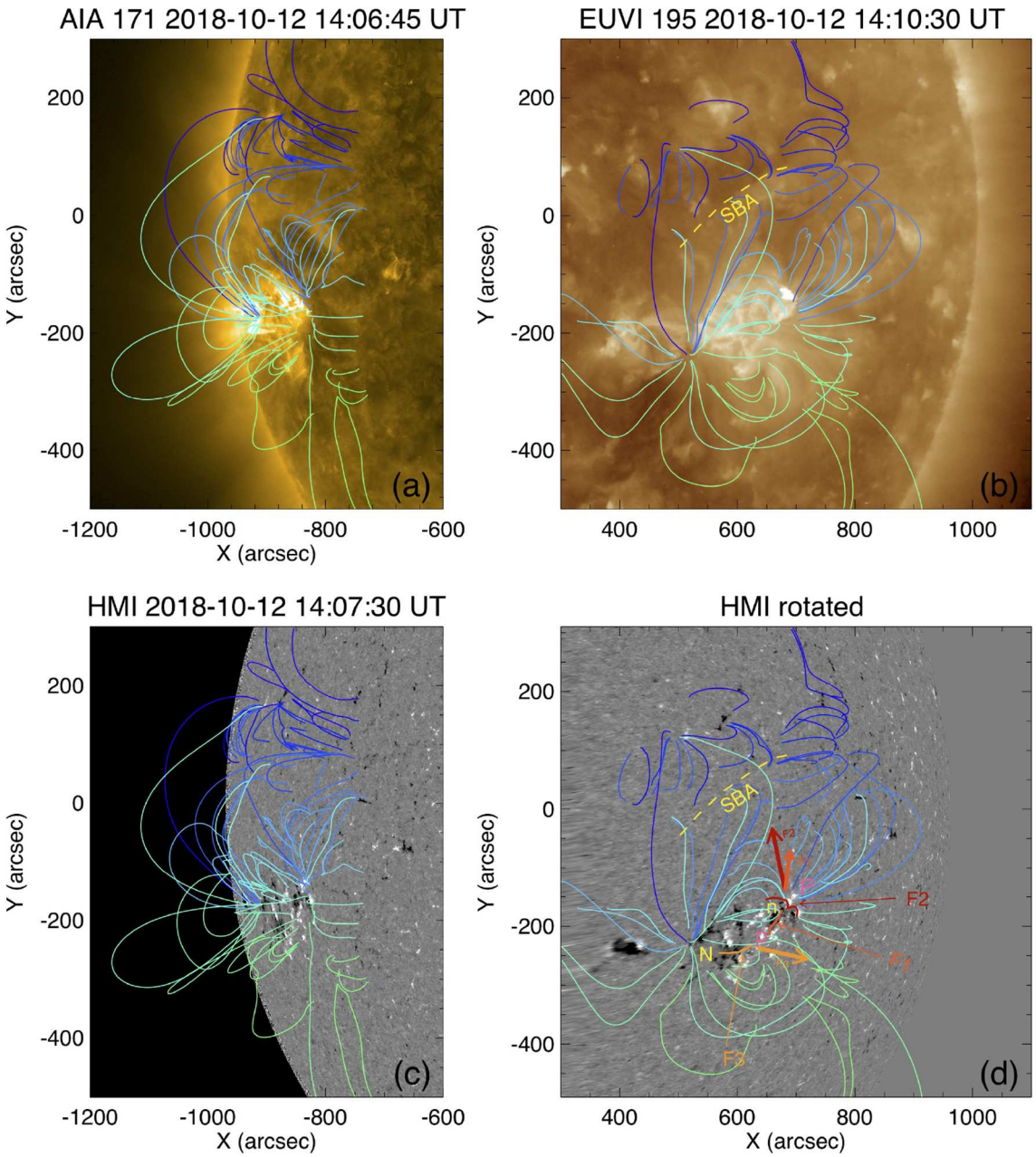

FIGURE 9 | The extrapolated magnetic field lines using the PFSS model are overlaid on the AIA intensity image **(a)**, the EUVI intensity image **(b)** and HMI magnetograms **(c,d)**. The yellow dashed curves in **(b,d)** indicate the location of the "SBA." "P" and "N" in **(d)** mark the leading and following magnetic fluxes of AR 12724. "p" and "n" in **(d)** denote the positive and negative parasitic magnetic elements surrounding N and P, respectively. The thick arrows in different colors in **(d)** point to the main eruption directions of F1–F3.

caused by the interaction between the north flank of CME2 and the magnetic separatrix layer.

4. SUMMARY AND DISCUSSION

Using radio dynamic spectra and dual perspective EUV observations, we investigate three successive solar eruptions (E1, E2, and E3) from the same active region AR 12724. All the eruptions were accompanied by a B-class flare and a poor WL CME. However, only the first two of them were observed to correlate with Type II radio bursts, suggesting the likely appearances of shocks (Shock1 and Shock2) only in the two events. From the radio dynamic spectra, we utilize the splitting bands of the Type II bursts to estimate the density jumps (1.44 and 1.30), Alfvén Mach numbers (1.35 and 1.23), and coronal Alfvén speeds (∼300 and ∼350 km s^{-1}) of Shock1 and Shock2. Through a comparative study, we found that

- The apparent speeds of the CMEs' leading edges (LE1–LE3) are different. LE3 has an obvious slower speed ($\sim$160 km s^{-1}) than LE1 ($\sim$320 km s^{-1}) and LE2 ($\sim$380 km s^{-1}). The speeds of LE1 and LE2 can exceed their corresponding local Alfvén speeds ($\sim$300 and $\sim$350 km s^{-1}).
- E1 and E2 originated from the northwest of AR 12724, while E3 took place from the AR's southeast region.
- The EUV imaging observations from two different perspective indicate that E1 and E2 erupted along the $\sim$45° north of their radial directions, while CME3 in E3 approximately propagated radially.

4.1. Trigger of Type II Radio Bursts

According to the *GOES* soft X-ray flux data, Flare3 is a B2.3-class flare and stronger than the B2.1 Flare1. However, Type II radio burst is associated with the weaker one. This is in agreement with the finding that the magnitudes of flares are not directly related to the occurrence of Type II radio bursts (e.g., Cliver et al., 1999). In addition, since all the eruptions took place from the same AR and all the associated flares are relatively weak (only B-class), it is hard to conclude that the Type II bursts studied here were initiated by the blast wave due to flares. Our calculations have shown that the speeds of LE1 and LE2 along certain directions can exceed the local coronal Alfvén speeds, which meet the requirements of the formation of a piston-driven shock. Thus, It would be more reasonable that the Type II bursts were triggered by their associated CMEs. On the other, it should be noted that the third eruption E3 has a different source region and eruption direction from E1 and E2. The coronal plasma and magnetic field environments that the erupting structures of E3 encountered would be also distinct from those of E1 and E2. The missing of Type II burst in E3 may be associated with this situation as well.

4.2. SBA and the Secondary Wave

In the eruption E2, a special brightening area SBA is detected where a magnetic separatrix may exist according to the results of the PFSS extrapolation (**Figure 9**). The occurrence or appearance of SBA in this event might be explained by this scenario: when the flank of CME2 and/or EUV wave W2 arrived the magnetic separatrix layer, it would be likely compressed and heated, which might give birth to SBA. Along with the occurrence of the reflection and refraction of the EUV wave near the magnetic separatrix, a secondary wave 2ND might be further produced and propagate outward. Similar situations can be found in some other studies (e.g., Ofman and Thompson, 2002; Shen and Liu, 2012; Chandra et al., 2016; Zheng et al., 2018). In addition, some studies have shown a close relationship between Type II radio bursts and such interactions (e.g., Feng et al., 2012; Kong et al., 2012; Shen et al., 2019). Using simultaneous radio and EUV imaging data, Chen et al. (2014) found that the source location of a solar type II radio burst coincides with the interface between CME EUV wave front and a nearby coronal ray structure, where an obvious EUV brightening also appeared. They conjectured that the CME streamer interactions may be important to the formation of type II radio burst. Unfortunately, there is no radioheliograph observation available for our study and we can not confirm the exact location of the type II burst in E2, but according to the results of Chen et al. (2014), it can be suspected that the special brightening area SBA corresponds to the source region of the type II burst in E2.

DATA AVAILABILITY STATEMENT

Publicly available datasets were analyzed in this study. This data can be found here: http://sdac.virtualsolar.org/cgi/search, https://rsdb.obs-nancay.fr, http://soleil.i4ds.ch/solarradio/callistoQuicklooks/.

AUTHOR CONTRIBUTIONS

SM downloaded and analyzed the data in both radio and EUV passband, and wrote the paper. HC analyzed the data in EUV passband and wrote the paper.

FUNDING

This work was supported by NSFC (11433006, 11533008, 11661161015, 11790300, 11790301, 11790304, 11941003, 11973057, and 41331068) and the B-type Strategic Priority Program of the Chinese Academy of Sciences, Grant No. XDB41000000.

ACKNOWLEDGMENTS

We were grateful to Prof. Jun Lin and Prof. Baolin Tan for their insightful suggestions and informative discussions. We acknowledge NASA's open data policy in using SDO data. STEREO is a mission in NASA's Solar Terrestrial Probes program. SOHO is a project of international collaboration between ESA and NASA. We were grateful to ORFEES, Learmonth and Greenland teams for offering the radio spectra data. We thank the referees for their constructive comments and suggestions.

REFERENCES

Benz, A. O., Monstein, C., Meyer, H., Manoharan, P. K., Ramesh, R., Altyntsev, A., et al. (2009). A world-wide net of solar radio spectrometers: e-CALLISTO. *Earth Moon Planets* 104, 277–285. doi: 10.1007/s11038-008-9267-6

Brueckner, G. E., Howard, R. A., Koomen, M. J., Korendyke, C. M., Michels, D. J., Moses, J. D., et al. (1995). The large angle spectroscopic coronagraph (LASCO). *Solar Physics*, 162:357.

Chandra, R., Chen, P. F., Fulara, A., Srivastava, A. K., and Uddin, W. (2016). Peculiar stationary EUV wave fronts in the eruption on 2011 May 11. *Astrophys. J.* 822:106. doi: 10.3847/0004-637X/822/2/106

Chen, P. F. (2016). Global coronal waves. *Am. Geophys. Union Geophys. Monogr. Ser.* 216, 381–394. doi: 10.1002/9781119055006.ch22

Chen, Y., Du, G., Feng, L., Feng, S., Kong, X., Guo, F., et al. (2014). A solar type II radio burst from coronal mass ejection-coronal ray interaction: simultaneous radio and extreme ultraviolet imaging. *Astrophys. J.* 787:59. doi: 10.1088/0004-637X/787/1/59

Cliver, E. W., Webb, D. F., and Howard, R. A. (1999). On the origin of solar metric type II bursts. *Sol. Phys*. 187, 89–114. doi: 10.1023/A:1005115119661

Dauphin, C., Vilmer, N., and Krucker, S. (2006). Observations of a soft X-ray rising loop associated with a type II burst and a coronal mass ejection in the 03 November 2003 X-ray flare. *Astron. Astrophys*. 455, 339–348. doi: 10.1051/0004-6361:20054535

Dodge, J. C. (1975). Source regions for type II radio bursts. *Sol. Phys*. 42, 445–459. doi: 10.1007/BF00149925

Dodson, H. W., Hedeman, E. R., and Owren, L. (1953). Solar flares and associated 200 Mc/sec radiation. *Astrophys. J*. 118:169. doi: 10.1086/145740

Eselevich, V. G., Eselevich, M. V., and Zimovets, I. V. (2019). Observations of a flare-generated blast wave in a pseudo coronal mass ejection event. *Sol. Phys*. 294:73. doi: 10.1007/s11207-019-1467-x

Eselevich, V. G., Eselevich, M. V., Zimovets, I. V., and Sharykin, I. N. (2017). Evidence for shock generation in the solar corona in the absence of coronal mass ejections. *Astron. Rep*. 61, 805–819. doi: 10.1134/S1063772917080030

Feng, S. W., Chen, Y., Kong, X. L., Li, G., Song, H. Q., Feng, X. S., et al. (2012). Radio signatures of coronal-mass-ejection-streamer interaction and source diagnostics of type II radio burst. *Astrophys. J*. 753:21. doi: 10.1088/0004-637X/753/1/21

Frassati, F., Susino, R., Mancuso, S., and Bemporad, A. (2019). Comprehensive analysis of the formation of a shock wave associated with a coronal mass ejection. *Astrophys. J*. 871:212. doi: 10.3847/1538-4357/aaf9af

Giovanelli, R. G., and Roberts, J. A. (1958). Optical observations of the solar disturbances causing type II radio bursts. *Aust. J. Phys*. 11:353. doi: 10.1071/PH580353

Gopalswamy, N., Lara, A., Kaiser, M. L., and Bougeret, J. L. (2001). Near-sun and near-earth manifestations of solar eruptions. *J. Geophys. Res*. 106, 25261–25278. doi: 10.1029/2000JA004025

Gosling, J. T., Hildner, E., MacQueen, R. M., Munro, R. H., Poland, A. I., and Ross, C. L. (1976). The speeds of coronal mass ejection events. *Sol. Phys*. 48, 389–397. doi: 10.1007/BF00152004

Grechnev, V. V., Lesovoi, S. V., Kochanov, A. A., Uralov, A. M., Altyntsev, A. T., Gubin, A. V., et al. (2018). Multi-instrument view on solar eruptive events observed with the Siberian Radioheliograph: from detection of small jets up to development of a shock wave and CME. *J. Atmos. Solar Terres. Phys*. 174, 46–65. doi: 10.1016/j.jastp.2018.04.014

Howard, R. A., Moses, J. D., Vourlidas, A., Newmark, J. S., Socker, D. G., Plunkett, S. P., et al. (2008). Sun earth connection coronal and heliospheric investigation (SECCHI). *Space Sci. Rev*. 136, 67–115. doi: 10.1007/s11214-008-9341-4

Huang, J., Démoulin, P., Pick, M., Auchére, F., Yan, Y. H., and Bouteille, A. (2011). Initiation and early development of the 2008 April 26 coronal mass ejection. *Astrophys. J*. 729:107. doi: 10.1088/0004-637X/729/2/107

Kaiser, M. L., Kucera, T. A., Davila, J. M., St. Cyr, O. C., Guhathakurta, M., and Christian, E. (2008). The STEREO mission: an introduction. *Space Sci. Rev*. 136, 5–16. doi: 10.1007/s11214-007-9277-0

Kennewell, J., and Steward, G. (2003). *Solar Radio Spectrograph [SRS] Data*. Sydney, NSW: IPS Radio and Space Serv.

Klassen, A., Pohjolainen, S., and Klein, K. L. (2003). Type II radio precursor and x-ray flare emission. *Sol. Phys*. 218, 197–210. doi: 10.1023/B:SOLA.0000013034.61996.c4

Klein, K.-L., Khan, J. I., Vilmer, N., Delouis, J.-M., and Aurass, H. (1999). X-ray and radio evidence on the origin of a coronal shock wave. *Astron. Astrophys*. 346, L53–L56.

Kong, X. L., Chen, Y., Li, G., Feng, S. W., Song, H. Q., Guo, F., et al. (2012). A broken solar type II radio burst induced by a coronal shock propagating across the streamer boundary. *Astrophys. J*. 750:158. doi: 10.1088/0004-637X/750/2/158

Lemen, J. R., Title, A. M., Akin, D. J., Boerner, P. F., Chou, C., Drake, J. F., et al. (2012). The atmospheric imaging assembly (AIA) on the solar dynamics observatory (SDO). *Sol. Phys*. 275, 17–40. doi: 10.1007/s11207-011-9776-8

Liu, W., and Ofman, L. (2014). Advances in observing various coronal EUV waves in the SDO era and their seismological applications. *Sol. Phys*. 289, 3233–3277. doi: 10.1007/s11207-014-0528-4

Long, D. M., Bloomfield, D. S., Chen, P. F., Downs, C., Gallagher, P. T., Kwon, R. Y., et al. (2017). Understanding the physical nature of coronal "EIT waves". *Sol. Phys*. 292:7. doi: 10.1007/s11207-016-1030-y

Ma, S., Raymond, J. C., Golub, L., Lin, J., Chen, H., Grigis, P., et al. (2011). Observations and interpretation of a low coronal shock wave observed in the EUV by the SDO/AIA. *Astrophys. J*. 738:160. doi: 10.1088/0004-637X/738/2/160

Ma, S., Wills-Davey, M. J., Lin, J., Chen, P. F., Attrill, G. D. R., Chen, H., et al. (2009). A new view of coronal waves from STEREO. *Astrophys. J*. 707, 503–509. doi: 10.1088/0004-637X/707/1/503

Mann, G., Classen, T., and Aurass, H. (1995). Characteristics of coronal shock waves and solar type II radio bursts. *Astron. Astrophys*. 295:775.

Maxwell, A., and Thompson, A. R. (1962). Spectral observations of solar radio bursts. II. Slow-drift bursts and coronal streamers. *Astrophys. J*. 135:138. doi: 10.1086/147254

Nelson, G. J., and Melrose, D. B. (1985). "Type II bursts," in *Solar Radiophysics: Studies of Emission From the Sun at Metre Wavelengths (A87-13851 03-92)*, eds D. J. McLean and N. R. Labrum (Cambridge; New York, NY: Cambridge University Press), 333–359.

Nindos, A., Alissandrakis, C. E., Hillaris, A., and Preka-Papadema, P. (2011). On the relationship of shock waves to flares and coronal mass ejections. *Astron. Astrophys*. 531:A31. doi: 10.1051/0004-6361/201116799

Nindos, A., Aurass, H., Klein, K. L., and Trottet, G. (2008). Radio emission of flares and coronal mass ejections. *Sol. Phys*. 253, 3–41. doi: 10.1007/s11207-008-9258-9

Ning, Z. (2016). Bi-directional flows in a C-class solar flare. *Astrophys. Space Sci*. 361:22. doi: 10.1007/s10509-015-2606-y

Ofman, L., and Thompson, B. J. (2002). Interaction of EIT waves with coronal active regions. *Astrophys. J*. 574, 440–452. doi: 10.1086/340924

Payne-Scott, R., Yabsley, D. E., and Bolton, J. G. (1947). Relative times of arrival of bursts of solar noise on different radio frequencies. *Nature* 160, 256–257. doi: 10.1038/160256b0

Pesnell, W. D., Thompson, B. J., and Chamberlin, P. C. (2012). The solar dynamics observatory (SDO). *Sol. Phys*. 275, 3–15. doi: 10.1007/s11207-011-9841-3

Reid, H. A. S., and Ratcliffe, H. (2014). A review of solar type III radio bursts. *Res. Astron. Astrophys*. 14, 773–804. doi: 10.1088/1674-4527/14/7/003

Schatten, K. H., Wilcox, J. M., and Ness, N. F. (1969). A model of interplanetary and coronal magnetic fields. *Sol. Phys*. 6, 442–455. doi: 10.1007/BF00146478

Schrijver, C. J., and De Rosa, M. L. (2003). Photospheric and heliospheric magnetic fields. *Sol. Phys*. 212, 165–200. doi: 10.1023/A:1022908504100

Shen, Y., Chen, P. F., Liu, Y. D., Shibata, K., Tang, Z., and Liu, Y. (2019). First unambiguous imaging of large-scale quasi-periodic extreme-ultraviolet wave or shock. *Astrophys. J*. 873:22. doi: 10.3847/1538-4357/ab01dd

Shen, Y., and Liu, Y. (2012). Simultaneous observations of a large-scale wave event in the solar atmosphere: from photosphere to corona. *Astrophys. J. Lett*. 752:L23. doi: 10.1088/2041-8205/752/2/L23

Sittler, E. C. J.r., and Guhathakurta, M. (1999). Semiempirical two-dimensional magnetohydrodynamic model of the solar corona and interplanetary medium. *Astrophys. J*. 523, 812–826. doi: 10.1086/307742

Smerd, S. F., and Dulk, G. A. (1971). In *Solar Magnetic Fields, Vol. 43 of IAU Symposium*, ed R. Howard (Dordrecht: Reidel), 616. doi: 10.1017/S0074180900023081

Smerd, S. F., Sheridan, K. V., and Stewart, R. T. (1974). "On split-band structure in type II radio bursts from the sun," in *Coronal Disturbances, Vol. 57 of IAU Symposium*, ed G. A. Newkirk (Dordrecht; Boston: Reidel), 389. doi: 10.1017/S0074180900234542

Stewart, R. T. (1985). *Moving Type IV Bursts*. Cambridge, New York, NY: Cambridge University Press. 361–383.

Su, W., Cheng, X., Ding, M. D., Chen, P. F., and Sun, J. Q. (2015). A type II radio burst without a coronal mass ejection. *Astrophys. J*. 804:88. doi: 10.1088/0004-637X/804/2/88

Swarup, G., Stone, P. H., and Maxwell, A. (1960). The association of solar radio bursts with flares and prominences. *Astrophys. J*. 131:725. doi: 10.1086/146885

Tan, B., Mészárosová, H., Karlický, M., Huang, G., and Tan, C. (2016). Microwave type III pair bursts in solar flares. *Astrophys. J*. 819:42. doi: 10.3847/0004-637X/819/1/42

Vlahos, L., Gergely, T. E., and Papadopoulos, K. (1982). Electron acceleration and radiation signatures in loop coronal transients. *Astrophys. J*. 258, 812–822. doi: 10.1086/160128

Vršnak, B. (2001). Solar flares and coronal shock waves. *J. Geophys. Res*. 106, 25291–25300. doi: 10.1029/2000JA004009

Vršnak, B., and Cliver, E. W. (2008). Origin of coronal shock waves. *Sol. Phys*. 253, 215–235. doi: 10.1007/s11207-008-9241-5

Vršnak, B., Magdalenić, J., Aurass, H., and Mann, G. (2002). Band-splitting of coronal and interplanetary type II bursts. II. Coronal magnetic field and Alfvén velocity. *Astron. Astrophys*. 396, 673–682. doi: 10.1051/0004-6361:20021413

Warmuth, A. (2015). Large-scale globally propagating coronal waves. *Living Rev. Sol. Phys*. 12:3. doi: 10.1007/lrsp-2015-3

Wild, J. P., and McCready, L. L. (1950). Observations of the spectrum of high-intensity solar radiation at metre wavelengths. I. The apparatus and spectral types of solar burst observed. *Aust. J. Sci. Res. A Phys. Sci.* 3:387. doi: 10.1071/CH9500387

Wild, J. P., Murray, J. D., and Rowe, W. C. (1954). Harmonics in the spectra of solar radio disturbances. *Aust. J. Phys*. 7:439. doi: 10.1071/PH540439

Wuelser, J.-P., Lemen, J. R., Tarbell, T. D., Wolfson, C. J., Cannon, J. C., Carpenter, B. A., et al. (2004). "EUVI: the STEREO-SECCHI extreme ultraviolet imager," in *Proceedings of the SPIE, Vol. 5171 of Society of Photo-Optical Instrumentation Engineers (SPIE) Conference Series*, eds S. Fineschi and M. A. Gummin (San Diego, CA), 111–122. doi: 10.1117/12.506877

Yan, Y., Pick, M., Wang, M., Krucker, S., and Vourlidas, A. (2006). A radio burst and its associated CME on March 17, 2002. *Sol. Phys*. 239, 277–292. doi: 10.1007/s11207-006-0202-6

Zheng, R., Chen, Y., Feng, S., Wang, B., and Song, H. (2018). An extreme-ultraviolet wave generating upward secondary waves in a streamer-like solar structure. *Astrophys. J. Lett*. 858:L1. doi: 10.3847/2041-8213/aabe87

Conflict of Interest: The authors declare that the research was conducted in the absence of any commercial or financial relationships that could be construed as a potential conflict of interest.

Advantages of publishing in Frontiers

OPEN ACCESS
Articles are free to read for greatest visibility and readership

FAST PUBLICATION
Around 90 days from submission to decision

HIGH QUALITY PEER-REVIEW
Rigorous, collaborative, and constructive peer-review

TRANSPARENT PEER-REVIEW
Editors and reviewers acknowledged by name on published articles

Frontiers
Avenue du Tribunal-Fédéral 34
1005 Lausanne | Switzerland

Visit us: www.frontiersin.org
Contact us: info@frontiersin.org | +41 21 510 17 00

REPRODUCIBILITY OF RESEARCH
Support open data and methods to enhance research reproducibility

DIGITAL PUBLISHING
Articles designed for optimal readership across devices

FOLLOW US
@frontiersin

IMPACT METRICS
Advanced article metrics track visibility across digital media

EXTENSIVE PROMOTION
Marketing and promotion of impactful research

LOOP RESEARCH NETWORK
Our network increases your article's readership